Cronfa
Swansea University's Research Repository

Computational Tools and Experimental Methods for the Development of Passive Prosthetic Feet

by

Benjamin William Morgan



Swansea University
Prifysgol Abertawe

Submitted to Swansea University in the fulfilment of the requirement for the Degree of

Doctor of Engineering in Materials, Modelling, and Manufacturing

2021

Copyright: The author, Benjamin W. Morgan, 2022. Released under the terms of a Creative Commons Attribution-Non-Commercial-Share Alike (CC-BY-NC-SA) License. Third party content is excluded for use under the license terms.

Computational tools and experimental methods for the development of passive prosthetic feet

by

Benjamin William Morgan

Abstract

Modern prosthetic foot designs are incredibly diverse in comparison to what was offered to amputees at the turn of the millennium. Powered ankles can supply natural levels of joint torque, whilst passive feet continue to optimise for kinematic goals. However, most passive feet still do not solve the issue of unhealthy loads, and an argument can be made that optimisation methods have neglected the less active and elderly amputee. This thesis creates a framework for a novel approach to prosthetic foot optimisation by focusing on the transitionary motor tasks of gait initiation and termination.

An advanced FEA model has been created in ANSYS® using boundary conditions derived from an ISO testing standard that replicates stance phase loading. This model can output standard results found in the literature and goes beyond by parameterising the roll-over shape within the software using custom APDL code. Extensive contact exploration and an experimental study have ensured the robustness of the model. Subject force and kinematic data can be used for specific boundary conditions, which would allow for easy adaptation to the transitionary motor tasks.

This FEA model has been used in the development of prosthetic experiment tool, which can exchange helical springs to assess effects of small changes in stiffness on gait metrics. A rigorous design methodology was employed for all components, including parametric design studies, response surface optimisation, and ISO level calculations. The design has been manufactured into a working prototype and is ready for clinical trials to determine its efficacy.

The conclusion of this framework is in the development of an experimental method to collect subject data for use in the models. A pilot study uncovered reliable protocols, which were then verified with ANOVA statistics. Proportional ratios were defined as additions to metric peak analyses already found in the literature. These tools are ready for deployment in full clinical trials with amputees, so that a new prosthetic optimisation pathway can be discovered for the benefit of less active or elderly amputees.

Declaration and Statements

Declaration

This work has not previously been accepted in substance for any degree and is not being concurrently submitted in candidature for any degree.

Signed ..[redacted]..... (candidate)

Date .....18/10/2022.....

Statement 1

This thesis is the result of my own investigations, except where otherwise stated. Other sources are acknowledged by footnotes giving explicit references. A bibliography is appended.

Signed ..[redacted]..... (candidate)

Date .....18/10/2022.....

Statement 2

I hereby given consent for my thesis, if accepted, to be available for photocopying and inter-library loan, and for the title and summary to be made available to outside organisations.

Signed ..[redacted]..... (candidate)

Date .....18/10/2022.....

Statement 3

The University's ethical procedures have been followed and, where appropriate, that ethical approval has been granted.

Signed ..[redacted]..... (candidate)

Date .....18/10/2022.....

Acknowledgements

Firstly, I would like to thank my primary supervisor, Dr Rajesh Ransing for the support and guidance over the entire duration of this doctoral body of research. His enthusiasm and patience have been invaluable to the completion of this work, and I look forward to continuing our research together, and discussing the next stages over a few beers.

I would also like to extend my gratitude to Dr Nicholas Owen, my second supervisor. His expertise in the field of biomechanics and advice for lab procedures was vital to the completion of the experimental studies. He was also excellent company during the 16-hour layover on the trip back from India!

My research would not have been possible without the M2A scheme and their team at Swansea University, and my sponsors; the Welsh European Funding Office, and Perpetuus Advanced Materials. To Ian Walters and Afshin Tarat, the Director and Chief Scientist at Perpetuus; I am incredibly grateful for your support in funding this project and making yourselves available for advice.

Finally, I would to express my eternal gratitude to my friends and family, all of whom have been incredibly patient when I would disappear into my work, yet still show their love and support whenever I would see them.

Contents

1 Introduction **1**

1.1 Scope . . . 1

1.1.1 Amputee Situation . . . 2

1.1.2 Current Research Trends . . . 4

1.2 The Research Goal and Objectives . . . 6

1.2.1 Objectives . . . 7

1.2.2 Novel Contributions . . . 8

1.3 Summary . . . 9

2 Literature Review **11**

2.1 Biomechanics . . . 11

2.1.1 Terminology and Key Conventions . . . 11

2.1.2 Introduction to the Gait Cycle . . . 12

2.1.3 Musculoskeletal System & Work . . . 17

2.1.4 Kinetics & Power . . . 25

2.1.5 Motor Redundancy & Kinematics . . . 30

2.1.6 Ankle-foot Complex . . . 36

2.1.7 Summary . . . 41

2.2 Prosthetic foot design . . . 41

2.2.1 Early passive prosthetics . . . 41

2.2.2 Powered Robotic Revolution . . . 44

2.2.3 Advancing Passive Feet . . . 46

2.2.4 Summary . . . 50

2.3 Experimental Studies & Procedures . . . 52

2.3.1 Gait initiation . . . 52

2.3.2 Kinematic Limitations . . . 53

2.4 Revisiting the Research Question . . . 54

3 Concept & ISO Models **56**

3.1 Concept Design . . . 56

3.2 Initial Model Testing . . . 59
3.2.1 ISO 10328 . . . 59
3.2.2 Contact Definition Validation . . . 61
3.2.3 ISO 10328 Criticism . . . 72
3.3 ISO 22675 Model . . . 73
3.3.1 Updated Ansys Geometry & Materials . . . 77
3.3.2 Contact & Joint Pair Definitions . . . 81
3.3.3 Boundary Conditions . . . 83
3.3.4 Initial Mesh & Analysis Settings . . . 91
3.3.5 Heel Contact Convergence Study . . . 92
3.3.6 Forefoot Mesh Dependency Study . . . 96
3.3.7 Final mesh & contact settings . . . 97
3.3.8 APDL Script: Roll-over Shape . . . 100
3.4 Concept ISO 22675 Results . . . 102
3.5 Summary . . . 105

4 Prosthetic Design Tool 106
4.1 Concept Reflection . . . 106
4.1.1 First Design Revision . . . 108
4.2 Rethinking the Design . . . 109
4.2.1 Energy Storage: Spring . . . 110
4.2.2 Reconsidering the Cam . . . 117
4.2.3 Shaping the Foot with N.U.R.B.S . . . 121
4.2.4 The Revised Second Design . . . 126
4.3 Prototype Optimisation . . . 128
4.3.1 Revisiting the Links . . . 129
4.3.2 Strengthening the Gears . . . 134
4.3.3 Foot Structure Parameterisation . . . 144
4.3.4 Minor Components . . . 153
4.3.5 Housing . . . 155
4.3.6 Lever Arm . . . 157
4.4 Final Prototype Design . . . 158
4.4.1 Manufacture . . . 159
4.4.2 Design Specification Appraisal . . . 161
4.5 Summary . . . 162

5 Biomechanics Experiments 163
5.1 Pilot Study . . . 163

5.1.1 Justification of the method . . . 163
5.1.2 Subjects . . . 165
5.1.3 Method . . . 165
5.1.4 Data Analysis . . . 166
5.1.5 Results . . . 169
5.1.6 Discussion . . . 172
5.2 Larger Study . . . 177
5.2.1 Subjects . . . 177
5.2.2 Method . . . 178
5.2.3 Data Analysis . . . 179
5.2.4 Results & Discussion . . . 180
5.3 Future experimental work . . . 187
5.4 Summary . . . 190

6 Conclusion **191**
6.1 Main Contributions . . . 191
6.2 Limitations . . . 193
6.3 Future Directions . . . 194

References **196**

A PC Specifications **i**

B MATLAB Code **ii**
B.1 NURBS Interpolation Code . . . ii
B.1.1 Master Control File . . . ii
B.1.2 Parameter Function . . . iv
B.1.3 Knot Function . . . iv
B.1.4 Control Point Function . . . v
B.1.5 NURBS Function . . . vii

C ISO Standards **ix**
C.1 Prosthetics . . . ix
C.1.1 ISO 22675:2016 . . . ix

D ANSYS **xi**
D.1 Intermediate Material Study . . . xi
D.1.1 Materials & Mechanical Properties . . . xi
D.2 Link FEA Data . . . xiii
D.3 APDL Code . . . xiii

D.3.1 Maximum Static Stiffness xiii
D.3.2 Rollover Shape Extraction xv
D.3.3 Plate Spring Gap Close xxiii
D.4 Foot Structure DOE xxv
D.4.1 Heel Parameter Study xxv
D.4.2 Response Surface - Goodness of Fit Metrics xxvi
D.5 Parameter Correlation xxvi
D.5.1 Sample Generation xxvi
D.5.2 Correlation Coefficient methods xxvi
D.6 Design of Experiments xxviii
D.6.1 Terminology xxviii
D.6.2 Central Composite Design (CCD) xxix
D.6.3 Box-Behnken xxx
D.6.4 Optimal Space Filling Design (OSF) xxx
D.7 Foot Structure Composite Model xxxi
D.8 Housing Supplementary Data & Results xxxiii

E Supplementary Design Data xxxiv
E.1 Composite Spring Study Setup xxxiv
E.2 Helical Compression Spring xxxvi
E.3 Gear Data xxxviii
E.3.1 Involute Gear Generation in CAD xxxviii
E.3.2 ISO Strength Calculation Factors xxxix
E.4 Technical Drawings xlv

F Biomechanics study xlix
F.1 Ethics, Consent, and Health questionnaire xlix

List of Figures

1.1 Prosthetic designs found in research 5
1.2 The prosthetic designs developed as part of the LLTE project at MIT [3]. 6

2.1 Anatomical reference diagrams 12
2.2 Gait cycle diagrams and terminology 13
2.3 Simple inverted pendulum diagram 14
2.4 Healthy and amputee gait initiation CoP paths 15
2.5 Plots of joint power from experiments on trans-tibial gait with increasing steady-state walking speed [74] 16
2.6 Simple diagram representing the potential to kinetic energy transfer of a frictionless swinging pendulum. 18
2.7 A refined concept model of the inverted pendulum theory by Kuo et al. [87] 19
2.8 Comparison diagram demonstrating the similarities of a dynamic walking model to a dynamic walking human [91] 20
2.9 Plots of power and element length change for muscles and tendons in a model of a single contraction 22
2.10 Diagram that illustrates the contributions of muscle modules to four phases of the gait cycle [117] 24
2.11 Three components of the GRF vector during stance 26
2.12 Plots taken from the PCA evaluation of vertical GRF [136] 29
2.13 Joint moment profiles for an amputee 32
2.14 Results of optimising amputee gait for kinetic joint symmetry, taken from [150] 33
2.15 Figures displaying the adaptive capabilities of the motor system [159] 35
2.16 The activation of different ankle joints at three key stages of the gait cycle [163]. 36
2.17 Results from a study on the timing of energy release 38

2.18 Figures taken from the study on combined models to capture distal structure behaviour [172] . . . 39
2.19 Plots of ankle quasi-stiffness through-out stance . . . 40
2.20 Cross sections of early SACH feet . . . 42
2.21 Plots of mechanical power during stance [7] . . . 43
2.22 The commercially available bionic feet, developed from research in US universities . . . 45
2.23 The nylon prototype foot manufactured using selective laser sintering [49] . . . 47
2.24 A visual representation of the optimised keel using the LLTE method 48
2.25 Schematics of the CESR and VSPA feet . . . 49
2.26 A tree diagram of prosthetic feet categories developed in research . 51
2.27 Anterior-posterior ground reaction forces from above-knee amputee subjects . . . 53

3.1 Isometric and exploded views of concept prosthetic foot . . . 57
3.2 Cross-section diagram of concept design, detailing phases in the loading operation of the TER system . . . 58
3.3 Setup diagrams taken from ISO 10328 . . . 60
3.4 Experimental testing rig model . . . 62
3.5 Diagram of FEA model setup using boundary conditions taken from ISO 10328 . . . 63
3.6 Photos taken of the validation experiment setup . . . 65
3.7 Experimental data in sub-plots . . . 67
3.8 Experimental data, basic metrics plot . . . 68
3.9 Comparison plot of simulation results, and experimental range & mean metrics . . . 69
3.10 Cumulative distribution plots of experimental and simulation data . 71
3.11 The sinusoidal waveforms defined in ISO 10328 . . . 73
3.12 Coordinate system used in the setup of tests defined by ISO 22675 [239] . . . 74
3.13 Diagrams of test structure used in ISO 22675 testing . . . 75
3.14 Diagram of the complete test apparatus for ISO 22675 . . . 76
3.15 Geometry setup for the static tests of ISO 22675 . . . 78
3.16 Contact pairs for ISO 22675 concept model . . . 82
3.17 Appendix diagram taken from ISO 22675, used in defining custom test force . . . 85
3.18 Experimental data was taken from a walking study . . . 86

3.19 Plot and diagram demostrating experimental ISO data 87
3.20 Mesh used for the initial simulation of forefoot test condition 91
3.21 The initial stress plot of heel test condition 93
3.22 Stress results from heel contact convergence study 94
3.23 Stress plot from the converged heel study 95
3.24 Stress plot from the initial simulation of the forefoot mesh study. Notice the same stress singularity at the site of first contact. 96
3.25 Converged solution that had settings left to the solver to determine. 97
3.26 Final mesh of concept model and Element schematics 99
3.27 Plots of the kinematic data, as it is transformed between different co-ordinate systems 100
3.28 A flowchart diagram of the rollover shape optimisation loop. 102
3.29 Simulation results from the P3 proof load on the heel test condition 103
3.30 Bar chart of von-Mises stress for all three P-levels of the Proof Test 103
3.31 A selection of results from studies where the housing component was made flexible 104
3.32 A progression of stills taken from the P3 cyclic study 105

4.1 Section view of CAD model, and schematic of mechanism principle 107
4.2 Section profile and front view of the first design revision 108
4.3 Plotting the wire diameter against tensile strength on a logarithmic scale 112
4.4 Scatter and Histogram plots of the Simulink spring parameter set. . 114
4.5 Contour plots of the Simulink parameter design space 115
4.6 Results of the Spearman Ranking correlation, generated from the Simulink parameter study. 116
4.7 A goodman indicating the fatigue life of the spring for three different life cycle levels 118
4.8 Cam design nomenclature 119
4.9 Plots of various cam characteristics 120
4.10 Generated cam profile using the sinusoidal equations within the CamTrax64 software built by Camnetics Inc. 121
4.11 A polynomial cubic curve composed of three sections 123
4.12 Diagrams of the truncated triangular table of basis functions 124
4.13 Plots generated using the NURBS MATLAB program 127
4.14 The second design iteration featuring the revised mechanism and composite foot springs. 128
4.15 Link DoE model and diagram 129

4.16 Sensitivity chart and response surface from the link DoE study . . . 131
4.17 A detailed version of the link schematic diagram 132
4.18 FEA setup for the plate link parameter study 133
4.19 Schematic diagrams of pinion torque components 134
4.20 A screenshot of one of the Excel tables generated to filter out initial gear pairings 135
4.21 Diagram from a textbook, detailing the pressure angle and line of action between the teeth of two mating gears [253]. 136
4.22 Diagrams of early derivations for bending stress on the left [254] and contact stress on the right [259]. 137
4.23 Plots of safety factor for contact and bending stress calculations. . . 142
4.24 Setup and results of the FEA bending stress model for the chosen gear pair. 143
4.25 Spline sketches created from points generated in the MATLAB NURBS program 145
4.26 The parameter points setup along the profile of the foot 146
4.27 Geometry models for the heel (left) and forefoot (right) loading conditions. 147
4.28 Convergence graphs and stress plots from the mesh studies completed on the forefoot and heel setup 148
4.29 A parameter correlation and determination matrix for the forefoot parameter study. 149
4.30 Response surface curves modelling the effect of K1 and K2 thicknesses on the lower surface stress 152
4.31 Stress results of the full structure, taken from the composite model 153
4.32 FEA results from the spring plate model 154
4.33 FEA stress results for torque load cases on the pinion (top) and wheel (bottom) shafts. 155
4.34 Profile views of the housing sections on the left and right 156
4.35 Selection of stress results from the housing simulations 156
4.36 Lever design table and schematic 157
4.37 Final design CAD renders of the prototype 158
4.38 Views of the final prototype CAD model 159
4.39 Photos of the manufacture prototype 160
4.40 Plot displaying rollover shape of prototype, with and without mechanism. 161

5.1 Pilot study experiment setup 165

5.2 Time sliced data of two subjects completing single trials of both setups . . . 167
5.3 Box-plots of the key gait metrics under the initiation task . . . 169
5.4 Box-plots of the key gait metrics under the termination task . . . 170
5.5 Mass normalised power curves for all subjects and trials under each protocol instruction . . . 171
5.6 Gait metrics plotted in Bland-Altman diagrams . . . 175
5.7 Mass normalised peak force, power and work plotted on Bland-Altman diagrams . . . 176
5.8 Force plate and walkway setup for the larger study. . . . 178
5.9 Example trials displaying the time sliced data for when the plate forces are un-combined and combined . . . 179
5.10 Box plots of key gait metrics . . . 180
5.11 Mass normalised force and power curves . . . 181
5.12 Bland-Altman plots of the gait metric peaks . . . 182
5.13 Braking ratio scatter plots, generated using left foot trailing data . 184
5.14 Propulsive ratio scatter plots, generated using left foot trailing data 185
5.15 Comparison of the peak ratio scatter plots between left and right foot leading data sets . . . 186
5.16 Potential force plates setups for future studies with amputees . . . 188

6.1 Possible steps that may be taken to refine the prototype tool in preparation for the stiffness exploration studies of the second work package. . . . 194
6.2 Flow diagram representing the process to be taken in defining effects of spring stiffness on amputee gait force metrics. . . . 195
6.3 Flow diagram representing the framework to be used in future prosthetic optimisation . . . 195

C.1 The first of two tables used to define the major dimensions of the test setup . . . ix
C.2 The second of two tables used for dimensions the test setup . . . x

D.1 Heel parameter correlation study . . . xxv
D.2 Response surface goodness of fit metrics from the forefoot DOE studies . . . xxvi
D.3 Monte Carlo sampling method on the left, with the modified Latin Hypercube method on the right. . . . xxvii
D.4 Correlation Example Plots . . . xxvii

D.5 Comparison scatter plots with regression lines. xxviii
D.6 Diagrams representing the variation from a central parameter value by the CCD and Box-Behnken methods. xxix
D.7 Comparison of design space distribution between the Latin Hypercube and Optimal Space-Filling methods. xxx
D.8 Screenshot of Ansys workbench project used for the composite modelxxxi
D.9 Screenshots of the layups generated in the ACP (Pre) modules, for Heel (top) and Keel (bottom). xxxii
D.10 Laminate failure mode results on the heel xxxii
D.11 Summary of connection parameters explored to determine the most suitable settings for reliable results. xxxiii

E.1 Screenshots taken from the simulation setup xxxv
E.2 Screenshot of the excel design spreadsheet used to check calculations, select parameters, and check critical outputs. xxxvi
E.3 Top: Simulink model used to perform a sensitivity analysis on the spring geometry parameters. xxxvii
E.4 Equations used to derive gear dimensions for involute shape xxxviii
E.5 Involute curve generation using the parametric equations xxxix
E.6 Reference diagram taken from ISO 6336-3, for selection of dimensional parameters h_{Fe} and S_{Fn} xliv
E.7 Spring plate and Plate link xlv
E.8 Gear link and Pinion xlvi
E.9 Wheel and Lever xlvii
E.10 Pinion shaft and Wheel shaft xlviii

List of Tables

2.1 Anatomical Directions 11
2.2 Muscle Groups 23
2.3 Muscle Contributions to gait events 25

3.1 Material properties of Stratasys Digital ABS™ 62
3.2 Simulation results for set of validation inputs. 64
3.3 Table summarising validation experiment samples and applied displacements 66
3.4 Table of statistical analysis on the experimental and simulation data 70
3.5 Concept model geometry specification and material assignment in cyclic and static simulations for ISO 22675. 79
3.6 Stiffness results taken from the table D.3 in Appendix chapter D . . 80
3.7 Material properties used in the ISO 22675 simulations. 81
3.8 Concept model contact sets used in cyclic and static simulations for ISO 22675 81
3.9 Static load boundary conditions for the Proof (P), Ultimate Lower (U_L), and Ultimate Upper (U_U) for heel and forefoot tests. 89
3.10 Cyclic test transient load boundary conditions with format of ISO 22675 89
3.11 Support and load boundary conditions used for the cyclic and static simulations of ISO 22675. 90
3.12 Initial mesh settings applied to the foot assembly 91
3.13 Analysis settings for static and cyclic models 92
3.14 Final mesh settings applied to the foot assembly, used for converged solutions in static and cyclic tests of 22675. 98
3.15 Key settings used for the frictionless contacts between prosthetic and force plate 99

4.1 Design specification points for the prosthetic concept revision 107
4.2 Deflection and strain energy results of the composite spring study . 109

4.3 Material properties used for the Music Wire, which is classified as ASTM A228 110
4.4 Table of final dimension parameters and outputs of the spring . . . 117
4.5 A summary table of possible gear pairs after the initial geometric constraints. 136
4.6 Summary of the factor symbols, description and value used 141
4.7 Summary of stress results from analytical calculations and FEA . . 143
4.8 Coefficient of determination R^2, and RMSE values taken from the table in the appendices 151
4.9 Results from the response surface optimisation for foot structure . . 151
4.10 Summary of the component materials and finishes used. 161

5.1 Instructions for the control, external focus attention (EFA), and internal focus attention (IFA) protocols. 164
5.2 Table of Intraclass correlation ICC(2,1) results for gait metrics in both initiation and termination activities. 171
5.3 Table of Intraclass correlation ICC(2,1) confidence intervals with α=0.05, for gait initiation. 173
5.4 Table of Intraclass correlation ICC(2,1) confidence intervals with α=0.05, for gait termination. 173
5.5 Table of Intraclass correlation ICC(2,1) results for gait metrics from the main study 182
5.6 Full cohort means of peak metrics in terms of bodyweight 187

D.1 General material information and mechanical properties for the isotropic woven prepregs. CF = Carbon Fibre. xi
D.2 Mechanical properties for the orthotropic woven prepregs found in the Ansys materials library xii
D.3 Results of the material study involving data from the materials in the other tables of this section. xii
D.4 Material properties used in the link parametric study xiii
D.5 Example table of two-factor experiments with the same levels, used to explain orthogonality of DOE types xxix

Nomenclature

Abbreviations

ABS Acrylonitrile Butadiene Styrene

ACP ANSYS® Composite PrePost

ANOVA Analysis of Variance

AP Anterior-Posterior

APDL ANSYS® Parametric Design Language

apGRF Anterior-Posterior Ground Reaction Force

B-Spline Basis Spline

BB Box Behnken

CAD Computer Aided Design

CCD Central Composite Design

CDF Cumulative Distribution Function

CESR Controlled Energy Storage and Return

CF Carbon Fibre

CNS Central Nervous System

CoM Centre of Mass

CoP Centre of Pressure

DAQ Data Acquisition

DOE Design of Experiments

DoF Degrees of Freedom

EDM Electric Discharge Machining

EFA External Focus of Attention

EMG Electromyography

ESAR Energy Storage and Return

FDM Fused Deposition Modelling

FEA Finite Element Analysis

FoS Factor of Safety

GCRF Global Challenges Research Fund

GRF Ground Reaction Force

ICC Intra Class Correlation

IFA Internal Focus of Attention

ISO International Organisation for Standardisation

K-S Kolmogorov-Smirnov

KPI Key Performance Indicator

LHS Latin Hypercube Sampling

LLTE Lower Leg Trajectory Error

M2A The Materials and Manufacturing Academy

MIT Massachusetts Institute of Technology

ML Medio-Lateral

NHS National Health Service

NURBS Non-uniform Rational Basis Spline

OSF Optimal Space Filling

P Proof

PCA Principal Component Analysis

PMMA Poly(methyl methacrylate)

PP Polypropylene

RMSE Root Mean Square Error

SACH Solid Ankle Cushioned Heel

TER Tension Energy Recovery

U_L Ultimate Lower

U_U Ultimate Upper

UTM Universal Testing Machine

vGRF Vertical Ground Reaction Force

VSPA Variable-Stiffness Prosthetic Ankle

Symbols

α Significance Level

α_1 Gear Link Elevation Angle

α_2 Gear Link Inclination Angle

α_{ISO} Resultant Inclination Angle

$\bar{u}$ Point Data Parameter Value

β Angle Between Links

β_c Cam Angle

β_{ISO} Resultant-Perpendicular Angle

γ Platform Tilting Angle

γ_1 Pinion Elevation Angle

γ_2 Gear Tangential Force Elevation Angle

γ_H Inclination Angle from Hip

γ_K Inclination Angle from Knee

γ_{fore} Forefoot Platform Angle

γ_{heel} Heel Platform Angle

ω	Rotational Speed
ϕ	Pressure Angle
σ_B	Bending Stress
σ_C	Contact Stress
σ_F	Tooth Root Stress
σ_H	ISO Contact Stress
σ_{F0}	Nominal Root Stress
σ_{FG}	Tooth Root Stress Limit
σ_{Flim}	Material Root Stress Limit
σ_{H0}	Nominal Pitting Stress
σ_{HG}	Pitting Stress Limit
σ_{Hlim}	Material Contact Stress Limit
τ	Shear Stress
θ	Plate Link Inclination Angle
θ_c	Cam Angle of Rotation
θ_{plate}	Plate Angle
a	Spring Allowance
a_x	Acceleration in X-direction
a_{CoM}	Centre of Mass Acceleration
A_w	Wire Cross-section Area
AJC_y	Ankle Joint Centre x-Coordinate
$AP1$	Force Plate 1 Anterior-Posterior
$AP2br$	Force Plate 2 Anterior-Posterior Braking
$AP2po$	Force Plate 1 Anterior-Posterior Push-Off
B	Material Constant

b	Face Width
BW	Bodyweight
C	Piecewise Polynomial Function
C_{dis}	Centre Distance
C_{sp}	Spring Index
CoP_x	Centre of Pressure x-Coordinate
d	Wire Diameter
D_b	Gear Base Diameter
d_b	Pinion Base Diameter
D_o	Gear Outside Diameter
d_o	Pinion Outside Diameter
D_p	Pitch Diameter
D_t	Tooth Tip Diameter
D_{exp}	Mean Spring Expanded Diameter
D_{gear}	Gear Diameter
D_{hole}	Hole Diameter
D_{pin}	Pinion Diameter
D_{sp}	Mean Spring Diameter
E	Young's Modulus
E_i	Cylinder Young's Modulus (i=1,2)
F	ISO 22675 Test Force
f	ISO 22675 Horizontal Axis
F_1	Heel Load
F_2	Forefoot Load
F_H	Test Force of Hip Angle

F_K Test Force of Knee Angle

F_P Perpendicular Force

F_R Resultant Force

F_r Gear Radial Force

F_s Spring Force

F_T Tangential Force

F_t Gear Tangential Force

F_x Force in X-direction

F_{res} Resultant Spring Force

F_{sh} Shear Force

G Shear Modulus

g Gravitational Constant

h Height

h_r Cam Total Rise

I Moment of Inertia

I_{CoM}, I Centre of Mass Impulse

J Second Moment of Area

K Spring Curvature Correction Factor

k Spring Rate

K_A Application Factor

K_B Bergstrasser Correction Factor

K_v Internal Dynamic Factor

k_v Dynamic Factor (Lewis Form)

$K_{F\alpha}$ Bending Transverse Load Factor

$K_{F\beta}$ Bending Face Load Factor

$K_{H\alpha}$ Contact Transverse Load Factor

$K_{H\beta}$ Contact Face Load Factor

KE_{rot} Rotational Kinetic Energy

KE_{tra} Translational Kinetic Energy

l Length of Elastic Member

L_0 Spring Free Length

l_c Chord Length

L_g Gear Link Length

L_p Plate Link Length

L_s Solid Length

m Mass

m_g Gear Module

m_i Body Segment Mass

m_k Number of Knots

m_p Gear Contact Ratio

m_{subj} Subject Mass

MS_C Mean Square for Columns

MS_E Mean Square Error

MS_R Mean Square for Rows

N Basis Function

N_a Number of Active Coils

n_k Number of Measurements

N_p Gear Minimum Teeth

n_s Number of Subjects

N_t Number of Total Coils

$P1$	Force Plate 1
$P2$	Force Plate 2
$P2^n_{br}$	Force Plate 2 Braking
$P2^n_{po}$	Force Plate 2 Propulsive
P	Control Point
p	p-Value
p_b	Base Pitch
p_d	Degree of Spline
P_{CoM}, P	Centre of Mass Power
p_{sp}	Spring Pitch
PE	Potential Energy
Q	Interpolation Point Data
q	Material Exponent
R	Rational Form Function
R^2	Coefficient of Determination
r_g	Gear Ratio
r_i	Cylinder Radii (i=1,2)
R_{circ}	Radius of Arc
r_w	Spring Wire Radius
S_F	Gear Bending Stress Safety Factor
S_H	Gear Contact Stress Safety Factor
S_{ec}	Spring End Condition Constant
S_{ut}	Spring Tensile Strength
SE	Strain Energy
T	Torsion

t	Time
T_{pin}	Pinion Shaft Torque
U	Knot Vector
u	ISO 22675 Vertical Axis
u_i	Knots
v	Velocity
V_{CoM}, V	Centre of Mass Velocity
w	Weights
W_{CoM}, W	Centre of Mass Work
x	Experiment Data Loading Period
x_0	Circle Centre x-Coordinate
x_{BR}^n	Braking Ratio
x_{circ}	Lower Half of Circle x-Coordinate
x_{PR}^n	Propulsive Ratio
x_{ROS}	Rollover x-Coordinate
x_{sp}	Spring Plate Horizontal Position
y'''	Cam Jerk
y''	Cam Acceleration
y'	Cam Velocity
Y	Lewis Form Factor
y	Cam Displacement
y_0	Circle Centre y-Coordinate
Y_β	Helix Angle Factor
Y_B	Rim Thickness Factor
Y_F	Form Factor

Y_M Mean Stress Influence Factor

Y_R Surface Factor

Y_S Local Root Stress Correction Factor

Y_X Size Factor

$Y_{\delta relT}$ Relative Notch Sensitivity Factor

y_{circ} Lower Half of Circle y-Coordinate

y_{coef} Order of Coefficient

Y_{DT} Deep Tooth Factor

Y_{NT} Life Factor

y_{ROS} Rollover y-Coordinate

y_{sp} Spring Deflection

y_{sp} Spring Plate Vertical Position

Y_{ST} Reference Stress Correction Factor

Z_β Helix Angle Ratio Factor

Z_B Single Pinion Tooth Factor

Z_D Single Gear Tooth Factor

Z_E Elasticity Factor

Z_H Zone Factor

Z_L Lubrication Factor

Z_R Roughness Factor

Z_v Velocity Factor

Z_W Work Hardening Factor

Z_X Size (Contact) Factor

Z_ε Contact Ratio Factor

Z_{NT} Contact Life Factor

Chapter 1

Introduction

1.1 Scope

The initial overarching question of this thesis was to ask:

> "Do the current passive prosthetic feet offer the optimum performance possible to a transtibial amputee, whilst maintaining affordability?"

This question would be driven by the development of a passive prosthetic foot with a bodyweight activated, spring energy harvesting mechanism. However, in searching for the answer, the scope evolved beyond questioning the viability of this novel design, to evaluating the design ethos of passive feet altogether.

There is a gap in the performance of powered and semi-active feet when compared to passive designs [1]. The BiOM® ankle system developed by Hugh Herr at Massachusetts Institute of Technology (MIT) is a prevalent example of these advanced technologies [2]. However, passive designs have a lighter mass advantage and are typically more accessible to the common amputee. There is clearly scope for advancing these designs, as evidenced by another MIT research group, who have developed an optimisation method for passive designs [3]. However, it has not been verified as to whether these new methods are the most suitable to take when considering the natural variation in physiology and biomechanics from person to person.

Indeed, the musculoskeletal system of an amputee is capable of adapting the motor pattern to the changes brought about by the amputation [4]. Mass perturbations introduced to amputee gait caused a kinematic invariant adaptation, where the kinetics were altered to maintain a kinematic pattern [5]. In doing so, the musculoskeletal system appears to be compensating for lost power generation

in the plantar-flexors [6]. However, passive foot designs have been shown to generate irregular power profiles which can cause health issues occurring from the unhealthy loads [7].

1.1.1 Amputee Situation

The procedure of an amputation has been prevalent for as long as warfare has occurred between tribes and nations on this planet [8]. Changes to combat and improvement in military trauma surgery has only served to increase the number of amputees who survive [9, 10]. Statistics from those involved in the conflicts of the 20th century have shown that the transtibial amputation was the most common of all types. A study from 2003 on a sample of the elderly populace with amputations in France (539 Subjects, 66.1 ± 14.1), had 69.02% because of trauma, 19.85% from vascular disease, and the remaining from other complications; with transtibial amputations accounting for 49.17% of all cases [11]. These numbers have changed in some respect as modern warfare has evolved again alongside medical practice into the 21st century. Whilst the overall amputation rates in the military are at historic lows [10], the use of explosives is now the single major cause of amputations and has helped maintain the proportion of transtibial amputees at around 48% [12].

Outside of military conflict, research has shown a concerning trend in the prevalence of civilian amputations. In 2005, the United States had an estimated 1.6 million living with an amputation, 65% of which were to the lower body. Just over a half at 54% were caused by dysvascular disease, 45% due to trauma, and the rest caused by cancer. This group was projected to grow to about 3.6 million in 2050, with a significant portion being persons over 65 years with a dysvascular disease [13].

Trends in other countries can vary slightly, but the overall picture remains the same. Scotland has seen 82.9% of lower limb amputations caused by dysvascular disease, with 80% of patients over the age of 60 [14]. Detailed studies in England have used NHS data, analysing those with dysvascular disease. Between 2003-2008 the lower limb major amputation rate of the general population was 5.1 per 100,000, with 39.4% being due to diabetes. A separate study looked at same data but restricted to between the ages of 50-84 found the rate increase to 26.3 per 100,000, 43.7% of which was attributed to diabetes [15]. An extension to this revealed that over 10 years the rate of major amputations fell from 27.7 to 22.9 per 100,000. In the diabetic population the rate dropped faster than non-diabetics, however they still remain at a much larger risk of major amputation [16].

The research suggests that whilst effective healthcare can help to reduce the rate of major amputations, there is always a higher risk with older age and a predisposition towards vascular disease. As the average life expectancy increases, it is possible that a portion of the general population will always be at risk of a lower limb amputation. In addition to this, veterans of conflict, and victims of severe trauma will also add to this group of disabled persons [12]. The World Health Organization has also estimated that as many as 30 million in developing countries across the world were in need of a prosthetic in 2011 [17].

A transtibial amputation removes key musculoskeletal structure utilised in ambulation. The plantar-flexor muscles provide active push-off [18, 19], although the exact mechanism through which this is achieved is debated [20]. It is likely that the tendons in the lower limb play a crucial role, as their mechanical efficiency is well suited to the generation of power [21]. In fact, research has shown the ankle to employ a "catapult" mechanism, producing a large impulse of power at push-off and producing net positive work over the gait cycle [22]. Without this functionality, the contralateral limb and residual muscles will overcompensate, [23], leading to increased risk of osteoarthritis [24].

With the loss of power generation, the mass of a prosthetic foot device becomes an additional consideration. Adding mass to the proximal end of the amputated limb has been shown to increase both metabolic energy costs and asymmetrical gait in segmental models[25, 26], and swing leg passive walking models [27]. Powered designs can accommodate a prosthetic mass similar to an intact foot, around 2kg or 2.5% of the total body mass due to their superior power generation [28, 29, 30]. However, the passive designs do not have this power to offset the mass, and as such must aim for a lower mass; around 350g for the MIT foot [31].

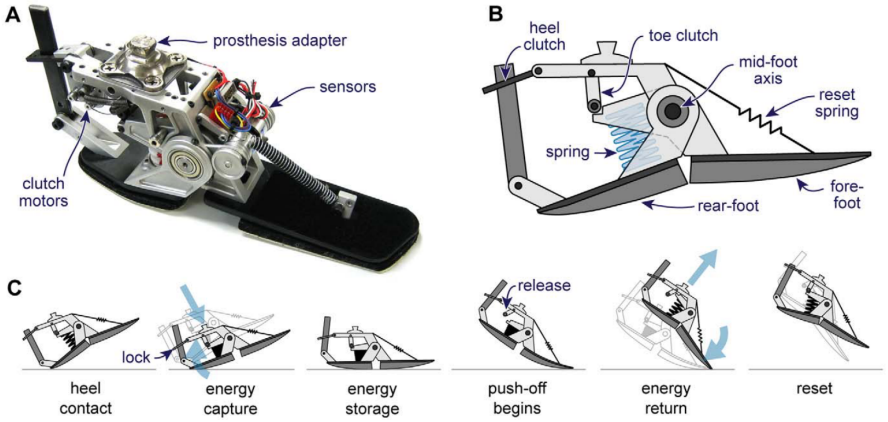
Much of the optimisation of prosthetic feet to date has been developed to bring natural gait back to previously active and healthy subjects. Typically, such methods use data collected in mid-stride, or what is referred to as steady-state walking. However, these performance goals are not representative of the typical older amputee, who are a significant demographic in the UK lower limb amputee population, and one with low levels of activity [32]. Studies have shown that the average healthy adult under 65 will walk 9,448 steps a day, whilst over-65's will hit a lower average of 6,565 steps [33]. In active job typical of those worked by blue collar workers this can reach 11,784 steps, and even the least active desk jobs will hit 7,207 a day [34]. Compare this to the 600 steps a day necessary to navigate a single-story house with moderate support; a value recommended by research and

used throughout amputee activity studies [35]. Other research indicates that their gait can be characterised by repeated sessions of gait initiation and termination, as amputees will still wear their prosthetic even when less active [36]. This is reflected in the selection of tests used to assess elderly amputees, for example the ability to get up from sitting and move a short distance within a reasonable timeframe [37, 38].

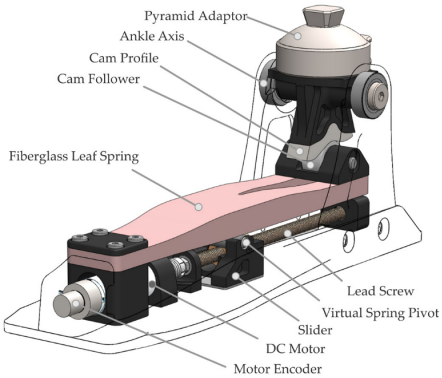
1.1.2 Current Research Trends

At the start of the EngD, universities and research collaborations were attempting to find solutions to the question posed in the scope of this thesis. To return natural gait to amputees many designs shared the common objective in designing a foot that can match the kinetic and kinematic joint data of a healthy individual, which involves the use of predictive models and inverse dynamics to predict joint parameters. However, there are inherent limitations in these methods which affect the accuracy of the results [39]. Inaccurate estimations of body segment parameters and movement noise of surface markers will create significant uncertainties in joint torque estimates [40]. Furthermore, studies applying able-bodied kinematic models to the inverse dynamic analysis of amputees have not considered the changes in amputee physiology and how this should be reflected in adaptations to the models [41].

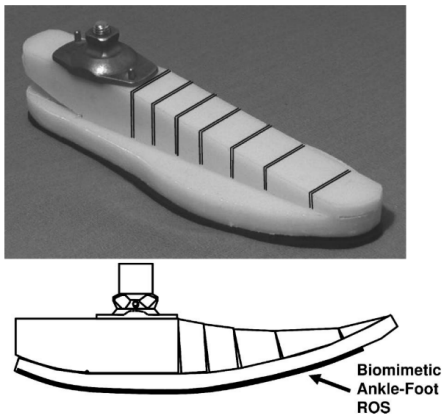
The Controlled Energy Storage and Return (CESR) foot, see Figure 1.1a, aimed to harvest energy lost at heel contact, returning it at push-off and therefore reducing the metabolic expenditure [42]. Whilst successful in recycling energy under steady-state walking, the release rate and control of this energy required further development as the metabolic cost was not reduced [43]. At Northwestern University in the United States, researchers produced a series of papers that investigated the ankle stiffness behaviour, discovering a method to model the non-linear behaviour of the ankle joint system [44, 45]. This knowledge has been used in the evolution of sophisticated robotic ankles [2], and the Variable-Stiffness Prosthetic Ankle-Foot (VSPA Foot, see Figure 1.1b) a novel design with an actively controlled, continuously variable stiffness [46]. The idea behind the VSPA foot is to create an affordable foot which can mimic the adaptive stiffness of the biological ankle-foot. Further experiments revealed a high sensitivity to stiffness changes during steady-state walking, which has directed the development to discovering a method to prescribe a personalised stiffness profile for amputees [47]. Whilst the semi-active CESR and VSPA foot designs are a positive step in filling the gap be-



(a) CESR foot [42]



(b) VSPA Foot [46]



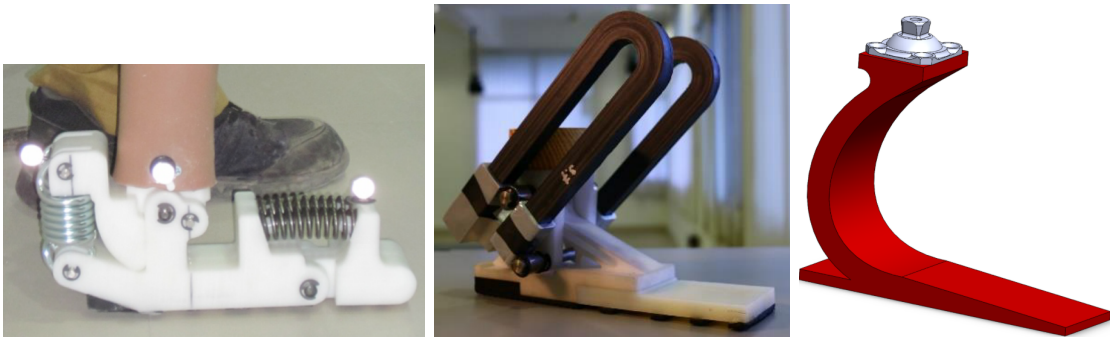
(c) Shape & Roll [48]

Figure 1.1: Examples of passive, and semi-active prosthetic feet designed by various research groups in American universities. Their scope is comparative to the framework outlined in this thesis, and the future work proposed.

tween the powered and passive ankle-foot devices, these concepts of personalised stiffness profiles and re-directing collision energy to push-off could also be applied to a novel passive design.

Ongoing research is exploring a variety of optimisation methods and parameter exploration for passive feet. A group of researchers in America have investigated the effect of foot stiffness on gait by using additive manufacturing to produce geometries with varying degrees of heel and forefoot. With this method, the effects on support and propulsion were clarified, but it proved difficult to balance the stiffness of the geometry to provide both without a trade-off [49]. This framework has been used to add to the knowledge of foot stiffness effects, by focusing on common key events such as turning [50].

From extensive studies into rollover shape effects, another group of researchers sought to better understand the effects of prosthetic foot rollover shape by de-



(a) Metatarsal Design [52] (b) Custom Springs [53] (c) Optimisation [54]

Figure 1.2: The prosthetic designs developed as part of the LLTE project at MIT [3].

signing an experimental foot that would deform to the rollover curve. The design displayed some ability to produce a biomimetic response [48], and has been used as a tool to analyse effects on the mobility and balance [51]. The rollover shape has continued to be used in the design optimisation of passive feet.

An MIT group have developed a novel optimisation methodology that minimises what has been defined as the Lower Leg Trajectory Error (LLTE) [3]. Their research began with the objective to improve the mechanical performance of affordable energy storing and return feet, in particular the Jaipur foot. By combining the rollover shape and the orientation of the lower leg, the optimisation directly includes the effect of prosthetic geometry on the kinematics of the lower limb. Through minimising the kinematic error between subject values and a healthy objective, the stiffness of a passive foot has been optimised [31]. The evolution of this method from 2015-2018, involved PhD research that designed and used multiple prosthetic tools to provide insight into the explored optimisation parameters; these are shown in Figure 1.2

1.2 The Research Goal and Objectives

It can be said that the semi-active and passive prosthetic research has been successful in achieving some goals in returning natural gait, but there are gaps in the research worth exploring. Many of the optimisation methods use kinematics or joint kinetics as optimisation goals, and the method of data collection is not necessarily representative of the amputee population. Research focuses on steady-state walking and not gait initiation or termination, where small changes to spring stiffness are yet to be explored.

A collaboration was formed with a PhD thesis which was completed in parallel to the work presented here [55]. Using a passive dynamic model, the author discovered a novel method to classify walking speeds using a dimensionless polynomial derived from the vertical ground reaction force (vGRF). Two optimisation strategies were also explored to minimise the unbalanced vertical loads during steady-state walking, one leg stiffness and the other roll-over shape. These two parameters formed targets for the Finite Element Analysis (FEA) model developed in this thesis, and a printable prosthetic foot was modified to match the performance. This demonstrates viability in the optimisation pathway but is still only focused on vertical forces during steady state.

In the last 5-6 years, researchers have been exploring the mechanical properties of structures created with minimal surfaces like the gyroid. By changing the density and direction of gradient, the full structure exhibits varying deformation and mechanical properties [56]. This ability to change the density also produces favourable compression and energy storage capabilities [57]. With these advantages in controlling the properties, the structures show promise in use as bone scaffolds [58]. They are also proving to be manufacturable across a range of additive manufacturing techniques, including Fused Deposition Modelling (FDM) [59] and Polyjet printing [60].

The gyroid structure's unique, directional parameterisation features provide the opportunity to expand the unhealthy force optimisation method into the additional Ground Reaction Force (GRF) components. Of the two, the Anterior-Posterior (AP) loads should be the primary focus. These forces are representative of the gait initiation and termination activities, tasks that are common for the typical less-active amputee. For this to be realised, a framework needs to be setup to research the effects of small changes to foot stiffness during those specific gait activities.

1.2.1 Objectives

For this approach to be realised, a set of objectives were defined to carve out a new scope for the research:

- Design a prosthetic foot to analyse the effect of forefoot spring stiffness on gait initiation. Primarily, the propulsive portions of the anterior-posterior ground reaction force. The nature of these unhealthy forces is acknowledged but not yet quantified in terms of an optimisation criteria. The K-levels of standard feet have stiffness levels that are too broad for the sensitivity of amputee gait.

- Develop an experimental method to assess unhealthy loading at gait initiation. This must be reliable in producing consistent results and avoiding random errors.
- Develop a computational methodology to design a person specific low-cost passive prosthetic foot that will minimise the occurrence of unhealthy loads generated in the daily routine of a typical amputee.

1.2.2 Novel Contributions

Whilst working towards the completion of the objectives listed above, a number of solutions were developed. As mentioned in Section 1.2, the FEA model has successfully been used to design, and then optimise a printable prosthetic. The experimental method will form part of the validation process in advancing the FEA model in future work and assist in optimising the prosthetic push-off stiffness tool, which itself is the third key deliverable from this research.

- An advanced, ISO 22675 compliant FEA model that goes beyond the basic recreation of tests used in industry. It has the following features:
  - Custom ANSYS Parametric Design Language (APDL) script to parameterise the rollover shape and stiffness across stance phase
  - Structural optimisation using sophisticated algorithms
  - Easily modified to fit any prosthetic design
  - Simple exportation of Key Performance Indicators (KPI)
  - Utilisation of ISO definitions to produce boundary condition tests force from subject specific data (Vertical & AP GRF components)
  - Verification completed with a printed polymer experiment
- A novel experimental method to measure unhealthy loads and peak power of amputees
  - With the prosthetic optimisation focus on the common tasks of gait initiation and termination, there is a requirement to have a robust experimental method to measure the ground reactions forces and power.
  - A pilot study was completed with five participants. The purpose was to assess the instructions and setup of equipment. Three instructional sets were trialled and the repeatability analysed with Analysis of Variance (ANOVA) statistics. All three reported sufficient intraclass correlations

(< 0.8), with the most repeatable set going forward for use in a full study.

- A full study was conducted on the gait initiation with 26 healthy subjects recruited from the university doctoral studies office (18 males, 8 females, ages 26 ± 2, 78.38 ± 16.8kg). Reliability results remained high for gait initiation.
- A MATLAB® script was created to conduct the analysis. A novel contribution of this script involves the use of statistical methods to detect the instant of gait initiation for purpose of generating reliable metrics of peak power.

- A novel prosthetic foot designed to estimate the effects of stiffness corrections in passive feet, gaining insight to minimised unhealthy loads produced in gait initiation.
  - Optimised using the FEA model and a robust series of simulation-based design parameterisation with response surfaces.
  - Used in conjunction with the experimental method to determine effects of delta changes to spring stiffness, expanding beyond the steady-state walking research found in literature.
  - A program written in MATLAB uses Non-Uniform Rational Basis Spline (NURBS) to define the shape of the structure for design parameterisation.

- The work leading to the contributions has been presented at a series of conferences.
  - M2A Conferences - Poster presentation: 2016, 2017, 2018
  - M2A Conference - Presentation 2019
  - International Conference - Dynamic Walking 2017

1.3 Summary

This thesis will cover the work completed in achieving the novel contributions detailed above. Chapter 2 will cover an extensive literature review, beginning with the foundations of gait cycle, progressing through topics of kinetics and kinematics to provide an insight into the biomechanical features of gait and identify the characteristics that occur from a resulting amputation. The design of prosthetic

foot devices is also explored. Chapter 3 follows the pathway taken in developing the FEA model, from the evaluation of ISO standards and extraction of boundary conditions, moving through to the development of the model itself, including an experimental study to verify the contact settings. In Chapter 4 the evolution of the prototype design will be documented. This starts with the evaluation of the original proof of concept design, using the FEA models developed in the previous chapter. It also covers the extensive optimisation methodology undertaken to arrive at the first built prototype. Chapter 5 will explore the development of the experimental method to assess the prototype. In this chapter, a further literature review will be conducted, providing more detail into the decision to forego the typically used kinematic analysis in favour of the kinetic approach. The concluding chapter will contain a discussion on the novel contributions developed and presented, concluding with a section of planned developments, derived as a result of the work presented here within.

Chapter 2

Literature Review

In the previous chapter, an overview was provided into how the gait initiation activity and elderly, less-active amputees are overlooked. The content in this chapter will begin with the fundamentals of gait analysis and biomechanics to provide the reader a foundation of knowledge for the proceeding sections. These are grouped thematically to cover aspects of neuromuscular control, power, motor redundancy, and the ankle foot complex. In all sections, the discussion is linked into the associated issues resulting from a lower limb amputation. The chapter concludes with a more detailed review of prosthetic technology and where the popular trends have succeeded or left uncertainties in research area.

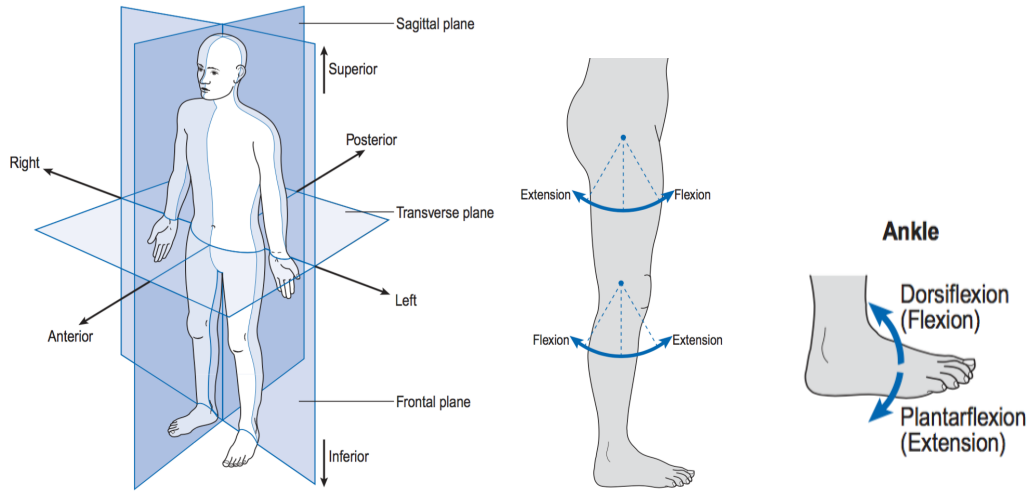
2.1 Biomechanics

2.1.1 Terminology and Key Conventions

Due to the use of biomechanics terms throughout this thesis, it is prudent to first explain terms and concepts that will commonly be used throughout. In respect to the main intention of this thesis, the details will be succinct.

Table 2.1: Anatomical Directions

Term	**Direction**
Medial	*Towards centre*
Lateral	*Away from centre*
Anterior	*Forward*
Posterior	*Backward*
Proximal	*Towards body*
Distal	*Away from body*



(a) (b) (c)

Figure 2.1: Anatomical reference diagrams of (a) Reference planes & directions, (b) Sagittal plane motion of hip and knee joints, and (c) Sagittal plane motion of ankle joints [61].

In the study of human gait, a spatial reference system has been used by biomechanists as the status-quo for decades. The body is bisected by three major planes: Frontal plane splits the anterior and posterior, Sagittal divides the left and right of the body, and Transverse cuts the lower and upper halves (Figure 2.1a). Much of the discussion in this thesis will be in the Sagittal plane as most of the useful information can be seen in this plane. With regards to lower limb joint motion in this plane, the hip, knee, and ankle joints can be seen to all be in either flexion or extension (Figure 2.1b). In the ankle, it is common for flexion to be known as Dorsiflexion, and extension as Plantarflexion (Figure 2.1c).
There are a few additional terms to identify, they have been summarised in Table 2.1. A list of every bone and muscles in the lower leg would be exhaustive, and so further reference should be made to suitable references [39, 62].

2.1.2 Introduction to the Gait Cycle

At this point it is prudent to acknowledge that the use of the word cycle does not necessarily mean that every step is identical, more so that the sequence of events will occur in a repeated cyclical pattern. Research has shown that there are intra- & inter-subject fluctuations in gait patterns, particularly when variations in walking speed are introduced [63, 64, 65]. Thus, it can be useful to perceive the gait cycle as being quasi-periodic over an extended period of time [66].

With the above in mind, a single gait cycle can be defined as the period between the same repetitive event which occurs during walking. Although any event can

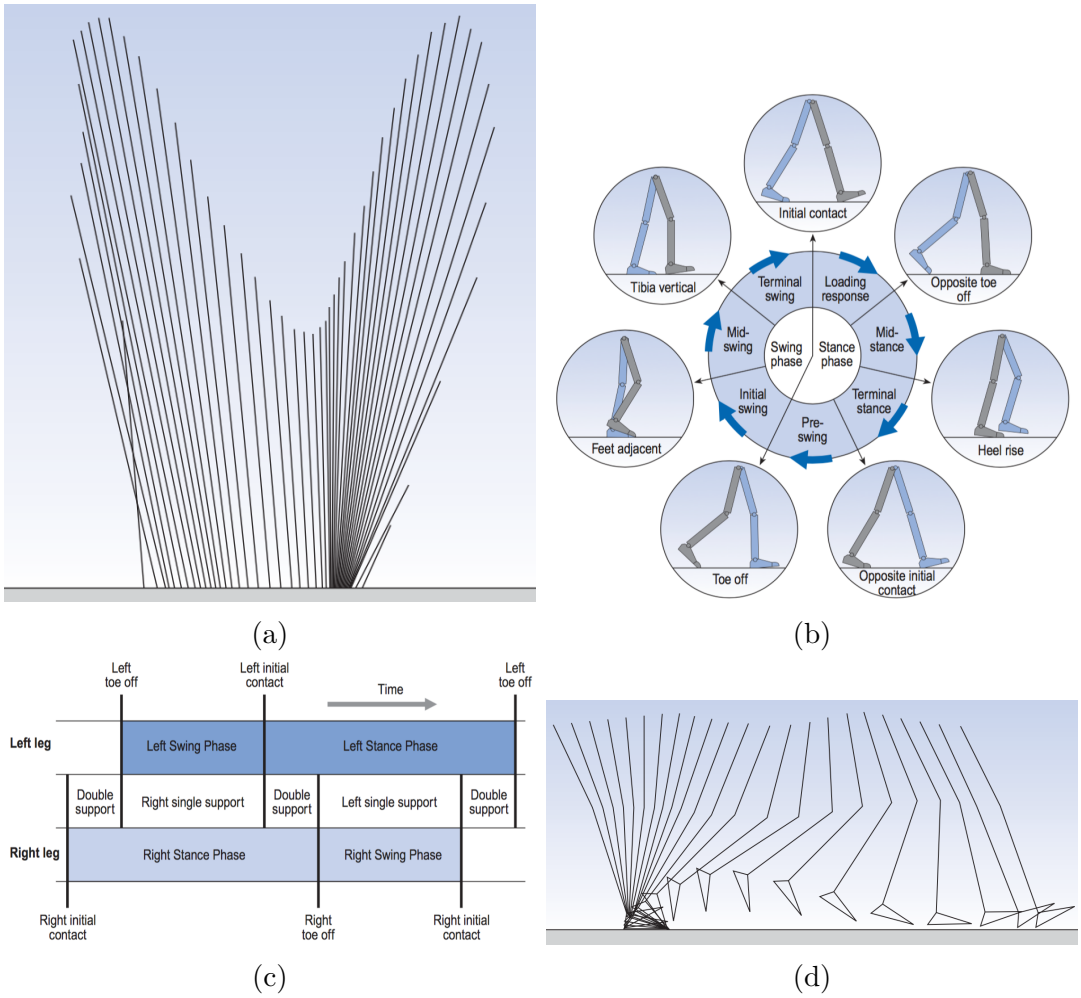


Figure 2.2: The gait cycle can be described using terminology in (a), with timing of events found to typically follow (c). A Pedotti diagram (b) displaying the sagittal plane ground reaction force vector during stance phase. The position of the leg during a single gait cycle is visualised in (d). All figures have been taken from [61].

be used, it is convenient to use the initial contact of a single side as the key event. The terminology used to describe the gait cycle can vary in literature. As such, a primary source will be referenced here, all future mentions of the gait cycle or appropriate nomenclature will be applied to this context [61].

In terms of mechanics, the gait cycle can be said to control the forward progression and positioning of the lower body (Locomotor Unit) through managing mechanical energy, whilst maintaining the support of the upper body (Passenger Unit) [62, 67]. Within this, the key objective appears to be to minimize the energy expenditure [68]. It can be divided into seven stages, with the transition between each stage defined by one of seven major gait events. Of these seven stages, four occur during the stance phase, and three during the swing phase. The loading

of the leg transpires during the stance phase, beginning with the initial contact event, and ending with the toe-off event. In this phase, the leg takes on a loading response to the initial contact, before generating the power to propel the leg through the swing phase and maintain forward momentum of the entire body's Centre of Mass (CoM). The resultant force vector within the sagittal plane can be seen in Figure 2.2a.

The complete nomenclature for these stages and events can be seen in Figure 2.2b, together with the typical timings of the swing and stance phase between the left and right side, Figure 2.2c. Ordinarily, the stance phase will last for about 60% of the gait cycle, and the remaining 40% will be the swing phase [61, 69]. Whereas the temporal difference in the two phases is relatively equal, Figure 2.2d demonstrates the significant spatial difference. The entirety of the stance phase is located on the left side, whilst the swing phase accounts for about 80% of the cycle. The events of initial contact and toe-off coincide with each other on opposite sides as a period known as double support. These double support phases occur at the transitions from stance to swing phase, where weight is shifted from the one side of the body to the other.

By examining the Centre of Pressure (CoP) in the sole of the foot and CoM of the body during a single stance phase, the human body appears to move as

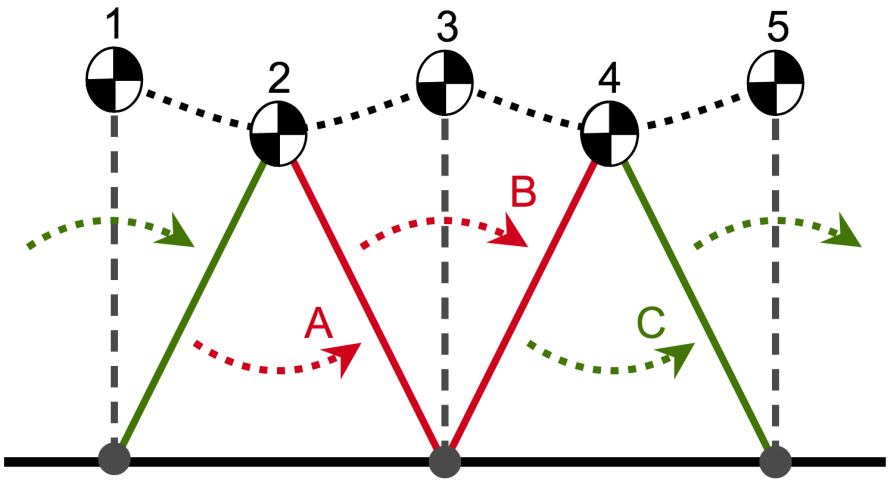
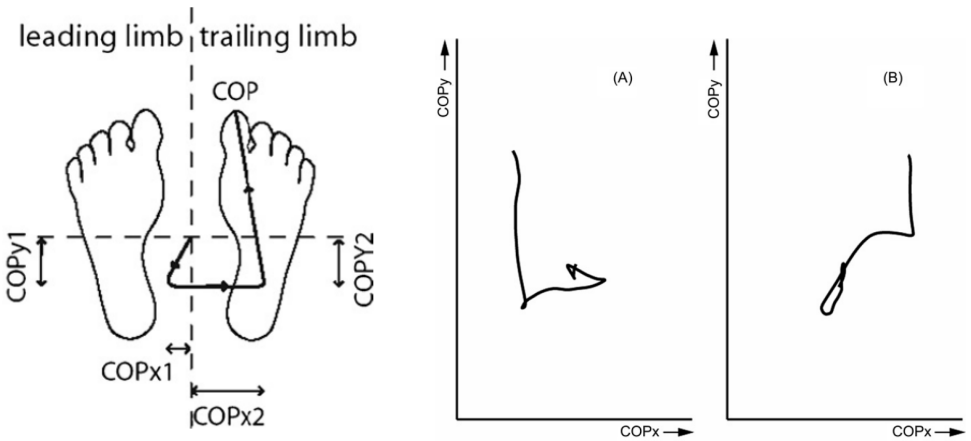


Figure 2.3: Simplified sagittal plane movement of the CoM (quadrant circle) and CoP (grey circle). From a stationary position 1, the CoM shifts forward, signifying gait initiation. For stability, the CoP moves ahead (A) of the CoM. The CoM is held within this base of support throughout ambulation, stabilising the pendular motion. The central nervous system controls the musculoskeletal system such that this balance occurs seamlessly.

an inverted pendulum, see Figure 2.3, with double-support denoting transitions between pendulum swings [39]. This simplified perspective formed the basis of early walking models to explore the mechanics & energetics of gait and will be discussed in later sections.

In able-bodied gait, there appears to be some natural asymmetry between the lower limbs, whether a functional preference based on the physiological motor task or neurological limb dominance, it is significant in pathological or amputee gait [71]. For unilateral amputees, the double support period as weight is transferred to the prosthetic side is comparatively extended with respect to contralateral side, because of uncertainty in loading the prosthetic [72]. This coincides with preferring extended loading periods of the intact limb and to lead with the prosthetic side during gait initiation [70]. Amputees may even find themselves loading the intact limb during the double support regardless of which leg is leading in gait initiation [73]. Such phenomena display both a physiological and psychological impact on the gait cycle due to the amputation of a leg. The amputees recognise a physical loss in propulsive function, which causes the uncertainty in using the amputated limb for support tasks.

Whether such effects increase in magnitude with higher walking speeds as seen in able-bodied walking has been disputed. One study detected reduced temporal



(a) (b)

Figure 2.4: Examination of CoP paths in the transverse plane during gait initiation, taken from Vrieling et al. [70]. On the left, 2.4a, is the typical CoP path for a healthy individual. On the right, 2.4b, are trajectories of an amputee. Plot A is when the prosthetic (right) limb leads, and plot B from the contralateral (left) limb leading. The preference in leading with the prosthetic limb is evident in the greater control and similarity of a healthy individual.

asymmetry with increased loading asymmetry on the intact limb when walking speed increased [75]. Whereas similar research observed a comparable difference in loading ratio between the two legs, but this was invariant to walking speed [74].

Such observations of asymmetry in the gait cycle of amputees have been documented in many journal publications. Initial results identified the compensatory mechanisms undertaken by the contralateral residual limb as an outcome of lost energy generation from the plantar-flexors during pre-swing [76, 77]. However, the consensus of effect on amputee health around this time was conflicting. Some researchers concluded minimal risk of developing degenerative arthritis [78], others found a positive correlation between larger forces on the residual joints and thus a higher risk of osteoarthritis [79]. More recent publications have agreed with the latter, postulating that prosthetic feet with increased push-off power could moderate the risk of contracting osteoarthritis [24, 80, 81].

It is clear that the amputation of the lower leg, even if only trans-tibial, can result in significant adaptations to the gait cycle. This incurred loss of propulsion

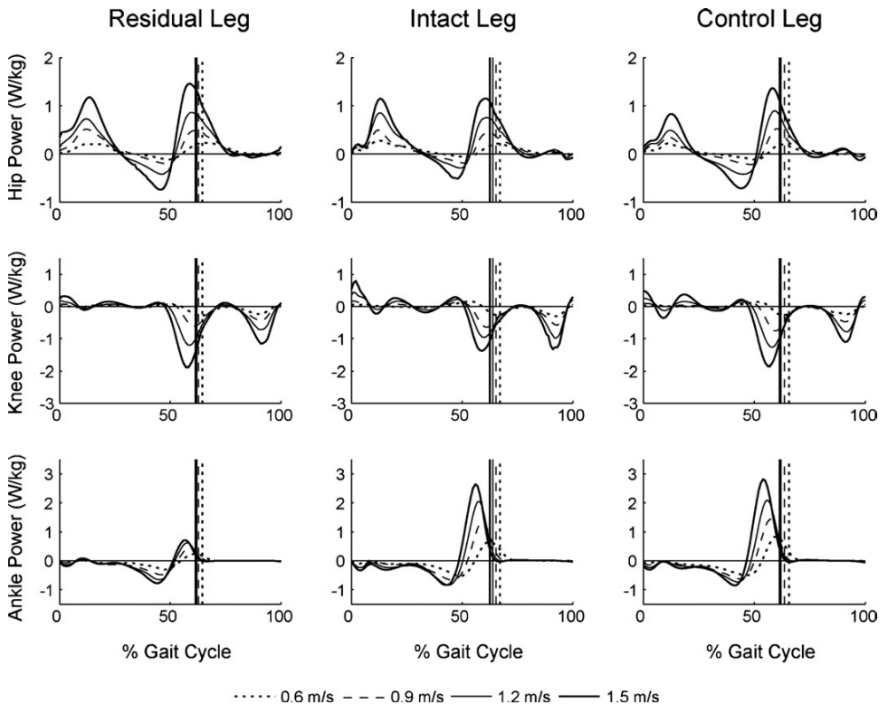


Figure 2.5: Plots of joint power from experiments on trans-tibial gait with increasing steady-state walking speed [74]. The significant differences in joint power between the intact limb and residual leg, an expected. All cases follow the typical responses expected when walking speed increases. Such adaptations in producing power will be explored further in sections 2.1.4 & 2.1.5

and asymmetry has links to the development of debilitating rheumatological diseases such as osteoarthritis. Numerous gait metrics have been explored to evaluate the asymmetry [82], and much research has been conducted to further understand the mechanisms and characteristics, using combinations of modelling and/or experimental analysis [83, 27].

The following sections in this chapter will expand on the above. Each focuses on a particular aspect of biomechanics, with the objective of all to provide relevant background discussion to assist in the design of prosthetic feet.

2.1.3 Musculoskeletal System & Work

The mechanics of human gait originate from within the brain, using the network of neural pathways. These transmit signals to the muscles which cause a chemical reaction at the cellular level, activating groups of agonistic & antagonistic muscles. The combination of muscular forces creates the moments acting at joints, which cause the corresponding motion of body segments.

Human gait is complex, the statement directly above covers a fundamental description of what occurs as a localised event throughout the body. To achieve bipedal walking, multiple motor tasks are simultaneously completed. A synergy between muscles occurs, as they generate and absorb energy, committing to the common goal of locomotion. To better understand this system of energy balance, researchers have employed a variety of exploratory methods to determine the internal work. A review of these has been concisely presented in [39], where the author evaluated the following methods:

- Energy Increases in Segments: - Sum of the increases in segment energies.
- Centre-of-Mass Approach: - Energies of the centre of mass.
- Sum of Segment Energies: - Sum of the energy within each segment.
- Joint Power and Work: - Power and work calculated at joints.
- Muscle Power and Work: - Power and work calculated in each muscle

Each successive method in the list includes aspects of energy balance that the previous method did not.

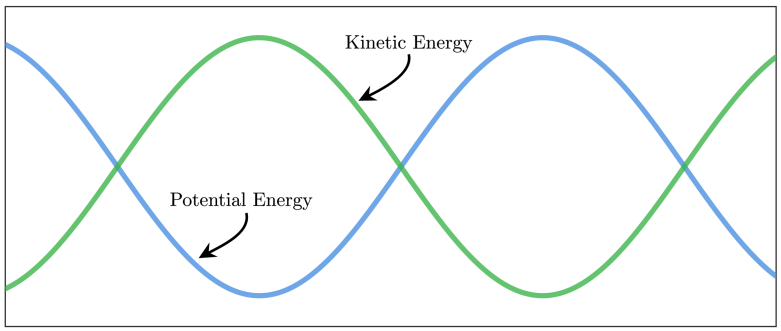


Figure 2.6: Simple diagram representing the potential to kinetic energy transfer of a frictionless swinging pendulum.

In principle, the entire body or any segment of the body will have three types of energy:

1. *Potential Energy*

$$PE = mgh \tag{2.1}$$

2. *Translational Kinetic Energy*

$$KE_{translational} = \frac{1}{2}mv^2 \tag{2.2}$$

3. *Rotational Kinetic Energy*

$$KE_{rotational} = \frac{1}{2}I\omega^2 \tag{2.3}$$

As motion occurs, and assuming all energy is conserved and not lost, then the exchange of these energies will follow a sinusoidal pattern, see Figure 2.6; a plot similar to that of a swinging frictionless pendulum mentioned in section 2.1.2.

Dynamic Walkers

The CoM approach utilised this pendulum theory to determine the external work of the lower body acting on the ground. It was suggested that this external work was imperative to maintaining the CoM pendular motion [84]. Although the assumption that this method would also represent the sum of segment energies was later proven false [85]. Whilst the external work could be measured accurately from the CoM, internal work required calculations of segmental energies summed together [86].

Passive dynamic walkers based upon the inverted pendulum have been explored as a method of understanding the classical mechanics of the gait cycle. An initial

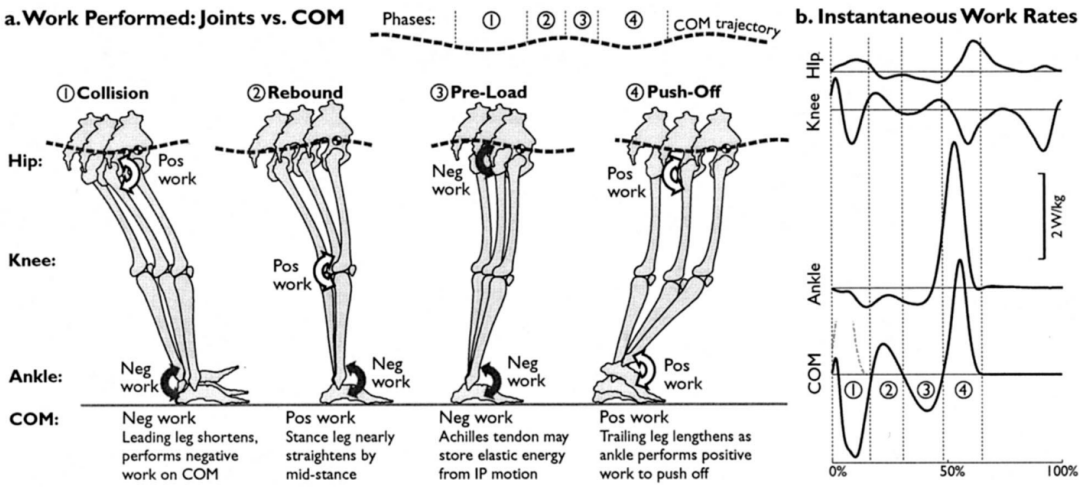


Figure 2.7: A refined concept model of the inverted pendulum theory by Kuo et al. [87], examining the link between mechanical work done on the CoM and joint power data. The stance phase is broken up into four subphases that are defined by a change in sign of CoM work performed. There is a notable metabolic cost in the step-to-step transition and redirection of CoM, as seen in the collision and push-off subphases. From this comparison, it can be seen that the rigid body dynamic model cannot account for all negative work seen on the CoM during collision, the positive work in push-off can be mostly attributed to the ankle joint.

model was comprised of rigid massless legs with point masses for the feet and hips. It was found to be stable and judged to be a suitable candidate for further studies [88]. Using this model for research on external work, individual rather than previous combined limb calculations [84, 86] were found more accurate for estimates during double-support due to simultaneous positive and negative work performed in the legs [89]. The CoM velocity is redirected downwards to initial contact, upon which negative work is performed, requiring large positive work to redirect the CoM velocity. It is suggested this external work is a major determinant in step-to-step transitions [90].

The addition of a toe-off impulse was found to improve energetics, reducing the collision loss, and further supporting the individual limb theory [92]. Comparisons to experimental data and more complex models have supported these findings and reinforced the passive/active dynamic walker model's use in understanding the simplified mechanics of gait [87]. One such study cross-examined experimental data with models to show that the ankle joint accounted for the majority of positive work, whilst indicating passive tissue is responsible for much of the negative work [93].

A detailed collisional model proposed a rolling shape would reduce collisional

costs, and that legs should be modelled with elastic behaviour [94]. Rolling foot shapes of a particular radii were later experimentally proved to reduce step-to-step transitions [95]. This reduction in negative work could also overcome the loss of active positive work with fixed ankles [96]. Further to this, it appears the length of the arc has more effect than the arc itself due to reducing the collisional work [97]. In amputees, the step-to-step transition cost was found to cause increased energy consumption due to the lack of positive work in the trailing prosthetic limb [98], an effect that could be mitigated through an active component [92], or the use of roll-over shapes [95, 96]. This will be discussed further in section 2.2.

Adding a spring to the model made some significant changes, suggesting that

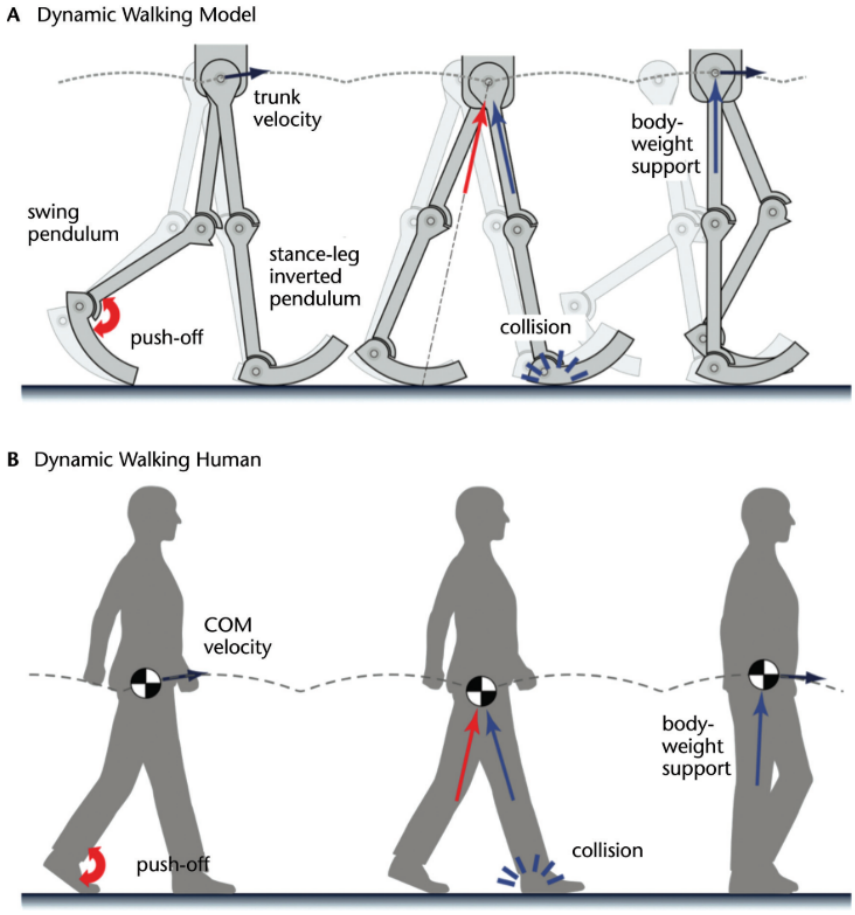


Figure 2.8: Comparison diagram demonstrating the similarities of a dynamic walking model to a dynamic walking human [91]. During single-support phase, the inverted pendular motion carries the CoM over into double-support. Negative work is done as the leading leg hits the floor, and with positive work from the trailing limb, the CoM is redirected into the subsequent single support. This dynamic model solves the paradox of passive pendular walkers assuming no positive work is completed.

walking gait was closer in nature to a bouncing running gait. Energetics of walking may be more dependant on the ability to elastically store energy during double support, rather than following the inverted pendulum arc [99]. Although too much flattening of the CoM displacement has been shown to enact increased energy expenditure [100]. The gradual changes to the dynamic walking model have facilitated its development into a comprehensive tool that can effectively model and predict gait mechanics [101]. With more recent adaptations extending their efficacy in examining asymmetric characteristics of gait [27].

Whilst these passive models have demonstrated their ability in analysing the sagittal plane, experiments have shown neuromuscular control in the medio-lateral planes to be important [102]. There are other areas where their elegant simplicity cannot explain all the complexities of walking. Single support estimates should be used with discretion due to the increased angular displacements in relation to the CoM [89]. By not considering kinematic and force trajectories as determinants of gait, the dynamic walker models suggest that singular optimum patterns for these could be inconsequential [91]. Such a view is supported by experimental work that discovered the gait cycle can be continuously optimised to improve energetic expenditure [103]. Although effective at analysing external work and mechanics, the dynamics walkers are unsuitable to estimating the musculotendon work that would allow an understanding of how such adaptations can occur. Appropriate use of them would be in conjunction with a model that calculates the muscle work directly, although joint estimations may be considered as a suitable alternative [104]. Research work on models that can calculate muscle work will now be discussed.

Musculo-tendon Contribution

The tendons and muscles have a synergistic partnership in producing the energy required to move the limbs. Much of the knowledge on tendon behaviour is founded upon studies using combinations of in-vivo and in-vitro avian experiments. These discovered that the elastic properties of the tendons are independent from the muscles, which makes them suitable for storing elastic energy in a controlled stretch-recoil cycle [105]. It has also been proved that this "separation" assists the muscles in generating efficient force and thus reduces the amount of positive work the muscles must undertake [106, 107, 108]. Further to this, the muscle's functional range is extended as the action of muscle fibres is uncoupled from the motion of the segments, allowing the muscles to operate isometrically [109].

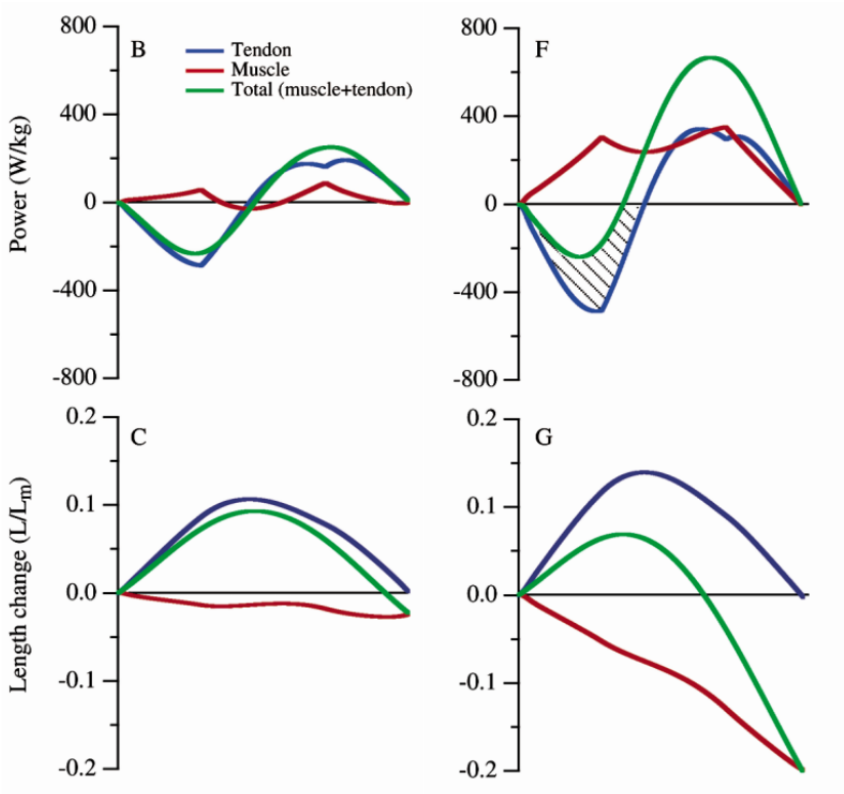


Figure 2.9: Plots of power and element length change for muscles and tendons in a model of a single contraction during steady-state running (left), and acceleration (right) [109]. Whilst a simplified model, the results highlight the tendon's ability in producing mechanical power independently, and in improving the efficiency of the muscle.

Interestingly, it is believed that a spring-like bouncing mechanism described by the dynamic walking models [99] is not an efficient analogy to describe the elastic recoil, which is more akin to a catapult action [110]; this will be expanded upon in Section 2.1.6. Additional research proposes that both models are valid as a bouncing running gait requires a more compliant spring action. The duality of these models is made possible by the tendon stiffness adapting to aid the muscles in completing the desired locomotion [111].

To facilitate the discussion on muscles contribution, it is useful to place the muscles into groups, and then collect those into the category of upper or lower leg; Table 2.2 summarises these groupings. Within the upper leg classification, the groups are formed of individual muscles that can be combined into the larger named group. Conversely, the lower leg groupings are based on their contribution to one of the two sagittal plane motions of the ankle, seen in section 2.1.1. Some muscles in these categories will be bi-articular, their connection to the skeletal frame will stretch over more than a single joint. For example, the Hamstrings will

Table 2.2: Muscle Groups

Upper leg	**Lower leg**
Iliopsoas	Plantar-flexors
Hip adductors	Dorsi-flexors
Gluteal	
Quadriceps	
Hamstrings	

cross over both the hip and knee joint. Nonetheless, the groupings used here are suitable to define their role in locomotion and discern the effect of their absence when the limb is amputated; a discussion held in section 2.1.5.

Analysing accelerations of the trunk and segmental energy has shown the plantar-flexors provide support and forward progression of the trunk and leg, whilst also contributing to swing initiation [112]. Their support role starts in early mid-stance, switching to forward progression in pre-swing. Early stance braking and forward progression is then moderated by muscles in the gluteal and quadricep groups [113].

Such contributions to support and forward progression are also seen when analysing the acceleration of CoM, calculated from the ground reaction force. At initial contact, the dorsiflexors may provide brief support, which is then transferred to the gluteal and quadriceps as observed in [113]; this is seen as the first peak of the vGRF. Support is then continued through midstance into pre-swing, where the plantar-flexors take over, producing the second vGRF peak [114, 115]. Likewise, the negative portion of the anterior-posterior can be proportioned to the muscles that aid in deceleration, whilst the positive section is distributed by the muscles providing forward progression [18]. Changes in the ground reaction force when walking speed is varied, can be attributed to adjustments in peak forces and contributions of the muscles, due to the new motor requirements [116].

Modular control of walking has provided similar insights. In early stance the gluteal and quadriceps muscles provide body support, which is taken over by the plantar-flexors in late stance together with forward progression. The plantar-flexors are aided in initiating leg swing by the iliposoas, with deceleration controlled by the quadriceps and hamstrings [117]. Such a control system is supported by a study which discovered the work contribution of muscles does not change but rather scales with walking speed [118].

However, this analysis and others that make observations in the sagittal plane

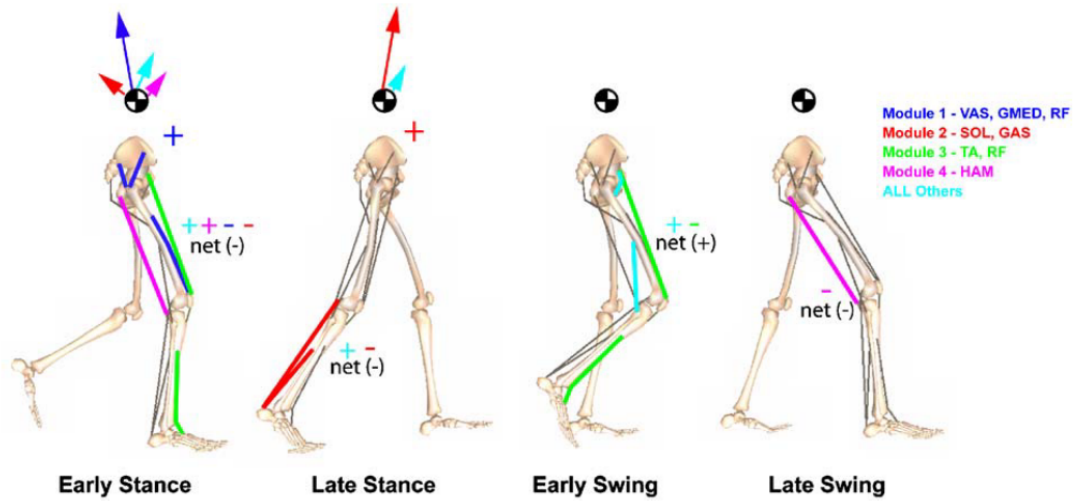


Figure 2.10: Diagram that illustrates the contributions of muscle modules to four phases of the gait cycle [117]. Whilst many groups are acting in early stance, it is the plantar-flexors in module 2 that have the largest role in late stance.

cannot account for control needed in the mediolateral control [119]. It seems that the major muscles that provide support and forward progression in the sagittal plane, also aid in mediolateral control of the frontal plane with the hip adductors [120]. A cursory overview of these muscle contributions can be seen in Table 2.3. Evidently, the muscles groups of the lower leg are active in almost every event of the stance phase in the gait cycle. The dorsiflexors are dominant in early stance, decelerating the leg and transferring energy proximal to the trunk. In late stance, the plantar-flexors provide the support and forward progression required as precursors to swing initiation.

As a collective, the muscles of the lower body produce the forces and stabilisation for efficient locomotion in the gait cycle. Understanding this coordination requires models that can accurately determine forces produced by each muscle, through which exchanges of segmental energy can be determined, providing insights into the energetics of the gait cycle [121, 122]. In general, it is appropriate to use modelling results for understanding muscle behaviour, but to acknowledge the significant limitations whilst doing so. Various methods and inputs have been used to different effects [123, 124, 125]. These models will conflict in the structure of their musculoskeletal representation and thus the muscle contributions they report[126], particularly with amputees where many researchers have not adapted the model to sufficiently represent the biomechanics of prosthetic users [127]. Such errors only add to the current misappropriations and generalisations that can obscure evaluations of the metabolic expenditure of amputee gait [128].

Table 2.3: Muscle Contributions to gait events

Muscle Groups		S	FP	SI	B	MC	SL
Upper Leg	*Iliopsoas*			✓			✓
	Hip adductors					✓	
	Gluteal muscles	✓			✓	✓	
	Quadriceps	✓	✓		✓	✓	
	Hamstrings						✓
Lower Leg	*Plantar-flexors*	✓	✓	✓		✓	✓
	Dorsiflexors	✓			✓		

Column headers denote events of the gait cycle muscles contribute to the stance phase events: Support(S), Forward Progression(FP), Swing Initiation(SI), Braking(B), Mediolateral Control(MC). Some of these muscles also contribute in aiding Swing Leg(SL).

2.1.4 Kinetics & Power

The preceding subsections of this chapter have already covered many relevant terms used in describing the kinetics of human gait. In exploring the step-to-step transition metabolic cost, researchers have examined the collisional and propulsive reaction forces. These act from the CoP located on the sole (plantar) of the foot; the location of which moves throughout the stance phase, as seen in Figure 2.4a. More commonly referred to as the GRF, this vector is the reaction sum of all forces the body imposes on the floor and is said to pass through the CoM. It is through these forces, originating in the muscles, that the motion of the lower limbs is achieved. Chapter 5 will explore the measurement of these forces in more detail. This section will investigate the analysis of these forces in understanding the gait cycle mechanics.

The GRF vector can be broken up into three components; a normal vertical force, and two shear forces referred to in this thesis as the anterior-posterior, and medio-lateral forces. From a simplified perspective, the entire vector is the sum of all body segment mass-acceleration products. Thus, for N segments, the reaction force in the x-direction can be given as:

$$F_x = \sum_{i=1}^{N} m_i a_x i \tag{2.4}$$

However, as has been explored in Section 2.1.3, it is not possible to determine the role of individual segments from metrics derived with the GRF without additional calculations and data. Many segments will have actions that will counter each

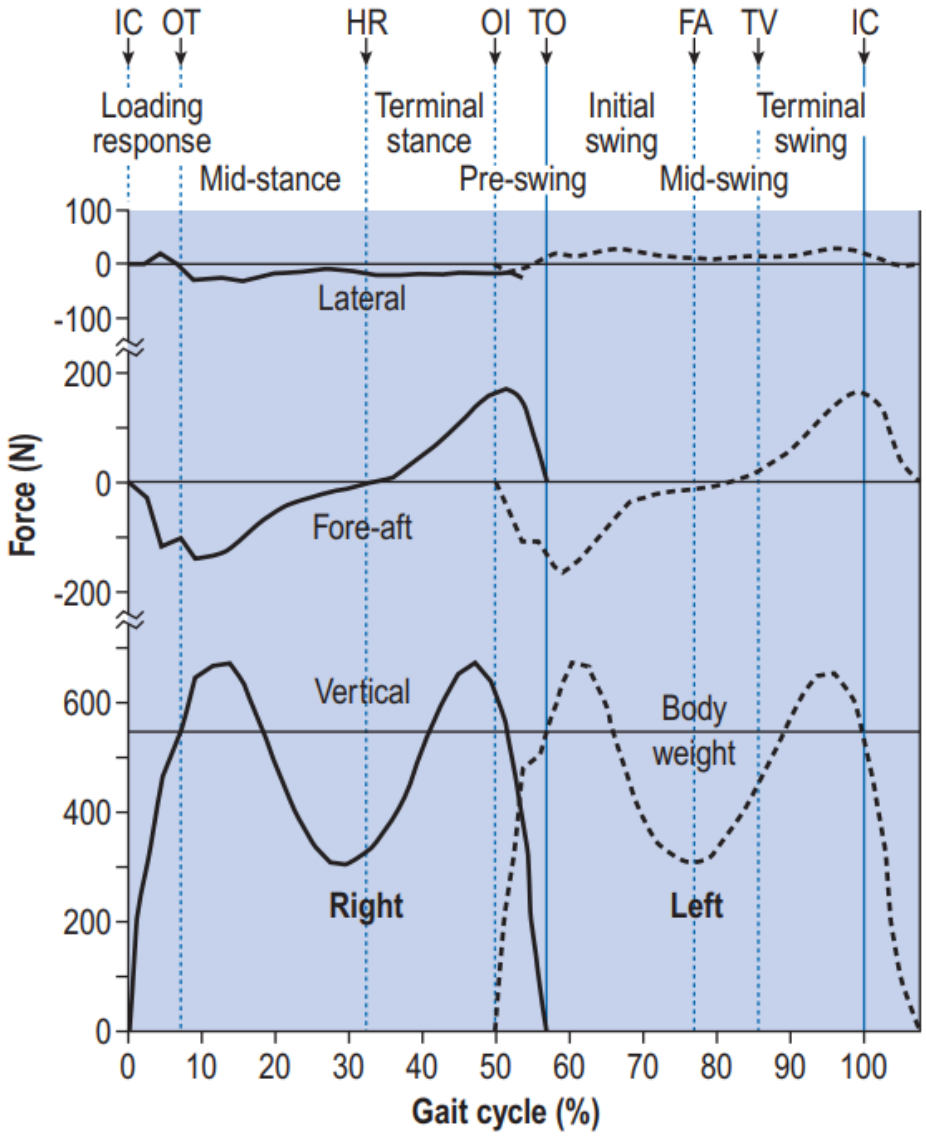


Figure 2.11: Three components of the GRF vector, data is from Whittle's book on Gait Analysis [61]. From the top: Medio-lateral, Anterior-posterior, and Vertical forces. The abbreviations at the top of the figure coincide with the gait events in figure 2.2b.

other and cancel out their respective summation.

Despite this, it is still possible to use the GRF as a tool for gait analysis, as long as the limitations are acknowledged. The plots in Figure 2.11 are typical of recorded forces in able-bodied gait. The medio-lateral component is smallest of the shear forces. It is unique in that the sign convention shifts across each foot rather than repeat, illustrating the displacement of CoM from one side to the other. Despite quite often being disregarded in analysis, a study found that it signifies an important metabolic cost in controlling lateral balance of the CoM, as muscles will

oppose each other in contributions [129]. It appears that amputees have increased step width variability, suggesting difficulty with such lateral balance [130].

The second shear force acts in the anterior-posterior direction. In the first half of this component, the force is negative, denoting the braking applied at initial contact. This progresses to a positive force as the heel rises, culminating in a peak that signifies the power generated in pre-swing. Studies on hemiparetic walking have shown the plantar-flexors to be the significant contributor to the anterior-posterior force [131]. Indeed, this has been verified with a study which cross-correlated the GRF with electromyography data [132]. A loss of the propulsive force has been shown to increase the hip muscle moment, which raises the risk of developing injury in that joint [23].

The normal, vertical force has a characteristic double hump. It is fitting to recognise that when standing still the vertical force is simply the body weight, and the inertial forces occurring throughout the gait cycle produce the peaks and trough. From initial contact, a sharp rise occurs as the CoM drops and weight is accepted onto a single leg, causing the first peak. In midstance, the CoM rises as it is carried over the CoP, creating an upwards inertial force, hence the drop in vertical GRF. Finally, the propulsive forces in late stance add to the body weight, generating the second peak. The external knee adduction moment is a strong index of weight distribution, with the waveform bearing similarity to that of the vertical GRF. In trans-tibial amputees, these unbalanced reaction force and knee moments have strong correlation to the risk of developing osteoarthritis in the joint [24]. Further to this, by analysing the vertical reaction and corresponding CoM work rate, the reduced push-off on the amputated side results in greater contralateral limb collision [83].

A cross-over between legs is evident where a portion of the leading leg could be superimposed with the trailing limb to provide an absolute value. In section 2.1.3, it was seen that disputes arise on whether calculations of external work should include both legs [84, 86], or just the trailing leg [89]. Data gathered in a biomechanics lab will be examined in Chapter 5, where this will be analysed and compared to the empirical studies.

Efforts have been made to provide a set of metrics that can be derived from the GRF data as an alternative to analysing the force waveforms themselves. One such attempt devised a list of eight and explored their viability in gait analysis [133]. Some of these seemed to focus on the alignment and interface of the prosthetic with the residual leg, whilst others were deemed ineffective in producing any valuable insight. Of the eight explored, the following appeared to be somewhat useful:

- **Time ratio between legs:** Indicate a preference to use a certain leg for support.
- **Vertical impulse ratio between legs:** Can provide a stronger qualitative measure to compare to the above time ratio.
- **Anterior-posterior impulse ratios:** Braking ratio can indicate confidence in the prosthetics ability to take on initial contact, whilst the propulsive ratio can reveal the mechanical performance. An absolute ratio will reflect on efficacy of the prosthetic.
- **Perturbations of the prosthetic apGRF:** Evaluations are made on the visual inspection of the data and the identification of errors.
- **Phasic time between braking & propulsion:** Provides an alternative measure to compliment analyses made with the impulse ratios.
- **Peak forces of the vGRF and apGRF**

Researchers appear favour analysing impulses as a gait metric. In examining the gait of elderly trans-tibial amputees, the knee joint impulses and reaction forces on the intact side had a significant correlation with increased tendency to develop osteoarthritis [79]. Braking and propulsive impulses show a positive correlation to walking speed, with the braking impulse having a larger effect size [134]. This would be expected as walking at a faster pace would require greater control at initial contact to ensure stability is maintained.

Many studies have concentrated on evaluations made from data collected during steady-state walking. However, experiments with able-bodied individuals have shown that whilst the within-subject variability of the GRF can be low, there is high variability in the moment patterns of the knee & hip joints [63]; which implies a range of neuromuscular activity can produce the same kinematic response. Further to this, many studies on healthy gait have small sample sizes, thus generalised conclusions applied to a broad population could be discredited [135]. In recognising this, the analysis of gait initiation has been proposed as it represents a transient period of the gait cycle that requires efficient coordination of the neuromuscular system, and thus any deficiencies can be promptly identified. Through examining the timing and peaks of the vGRF and Anterior-Posterior GRF (apGRF), amputees preferred to use their intact limb for support and loading [73].

Some researchers argue that analysis in the time domain is unsuitable due to the intra-subject variability. A method of analysing the symmetry of the GRF in the frequency domain was explored. The harmonic analysis found there to be no variability between the left and right sides, although the temporal-force measurements of the medio-lateral force were inconsistent [137].

The use of principal component analysis (PCA) has also been explored as an alternative method to analysing the temporal-force domain. It has a similar benefit to frequency analysis, as it produces a smaller set of dimensionless parameters, whilst retaining the variance of the real dataset. The basis of this method is similar to one which compared the eigenvectors of joint waveforms to assess symmetry [138]. In the examination of vertical GRF, the PCA method was able to identify variance in step-to-step transition, and then differentiated the group it was attributed to [136]. This success also led to its use in a study in which it identified

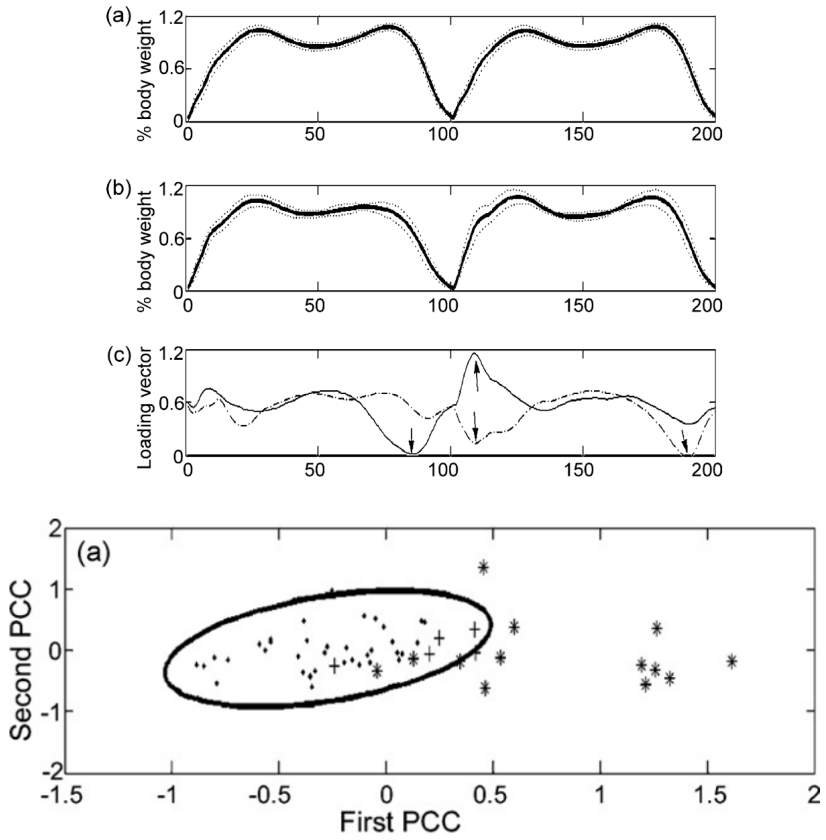


Figure 2.12: Plots taken from the PCA evaluation of vertical GRF [136]. From the top-down: the waveform of a control group (CG), the waveform of the target group (TG), plot of the first (solid) and second (dotted) principal components, spread of data between groups CG (dots) and TG (stars). Large negative and positive amplitudes in the first principal component denote a push-off deficiency for the TC which affected both limbs.

deviations in the timing and amplitude at push-off [139]. That particular study also incorporated it with a support vector machine, a type of machine learning algorithm. A modification which allowed for the data to be quantified with less involvement from the researchers.

Classical analysis methods of identifying key variables of symmetry are still successfully used. However, they require significantly more preliminary work and additional input from the rater; which ultimately results in a longer and more convoluted process [140]. In the assessment of trans-femoral amputees, the PCA method was able to identify and explain 74.5 - 93.9% of the variance in the data. Furthermore, what was detected as abnormal in the waveform is not targeted in the commonly used methods [141].

There is a lack of clarity with regards to the symmetrical nature of kinetics in able-bodied people. It seems to be dependent on the sample taken, and methods used in the analysis [71]. For amputees, the loss of important muscles has a direct effect on the ability to generate similar GRF profiles. These force profiles can indicate general performance of an individual's CoM throughout the gait cycle. With improvements to analytical techniques, it is now possible to provide efficient evaluations of performance. Such analysis can be expanded to calculation of forces in individual muscles; a method recommend to gain complete understanding of the energetics. However, it has been found that similar force profiles can be generated with varied joint moments [63]. Thus, the notion of motor redundancy should be explored in order to understand how the body will adapt to changes brought on in the amputation of the lower limbs.

2.1.5 Motor Redundancy & Kinematics

Motor redundancy is a well-studied problem of human motor control. At the start of Section 2.1.3, a concise description was provided on the principles of muscle activation. In the study of how the central nervous system decides on these activation patterns, researchers have come across the problem of motor redundancy. This topic could merit an entirely separate research thesis in itself, so in this section the explanations will avoid in-depth detail, serving only to provide a rationalisation for the research contained within.

From a mechanics perspective, motor redundancy refers to the issue of excess degrees of freedom (DoF) existing in the completion of a simple motor task. Consider the task of picking up a pen from any surface. Theoretically this can be achieved in an almost infinite number of ways. The body has multiple redundant

DoF, such as the anatomical muscles & joints, or the kinematic waveforms. The question is how the nervous system eliminates these redundancies to arrive at the control solution [142].

An extensive study with healthy subject found that despite generating similar GRF and kinematic patterns, the high variability of hip and knee moments led researchers to believe that a range of these moment patterns can create near identical joint angle patterns [63]. This area of interest was expanded and discovered that the hip moments are under consistent modulation throughout the gait cycle to maintain balance of the passenger unit. However, support must also be ensured and thus the knee moments will covary with opposite polarity. There is also evidence that the central nervous system (CNS) will favour motor patterns in which a maximal amount of energy is conserved between segments [143]. It is also possible that this ability to adapt is not hampered by a trans-tibial amputation, at least in terms of achieving step length symmetry [144].

In the gait of amputees, the high variability of the hip and knee joint moments appear to hold a key role in their adaptation strategies [145]. With the absence of push-off power generated by the plantar-flexors, an amputee will compensate with increased hip activity [76], see joint moment plots in Figure 2.13. It is also suggested that such an adaptation be strengthened by rectifying the lack of propulsive forces from the absent muscles [4].

This could be achieved with passive prosthetics and improving the residual hip output. It seems that the residual leg is capable of compensating when coupled with a passive energy restoring prosthetic [146], as even increased walking speeds failed to worsen the asymmetry [74]. The amputation and resulting compensatory methods lead to increased collisional CoM work & motion asymmetry, due to the loss of push-off power and loss of control. [83]. It was suggested that sufficient additional positive work in the hip would return some symmetry.

However, the implementation of compensatory strategies has been shown to vary between studies. When unilateral trans-tibial amputees have generated similar kinematic profiles, it was achieved without using the knee joint. The residual knee moment was not extensor during stance, and this vertical alignment reduced the braking and propulsive forces [147]. It is possible this occurred due to the loss of muscles that usually provide rigidity about the joint. Most interestingly, this shift to a proximal power generation and stiffening of the knee has been seen in the gait of healthy older adults [148]. This indicates that the adaptation strategy is a natural optimisation route formed by the neuromuscular system. A detailed

musculoskeletal model used in a forward dynamics simulation was also able to match kinematic profiles, but this required non-amputee muscle activation patterns and was thus deemed non-optimal [149]. Indeed, it appears to be impractical to achieve both kinetic and kinematic symmetry [151]. Attempting to optimise kinetic symmetry with a model was somewhat successful in reducing the joint contact forces of the intact limb. The symmetry gained came at a cost of increased energy cost and abnormal kinematics, with a diminishing return when attempting to completely match the joint moments [150].

Conversely, a separate study declared asymmetrical gait, where the hip and knee actions significantly differ from normal values. Although the general causation (loss of ankle power) and end effect (modulated residual joint moments) was the same [152]. When mass perturbations were introduced into the gait cycle of an amputee, they appeared to take on the same kinematic invariant strategy during the swing phase [5]. At the time, the effects of such changes on the energetics were

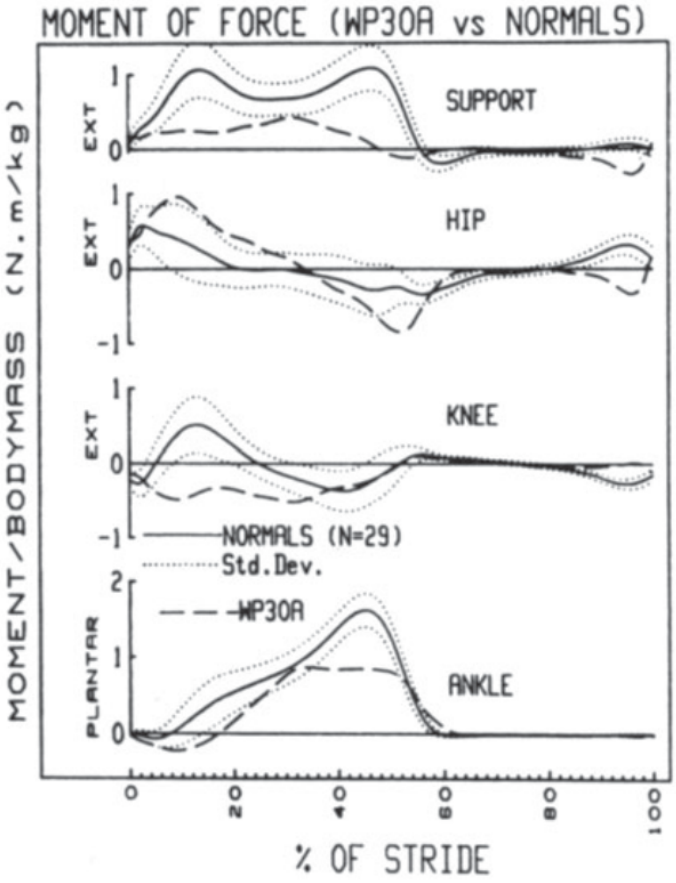
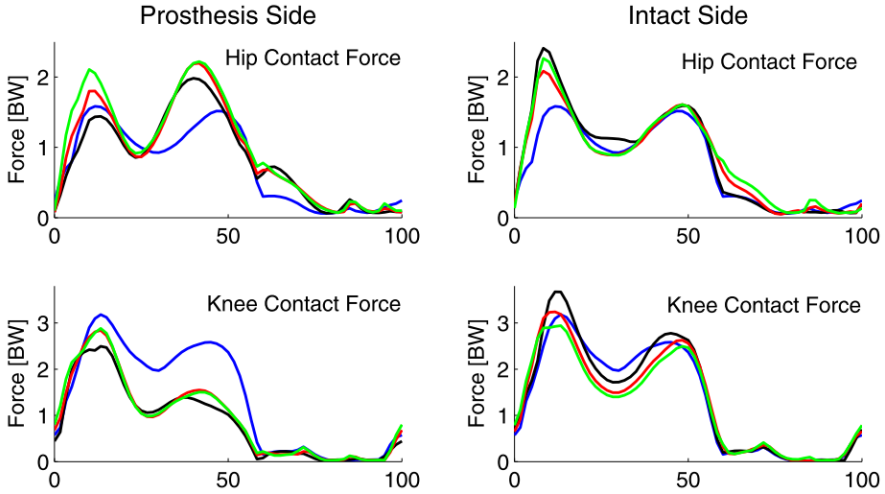
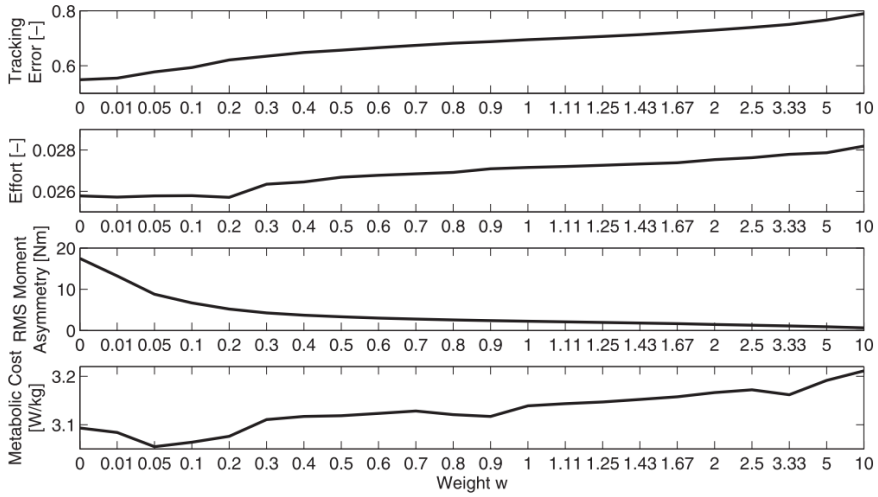


Figure 2.13: Joint moment profiles for an amputee (dashed) compared against an average for normal (solid), with dotted lines representing the standard deviation [4]. Note the larger hip moment compensating for the reduction of power produced about the ankle.

unclear with only suppositions that energy costs do not drive swing mechanisms, or that the action was behavioural in nature. Extensions to this study have determined that attempting to match the prosthetic limb with the intact limb has negative results [153]. The amputees had increased temporal asymmetry, and the same kinetic joint symmetry as previously reported [5]. However, the results suggest that this required considerably more muscular effort. Possibly because the



(a)



(b)

Figure 2.14: In the top figure the plots are of joint contact forces against % gait cycle, under the different model solutions. The blue plot represents able-bodied gait, whilst the others are the amputee symmetry optimisations; in order of symmetry: black, red, green. The lack of push-off force caused higher contact forces in the intact limb joints. Also of note is the degree of symmetry needs to be controlled as the contact force become unsuitable is the aim is too high. This is clear in the bottom figure where the weighting of the objective function has a negative trend with asymmetry, at the cost of increasing the metabolic cost and effort [150].

soleus muscle is the major muscle involved in the modulating the leg in response to perturbations [154]. With it missing due to amputation of the lower leg, other muscles compensating do so in an inefficient manner from their usual role.

Most adaptations appear to reduce the loading on the residual limb, which then causes the higher loads on contralateral side, corresponding to higher rates of osteoarthritis [6]. The CNS is not capable of recognising these long-term effects, but it does seem capable of providing functional adaptations, and symmetry may not be a necessity.

Gait initiation is again a useful transient period in which to evaluate motor adjustments to gait. Amputees will employ different motor strategies to achieve the same propulsive force initiation goal. When the prosthetic side initiated the step, the inability of the prosthetic in generating any of the early propulsive forces resulted in the intact limb taking longer to execute gait initiation after the CoP had shifted to the stance side. When the initiation was with the intact limb, it took longer for the amputees to shift the CoP balance onto the prosthetic. Despite these differences, the velocity at the end of the step was the same regardless of which limb initiated, highlighting the ability to adapt the propulsive forces [155].

It is clear then that the CNS is quite capable of managing multiple simultaneous controls to complete motor tasks in the gait cycle, and when confronted with a new normal, adapting these controls in an attempt to overcome deficiencies [142]. With the control coming from muscle activation patterns, and variations in the success, it has been important to understand how these are selected. Researchers have taken on this problem from a mathematical perspective, studying optimisation models that minimise biomechanical objective functions. A shortlist defined three objective functions that would be determine the muscle activation patterns, these were; Metabolic energy expenditure, Muscle fatigue, and Sense of perceived effort[156]. It seems to be that minimising the energy cost is particularly important, being pursued even when the positive gains are minimal [103].

Such optimisation methods have been criticised, due to the opinion that the constraints they apply in solving the problem, prevents the complete understanding of the full motor control system [157]. The modular control system [117], previously mentioned in section 2.1.3, has been shown to alter the excitation of muscles within modules in response to new demands [158]. These results provided a theory which suggests the modules will be favoured in exploring new adaptive motor control. However, this has doubts as swing leg adaptation patterns have been shown to deviate from the standard module groupings [159].

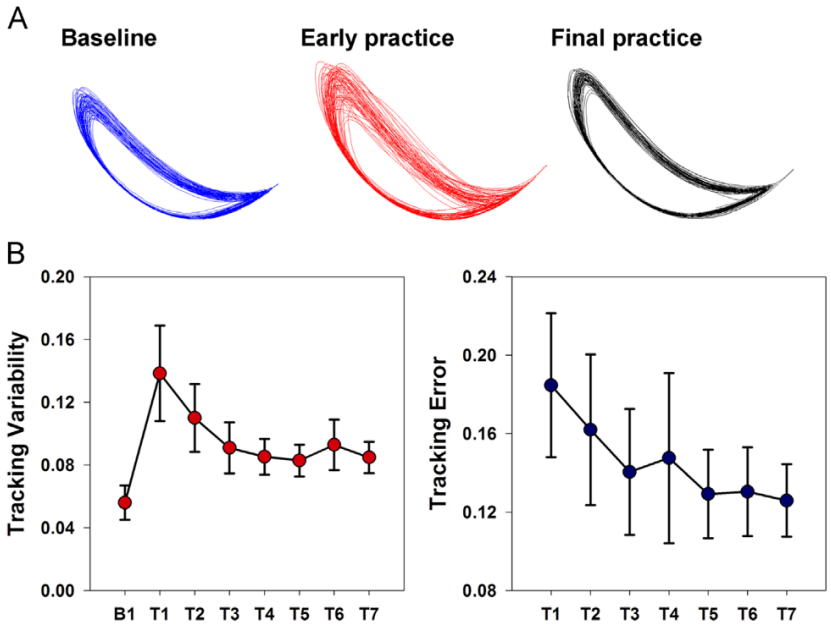


Figure 2.15: Figures displaying the adaptive capabilities of the motor system [159]. The top set of figures show the trajectories of the subject's foot; a baseline measurement is used for comparison. Whereas the initial trials show large variation, by the end of the experiment, the subject has adapted to the new pattern with a comparable margin of error to the baseline. The learning process can be tracked in the bottom two plots of variability and error.

The method in which the joints and muscles have been shown to compensate for each other has given rise to various motor control theories. The 'uncontrolled manifold' approach has gained the most traction since it originated. This theory works on the idea that rather than solving for a motor redundancy, the problem should be thought of as a motor abundance [160]. A motor task will have a 'uncontrolled manifold' in which all possible kinetic & kinematic variances that can achieve the task exist. The CNS then stabilises the system within the bounds of these variances in order to achieve the end goal [161].

Whilst studying the adaptation when fitted with a new prosthesis, researchers indirectly discovered the mechanics of this process [162]. The extent to which the step patterns fluctuated varied between each data collection session, an apparent reaction to adjusting to new DoF. Furthermore, the prosthetic ankle was the primary source of fluctuation, suggesting that better controlled prosthetic would improve coordination of the DoF [162]. It is also possible that the continuous pursuit of optimal energy cost occurs as part of the exploration into the uncontrolled manifold [103].

The control scheme of the musculoskeletal system is clearly adept in compen-

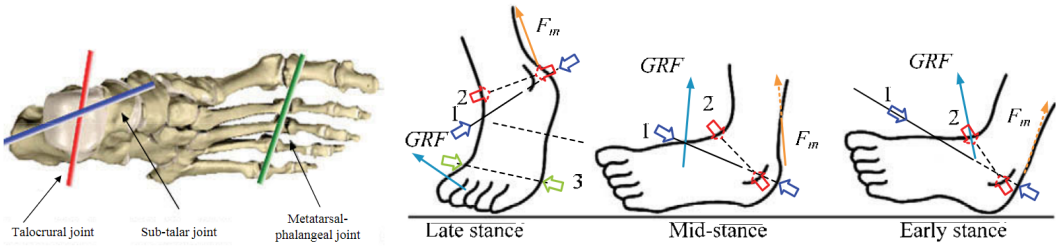


Figure 2.16: The activation of different ankle joints at three key stages of the gait cycle [163].

sating for significant changes brought about by an amputated limb. It appears to favour invariant kinematic patterns but is capable of learning new pathways. However, these adaptations come at a cost of unfavourable joint kinetics, which leads to a higher risk of osteoarthritis. The exact mechanism in which the CNS determines the muscle activation patterns is somewhat unclear, although minimising the metabolic cost appears to be a significant condition. Due to the loss of the plantar-flexor muscles, those in the upper leg take on a larger role in providing support and propulsion. The ankle-foot complex is a well-studied area due to its apparent importance in gait mechanics, and as such deserves some focus in the next section.

2.1.6 Ankle-foot Complex

The capabilities the lower limbs have demonstrated in the research is indicative of a sophisticated biological system. Of all the "subsystems" composing these appendages, the ankle-foot system has shown particularly impressive characteristics. As a segmental structure of complex joints, it is capable of adjusting the axis position and coupling rotational motions to perform simultaneous poses across multiple planes [69]. A four-link segment model has been used to demonstrate the adaptability of the structure. The combination of three joints allows for combined 3D rotations (see Figure 2.16), which is used to activate different segments from early-to-late stance. This pseudo-flexible state reduces the GRF moment arms, enabling the muscles to optimise their mechanical effort to a high efficiency [163]. A comparable level of performance has also been seen with a reduced three link segment model [164]. It appears that the ability to adapt in more than just the sagittal plane is a baseline feature requirement of the ankle-foot complex.

In section 2.1.3, the mechanical characteristics of the tendons were highlighted, and these specialised biological structures are fully utilised in the ankle-foot complex. The plantar fascia is composed of the same fibrous connective tissue which

is capable of adjusting the stiffness to suit particular phases of gait [165], such as providing stability during balanced standing [166], or acting as a lever transferring the propulsive force into the ground [167].

In vivo methods were used to record the Achilles tendon force and scan the fascicle lengths of the medial gastrocnemius and soleus [110]. The results displayed the tendinous tissue stretching slowly throughout early to mid-stance, after which they rapidly recoiled at the onset of the push-off event. However, the muscles act isometrically during this tendon activity, indicating that they are unable to contribute to work [108]. From this, it was suggested that walking can be modelled as an elastic recoil catapult action, possible due to the coupled nature of the tendons and muscles [110].

Under focused examination, the Achilles tendon demonstrated specialised compliancy to suit particular gait tasks and was thought to contribute to optimising muscle efficiency [111]. An experiment using exoskeletons produced evidence to support this theory, where attempts to improve the lower limb joint efficiency hitting limits due to the natural biological advantage. When delivering 22% of power across joints, the exoskeleton only achieved a net metabolic saving of 10%, which indicates the Achilles tendon as a significant contributor to the push-off phase of stance [168]. The efficiency of the ankle joint is also higher than that of the knee or hip. Due to the smaller articulation and shorter tendon tissue, the more proximal joints are unable to utilise the efficient stretch-recoil cycle of the tendons. This explains why the metabolic cost of walking increases when the mechanical work is redistributed to other joints [21].

It appears that delivery of power stored in the tendons is important to economical gait as a way of progressing the CoM and counteracting the collision losses at heel-strike [169]. In addition to this, the timing of the power release is critical - perhaps more so than amplitude of the power itself [170]; see Figure 2.17 where results show an increase of power just from suitable timing. Both parameters are intrinsically linked to the collision losses at heel-strike, and redirection of the CoM mechanics.

Other modelling and experimental work have demonstrated how the ankle joint assists in this forward re-direction of the CoM velocity, which is essential in reproducing the characteristic rocking motion. [93]. The same research further suggested that the collision work is predominantly conducted by passive tissue. When the heel structure was studied, the biological coupling of the fatty tissue and connective fibres had beneficial impact attenuation and energy storage [171]. This passive behaviour would explain why little power is transferred forward during heel

strike, instead being used to support the transfer of vertical mass [22]. Following this braking period, the catapult stretch-recoil pattern is seen in power analysis, which indicates a quasi-uncoupled nature between heel-strike and ankle power generation. Such behaviour would suggest that the CoM is less affected than previously determined in dynamic walking models. But this unexpected outcome can be suitably explained when considering the localised acceleration of the limb would aid in the full body CoM mechanics [20].

For the sake of improving computations, it is common to try and reduce the unknowns by combining structures. In the foot this would be the bones comprising the tarsus, metatarsals, and phalanges. However, removing some of these structures from rigid body models can cause irregularities in joint power estimations, and these additional segments are needed to capture accurate behaviour of the ankle-foot complex [173]. It has also been argued that models using anatomical representations of the ankle-foot do not consider how motion with a prosthetic foot is inherently different to that of a biological system [174]. Thus, care must be taken when using such techniques to inform design optimisation. Nevertheless, combining different models can allow researchers to understand how different structures contribute to the overall output. Whilst the ankle joint is definitive in being the primary source of power, the distal foot structures are adept at absorbing energy. When the two models are combined, the ankle-foot complex is comparable to a mechanical spring due to the work ratio - see Figure 2.18 [172].

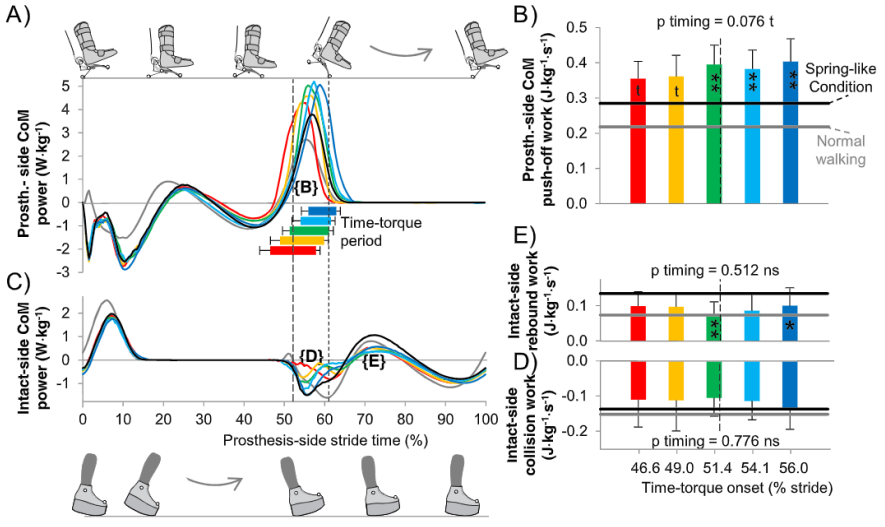


Figure 2.17: Results from a study on the timing of energy release. The colours used represent different timings as can be seen on the horizontal axis. The research identified a release close to contralateral heel strike to be the most optimal for reducing collision losses and metabolic rate - see the green (middle) data set [170]

To overcome this, novel solutions have been developed. Rather than recreate an anatomical representation with segments, researchers have replaced the structure below the knee with a deformable component. This model was able to deliver a total power comparable to that of the anatomical segment models [175]. Although its simplified nature can conceal isolated effects and sources of power, results from other studies suggest this loss would have more effect on pathological gait analysis [173].

Hysteresis loops of ankle moments and angles demonstrate the quasi-stiff nature of ankles. It has been suggested that a passive device would be capable of

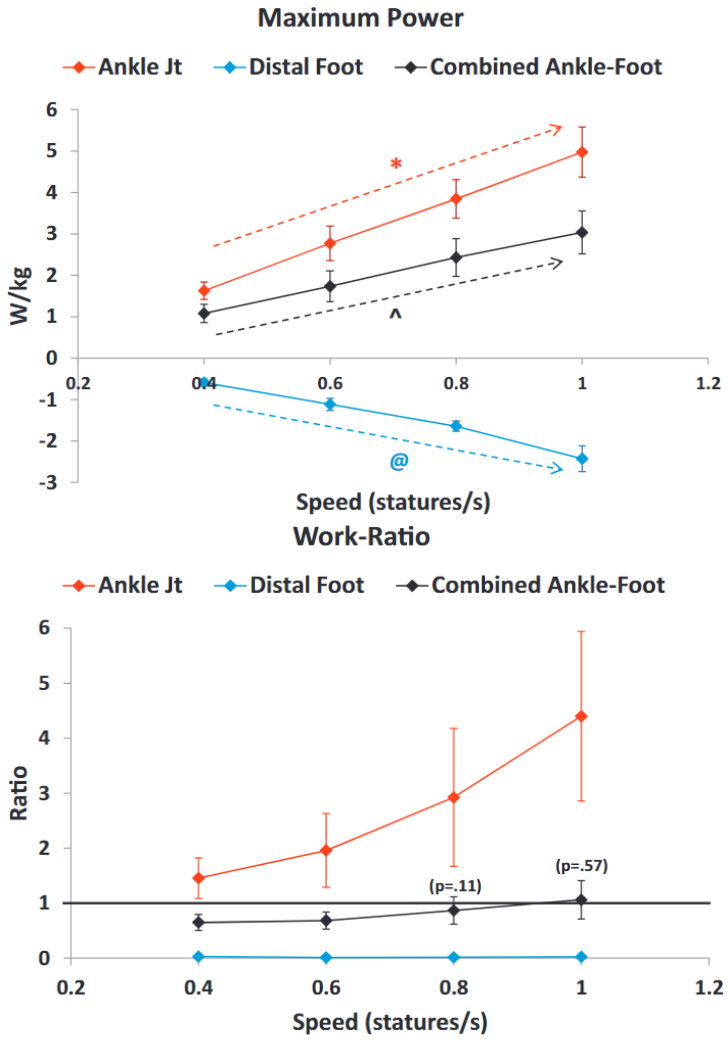


Figure 2.18: Both figures are taken from the study on combined models to capture distal structure behaviour [172]. In the top plot of maximum power, the Ankle Joint model in red and Distal Foot model in blue, are compared to the combined model. A significant portion of negative work appears to be completed by the distal structures, enough to have an effect on the combined work ratio. In the bottom plot, this ratio is less than 1 for three of the four recorded statures.

replicating behaviour up to normal walking speeds [176], after which the behaviour changes - see Figure 2.19. Such a device would need a rotational spring or have a structure capable of reproducing the same behaviour. The work on rollover shapes has demonstrated that a relatively simple curved shape can contribute to replicating some of this complex rotational action [95], and somewhat negate the loss of power [96].

The terms "stiffness" - referring to the impedance of a system, and "quasi-stiffness" - related to the derivative of the ankle angle-torque curves, are commonly used as performance metrics of prosthetic feet. A research group using inverted pendulum and bipedal models studied the definitions of these terms. For passive feet, the quasi term is redundant as the two stiffness definitions are equal. The modelling also confirmed that the angle-torque relationship does not match the stiffness, and suggested that the mechanical stiffness, not quasi-stiffness was key to understanding the dynamics of gait [44]. Following on from this study, experimental data was collected to analyse the ankle stiffness, and establish a linear regression model that defines the stiffness as a function of ankle angle. The relationship was found to be quadratic with an $R^2 = 0.98$ [45]. This ankle stiffness function would make it possible to tune a series stiffness element that would efficiently recreate the passive elastic behaviour of the ankle-foot complex.

To offer an adaptable series stiffness during stance has been demonstrated as beneficial in other modelling efforts, where suitable control of elasticity and timing aids in the mechanically economical walking [177]. For control of the timing, it was suggested that the optimal ration of foot length to stiffness be used, which would time the release of energy with contralateral heel-strike and redirect the

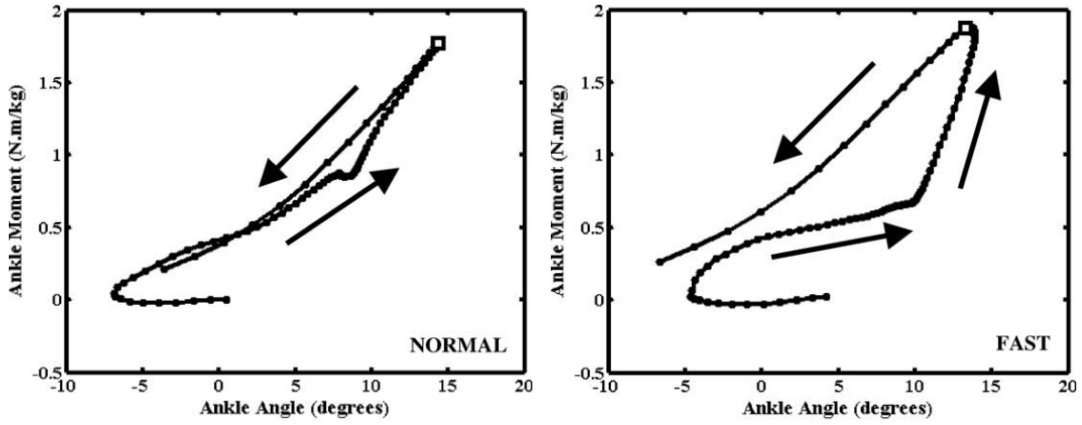


Figure 2.19: Plots of ankle quasi-stiffness through-out stance. With normal walking speed on the left, and fast on the right, there is a clear difference in behaviour. Normal walking is almost linear, whilst fast has a steep controlled dorsiflexion in which energy is stored [176].

CoM velocity forward.

Some research has dedicated attention to quasi-stiffness profiles for mechanical optimisation of prosthetic feet. Statistical models have been created to estimate the quasi-stiffness and mechanical work of the ankle during stance. With two forms, one general and the other stature-based, the models were able to predict the two parameters with reasonable R^2 values of $> 75\%$, for error values between 13% and 30%. Indicating that these models could be used to tune a mechanical spring at self-selected gait speeds [178]. However, the fit of data to average values outside of the sample group revealed much larger errors due to the regression-based models being tuned only to their sample group. Similar studies on quasi-stiffness profiles have also identified the effect of gait speed, specifying linear elastic behaviour at preferred speeds [179]. However, these types of studies will also attribute power absorption characteristics to the ankle, which could be ignoring the contribution of distal structures [172].

2.1.7 Summary

This section has covered key aspects of biomechanics necessary to understand the functionality of the lower limbs and ankle-foot complex. The musculoskeletal system is capable of highly efficient work output, utilising specialised tissue like the Achilles tendon to provide important power absorption and generation throughout stance. Varying adaptation strategies are seen after amputation, and literature is agreed in the use of linear springs for self-selected gait speeds. In the next section, the review will explore how such understandings have influenced the design of prosthetic feet.

2.2 Prosthetic foot design

2.2.1 Early passive prosthetics

Originally, energy storing feet were designed for sports, but research led to adaptations suited for normal walking [180]. The earliest of these designs, termed Dynamic Elastic Response feet, borrowed the flexible keel and merged them with the cushioned heel of Solid-Ankle Cushioned-Heel (SACH) feet, see Figure 2.20 [181]. This was in an effort to extend the roll-over shape with the additional forefoot stiffness [182]. Soon enough designs that could be recognised as a modern example were developed, utilising a spring keel and heel typically constructed from composite materials to improve the viscoelastic response under load [181].

Initial studies noted increased energy return compared to SACH feet as expected, but little else of significance [183]. It was suggested that the energy storing foot had less resistance to dorsiflexion, which resulted in closer to normal dynamics on the prosthetic side [184]. Research into sound limb loading of these feet found more symmetric vertical ground reactions forces, leading to decreased loading on the sound limb [185]. It was thought that the increase of controlled dorsiflexion prevented the centre of gravity from rising.

Due to the growing interest of theses designs, studies were completed on a more expansive range of feet. Despite the poor sample size of a single subject, subject-specific tuning was highlighted when the subject indicated a preference towards higher energy absorption rather than generation [186]. It is difficult to judge the validity of these early studies, due to insufficient sample groups or inaccurate analysis. Such issues would explain discrepancies between conclusions of similar studies [187], and the inability to find significant differences in varied designs [185, 188, 189].

The inconsistencies in energy storage analysis were problematic, and depending on the research method, a foot could be top or bottom of the ranking. Part of the issue was confusion with terminology and disagreement on how energy should be quantified. Many early designs treated the heel and keel energetics as separate, whereas redirecting the energy forward from heel contact was suggested as a potential benefit [181]. This is where the terminology for these designs to switch to Energy Storage and Return (ESAR) feet.

Further reviews into the analysis of these early designs revealed positive effects on the restoration of energetics for active gaits. Primarily, this was increased self-selected velocity, reduced loading on limbs, and improved push-off. However, less active amputees did not see these benefits, possibly due to the increased shock in

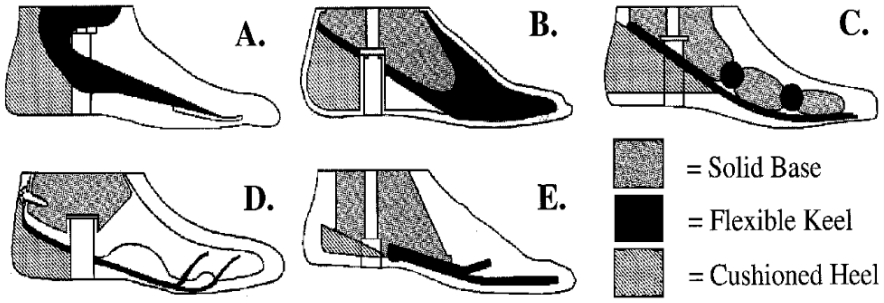


Figure 2.20: Cross sections of early energy-storing prosthetics that utilised a soft heel and flexible keel spring. In order of alphabetical notation: Seattle Foot, Dynamic Foot, STEN Foot, SAFEFoot, Carbon Copy II Foot [181].

the heel and inability to sufficiently load the keel for elastic return. Analytical techniques such as treadmill walking were also inadequate for represent these less able amputees, which include the elderly [188]. Hence, lower activity amputees, need a foot better suited to shock absorption, but also one that possesses enough propulsive action.

A model was developed to understand the behaviour of this heel region, finding the behaviour to have a non-linear elastic response. The energy dissipation at lower speeds was below expected, which indicates an increased compliancy [190]. This shock absorption effect is important in reducing the unhealthy impact loading that when high can lead to tissue damage of the residual limb. To better understand the functional requirements, it was suggested to explore the shock and ground reaction forces [191].

Other research looked to solve where previous studies had failed to determine difference between mechanically different designs. This analysis was successful in revealing significant differences in the performance of different feet through the

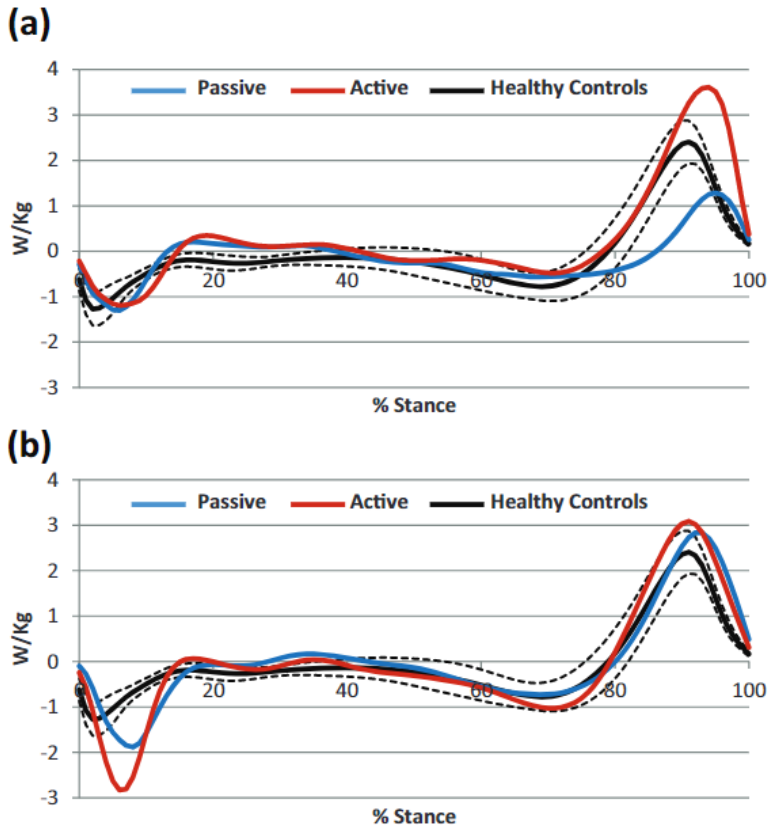


Figure 2.21: Plots of mechanical power during stance [7]. Used to examine a healthy control group against an active and passive prosthetic. Many active feet will produce more power than the biological system.

analysis of roll-over shapes [192]. In a previous section of this chapter, research demonstrated how a suitable roll-over shape could overcome some deficiencies of a fixed ankle [96], combining with multi-axis ankles could make further improvements to the range of motion. This hypothesis was confirmed when combining the ankles with a stiff SACH foot; seeing an improvement in mobility and ability to navigate stairs and ramps [193]. Focusing on the rollover shape and push-off characteristics has also been suggested as an alternative to metabolic targeted studies, due to a lack of progress in improving the energetics directly [194].

Previous use of ground reaction forces was successful in determining characteristics such as shock absorption, and the performance in general. Although power generation characteristics were difficult to ascertain with just forces [195]. Later analysis looked at the braking and propulsive impulses as being important performance measures, representing the force and time in a vector value. The study was on the effect of a multi-axis ankle, finding the increased range of motion to increase the residual limb propulsive impulse. Furthermore, this statistical difference was only seen in the impulse and not time or force individually, which suggests the delivery of force over time is more important the just the magnitude of the force itself [196]. These impulses also proved useful in measuring the asymmetry in an amputee's gait, where simple instructions to increasing push-off led to higher impulses and reduced hip loading [23]. Therefore, it could be argued that focusing on these impulses as a key performance indicator would provide a more straightforward optimisation towards achieving key biological functionality like the catapult action [22]. The motor redundancy of the neuromuscular system seen in Section 2.1.5, could then utilise this efficiently. When controlled, these impulses could be optimised to target more complex performance derivation. For example, it has been suggested that passive prosthetics need to optimised the magnitude and timing of energy release [7].

2.2.2 Powered Robotic Revolution

Elsewhere, research into the quasi-stiffness of the ankle revealed that whilst passive components would suffice at lower speeds, active components would be needed for higher speeds [176]. This is roughly around when the split of research into powered prosthetic designs gained momentum. The active ankle-foot emulator developed at MIT was able to mimic the normal behaviour during walking after being tuned to match the quasi-stiffness values [197]. This design continued development into a powered ankle-foot prosthetic, using series and parallel elastic control to simulate healthy torque profiles and reduce metabolic cost [28, 198]. A particular advantage

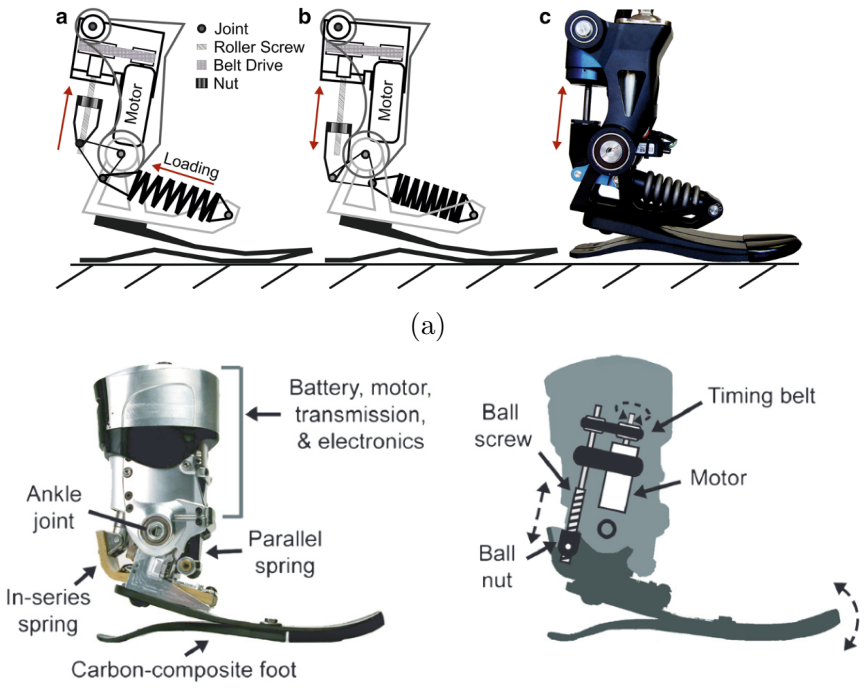


Figure 2.22: The commercially available bionic feet, developed from research in US universities. Top: Springactive Walk-Run ankle [203], which began as the SPARKy prototype [204]. Bottom: The iWalk® BiOM ankle. A powered ankle developed by Hugh Herr and his team at MIT [205]. Note the similarities in design, despite the separate research methods. The series elastic actuator system can deliver biomimetic levels of power throughout stance.

to this powered design was the ability to switch the controllers to a new gait task such as stair navigation [199]; a task modelled previously with a system of mechanical elements including springs, dampers, and torque actuators [200]. Review papers further highlighted the difference between this new generation of bionic feet and the passive restorative energy designs. The ability of the bionic designs to produce additional power without energy input placed them at an advantage, despite being in early development [201, 202].

The other notable powered design focused on optimising towards a motor power requirement by adjusting a linear spring [204], similar to a suggestion made in later research [44]. This was successful in matching the required power at push-off and range of motion, but the experiment only included a single subject, and the prototype design was bulky [204]. It did however demonstrate a successful attempt at optimising towards a kinetic rather than kinematic goal, in this case mechanical power. Further work on this design produced a version with improved power/weight ratios, which further evolved into a design capable of switching between

walking, running, and jumping tasks [206]. Eventually this progressed towards commercialisation as the Walk-Run ankle by Springactive, which demonstrated some promise but required further work to adapt to higher speeds [203].

Also moving into commercial development, the MIT foot advanced in design and the focus shifted towards creating a sophisticated control system [207]. The requirement for all gait tasks to be coded into these powered systems was seen as a possible weakness in the designs, alongside the proclivity for mis-identified gait tasks and thus selection of stiffness profiles [208]. Nevertheless, the Powerfoot BiOM provides a level of mechanical performance unmatched by passive devices [209].

Perhaps the most beneficial outcome is the ability to reduce the collateral side loading in the knee, clinically reducing the chances of knee osteoarthritis. However, it should be noted that this gap in performance was more significant at higher gait speeds, which require adaptations to the quasi-stiffness profiles [178]. Slower speeds saw less of a difference in peak knee adduction moments between the control, powered and passive. This indicates how only a more active amputee is likely to experience the upper performance benefits of these powered designs [205].

The Springactive and BiOM powered ankles are the two notable examples of powered prosthetic feet. Generally, designs will use a series elastic actuator which has demonstrated success in producing healthy kinetics [1], and minimising the work required by a motor to actuate a prosthetic ankle [45]. Other concepts exist in research labs and employ a variety of actuation methods, each with distinct advantages and disadvantages; the AMP foot being another prominent example [210].

2.2.3 Advancing Passive Feet

Despite the performance advantages in powered designs [211], research into passive models did not stagnate. A research group at the University of Texas, Austin, developed a rapid prototyping method. Using a selective laser sintering method, they could quickly modify a simple foot design, thus allowing them to begin exploring effects of stiffness on amputee gait [212]. Through implementing this method, different ankle geometries were assessed based on shape and compliancy. Improvements to the energy storage with more compliant ankles also led to high braking impulses of the intact leg, which suggests moving towards localised stiffness optimisation as preferable to an overall value [213]. The geometric differences in this

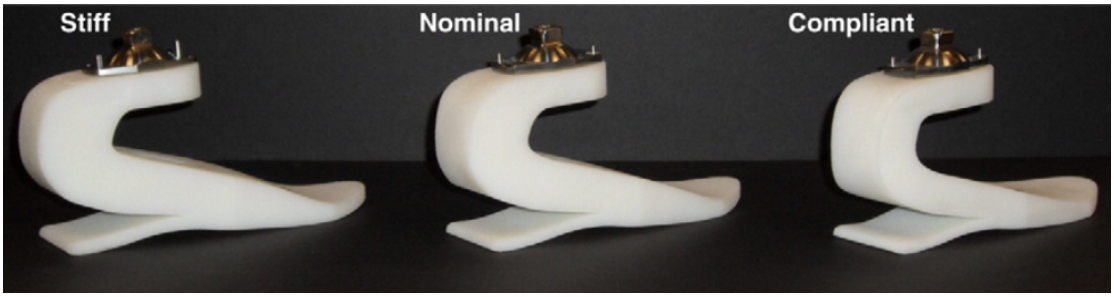


Figure 2.23: The nylon prototype foot manufactured using selective laser sintering [49]. The efficient production allowed the research team to quickly produce multiple versions to assess in clinical studies

study pertained to a forward and reverse facing c-shaped ankle, with the former having a larger effect on muscle energetics, but some results suggested patience preference & suitability may also factor into the performance [214].

Additional investigations were made into the stiffness effects of forward-facing ankles. Results indicated a compliant foot is capable of improved motion and energy return but requires increased muscular activity to provide vertical support [49]. Such results are also seen in modelling efforts, where a prosthetic is capable of providing body support, but is impaired in anterior-posterior functionality [146]. It was therefore proposed to optimise localised areas of foot stiffness by modelling it as a series of rigid segments with rotational joint stiffnesses, which if successful, would more accurately model the behaviour of distal structures reported as missing in other research [172]. Furthermore, whilst the sagittal plane motion is well researched, behaviour in the transverse directions is not. It has been proposed that exploration into this area is needed for understanding optimisation beyond straight-line walking [50].

Even powered robotic ankles have seen performance improvements from incorporating localised stiffness control in the distal structures [215]. From modelling results of a passive foot, optimisation by stiffening the toe and mid-foot and keeping the ankle and heel relatively compliant, improved functionality of both heel-strike and push-off. However, the fit of data was not reported and the analysis required experimental validation [216]; although it did demonstrate the potential of modelling as a tool of passive foot optimisation.

This was not the only case of rapid prototyping used to explore design parameterisation. From early studies on the rollover shape [192], the Shape & roll foot was created to assess the effects of forefoot stiffness. It confirmed the link between a highly flexible keel and insufficient progression of the ground reaction force, which leads to unhealthy loading on the contralateral side [217]. Further

modifications to the design explored the effect of a flatter section in the prosthetic rocker shape on the stability of gait; but no significant results were seen [51].

A different research group from the robotics team at MIT recognised further potential of the roll-over shape and designed a foot with rotational stiffness joints in an attempt to mimic the torque curve. Patient feedback was positive and drove the research towards optimising the design with a novel method [52]. Combining the ankle-foot and tibial structure into a single objective parameter, the LTTE, allowed for an optimisation that considered a more complete kinematic performance target rather than the narrower focus of targeted joint mechanics [3].

An additional prototype was created with interchangeable rotational springs to provide additional data to tune the optimisation method [53]. Through using this data to tweak the optimisation method, a passive prosthetic foot shape was designed using Bezier curves to reduce the kinematic error. The foot was evaluated with FEA and verified with mechanical tests before being analysed in a pilot study. Initial feedback was positive and confirmed the viability for subsequent clinical studies [31].

Prosthetic tools are commonly used to analyse effects of stiffness on amputee gait. One such tool was used to explore variations in heel and forefoot stiffness, at various steady state speeds on a treadmill. A stiffer heel led to reduced energy return, increased loading rates and knee moments, whereas a stiffer forefoot reduced push-off work and increased knee moments [218]. It also corroborated earlier research that found more compliant ankles to improve energy return [49].

Such studies utilise these prosthetic tools to provide accurate quantification of parameters and effects, and occasionally they will lead to novel designs. At Northwestern University in the US, a device was designed to assess the effects of

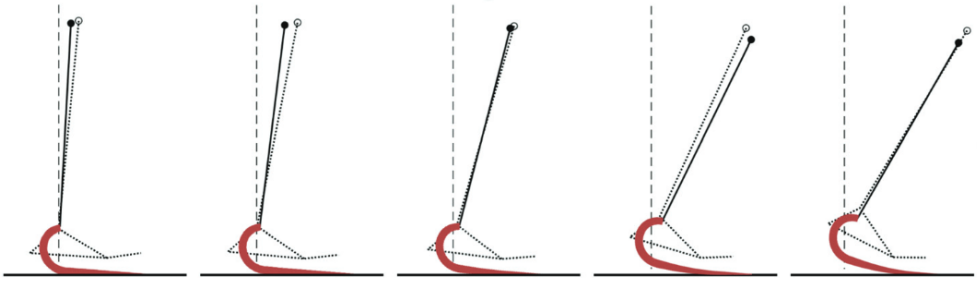
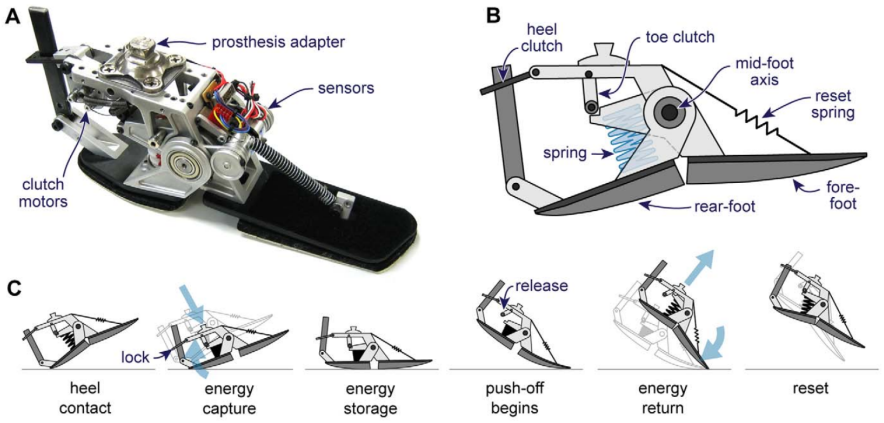
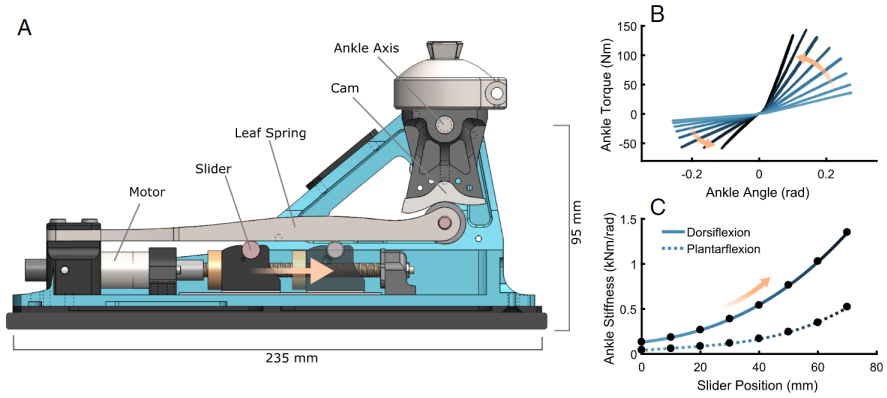


Figure 2.24: A visual representation of the optimised keel in red matching the ideal lower leg trajectory of the model [31]. The optimisation method of using relatively simple kinematic measures and stiffness tuning has demonstrated that passive feet do not require the focus on joint parameters as seen with bionic feet.

ankle rotational stiffness. An initial pilot study discovered some interesting effects but not at statistical significance [220]. Additional research into this rotational stiffness and the relation to quasi-stiffness profiles was completed to better understand the mechanical requirements. From this, a quadratic relationship was established between the ankle angle and stiffness [45]. This eventually led to the development of the VSPA foot, a quasi-passive design that has a variable stiffness leaf spring mechanism, and a cam shaped to translate the spring stiffness into a desired torque-angle curve. It is a design capable of using the varying stiffness to adjust the prosthetic to complete different gait tasks like stair ambulation [46]. This foot was modified to improve the variable stiffness characteristics, and then used in an experiment to assess the amputee's sensitivity to stiffness during stance. Results found the subjects to be capable of detecting a 7.7% difference in the stiffness, and it was determined that future work should develop a method of



(a)



(b)

Figure 2.25: Top: The CESR foot, designed to recycle energy from heel-strike. Whilst successful in returning a sufficient magnitude of energy, the timing of release was too problematic for an amputee. Bottom: The VSPA foot, designed to adapt the stiffness to suit different gait tasks. A modification of this foot was used to decouple the energy storage and return [219].

determining optimal stiffness [47].

Research earlier had suggested recycling the collisional losses at heel strike and redirect for forward propulsion [181]. The CESR foot used a clutch system to transfer energy captured in a heel spring to a forefoot section that released it at push-off. Initial tests using a prosthetic simulator boot displayed some success in restoring the lost collisional energy, although the limited sample size and use of healthy subjects contributed some doubt [42]. Further tests were completed, again validating the shock reduction and propulsive capabilities, but also failing to find an improvement to metabolic expenditure. It was thought that part of this may be related to the rate of energy release and additional control required. The restorative energy release comparable to the catapult action may have been too difficult to manage without the supporting musculoskeletal structure [43]. Even tested with an amputee, this design saw no benefits to the metabolic cost of walking, which was thought to indicate that push-off power was not a principal determinant of efficient gait [221].

The importance of timing release has been explored with the use of mechanism fitted to a standard passive foot. Experimental results from a pilot study indicated that there was no single optimal value, and the timing should be tuned to a user preference [222]. However, it was found that increasing the impulse duration made the foot more comfortable to use, which would explain the issues with the CESR design. To test this hypothesis, a modification was made to the VSPA foot by employing a dual-cam system that would switch cams from dorsiflexion to plantar flexion and return positive energy at a manageable rate. Initial experiments failed to provide statistically significant results, but the mechanism which de-coupled the energy release and storage is an interesting concept and further studies are planned [219].

2.2.4 Summary

This section has provided an overview of prosthetic ankle-foot design. Bionic and semi-active ankles have superior power production and ability to adapt to different gait tasks. But they also have shortfalls with the additional complexity and weight; the latter being a particular issue with semi-active feet that don't produce enough supplemental power. Further to this, the bionic feet are expensive, and arguably unnecessary for an older, less-active amputee who will not benefit from the potential boost in performance.

In that respect, it is important to consider what amputees require from their

device. The less active amputee may only need to manage limb loading and avoidance of further health complications, such as osteoarthritis. The optimisation and analysis of designs has primarily focused on steady state walking, using an instrumented treadmill, which has left a gap in knowledge with gait initiation and termination activities. Furthermore, much analysis of passive feet is done within the bounds of the sagittal plane, whereas the biological ankle-foot complex requires more complex reactions to overcome various gait tasks and obstacles.

From this, it could be argued that design optimisation to match force peaks, impulses, and mechanical CoM power curves, could unlock a novel potential in performance. Especially if gyroid structures can release the potential of tuning a design in the transverse planes of action. Rapid prototyping has been well established as a practical manufacturing method to test such experimental ideas in prosthetic design and is particularly well suited to constructing the aforementioned gyroid structures.

Passive designs still see interesting research completed and with the potential gaps in knowledge, it stands to reason that additional performance can be gained

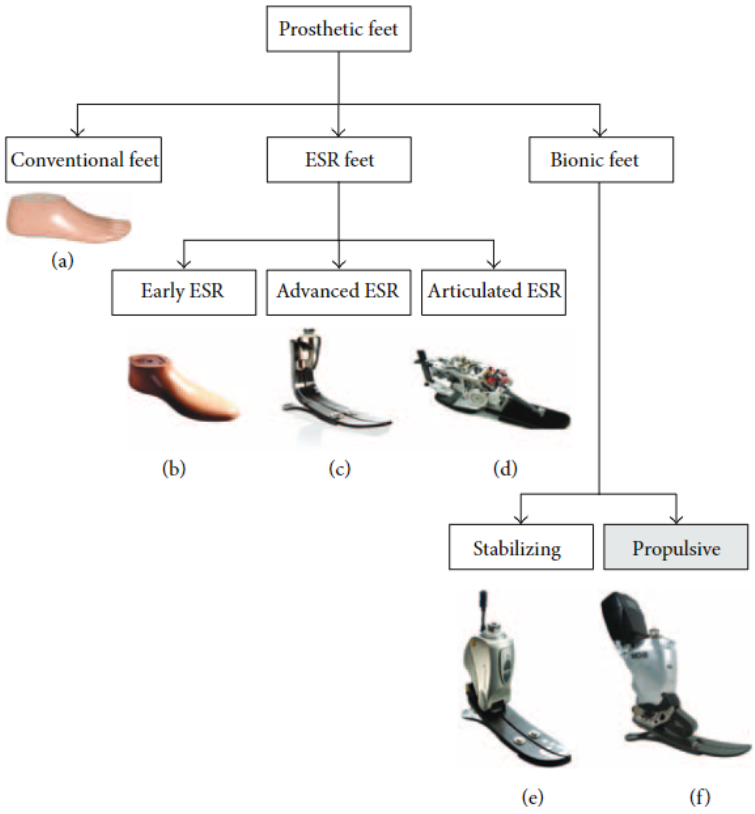


Figure 2.26: A tree diagram of prosthetic feet categories developed in research. Despite the separation in the tree the articulated feet arguably have more in common with the bionic than advanced ESAR.

from continuing to explore these designs.

2.3 Experimental Studies & Procedures

From the literature review of the previous two sections, it has been shown that amputee gait has significant asymmetries in the kinetic parameters. Powered prosthetic feet have focused on returning the quasi-static ankle-torque [1], to rebalance the kinetics. On the other hand, the passive MIT foot has opted to match the kinematic profile [31]. However, other research has shown that the existence of multiple motor redundancies in the body makes achieving symmetrical gait less straight forward than it would seem. Often the cost of matching kinematics is increased energy expenditure or unbalanced loads that can lead to later health complications, see section 2.1.5 of the literature review.

2.3.1 Gait initiation

Gait initiation studies are form only a small percentage of the overall amputee and prosthetic literature. To generate the forward motion, a large horizontal propulsive force is required. Amputees, particularly the elderly have difficulties generating this force with the residual muscles, whilst also maintaining their balance as the centres of mass and pressure shift [223].

Early comparisons of the ground reaction forces revealed the intact limb produces higher peaks regardless of which leg leads the initiation [73]. A common adaptation appears to involve leading gait initiation with the prosthetic limb, and then increasing the push-off duration of the trailing healthy limb. It appears this is to achieve a larger propulsive impulse, accounting for the decreased anterior GRF [70]. This temporal adaptation was found in the earlier research but was not elaborated on [73]. Despite the anterior force differences, the progression velocity between leading limb conditions is similar. This phenomenon has been uncovered in other studies when the trailing limb activity is broken into anticipatory and execution stages. When the prosthetic limb leads, the anticipatory weight shifting phase has a shorter duration with lower velocity, meaning the execution phase last longer with a higher velocity [155]. The inverse occurs when the intact limb leads and is thought to be due to an uncertainty with the prosthetic limb providing support. Both strategies are methods though to modulate the propulsive forces required for gait initiation.

In terms of assessing stiffness effects on gait initiation, the number of research papers drops considerably. The most notable contribution is from a conference

proceeding, where the effect on centre of mass and pressure was investigated [224]. Conclusions were limited, but there was a strong indication that further work should be completed.

2.3.2 Kinematic Limitations

Despite the propensity in the analytical use, there are inherent limitations in kinematic methods that if not properly accounted for, can affect the accuracy of results produced. Errors in readings can accumulate from markers placed on the body to represent joint centres. The malleolus is simple to locate due to its protrusion at the ankle, whereas the lateral femoral condyle can be difficult due to its location deep in the muscles. What is more, the skin is tissue that stretches and moves, displacing the position of the marker from its origin [39]. This inaccuracy also affects models due to the generalisation of results for the population. Large errors have been found in results when the joint position and orientation are not representative of the patient [225]. These issues have been found to produce significantly high uncertainties (between 6 – 232%) in torque estimates for a 13-segment linkage model. Values increased from the distal ankle to proximal hip joint, exposing the error propagation inherent in inverse dynamic calculations [40].

The ground reaction forces used as inputs are generated by the muscle and joint dynamics of the body. However, the models they feed will not necessarily behave in the same way as the natural source, and the joint parameters calculated will be

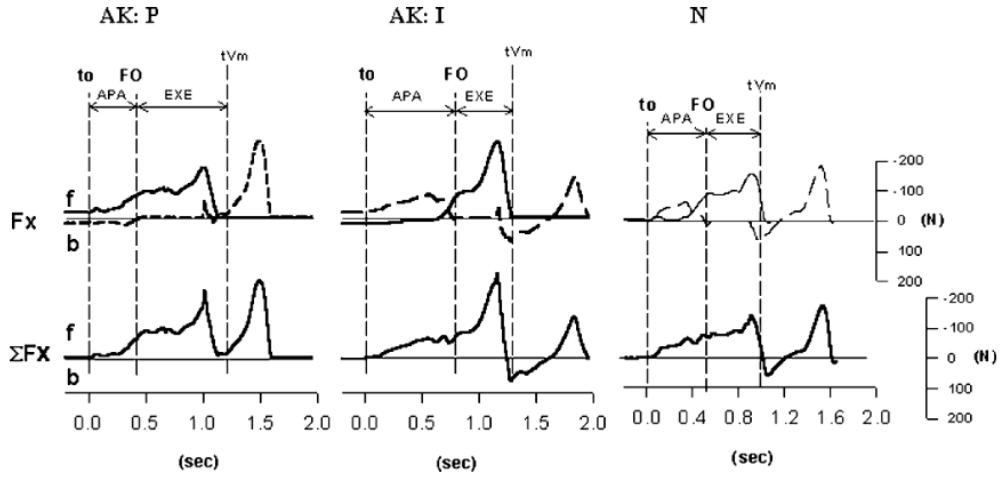


Figure 2.27: Anterior-posterior ground reaction forces from above-knee amputee subjects [155]. From left to right: Prosthetic leading, Intact leading, Healthy subjects. APA: anticipatory postural adjustment, EXE: step execution. Dashed lines: leading limb, Solid line: stance limb.

erroneous and unpredictable [226]. Overcoming this problem inevitably requires large scale neuro-musculoskeletal models, with enough complexity to accurately model the functional relationships. Once accuracy is achieved to within a sufficient tolerance, then practical simplifications can be made [227]. Variation in force plate measurements have been shown to create similar errors to kinematic inaccuracies. Whereas the force will only have a large effect on the joint torques of the knee and hip, an error in force plate torque has significant effects on the torques of all joints in the lower leg [228].

The problems above cause further concern when the application changes from healthy adults to amputees. Assumptions for these models were made without consideration for when a prosthetic device is used. The changes brought about in segment parameters, joint locations and function need to be adapted into the model to avoid miscalculations of joint values [229, 41, 230].

2.4 Revisiting the Research Question

At the start of the introduction chapter of this thesis, a question was posed regarding the current state of passive prosthetic feet design:

> "Do the current passive prosthetic feet offer the optimum performance possible to a transtibial amputee, whilst maintaining affordability?"

In searching for an answer, it was realised that there is a lack of disability focus on less active/elderly amputees, particularly with transitionary gait tasks like initiation. Whilst the development of new feet and optimisation has seen success, these have been based on methods concentrating on active steady-state walking. Furthermore, there is a prevalence for these projects to focus on kinematic optimisation or inverse-dynamics to match up joint torque profiles.

The implications of these research trends are gaps in the potential knowledge, and in some respects the passive exclusion of a portion of the amputee population. Kinematic analysis has been useful, but the highly adaptive neuromuscular control system may not need to match healthy gait profiles in passive feet, which typically causes delayed health issues. Instead, an alternative method may seek to restore kinetics and allow the neuromuscular system to adapt the kinematics based on what it regards as suitable for the changes caused by an amputation.

With these considerations, the research question was reconstructed to reflect the perspective above, creating a novel focus for the body of work to follow. It was

important to make sure this was succinct, whilst still covering the revised research goals. Thus, the question became:

> "Can a disability focused approach, targeting personal stiffness optimisation in a passive foot design, improve the gait of less active amputees?"

The following chapters of this thesis contain work which has delivered the tools required to begin this novel exploration into a new design methodology.

Chapter 3

Concept & ISO Models

In the previous chapter, a potential gap in research was identified, where kinetic based optimisation methods could be used to improve passive designs for transitionary gait tasks like initiation. This chapter begins with an introduction to an existing prosthetic concept developed by the author. To refine this concept, a new FEA model was developed using ISO test standards to define the boundary conditions. Development of this model forms the main narrative of the chapter and concludes with the concept evaluation using the ISO model.

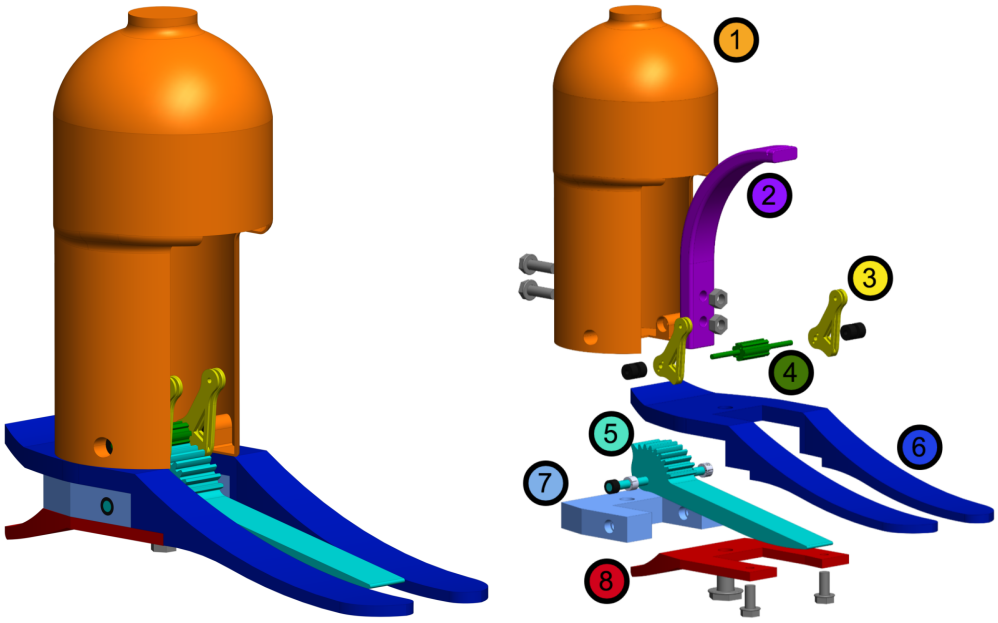
3.1 Concept Design

Prior to beginning the EngD, the author was part of a group project for a master's level design project. The design brief was to create a passive prosthetic design to fulfil the performance of bionic ankle-foot devices, but without the increased complexities, or higher cost and weight. Beginning with concept exploration and then refining with FEA optimisation, a passive prosthetic concept with a novel energy storage and return mechanism was designed.

The images in Figure 3.1 show the assembled concept design and exploded view with key components labelled. These key components can be grouped into sub-assemblies:

- Foot Base comprised of the Keel, Heel, and Bearing Plate
- Lever Mechanism includes the Lever with integrated Gear, Pinion, and Mechanical Cam
- Energy Housing Unit which holds the Carbon Fibre Spring in the Housing

The core principle of the design was based on attempting to emulate the catapult



(a) (b)

Figure 3.1: Isometric view of the concept design on the left and exploded view with key components numbered on the right. List of components is as follows: (1)-Housing, (2)-Carbon Fibre Spring, (3)-Mechanical Cam, (4)-Pinion & Shaft, (5)-Mechanism Lever with integrated Gear, (6)-Keel Spring, (7)-Bearing Plate, (8)-Heel Spring

function discovered in research and use this as a method of storing lost energy and returning to assist in push-off [110, 22].

Inspiration for the energy storage mechanism came from the design of compound bows and the way strain energy is stored in the tensioned limbs. It was thought that this energy storage and release principle could be replicated in a prosthetic foot system. Thus, the mechanism was given the title of Tension Energy Recovery (TER) system. With this as the prominent feature, the other components were designed to facilitate the operation of the TER system.

The following explanation of function is supported by the schematic diagram in Figure 3.2. At initial contact, the heel absorbs the impact and the supports a smooth transition into flat-foot. Just prior to this mid-stance foot position, the lever which sits below the base line of the toe spring makes contact with the floor and rotates on its shaft. This rotation is stepped up through the gear pair and causes the cams to pull down on the carbon fibre spring with the attached wire. As the foot moves from mid-stance to push-off, the keel spring activates and deflects. This allows for additional rotation of the lever, maximising the energy stored. Strain energy is held in the spring whilst the centre of pressure on the

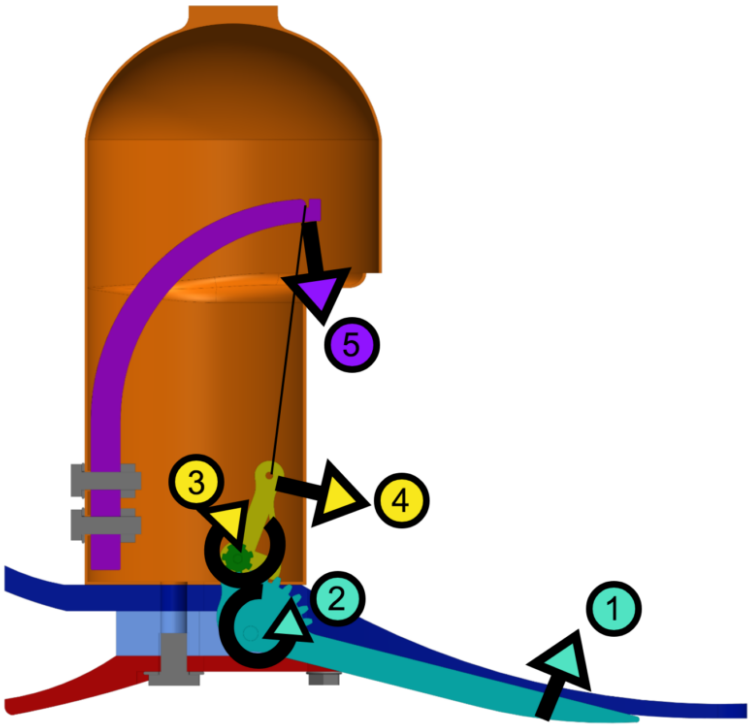


Figure 3.2: Cross-section diagram, detailing phases in the loading operation of the TER system. (1)-The lever is pushed up as it contacts the floor. (2-3)-Rotating on its shaft the integrated gear causes a step up in rotation with the pinion. (4)-The rotation of the cams creates a tensile pulling action on the wire connection. (5)-This action places the carbon fibre spring under strain, storing elastic energy.

lever remains in-front of or in-line with the centre of pressure on the keel. Once this point is passed, the energy held in the limb is released in a controlled manner through the system.

Transition to a Research Tool

Whilst the initial purpose of the foot was to be a consumer/patient model, some concerns were drawn to the operation under real-world conditions. The primary issue was that the majority of amputees will wear a cosmetic foot over the prosthetic, which would then allow them to wear shoes. This would render the mechanism ineffective as the lever would not be able to transmit forces to store energy in the limb. It was decided that whilst the real-world application of the foot would not be suitable, there would be validity in refining the design to be suitable as a research tool to investigate gait initiation as discussed in Chapter 5.

3.2 Initial Model Testing

Finite Element Analysis emerged as a tool for design optimisation at around the same time energy storing feet began development. However, whilst initial results were adequate and used gait lab data for boundary conditions, the models themselves were relatively rudimentary to modern comparisons, and the researchers only able to model static cases [231].

Success with FEA was seen when focus was kept on a simpler component, such as a monolimb composed of the shank and socket. Applying a robust design method, a genetic algorithm optimised the design for a specific patient's needs [232]. Physical experimentation with these designs revealed small improvements to limb loading and higher comfort, although further experimentation was needed [233].

Additional FEA modelling efforts sought to increase model complexity for improved representation of realistic performance. The inclusion of pylon components including the set screws demonstrated some useful potential in capturing realistic boundary conditions [234]. However, the increased computation required for the contact pairs in the pylon assembly is overlooked, and no comparison was made to a model without them. It could be possible that an equivalent effect could be obtained from a beam element with equivalent stiffness. The model also failed to produce a set of boundary conditions more advanced than the static cases of heel-strike and push-off. In fact, many papers utilising FEA models for prosthetic evaluation fail to move beyond these basic, static reconstructions of gait provided in ISO 10328 [235, 236].

An earlier study had recognised this failure to capture the dynamic stance phase of gait. The inertial forces were derived and then applied to a model of the socket and residual limb. Whilst the analysis was not fully dynamic, it was determined to be a useful step forward in capturing the transient nature of stance [237]. Despite the comprehensive use of FEA in many aspects of prosthetic engineering, it is rare to see a transient model representative of real application [238]. If a model can be created to represent the dynamic loading conditions throughout stance, then enhanced design analysis could be performed.

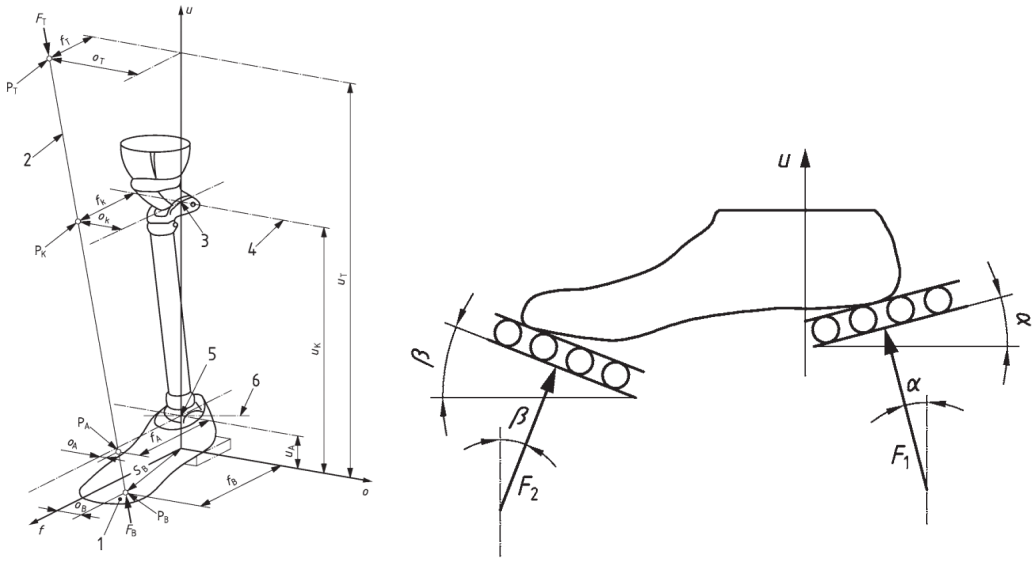
3.2.1 ISO 10328

Whilst preliminary simulations were completed as part of the undergraduate group project, these were not rigorous, serving only as a preliminary tool to drive the

proof-of-concept design process. They used a mix of boundary conditions loosely based on an ISO document for testing prosthetics ISO 22675 [239], and ground reaction force data from papers [147]. A reliable evaluation of the design required revisiting the ISO documentation in order to produce a more accurate representation of boundary conditions.

Upon revisiting the ISO document, the initial attempt at reproducing the exact test conditions proved difficult due to the complexity of the contact setup. With research papers showing successful modelling with a different prosthetic testing standard [235], a decision was made to look into reverting to this simpler test standard to resolve the issues at this "lower resolution" which could then be translated into the dynamic model.

The ISO 10328 document includes procedures for static, cyclic, and torsional structural tests for all lower-limb prosthetic components; only the static tests were considered at this early stage [236]. Test structures for the documented procedure can either be complete, see Figure 3.3a, or partial, with the latter option requiring suitable replacement components of similar behaviour; for example, a partial foot structure would require an equivalent pylon component. The load is then applied through a load plate positioned on the heel or forefoot, Figure 3.3b. This comes with a stipulation that the application should be such that



(a) (b)

Figure 3.3: Setup diagrams taken from ISO 10328. Left: Complete structure setup for a transfemoral prosthesis, including the foot, pylon, and knee. Right: Loading plate setup for heel and forefoot loading. Note, the angle symbols in these diagrams are not used again in reference to ISO 10328

quasi-frictionless motion is achieved in both tangential directions.

In terms of applied load, the standard defines two procedures for the static forces: Proof test & Ultimate test. These represent occasional and severe loading events respectively, with function expected to continue only after the former, the Ultimate test levels are designed for failure. Furthermore, each of these procedures also has three load levels which are associated with a particular subject mass; P3 (60kg), P4 (80kg), and P5 (100kg). The rate at which these loads are applied should be between 100N/s and 200N/s.

The above presents a comprehensive overview of all boundary condition requirements to setup an FEA model. The test structure can be reduced as the model can apply a boundary condition to a suitable equivalent surface to provide the same fixed space condition in the standard. Rigid plates can be modelled with appropriate contact to create the loading condition, with the prescribed loading rate used to define load steps for improved convergence.

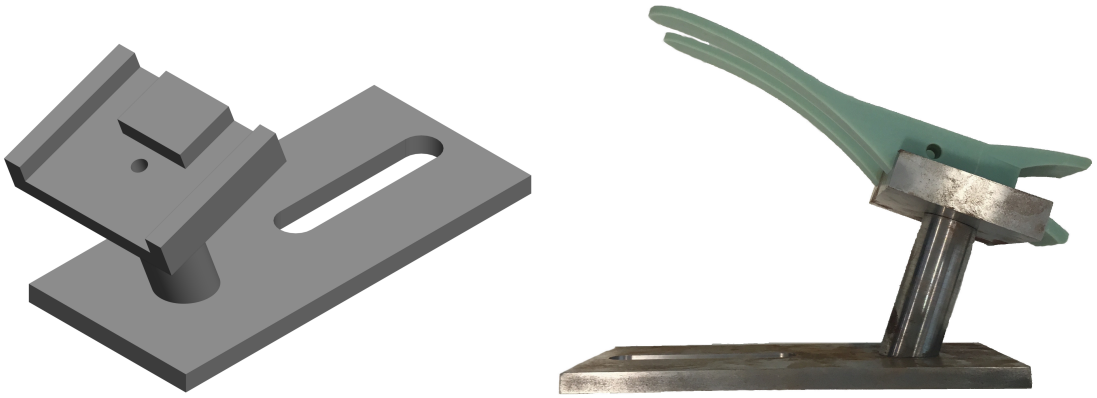
Before full design studies are completed it is important to verify boundary conditions that have some proposed uncertainty. In this case, the contact type definition between the loading plate and foot needs to be resolved; to this effect, a validation experiment was completed.

3.2.2 Contact Definition Validation

Experiment Design

It was decided that only one test condition was needed for this validation. The forefoot setup was chosen due to the predicted flexibility of the keel providing favourable deflection results to compare against the simulation. A further simplification was made to disregard the toe-out angle defined in the standard; it is an unnecessary addition to determine the contact validation. As such the design of the test rig could be kept simple, required only to hold the foot at the required angle and provide a stable base for fixture to the testing machine.

The rig was designed in three parts; a base, central support cut at an angle, and the mount plate. The angle of cut for the central support is such that the prosthetic will be aligned with the horizontal load plate at the 20°angle prescribed in the ISO document. The mount plate is cut such that the planar top face of the keel slots into place and is then secured using g-clamps. A CAD model of the test rig and photo of assembly can be seen in Figure 3.4.



(a) (b)

Figure 3.4: Experimental testing rig model, designed to work with a tensile testing machine. The rig is simple, holding the foot upside-down at the prescribed 20° for the forefoot test, the load is then applied using a compression plate.

To reduce complications from part interaction and bonding, the foot base parts were combined into a single geometry and printed on a Stratasys® Objet using the Stratasys Digital Acrylonirtile Butadiene Styrene (ABS)™ material; the key properties of which can be found in Table 3.1. Costing roughly £325 each, only two test samples were created.

The testing machine used was an Instron® 100kN Universal Testing Machine (UTM). However, the load cell installed was calibrated to deliver loads at higher values than those rated in the standard. It was possible to recalibrate down to the required accuracy, but this posed the risk of destroying a sample in the process. With only two prints available for testing, it was decided that the experiment variables would be switched to apply a displacement and record the resultant forces. In doing so, no calibration on samples would be needed, thus data could be collected from both samples. Even though the input and output variables were switched, the objective of determining contact setting accuracy was still realisable. An initial simulation was put together to determine a sensible displacement to

Table 3.1: Material properties of Stratasys Digital ABS™. The main source for the data is the PolyJet data sheet, available upon request from Stratasys [240]. Variation in the manufacturing process creates a range of values. The Poisson's ratio is taken from a research paper on printed material properties [241].

Property	**Unit**	**Value**
Elastic Modulus	MPa	2600 - 3000
Poisson's Ratio	–	0.36
Tensile Strength	MPa	55 - 60

apply in the experiment so that sample failure could be avoided unless desired.

FEA Simulation

The geometry of the model was simply composed of the combined foot base, and the loading plate. To simplify the modelling, the plate body was set as rigid so that the plate could transfer the full load to the foot. The material properties for the foot base follow those in table 3.7 and the associated sources [240, 241].

Boundary conditions are straightforward and can be seen in Figure 3.5. The model is anchored in place with a fixed support on the foot surface that would contact the housing. To keep plate conditions simple within the global coordinates, the fixed foot was rotated into position. A load is applied on the bottom surface of the plate in the vertical y-direction. To maintain this direction, a displacement condition is placed on all sides faces, restricting motion to only the y-axis.

Contact between the two bodies is defined between the top surface of the plate, and the surfaces along the toe of the foot. The standard defines that the transmission of force must occur with quasi-frictionless travel in the tangential directions. As such, the contact type was set to frictionless, and the solver directed to adjust the interface elements when it detected a change in contact.

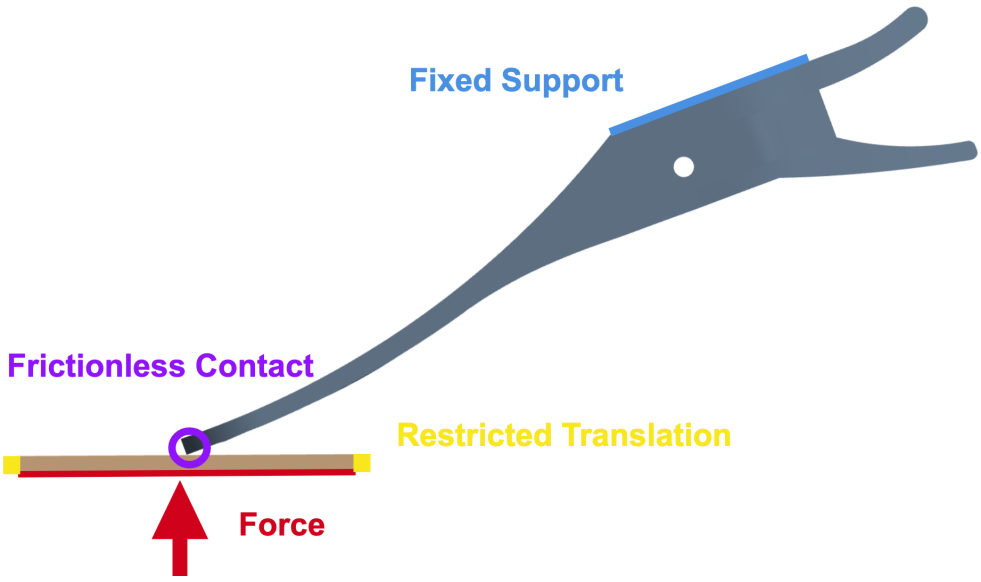


Figure 3.5: Diagram of FEA model setup using boundary conditions taken from ISO 10328. The foot is fixed on the surface marked blue. A frictionless contact exists between the toe edge and top face of the load plate (purple circle). The load plate itself is rigid, with a force applied upwards on the bottom face (red line) and perpendicular surfaces restricted to translation in the vertical plane (yellow blocks).

Mesh settings were simple, a global element size of 4mm and forcing 2 elements across the smallest face; a convergence tool verified this to produce mesh independent results. Analysis settings were left as program controlled with default time-step settings; the simplified nature of the model required minimal user input.

Using the settings above, a set of simulations were run to test both the maximum displacement. As the elastic modulus had a range of values to account for the variation in filament printing, it was important to duplicate the displacements for the minimum and maximum of this range. The simulation was setup once with the first row of inputs from Table 3.2, and a parameter set was created to complete the remaining input values. Thus, each modulus value four displacements of 15, 20, 25, and 30 millimetres applied in a single load step with a duration of 1 second. The reaction forces and von-Mises stress results of these simulations can be found in Table 3.2. It should be noted that a stress concentration occurred at the tips of the keel, and that this was removed with a small radius fillet. This will be explained further in Section 3.3.

The objective of these was to assess a suitable displacement to apply in the experiment. Given the uncertainty over the properties it is important to determine what displacement could be applied before failure occurred. The trend for all results appears to be linear, as expected. Variation in results across both modulus values increases with the applied displacement. Due to the lowest potential yield being 55MPa, a displacement of 30mm was thought to be too risky, unless the failure of the sample is the target. To account for additional uncertainties and if failure is to be avoided, then a displacement of 20mm would be appropriate to gather an initial response. If results are as expected, then the displacement could be increased until failure is reached. These initial models predicted an appreciable

Table 3.2: Simulation results for set of validation inputs.

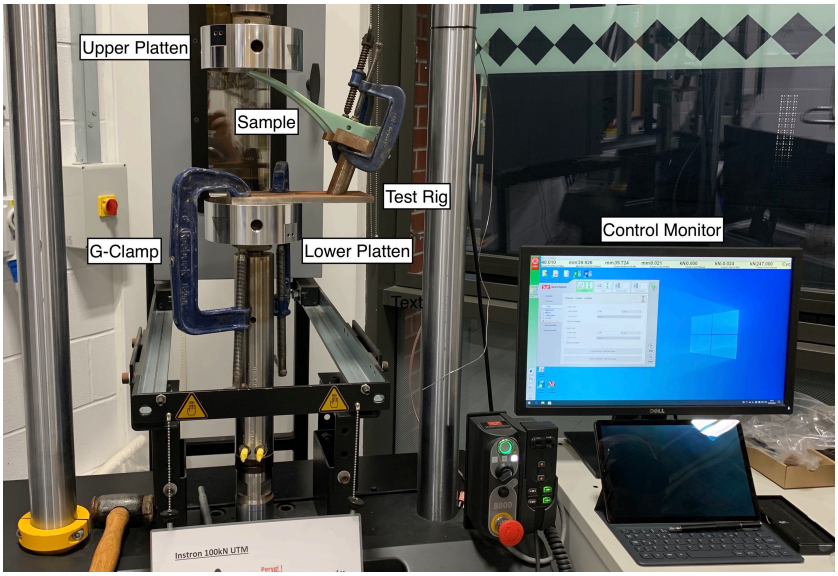
Elastic Modulus (MPa)	**Applied Displacement** (mm)	**Reaction Force** (N)	**Stress** (MPa)
2600	15	104.18	23.769
	20	136.30	31.833
	25	193.37	41.951
	30	242.34	51.274
3000	15	120.20	27.426
	20	157.27	36.730
	25	223.11	48.405
	30	279.63	59.162

displacement of between 25-30mm can be applied before failure is reached. These results will be revisited alongside the experiment results, with the possibility of re-running a model under increased load steps.

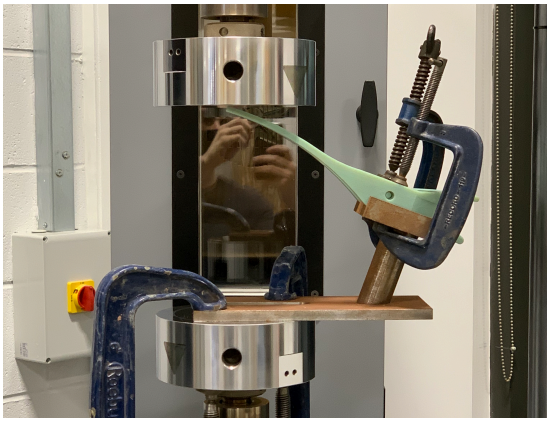
Validation Experiment Results

The sample and test rig were setup in the Instron machine using G-clamps to hold parts in place. Positioning of these components with respect to the machine were such that the toe of the foot was touching the centre of the top platen, with the profile face of the rig parallel to the front of the machine. This setup can be seen in Figure 3.6.

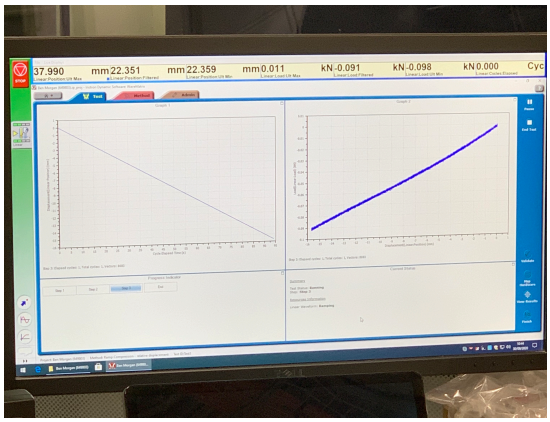
The machine was calibrated by the lab technician beforehand, and the loading



(a)



(b)



(c)

Figure 3.6: Photos taken of the validation experiment setup. (a) View of entire setup. (b) Close up of clamped rig and sample held between loading platens. (c) Machine software, the plots show the linear application of displacement over time.

rate set at 10mm/min. Whilst this was not at the rate prescribed by the testing standard, due to the FEA models not using plastic properties, any transient-viscoelastic response could be disregarded by either not applying a displacement to cause plastic deformation, or to simply analyse only the elastic region.

This is an acceptable based on known behaviour of other polymers. The mechanical properties of Digital ABS show that there is some ductile behaviour before fracture, where values for elongation at break of 20-45% are closer to a stiffer polymer such as Polyether Ether Ketone (PEEK - 50%), rather than a very ductile polymer like Polypropylene (PP - 250%) [240, 242, 243].

As this experiment is to validate the accuracy of the contact condition, the analysis only needs to be accurate for the material behaviour that can be modelled with the data given. In this case, material data known is in the elastic region, and the elongation suggests that the material tensile limits can be pushed somewhat without sudden failure. The contact accuracy can be determined within the elastic bounds, but care must be taken with repeating tests on samples due to possible elastic hysteresis behaviour.

As mentioned, two printed feet were created for testing. It was decided that the first sample would be first tested at 25mm as this fell below the FEA predictions for failure; if this passed, then 30mm would be applied for a second test. The second sample displacements were not decided before, instead the behaviour of the first sample would dictate the applied displacement; see Table 3.3 for a summary of applied displacements. The UTM recorded the load as the displacement was applied, at an acquisition rate of 500Hz, which was then filtered through a 4th order low-pass Butterworth filter with a 100Hz cut-off frequency. After each test, the toe of the foot was checked to ensure contact with the plate. The transducer produced a small amount of noise between 7-14N, but at the expected scale of results, this was deemed acceptable.

Table 3.3: Table summarising validation experiment samples and applied displacements

Sample #	**Test #**	**Displacement (mm)**
1	1	25
	2	30
2	1	30
	2	35
	3	55 (Failure)

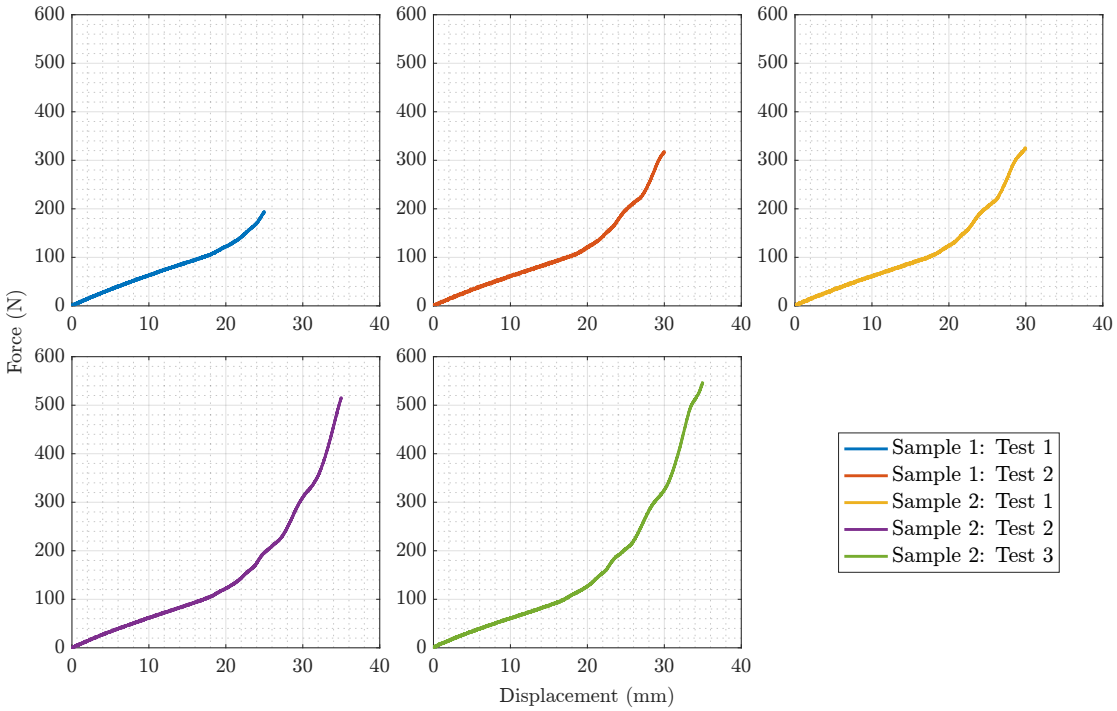


Figure 3.7: Experimental data in sub-plots. Tests 2 & 3 of sample 2 have had data cut after 35mm, and all data has been sorted as described in main text.

A small gap immediately after the first test was noticed, but the plastic relaxed after a short period of time and returned to the plate. The first sample withstood the two applied displacements with no obvious signs of plastic deformation. As a result of this the first test displacement of the second sample was set to 30mm, and then a second displacement of 35mm. The sample survived the 35mm displacement, and so a final displacement was applied to cause failure, which occurred at ≈41mm. Data from this experiment was written into an excel file, which was then imported into MATLAB for analysis and plotting of graphs. Due to the plastic behaviour of the final test, it was decided to cut the data to a maximum applied displacement of 35mm.

All tests were re-sampled to aid with running statistical analyses. It was decided to store the displacement-force data at 0.01mm intervals. The sorted data was then plotted and can be seen in Figure 3.7. There is a distinct linear behaviour and pattern across all tests up until shortly before 20mm. This can be more clearly seen if the basic metrics of the experimental data are plotted together.

Figure 3.8 shows the experimental range, mean, maximum, and minimum line plots; with error bars at 5mm intervals. The linear range can be seen to exist between 0 to ≈17mm, within which the range of force values is very tight to the mean. Once the deformation becomes non-linear at around 20mm, the varia-

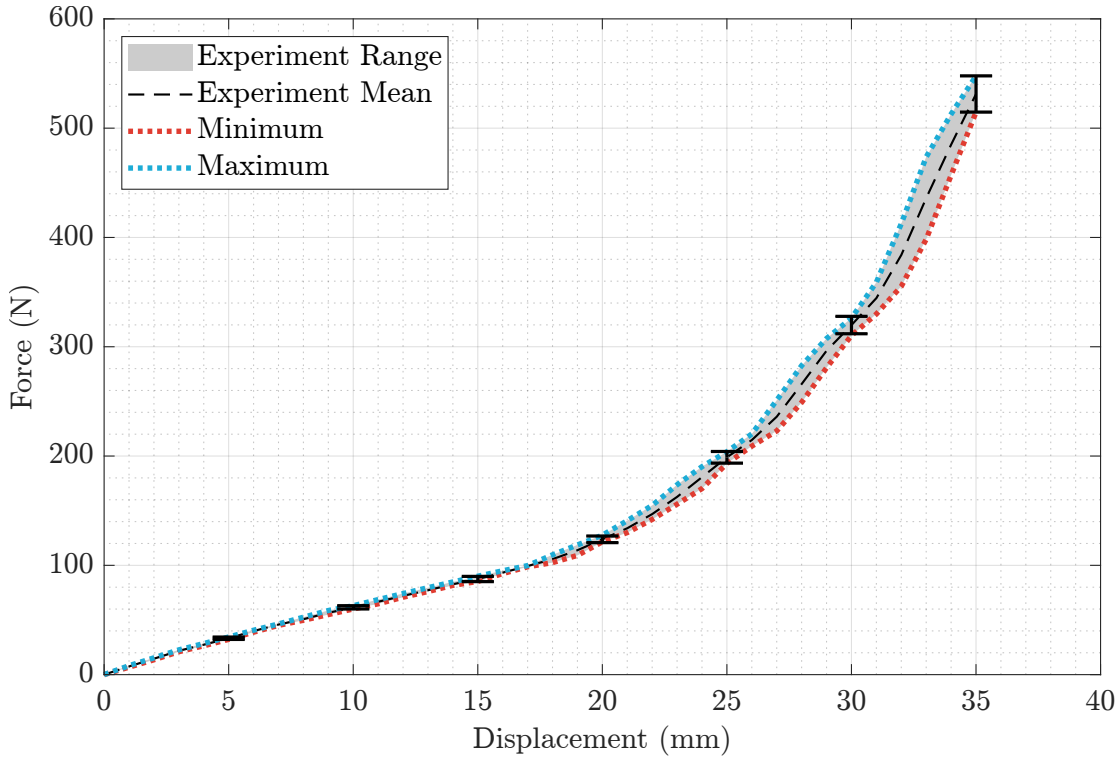


Figure 3.8: Experimental data, basic metrics plot. The range, mean, maximum, and minimum line plots have been generated. At each 5mm interval an error bar has been added to displace the range of data at that displacement.

tion in the results becomes noticeable. Whilst not ideal, the manner and degree of variation in data for this particular experiment is good enough for analytical comparison to a simulation model.

Two simulations were run again to capture data throughout the model rather than the maximums used in the preliminary models. The simulations were identical other than elastic modulus used, one set at 2600MPa, the other to 3000MPa as per the data sheet [240]. Final displacement input was 35mm, and the solver instructed to store data at every iteration. The data from the model was imported into MATLAB and interpolated to the same range of interval displacements as the experimental data, again this was done for statistical analysis and had no impact on the validity of the data.

Both simulation results, and the experiment range & average have been plotted in Figure 3.9. The data shows similar curves between the two simulation results, with the expected results of the stiffer material causing higher scaled reaction forces. Of the two, the less stiff 2.6GPa material bears the closest visual similarity to the experimental results. Having said this, both simulation results have the non-linear behaviour occurring later in displacement, at ≈22mm as opposed to

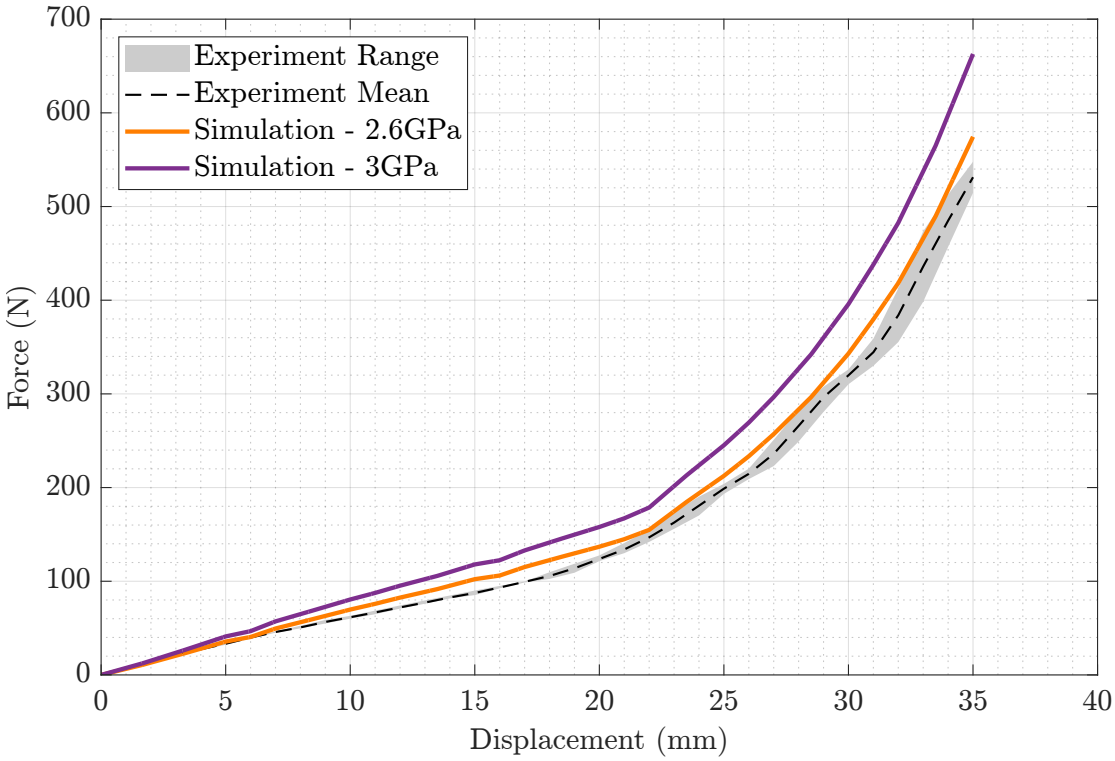


Figure 3.9: Comparison plot of simulation results, and experimental range & mean metrics

≈17mm in the experiment. The visual differences could be the result of many small effects, including irregularities in the printed samples, or the unrealistic behaviour of the perfectly elastic material model.

Some statistical measures can be utilised to express the similarity as a quantifiable number. Due to the discretisation of the data, the statistics will focus on the vertical difference in values. The Root Mean Square Error (RMSE), used to measure the difference between estimated model results against measured, is used here to compare the two curves by looking at the error between the y-values. Whilst not the intended use, a two-sample version of the Kolmogorov-Smirnov (K-S) hypothesis test can also be applied. It is a non-parametric test that measures the maximum absolute difference between the empirical distribution functions of two samples, providing a quantified test statistic on the null-hypothesis that the two samples are from the same distribution, at significance level $\alpha = 0.01$.

A selection of experiment and simulation pairs were matched up, including various displacement sample rates, the results of which can be seen in Table 3.4.

The RMSE values provide insight in showing that at 0.01mm increments the experimental mean is closest to the curve of the 2.6GPa model with an error of 16.5101. A closer fit is only seen when the 2.6GPa model is compared to the

Table 3.4: Table of statistic analysis on the experimental and simulation data. The experiment mean (Exp Mean) is the dashed black line seen in Figures 3.8 and 3.9. The experiment max (Exp Max) is the dotted blue line in Figure 3.8. Rate is the incremental increase of applied displacement. A pair of values are generated for the K-S test. The stat is a binary 0 or 1 for respectively accepting or rejecting the null hypothesis at $\alpha = 0.01$, with the associated p-value in the final column. The row with the asterisked data labels had the analysis cut-off at 20mm of displacement.

Data	**Data**	**Rate (mm)**	**RMSE**	**K-S Stat**	**K-S p-value**
Exp Mean	Sim 2.6GPa	0.01	16.5101	1	<< 0.0001
Exp Mean	Sim 3GPa	0.01	48.7605	1	<< 0.0001
Sim 2.6GPa	Sim 3GPa	0.01	33.3981	1	<< 0.0001
Exp Max	Sim 2.6GPa	0.01	12.1334	1	<< 0.0001
Exp Mean*	Sim 2.6GPa*	0.01	12.7322	1	<< 0.0001
Exp Mean	Sim 2.6GPa	0.1	16.6824	0	0.2800
Exp Max	Sim 2.6GPa	0.1	9.2045	0	0.3729
Exp Mean	Sim 2.6GPa	1	17.2258	0	0.9993
Exp Max	Sim 2.6GPa	1	9.4117	0	0.9993
Exp Mean	Sim 3GPa	0.1	-	1	0.0043
Exp Mean	Sim 3GPa	1	-	0	0.8514

experimental max at an error of 12.1334, or when the mean & 2.6GPa model comparison is stopped at 20mm with an error of 12.7322. This displacement cut-off is where the relationship switches from linear to non-linear, see Figure 3.9. However, for all analyses at the 0.01mm rate, the K-S test rejected the null hypothesis and determined the distributions to be different at $p < 0.001$. It was thought that this be may due to the sensitivity of the test to the sampling rate.

Upon observing the results at rates of 0.1 & 1mm, this would appear to be correct. At a rate of 0.1mm, both the comparisons shown in the table have similar if not lower error values, and accept the null hypothesis at p-values of 0.2800 & 0.3729. When the displacement incrementation is set to 1mm the error values marginally increase by a fraction, but the K-S test again accepts the null hypothesis at p-values of 0.993. This result can be explained by examining the cumulative distribution plots (CDF) in Figure 3.10.

All the distribution plots are discretised, but only the 1mm rate is noticeable at full scale. It is possible to see a smoothing in the plot lines from 0.01 to 0.1mm, but the general shape is still the same. The difference in degree of discretisation can be more clearly observed when zoomed into the plots, and the noise in the data for 0.01mm becomes apparent; it is possible this noise is attributed to the

transducer. The increase in data points provides more opportunities for the K-S test to detect a larger absolute difference. An argument can be made that dropping the sample rate to 1mm risks discretising the data to the point where it has lost information. Two further K-S tests were completed between the experiment mean and simulation data at 3GPa, as from a visual inspection, there are differences in the material properties. At 0.1mm and as would be expected, the test detected a large enough distance to reject the null hypothesis at a p-value = 0.0043. However, at 1mm the test could not detect a large enough distance and falsely accepted the null hypothesis of the data being equal at a p-value = 0.8514. Thus, we can discontinue the analysis on data sampled to 1mm increments, as it is not a true representation of the data.

The simulation that used the material with a modulus of 2.6GPa is closer in nature to the experiment than the simulation using 3GPa for the modulus, a claim quantified through the RMSE and K-S test statistics. At the respectfully accurate increment rate of 0.1mm, these statistical methods suggest that the two sets of data are close enough to state the FEA simulation has accurately modelled

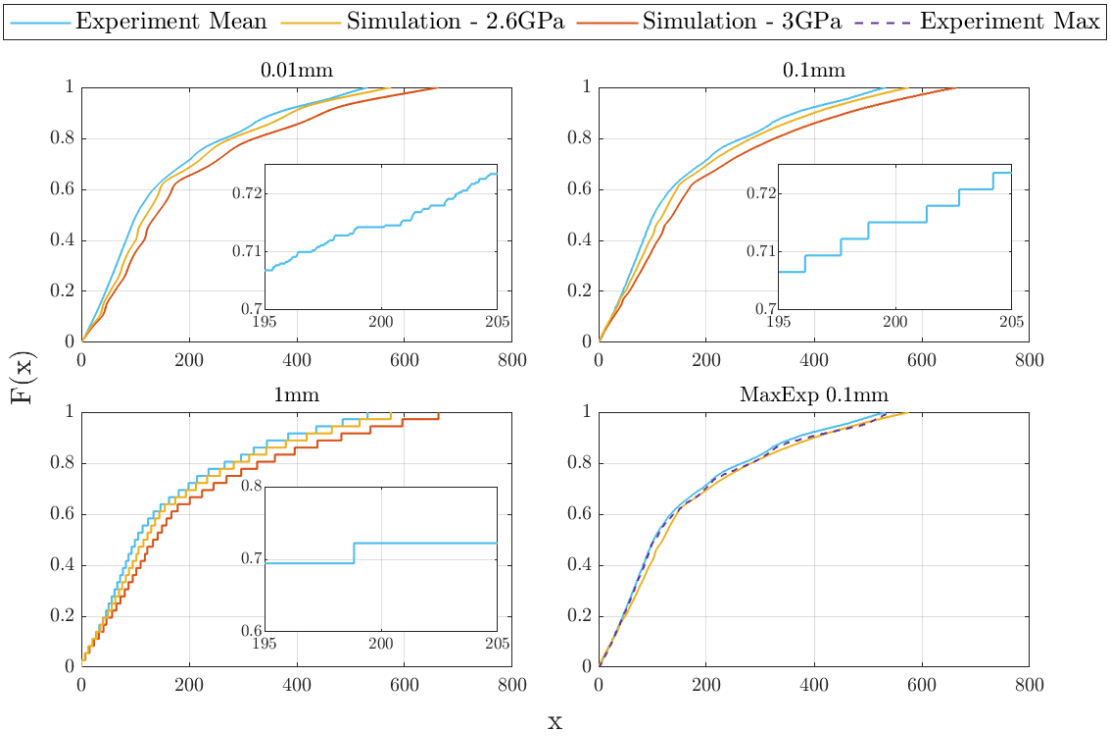


Figure 3.10: Cumulative distribution plots of experimental and simulation data. These are what the K-S hypothesis test analyse through checking the spacing between points. They are horizontally flipped counterparts to the plots of the actual data seen in Figure 3.9. It is possible to visualise how the changing sample rate affected the results of the statistic tests, see plot legend and sub-titles.

the system. The RMSE of 16.6824 is a relatively small error on the scale of the input, approximately 3% of the maximum force. The failure to reject the K-S null hypothesis at $p = 0.28$ also suggests that the difference we see is a statistical anomaly and the data is from the same distribution.

With that in mind, it can be said that the contact method used between the prosthetic and loading plate is suitable in replicating the physical test condition. As such, confidence can be had in further model developments as this previously unknown contact in the setup can now be modelled to a reasonable standard of accuracy.

3.2.3 ISO 10328 Criticism

With the success in modelling contact with the loading apparatus, it was decided to re-evaluate the disadvantages of using the ISO 10328 test procedures to replicate dynamic loading. Initially, the ISO 22675 standard was temporarily abandoned to determine contact conditions with ISO 10328. A prosthetic foot is only required to pass one of these standards, as both test the feet to sufficient peak loads that represent the extremes in the stance phase. However, whilst the static heel and forefoot test setups are similar, the loading profiles and conditions for cyclic loading are not.

In Figure 3.3b, we can see the dual plate system of ISO 10328. With this setup, the cyclic test is simply an oscillating sinusoidal waveform of loading and unloading to a prescribed value defined in the standard. Both heel and forefoot plates are active, but subject to a phase shift of π, such that the loading of the forefoot is concurrent with the unloading of the heel. The standard defines four sinusoidal waveforms that can be selected for testing, these are seen in Figure 3.11. From these waveforms, the document states only the last is somewhat representative of authentic loading conditions in walking. However, the loading angles of the two plates are fixed, which causes the hollow shape in the trough of the waves.

Thus, it can be argued that the ISO 10328 standard is not sufficient in representing the complete phase of stance in the gait cycle, which encourages the decision to move to the ISO 22675 document. The next section will provide an insight into the test conditions, presenting an argument for its use over the ISO 10328 document, and development of the models.

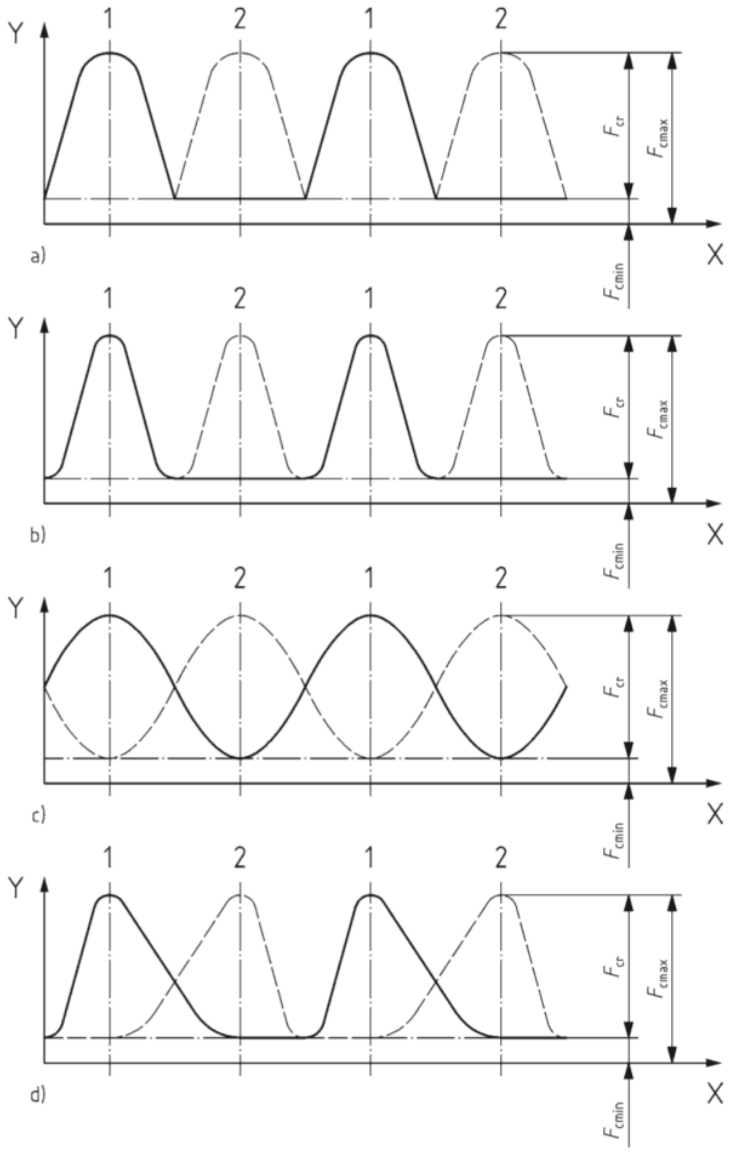


Figure 3.11: The sinusoidal waveforms defined in ISO 10328 [236]. Waveforms (a) and (b) were the original profiles intended for the test. These do not include phase shifting; thus the load cycles of the plates are asynchronous. The profile of (c), is the synchronous, phase shifted waveform of a typical sinusoidal as described in the text. The final waveform (d) is created to resemble the conditions of realistic walking, with a phase shift of the classic sinusoidal in waveform (c).

3.3 ISO 22675 Model

Whilst the ISO 10328 document is for testing entire lower limb prosthetic structures, ISO 22675 is focused specifically on ankle-foot devices [239]. The collection of tests are mostly the same, with the caveat of no torsional test for ISO 22675. Static tests are conducted separately for the heel and forefoot, using the same plate rotated about an axis. Each has the same definition of proof and ultimate

conditions with the loading levels representative of amputee mass.

Beyond theses definitions of test procedures, the setup of the tests in the two standards become divergent. Figure 3.12 shows the coordinate system used in defining the tests of ISO 22675, where f is the forward (horizontal) axis, and u the upward (vertical) axis. This system is critical in dimensioning the test structure and setup for these tests. Unlike the test procedure of ISO 10328, the load in this standard is applied only from the top reference point with the foot supported by the plate. As the ankle-foot test samples will not extend upward far beyond the ankle joint centre, there is a need for an end attachment to complete the whole test structure.

The top reference point is offset to the right of the upwards axis, so the test structure geometry needs to have an extended pylon with a connected application

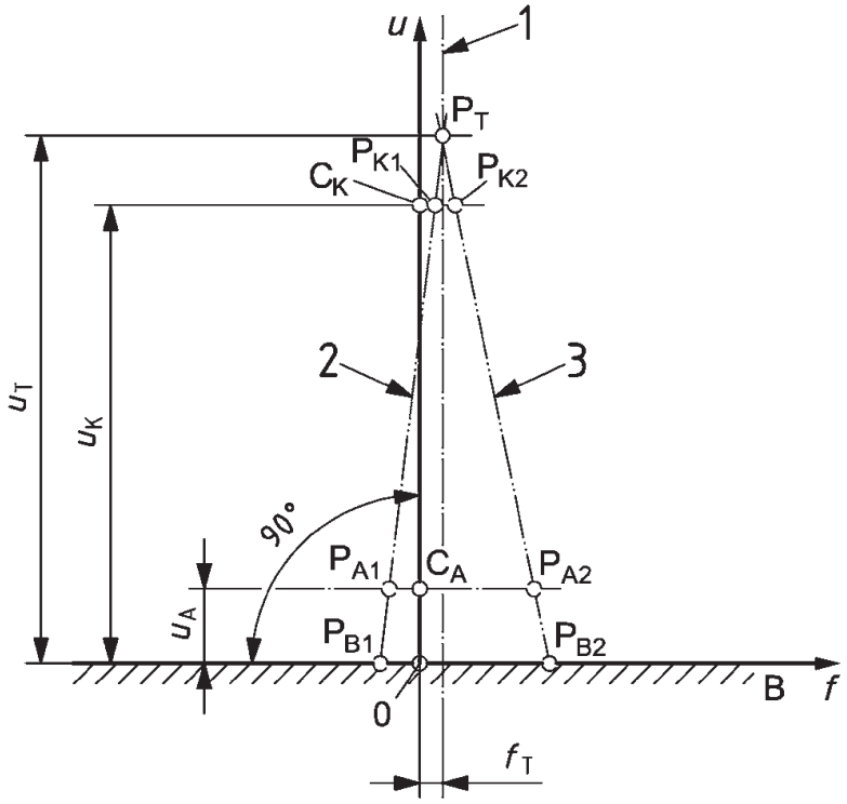
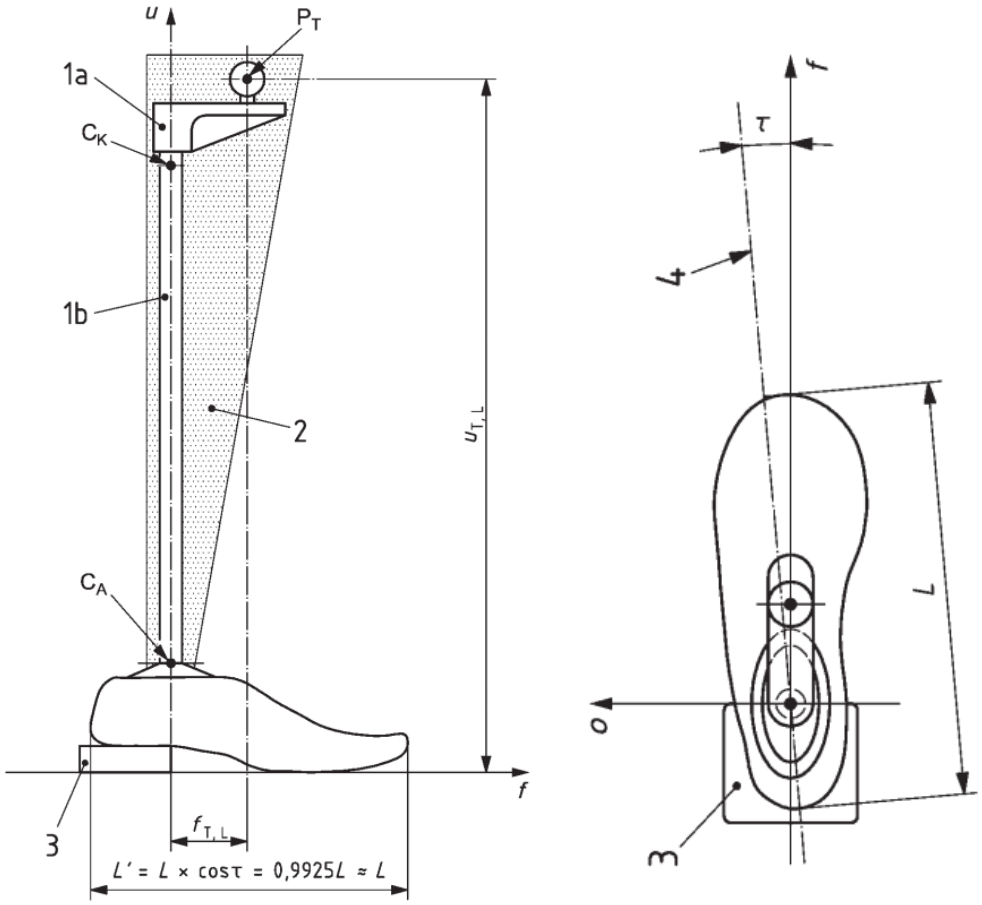


Figure 3.12: Coordinate system used in the setup of tests defined by ISO 22675 [239]. The origin of the system lies at 0 with the vertical axis defined as u and horizontal axis as f. Load reference points are labelled P, with subscripts denoting their location; T=top, K=knee, A=ankle, B=bottom. Each of these has a coordinate defined by the system, using the same subscript notation. Along the vertical of the origin lies the joint centres labelled as C, with the appropriate subscript for the knee and ankle. The numbered dash-dot lines are the lines of action for (1)=Test Force, (2)=Resultant heel force, (3)=Resultant forefoot force.

lever, as can be seen in Figure 3.13. The dimensions of the end attachment are specified through a table of values provided in the ISO document, with the length of the foot acting as the input variable. Whilst the tables values can be used, they are not essential, and simple equations are provided for calculation of dimensions in accordance with the system of Figure 3.12. Three categories of equations exist based on where the end attachment begins in relation to the joint centre u-coordinate. For this initial design with a tall housing, the B category was selected. Then, using the foot length to determine the initial values, all other co-ordinates were calculated. The tables of values and calculations can be found in Appendix C.1.1.

Whilst the co-ordinates do not fully dimension the test equipment, together



(a) (b)

Figure 3.13: Diagrams of test structure used in ISO 22675 testing [239]. The end attachment assembly is connected to the foot at the ankle joint centre C_A, and the load application lever fixed to the top of the extension at the knee joint centre C_K. The dimensions of this structure are determined from tables in the ISO document and are explained in the text here. The τ in the right diagram is the previously un-used toe-out angle, which is set to a constant value of 7°.

with both Figures 3.13-3.14 & description in the ISO document, it is enough to generate the geometry. The pylon is a simple recreation of the general shape, using the joint centres and top load point to inform the complete dimensions. It should be noted that the document also defines where the theoretical ankle joint centre would be positioned on any prosthetic. This is essential to the anchoring

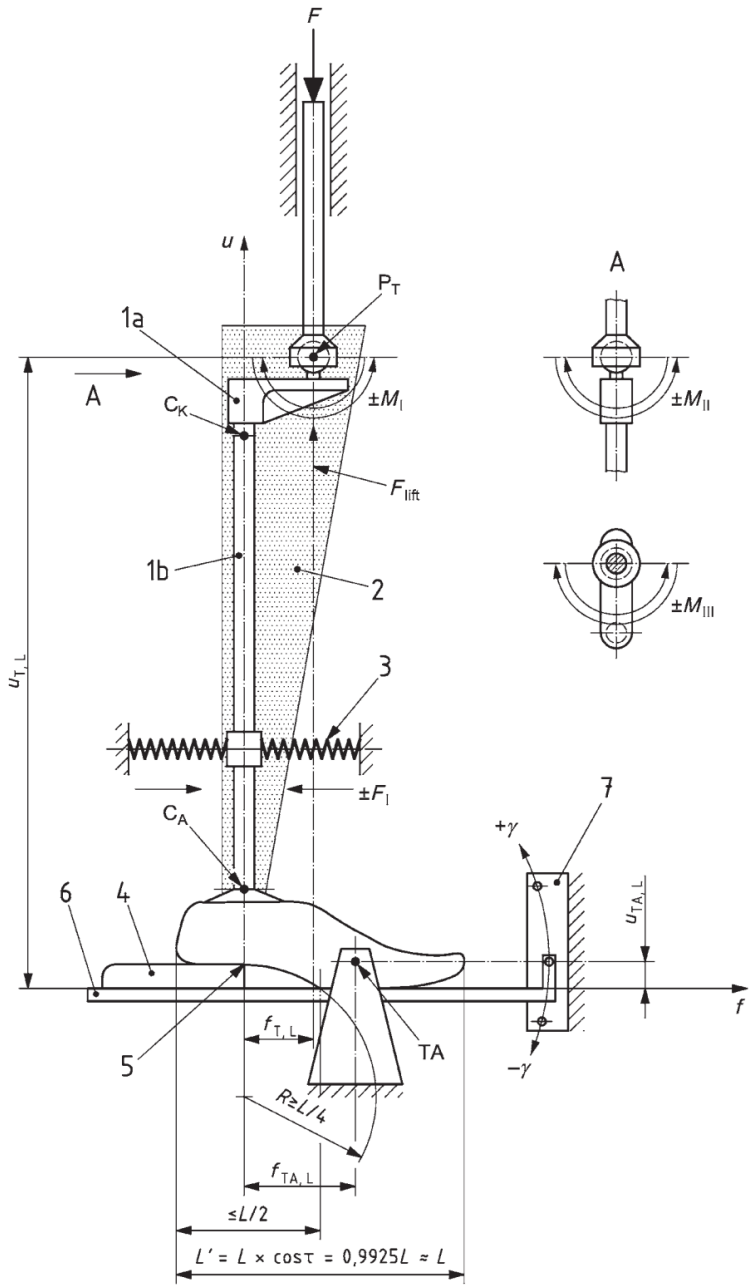


Figure 3.14: Diagram of the complete test apparatus including the stabilising equipment, tilting plate, pylon, and force lever. This setup and the associated description in ISO 22675, are useful for defining the boundary conditions of the system.

of all other dimensions due to its alignment with the origin along the u-axis. The plate is rotatable about an offset axis that is positioned to the right and below the ankle joint centre and is large enough in area to account for extreme deformation in all loading positions. A heel block can also be seen in the diagram, but this was omitted as the design at this stage will not be used with footwear.

The diagram of Figure 3.14 is taken from a section in ISO 22675 which describes the complete set of test equipment and requirements. All of this information was broken down into simple boundary conditions. The force must be applied vertically, with stabilising forces and moments applied at the application point to ensure load and rig alignment are maintained. Positioning and alignment of equipment during the test procedure is an important factor, with three conditions that can be directly translated into boundary conditions [239]. These are:

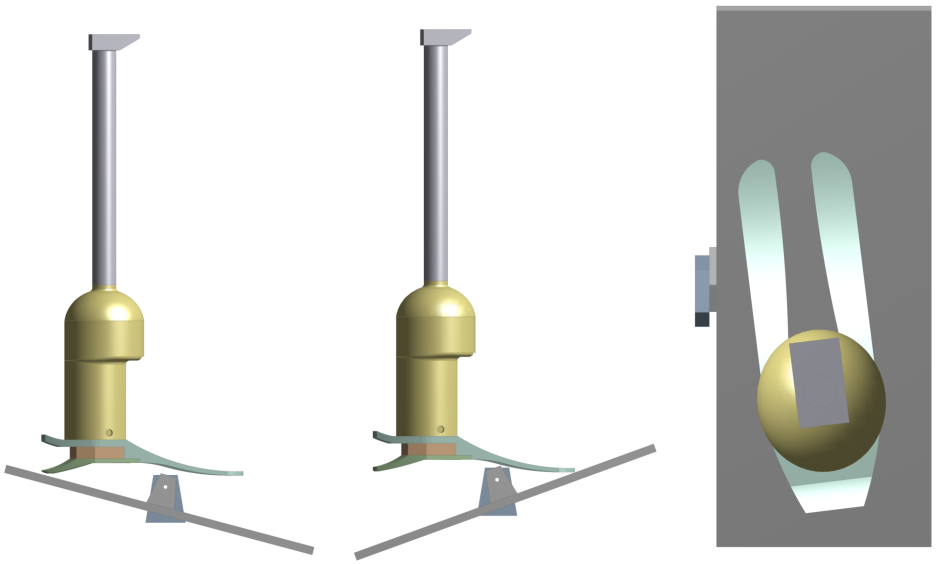
- Resistance to translatory dislocation of the foot in the $f - u$ plane
- Resistance to translatory dislocation of the foot perpendicular to the $f - u$ plane
- Resistance to rotary dislocation of the foot about the long axis of the test sample

All of the above should be controlled using the previously mentioned stabilising equipment attached to the top load point, and any additional control elements that can fit on an appropriate point along the pylon length. The standard continues to define loading profiles, applications rates, and full test procedures. Most of this information goes beyond the scope of determining FEA boundary conditions, except for the load profiles which be detailed in the one of the following subsections. Before that, the updated test CAD geometry must be established, including the material assignments and contact between bodies.

As a note for symbol use, the notations in Figures 3.13 and 3.14 are not used again in this text, and as such they are not defined in the list of symbols.

3.3.1 Updated Ansys Geometry & Materials

The new test CAD geometry can be seen in Figure 3.15. These views include the start position of the two static tests and a top-down view to illustrate the toe-out rotation. Further simplifications were made to the geometry for optimisation of the solve time. Faces and edges were tidied up, removing very small features and merging adjacent faces. Holes were filled and merged with the larger geometry,



(a) (b) (c)

Figure 3.15: Geometry setup for the static tests of ISO 22675. Left-to-right: Heel test, Forefoot test, top-down view of toe-out angle.

and all the internal mechanism parts were removed. The idea being the tests are focused on the structure, so only components important to that function need to be included.

The number of components was reduced to seven needed to assess the foot structure. Three equipment pieces (Force Plate, Plate Mount, and Force Pylon), and four prosthetic parts (Heel, Keel, Bearing Plate, Housing). These all need a material assigned and behaviour defined. As the focus was on the performance of the design, it was decided that the test equipment should have as small effect on the results as possible. To this end, all three test equipment parts were set as rigid, and their material left as the default structural steel material in the Ansys linear materials library. This keeps them as useful geometry for applying boundary conditions, as by limiting the behaviour to rigid body, they only transfer forces through rigid elements. It was also decided to set the housing behaviour as rigid during these early stages of modelling. The design was thought to be susceptible to buckling/collapse failure due to thin-walled geometry; if left in, it could cause simulation failures due to rigid body motion errors.

The full list of parts in the model assembly, the respective behaviour definitions, and material assignments can be seen in Table 3.5. Two other materials were used to for the prosthetic design. The first is a 6082 - T6/T651 Aluminium plate alloy, used for the bearing plate. In the undergrad project, the material was defined as Ti-6Al-4V titanium alloy. However, it was decided this would be replaced by

Table 3.5: Concept model geometry specification and material assignment in cyclic and static simulations for ISO 22675.

Part	Behaviour	Material
Heel (*Base Assembly*)	Flexible	Carbon Fibre Composite
Keel (*Base Assembly*)	Flexible	Carbon Fibre Composite
Bearing Plate	Flexible	Al Plate - 6082
Housing	Rigid	CF Epoxy Twill
Force Plate	Rigid	Structural Steel
Plate Mount	Rigid	Structural Steel
Force Pylon	Rigid	Structural Steel

the cheaper but more manufacturable aluminium alloy. The material properties are taken from the data sheet of a major supplier [244], which is in accordance with the BS EN 485-2 document [245]. Modelling the intended composite layup was seen as an unnecessary complexity at this early stage of the project. As such, the composite was modelled as an isotropic material, under the assumption that the layup of the final design and resultant orthotropic nature, would cause only minimal differences of performance in the planes of action. A few different sources of composite material properties were considered, a recommended supplier's data sheet, the material database of Granta EduPack [246], and the Ansys material library. To determine which would be the most suitable, or if there would be any significant difference, a selection of basic studies were completed.

Intermediate material study

Five materials were featured in this study, all representing some form of an epoxy carbon fibre prepreg laminate. The selection of materials and their mechanical properties can be found in the Appendix section D. One of these was sourced from a supplier's data sheet, the XPREG® XC130 210g twill laminate produced by Easy Composites [247]. The properties given are non-directional and typical for the quasi-isotropic behaviour expected with woven fabric composites.

Two other materials have non-directional approximate material properties, both are from the EduPack database [246]. One is an example of a biaxial laminate, using a [0/90] layup. The other is another quasi-isotropic laminate formed from a layup of [0/90,+45/-45]s, its properties are similar to the quasi-isotropic XC130's woven twill.

The final two materials are sourced from the Ansys composite database, primarily to be used in the composite modelling module of the software. Both are representative of a woven laminate much like the XC130 Twill, but have orthotropic

Table 3.6: Stiffness results taken from the table D.3 in Appendix chapter D

Source	**Name**	**Stiffness** N/mm
Easy Composites	XC130 210g	119.27
Granta Edupack	Biaxial	148.44
Ansys	230GPa	116.93
	395GPa	151.31

properties. They are given differentiated names by the tensile modulus of fibres, one being 230GPa and the other 395GPa.

The study was run on the ISO 10328 model as the setup and analysis parameters were established, and the purpose of the study did not require the use of the newly updated geometry. An Ansys workbench project was setup with five separate simulations, one for each carbon fibre variant. All settings were kept the same, with the exception of applying the originally intended force. The stress and deformation were both extracted using the built-in results of Ansys. In addition to this, the stiffness was generated using a custom written APDL code snippet; the full APDL script and set of results can be found in their respective sub-sections of Appendix D.

These results indicate some correlation between the composite variants, but this is likely to be coincidental. However, some inferences can be made to come to a decision on which composite to use. It appears that the Biaxial layup bears a similar stiffness value to the 395GPa Woven composite from Ansys. Both are woven, but there is no further detail on the Ansys material. The other apparent similarity is between the 230GPa Ansys weave and the XC130 from Easy Composites. Again, it appears that they share similar stiffness properties (see Table 3.6), and whilst some additional information is known on the XC130, there is no layup information within the Ansys database. It is known that the two Ansys materials are the same layup but with different fibre moduli. So, it could be inferred that both pairings are related, but this would not be possible as it is known that the biaxial and XC130 are different weaves. Thus, only one pair could be a possible match and it is believed to be between the 230GPa Ansys weave and the XC130. The reasoning for this comes from further inspection into the fibre components of the XC130. Produced by TorayCA®, the fibres have a modulus of 230GPa [248], which incidentally is the same fibre modulus of the Ansys material. It is possible then that the Ansys 230GPa weave is representative of a twill weave, just with orthotropic properties; giving possible reason to the small differences in results.

Table 3.7: Material properties used in the ISO 22675 simulations.

Property	**Material**		
	XC130 210g	Al Plate - 6082	Structural Steel
Density (kg/m^3)	1610	2700	7850
Young's Modulus (GPa)	55.2	70	200
Poisson's Ratio	0.399	0.34	0.3
Tensile Yield (MPa)	645	255	250
Tensile Ultimate (MPa)	645	300	460

With the study completed, the decision came down to the Ansys 230GPa, and the XC130. A biaxial layup for production would not be capable of providing the directional properties needed for deflection of the structure. The XC130 can be sourced for manufacture of the prototype and given that the Ansys 230GPa model has similar stiffness properties, the Ansys 395GPa model would not be suitable. There is little difference between them, but at this stage the XC130 was chosen. The geometry of the concept is not suitable for a layup and as such the use of orthotropic properties would be of little benefit. It is simpler to continue with the assumption of isotropic properties for now but keeping the Ansys 230GPa as an option for future studies with directional properties. The final selection of material properties can be seen in Table 3.7.

3.3.2 Contact & Joint Pair Definitions

The next step in developing the model was to setup the contact pairs between the various parts. From the list of seven bodies in Table 3.5, there are six contact pairs to join them. Of these seven, four are static connections between the test structure

Table 3.8: Concept model contact sets used in cyclic and static simulations for ISO 22675. All contacts use Gauss integration point detection. Bonded contacts assume small sliding. Frictionless contacts adjust interface to touch, depending on the static setup, one is disabled.

Contact Set		**Type**	**Behaviour**	**Formulation**
Contact	*Target*			
Housing	Pylon	Bonded	Asymmetric	Penalty
Keel	Housing	Bonded	Asymmetric	Augmented Lagrange
B. Plate	Keel	Bonded	Asymmetric	Augmented Lagrange
B. Plate/Keel	Heel	Bonded	Asymmetric	Augmented Lagrange
Heel	Force Plate	Frictionless	Asymmetric	Augmented Lagrange
Keel	Force Plate	Frictionless	Asymmetric	Augmented Lagrange

and simplified foot, whilst the other two are non-linear transient connections to the force plate.

A summary of these contacts can be seen in Table 3.8, which follows the same order of presentation as the selection of images in Figure 3.16. The static contact pairs are all bonded, and non-linear pairs use frictionless contacts as determined by the experimentation in Section 3.2.2. This activates the small sliding assumption in bonded contacts, and Gaussian integration point detection between nodes and elements of contact pairs; both settings improve solver efficiency. Each pair also uses an asymmetric pairing behaviour, with rigid bodies prioritised as the

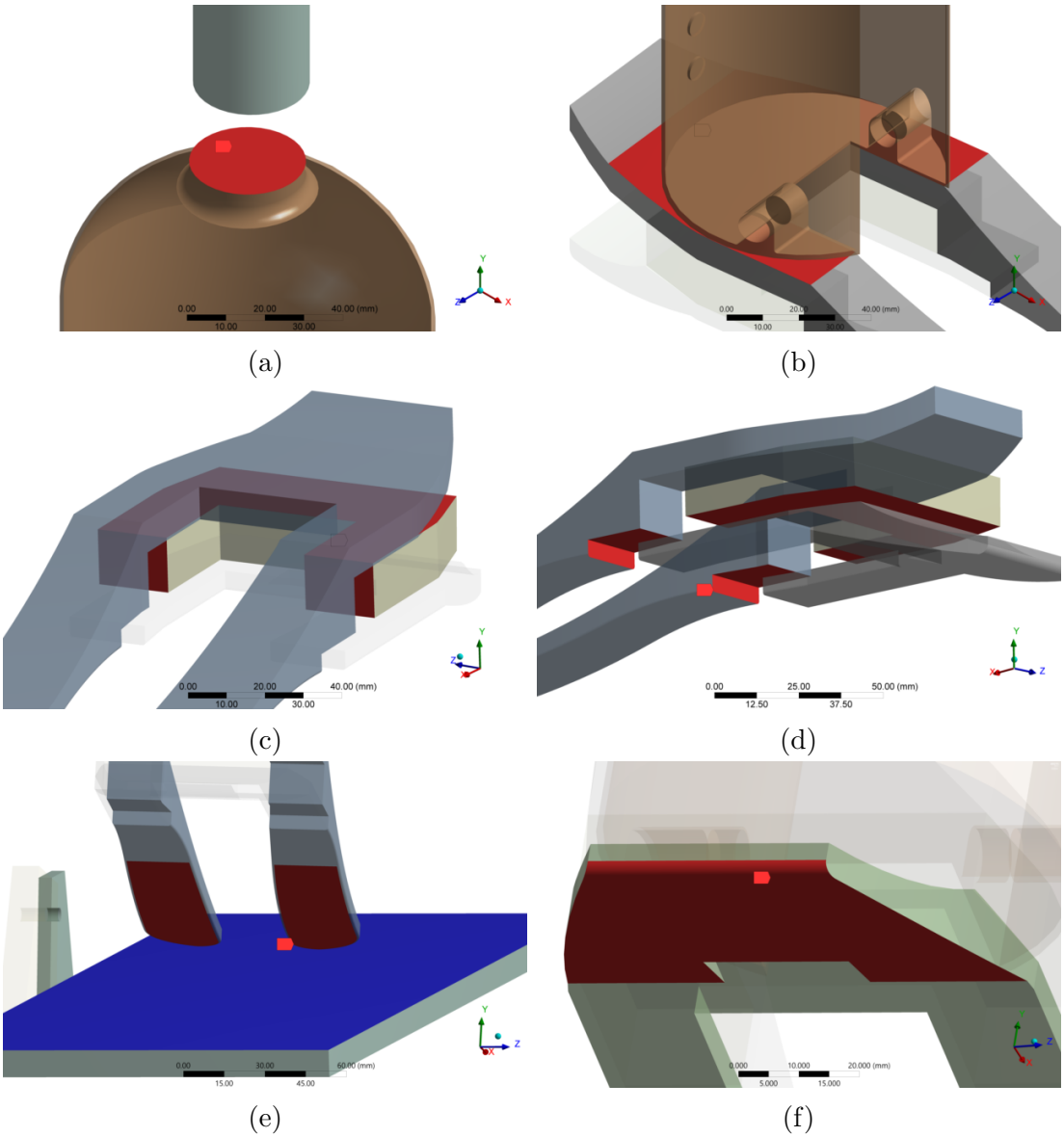


Figure 3.16: Contact pairs. (a)=Pylon - Housing, (b)=Housing - Keel, (c)=Bearing Plate - Keel, (d)=Bearing Plate & Keel - Heel, (e)=Keel - Force Plate, (f)=Heel- Force Plate

target; part behaviour was also summarised in Table 3.5. All but one pair uses the Augmented Lagrange formulation as this activates an algorithm to limit the penetration of elements and nodes. A penalty formulation is applied to the housing and pylon pair, as it is a simpler computation, and penetration between the two rigid bodies is of no concern. Other settings were left to the algorithm to resolve, with the intention to revisit them should the need arise.

Another type of connection used in Ansys are the joints, which are used to represent the mechanical behaviour between two parts. In this model, two joint pairs are used on the test equipment geometry. A body-to-ground joint is applied to the bottom surface of the plate mount, acting to anchor the full model in the simulation space. The other joint is a revolute connection between the plate mount and the force plate, using the aligned axle holes. An additional benefit of this second joint is that it can be used to apply a rotational boundary condition for use in the transient analysis. Due to this, the revolute joint is only kept active for the transient problems.

3.3.3 Boundary Conditions

The ISO 22675 document provides thorough explanations of test equipment, loading rates, and degrees of freedom. Within this document, two types of test are defined; static and cyclic.

The static tests include loading levels expected to push the prosthetic to failure, representing the worst conditions at heel-strike and push-off. Each of these then has three categories: a proof test, lower ultimate, and upper ultimate. Under these conditions, the prosthetic is expected to pass the proof test, and then aim for the highest success under the ultimate test, but failure is expected. There is also an additional level of load definitions, which represent different weight categories of an amputee; to avoid repeating detail see the text in Section 3.2.1 for the classifications of these levels.

The cyclic test procedure recreates loading conditions throughout the stance phase of walking, and only has loading level categories based on weight. These forces are applied in the same manner as the static test, but the force plate tilt angle also progresses in a synchronous manner. Within the test standard, this tilt angle is declared as the range of angular movement from heel-strike to push-off, defined by the lower leg angle in the sagittal plane as a function of time.

ISO & Experimental Data comparison

All of the test data in the standard has been derived from experimental data sets, collated together from various sources when ISO 10328 was drafted in 1996. The purpose of the test document and procedures is to provide a framework in which any prosthetic foot device can be tested, with the option of using personalised gait data. As such, the standard provides a method in which to recreate the test forces and plate angles. To understand how these forces are derived, the reader is directed to the appendices of the document which contain the reference data details. A key figure from this appendix is shown here in Figure 3.17 and will be used as the visual reference for this sub-section.

There are four key forces in this diagram. The test force, F is applied vertically at the top load application point. At the force plate, this creates a resultant force F_R and its two components, the tangential force F_T and perpendicular force F_P. These forces are then related through geometric properties and three angles: α_{ISO}, β_{ISO}, and γ. Further to this, the following equations are also defined:

$$\alpha_{ISO} + \beta_{ISO} = \gamma \tag{3.1}$$

$$\beta_{ISO} = arctan(F_T/F_P) \tag{3.2}$$

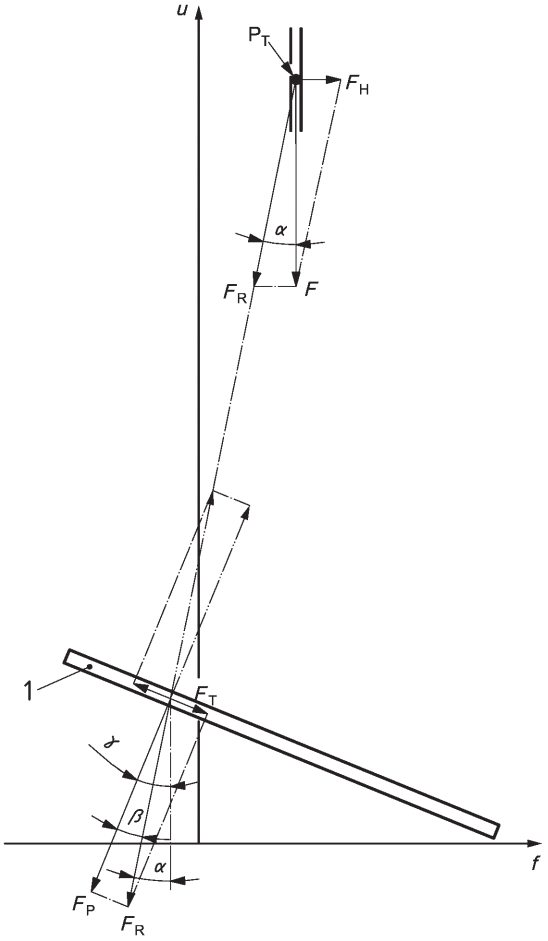
These relationships alone are not enough to derive all the force components, but with some simple manipulation, two additional equations can be defined:

$$F_R = F_P/\cos\beta_{ISO} \tag{3.3}$$

$$F = F_R \cos\alpha_{ISO} \tag{3.4}$$

A test force profile can now be defined with 3.4, using the resultant force and α_{ISO} angle. The resultant force can be derived from experimental force data and using equations 3.2 and 3.3. However, the α_{ISO} angle can only be calculated using equation 3.1, which requires the tilt angle, γ. It has already been stated that this angle corresponds to the lower leg angle made in the sagittal plane. Should the collection of kinematic data be unattainable, the standard has also defined a 5th order polynomial, derived from the large dataset:

$$\begin{aligned}\gamma(t) = 2.45074 \times 10^{-12} \times t^5 - 3.75984 \times 10^{-9} \times t^4 \\ + 1.77519 \times 10^{-6} \times t^3 - 1.08409 \times 10^{-4} \times t^2 \\ + 2.07217 \times 10^{-2} \times t - 20.041\end{aligned} \tag{3.5}$$



Key

1	foot platform
f, u	axes of coordinate system
P_T	top load application point
F	test force
F_H	force component transverse to line of application of test force F
F_R	resultant force
F_P	force component perpendicular to foot platform
F_T	force component tangential to foot platform
α	inclination angle of line of action of resultant force F_R
β	angle between resultant force F_R and force component F_P determining ratio F_T/F_P
γ	tilting angle of foot platform

Figure 3.17: Appendix diagram taken from ISO 22675 [239]. This provides a visual reference for the calculations used to derive the test force from experimental ground reaction forces.

This equation will produce a suitable tilt angle profile for loading periods of exactly $600ms$. In order to use this for other test frequencies, each coefficient of the polynomial must be multiplied by the following ratio:

$$\left(\frac{600 \text{ ms}}{x \text{ ms}}\right)^{y_{coef}} \tag{3.6}$$

Where x ms is the loading period of the experimental data, and y_{coef} is the order of the t parameter for the given coefficient. Data was shared from a PhD body of work, where force plate and marker kinematic data was collected during steady-state walking [55]. A sample of this data was then selected and fed into equations. The tilting angle equation became:

$$\begin{aligned}\gamma(t) = 2.45074 \times 10^{-12} \times \left(\frac{600}{733}\right)^5 \times t^5 - 3.75984 \times 10^{-9} \times \left(\frac{600}{733}\right)^4 \times t^4 \\ + 1.77519 \times 10^{-6} \times \left(\frac{600}{733}\right)^3 \times t^3 - 1.08409 \times 10^{-4} \times \left(\frac{600}{733}\right)^2 \times t^2 \\ + 2.07217 \times 10^{-2} \times \left(\frac{600}{733}\right) \times t - 20.041\end{aligned} \tag{3.7}$$

This new tilting angle profile has been scaled to fit the new loading period. With β_{ISO} given by the ratio of vertical and anterior-posterior ground reaction forces 3.2, these two parameters were fed into equation 3.1 to give the α_{ISO} angle. The final steps of this conversion were the use of equations 3.3 and 3.4, to find the

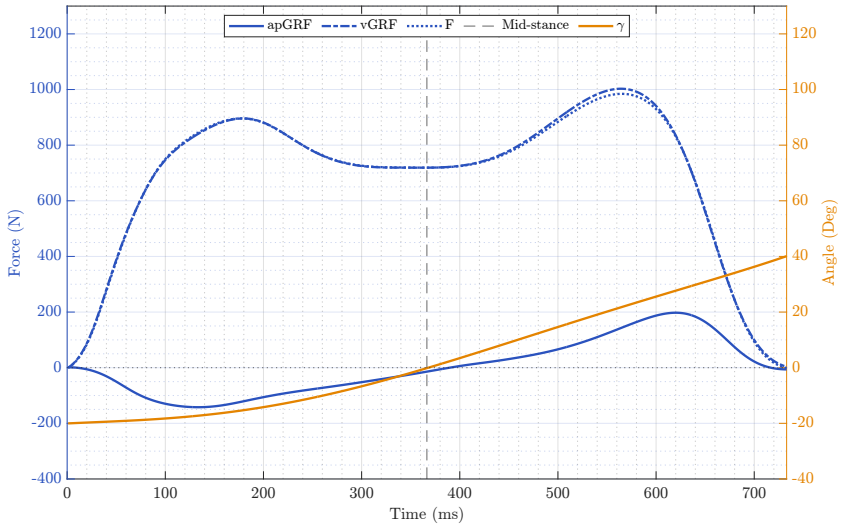
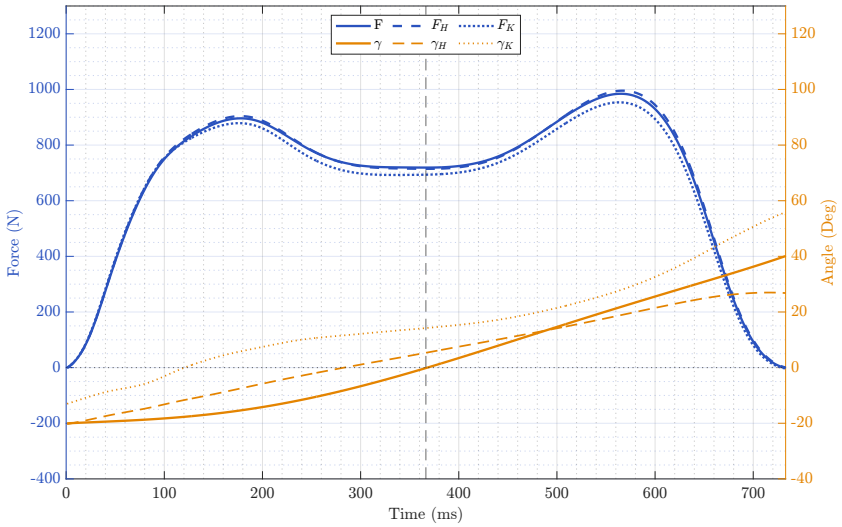


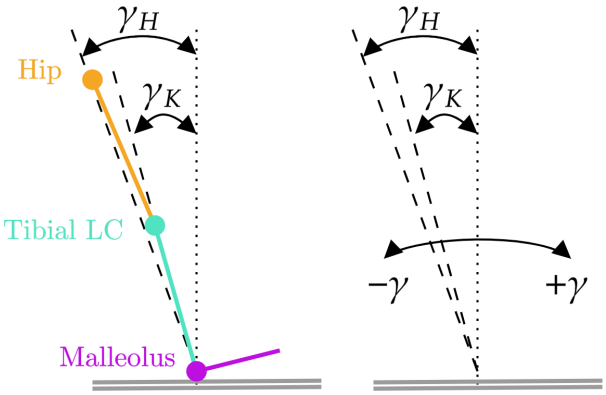
Figure 3.18: Experimental data was taken from a walking study [55], see the apGRF & vGRF for the anterior-posterior and vertical components. The Test force F and Tilting angle γ values were then calculated

resultant, and test force profiles.

A MATLAB script was written to calculate these values and export a plot of the experimental data and resultant ISO test parameters; see Figure 3.18. For this particular sample, the effect of the anterior-posterior force is minimal, serving



(a) Comparison of test force data input angles. The ISO data is calculated using the fifth order polynomial of equation 3.7. Experimental marker data is used to calculate the other two data sets, with F_H, and F_K corresponding to different measurements of leg angles. See the accompanying figure below.



(b) Diagram to visualise the different leg angle measurements taken for comparison with the ISO equation. A vertical line is made from the centre of the malleolus (ankle). A secondary line is then made between the malleolus, and either the tibial lateral condyle (knee), or the greater trochanter (hip). The angle between these two lines is then found and denoted as γ_H or γ_K for the hip and knee leg angles.

Figure 3.19

only to dampen the second peak of the test force. To compare the analytical and experimental derivations of the γ angle, two additional test force sets were calculated. See Figure 3.19 for detail on how these were derived.

The first thing to note is the similarity between the ISO angle data, and the hip angle data from the experiment. Both angles begin at around $-20°$, and generally follow the same trajectory. The differences seen can easily be attributed to the small sample of a single experimental result in comparison to the large dataset used to derive the ISO polynomial. Furthermore, although the angle profiles are not an exact match, they do result in a distinctly similar test force profile.

On the other hand, the knee-angle data follows a noticeably different trajectory, especially when comparing the terminal and mid-stance values. Thus, the test force data diverges from that of the ISO profile. Such a noticeable difference is due to the flawed use of the knee joint as the leg angle determinant. This measurement does not account for the flexion of the knee at heel-strike, hence the shallow angle. At push-off, the angle is accentuated again because the flexion of the knee is discounted, resulting in an exaggerated leg angle.

The ISO standard does not go into detail on how the leg angle was determined. However, based on the above analysis, it is likely to be taken as the angle between the vertical, hip, and ankle joint centres. Whilst this analysis sufficiently demonstrates the use of personalised biomechanics data, the ISO data will be used for the continuation of this work; due to the reliability of that data, and that the experimental data used in the example derivation came from a small sample size and would not necessarily fit within a population mean.

ISO Force Boundary Condition

Once the various levels of loading are taken into consideration, the static tests have nine forces that can be applied to each static condition. A summary of these loads can be found in Table 3.9. Included in this table are two values of tilt angle for the force plate to be aligned at for a suitable reconstruction of the ground reaction forces at heel-strike and push-off.

Whilst the standard does not provide an explanation on why specific scaling factors are used, it can be assumed that they were simply derived much in the same way the cyclic data was. The proof loads are the cyclic peaks multiplied by a factor of 1.75, and the lower/upper ultimate values are the proof load multiplied by a factor of 1.5 & 2 respectively.

Table 3.9: Static load boundary conditions for the Proof (P), Ultimate Lower (U_L), and Ultimate Upper (U_U) for heel and forefoot tests.

Setup condition		**Heel**			**Forefoot**		
		Tilt angle: -20°			*Tilt angle:* 15°		
Loading level		*P3*	*P4*	*P5*	*P3*	*P4*	*P5*
Test Force (N)	P	1601	2053	2227	1580	2026	2198
	U_U	2401	3079	3340	2369	3039	3297
	U_L	3201	4106	4454	3159	4052	4396

The cyclic loading data is split into discrete points at intervals of 30ms, with the accompanying force and tilt angle data being synchronously split. These discrete data points have been presented in Table 3.10. The only modification required for translation into FEA boundary conditions was to re-define the tilting angle as

Table 3.10: Cyclic test transient load boundary conditions with format of ISO 22675. Within the Ansys models, the signs of tilting angle and forces are reversed. In the tilting angle column, the value in brackets is the cumulative change in angle used in the model boundary conditions.

Time (ms)	**Tilting angle** (°)	**Test Force levels** (N)		
		P3 (60kg)	*P4 (80kg)*	*P5 (100kg)*
0	-20 (0)	0	0	0
30	-19.5 (0.5)	238	306	331
60	-19 (1)	477	612	663
90	-18 (2)	716	919	996
120	-16.5 (3.5)	878	1126	1221
150	-15 (5)	915	1173	1273
180	-13 (7)	873	1120	1215
210	-10.5 (9.5)	785	1007	1092
240	-7.5 (12.5)	697	893	969
270	-4 (16)	632	811	880
300	0 (20)	611	783	850
330	4 (24)	632	810	879
360	8 (28)	694	891	966
390	12 (32)	781	1003	1086
420	16 (36)	866	1110	1204
450	20 (40)	903	1158	1256
480	24 (44)	861	1105	1198
510	28 (48)	698	895	971
540	32 (52)	463	593	643
570	36 (56)	231	296	321
600	40 (60)	0	0	0

a cumulative series initiating at 0°. An adaptation required, as the force plate in the model begins at −20° for heel-strike, and each successive step in rotation must be applied in accumulation.

Translation to FEA Boundary Conditions

At the start of Section 3.3, the test apparatus was presented alongside the test procedures. Together, they formed a set of rules on how the structure should be restrained in order for the correct application of load. A key difference between the conditions for static and cyclic loading is the application of the revolute joint on the force plate axis. When this is active for the cyclic loading, an additional degree of rotational freedom in the sagittal plane is provided for the force plate.

A summary of these support boundary conditions can be seen in Table 3.11. When applying the conditions to model geometry, it is important to ensure mesh nodes do not share separate boundary conditions to aid the solver computations. The remote displacement condition on the force plate is applied to the bottom surface. The pylon structure has two conditions applied to it. A remote displacement to limit translation to the vertical axis is applied on the cylindrical surface, and the remote force is applied to the top load application point. Use of a remote force on the pylon is required as the rigid body cannot accept a direct force application. An additional boundary condition for just the cyclic tests is the revolute joint, which was explained previously.

Table 3.11: Support and load boundary conditions used for the cyclic and static simulations of ISO 22675.

Static Model		
Geometry	*Type*	*Description*
Force Plate	Remote Displacement	Translational & rotational axes fixed
Pylon	Remote Displacement	Free to move along y-axis
Pylon	Remote Force	Applied force from table 3.9
Cyclic Model		
Geometry	*Type*	*Description*
Force Plate	Remote Displacement	Free to rotate about z-axis
Pylon	Remote Displacement	Free to move along y-axis
Pylon	Remote Force	Applied force from table 3.10
Revolute Joint	Rotation	Cumulative angle values in table 3.10

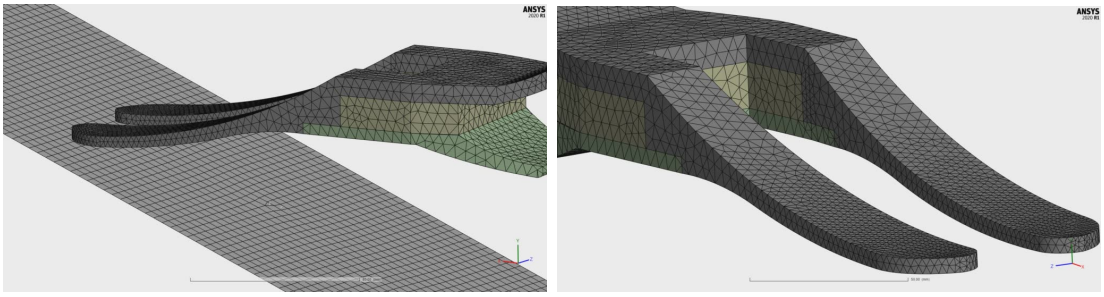
Table 3.12: Initial mesh settings applied to the foot assembly, used to provide first solutions of mesh study for static and cyclic tests of 22675. Local controls were used only in the static setup that required them.

Global Mesh			
Element Order	*Element Size*	*Growth Rate*	*Max Size*
Quadratic	5mm	1.85	20mm
Local Control			
Geometry	*Size*	*Curvature*	*Proximity*
Heel Body	4mm	—-	2 Cells
Keel Body	5mm	70°	2 Cells
Statistics			
Setup	*Elements*	*Nodes*	*Mesh Quality*
Forefoot	31939	55456	0.827
Heel	38228	65850	0.818

3.3.4 Initial Mesh & Analysis Settings

The final stages of FEA setup involve generating an initial mesh and selecting analysis settings. This section title includes "Initial" in the title as with any FEA modelling process, it is expected that these settings will require some tweaking to achieve convergence and realistic results.

As such, the preliminary models would be run under the static conditions so the model would solve quicker and further tweaks could be made in a timely manner. A general set of mesh controls were applied in each static condition, and then depending on which event was being modelled, further local controls were applied to specific bodies. A summary of these mesh controls and associated statistics can be seen in Table 3.12, with screenshots of the mesh used in the forefoot condition presented in Figure 3.20.



(a) (b)

Figure 3.20: Mesh used for the initial simulation of forefoot test condition

Table 3.13: Analysis settings for static and cyclic models. Output controls were set to record all possible streams of data

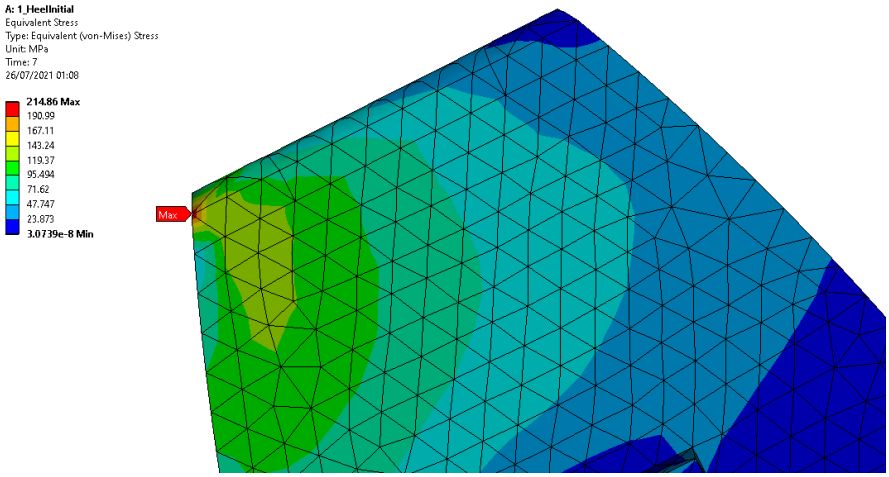
Setting	**Static**	**Cyclic**
Analysis system	Static structural	Transient structural
Solver type	Direct sparse matrix	
Number of steps	Load variant	20
Initial time step	1s	1E-02s
Min. time step	1E-01s	1E-03s
Max. time step	1s	3E-02s
Large deflection	On	On

With these local controls the element count can be reduced in areas it is not required, and subsequent mesh refinements can be focused. Likewise, the analysis settings were mostly left as default. The solver was set to a direct sparse matrix type, and time steps set to 1 second intervals. As mentioned before, the standard defines a set rate of load application between 100-250N/s. The maximum value of this range was used to split the full given load into a suitable number of load steps. Whilst this has little effect on the material effects due to no plastic behaviour, it would help to resolve potential convergence issues. The final control was turning on 'Large Deflection', which instructs the solver to account for large strains; a predicted results based on the simulations ran during the original design work. A summary of these settings with values is included in Table 3.13.

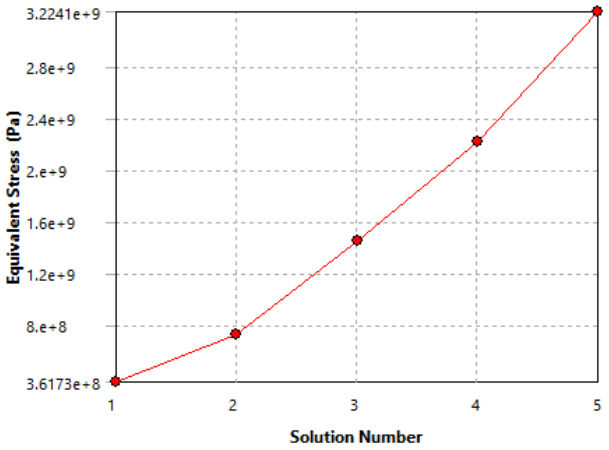
3.3.5 Heel Contact Convergence Study

With the setup completed, preliminary simulations were run beginning with the heel test condition. An immediate issue arose with a stress singularity in the corner of the heel which makes first contact with the plate. A convergence tool was used to assess the extent at which this would distort the true result; see Figure 3.21. The software was instructed to aim for a 10% maximum change and was stopped after the 5th iteration regardless.

It can be seen that the singularity causes an exponential increase in stress with no indication of levelling off. Such a phenomenon is common in FEA modelling, and a simple workaround is to apply a fillet to the sharp geometry to assist in the redistribution of stress. If the fillet is not an original design feature, then it is important to ensure the scale of the fillet relative to the original geometry is kept to a respectable minimum. With this in mind, a 1mm fillet was applied to the longitudinal bottom edge of the heel spring.



(a)



(b)

Figure 3.21: The initial stress plot of heel test condition. Notice the peak stress occurring on a node located on the edge where first contact is made. The second image is the plot generated by the Ansys convergence tool, which refines the mesh in key areas to resolve convergence.

The initial stress result was higher than the before, but the final value was lower, albeit still too high for a reasonable result. It was therefore suspected that contact settings needed adjusting. To confirm this, the contact formulation was switched from Augmented Lagrange to a Normal Lagrange which creates a much more rigid contact and would be expected to raise the stress even higher, which it did by an increase of 22%.

Following this a series of simulations were ran to assess the effect of changing the contact normal stiffness factor. As expected, the increasing the stiffness factor also raised the stress values. Furthermore, the highest value tested of 0.9, which is close to the default value of 1, resulted in a converged value. An additional setting was adjusted, which directed how the stiffness should be updated, forced either

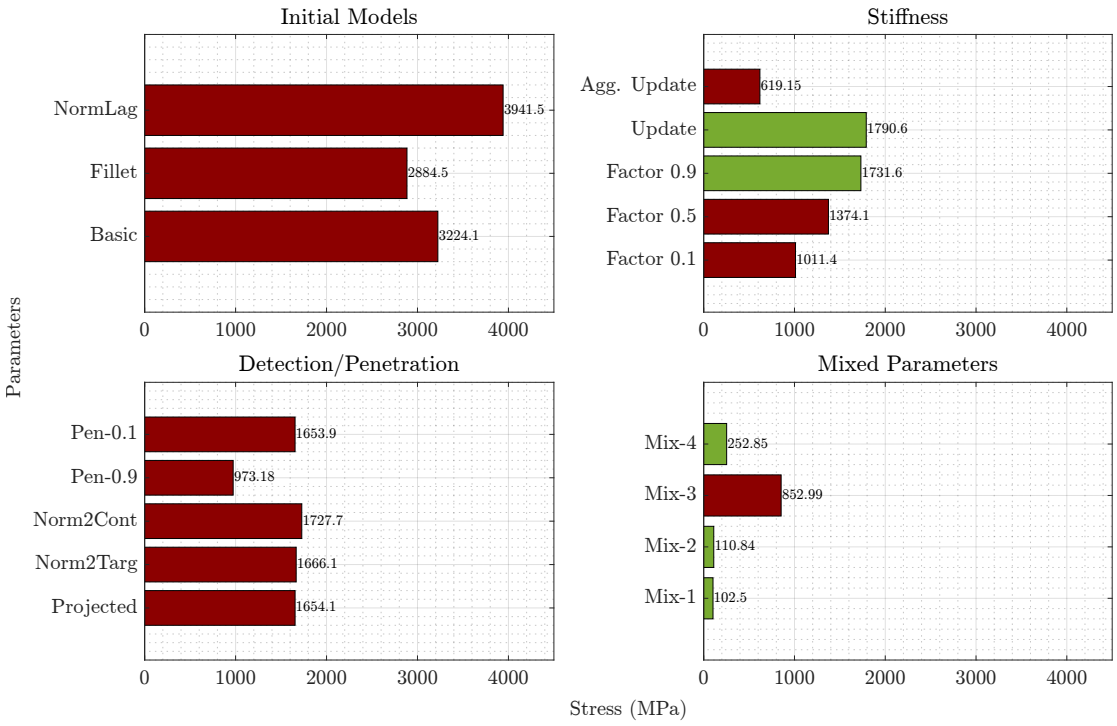


Figure 3.22: Stress results from heel contact convergence study, with failed convergence in red and successful in green. See the accompanying text for additional explanation of the explored parameters.

normally or aggressively each iteration. The standard update also converged, but these two results were deemed inaccurate as the stress values were still too high, and the stress distribution highly localised. The aggressive stiffness update was able to resolve the stiffness to a more appropriate stress. It failed to converge after five iterations, but the final iteration did see a drop of 83%.

Contact detection and node penetration tolerances were also explored. A projected node detection method was marginally better than the other methods. It would also benefit this particular type of initial contact which relies on the accurate detection of the point contact. Increasing the penetration factor to 0.9 significantly dropped the stress in comparison to the value generated from the default factor of 0.1. However, as this factor represents a threshold it resulted in an increased penetration of meshed bodies which caused peak stresses to occur inside the heel body.

Next, a series of models were run with a mixture of the most effective parameters explored in the pilot models. The formulation was kept to Augmented Lagrange, with the detection method set to Nodal-Projected Normal from Contact as this is better suited to accommodating some initial penetration issues. In addition to these two settings, the stiffness factor was left to the default programme

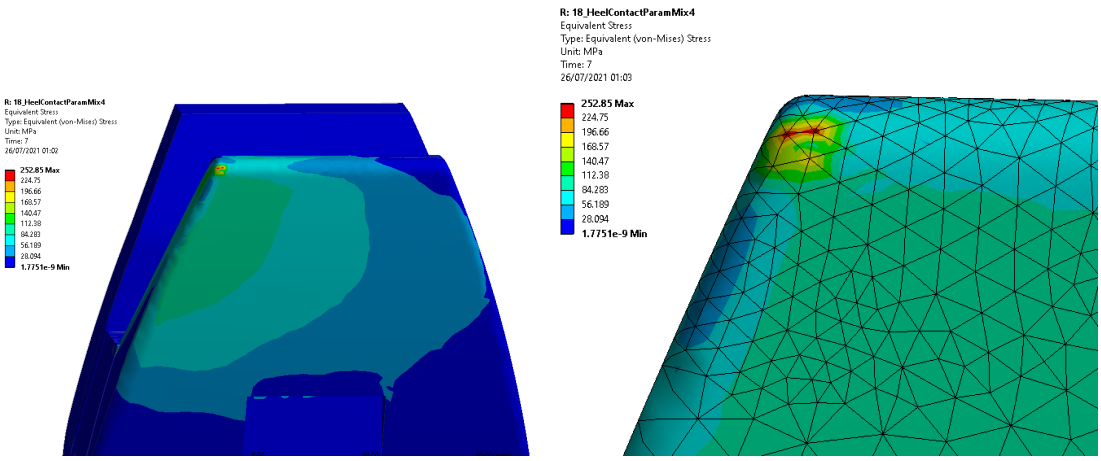


Figure 3.23: Stress plot from the converged heel study. Although the maximum value converged, it still has a localised area of effect to two nodes proximal to the corner. See the main text for further explanation.

control of 1, but the solver was instructed to aggressively update the stiffness based on the changing contact. This left the penetration tolerance as a potentially explorable value. The mixed models from 1-3 had the penetration tolerance factor set to 0.9, 0.5, and 0.1 respectively.

The first two mixed parameter models successively converged to a maximum von-Mises stress of around 100-110MPa. However, these two results were achieved with tolerance values set to accept much higher levels of contact penetration. When the tolerance factor was set to 0.1 in the 3rd mixed parameter study, the stress failed to converge again. In the final study, this tolerance value was left to the programme to adjust based on the other contact parameter settings. This final study was successful in converging on a reasonable estimation of stress, which also happened to align with the results seen in the very first failed study. These similarities can be seen when comparing the plots in Figures 3.21 & 3.23. The maximum stress could still be identified as a local effect, but this would be expected of a very stiff structure, unable to elastically deform to displace the build-up of stress from the point of contact; the corresponding deflection is 0.62mm.

Based on these results, the settings required to achieve a satisfactory stress convergence on the heel have been determined. By instructing the solver to aggressively search for a stiffness, and projecting the nodes to overcome initial penetration errors, the additional tolerance factor parameters need no modification. Arguably, this is preferable as the parameter study results seen in Figure 3.22 reveal how sensitive the stress maximum value is to these.

Mesh Dependency Comment

As a result of the contact convergence study, the heel study converged in a single step of 0.75% change. The mesh settings in Table 3.12 were slightly adapted in this successful study, where the body size control on the heel changed to an element size of 3mm with 3 elements across a gap. As such, there was no need for an additional mesh study.

3.3.6 Forefoot Mesh Dependency Study

The attention turned to the static forefoot case. No contact changes from the heel study were used in the initial simulation as the previous experimental and analytical work had suggested no issues. The result of this initial study revealed the same issue with a contact stress singularity, see Figure 3.24. This peak of 840.77MPa right on the tip is unexpected behaviour. It would be reasonable to treat this structure as a curved cantilever beam, where the anchor point is on the thickest section of the toe springs. Therefore, it would also be plausible to assume the largest bending stress would occur proximal to this anchor point on the surface, instead of on the distal toe edge.

A convergence tool was applied and confirmed the singularity with over a 300% increase after three iterations. To seek a solution, a 1mm fillet was applied to the bottom edges of both toe springs, and the frictionless contact settings were reset back to programme control. With these changes, the solver was able to converge upon a solution of 433.25MPa, which midway along the toe spring making the initial contact; see Figure 3.25.

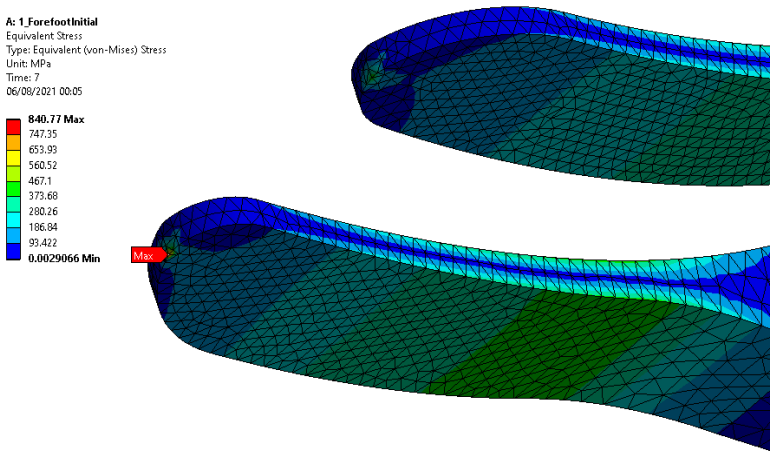


Figure 3.24: Stress plot from the initial simulation of the forefoot mesh study. Notice the same stress singularity at the site of first contact.

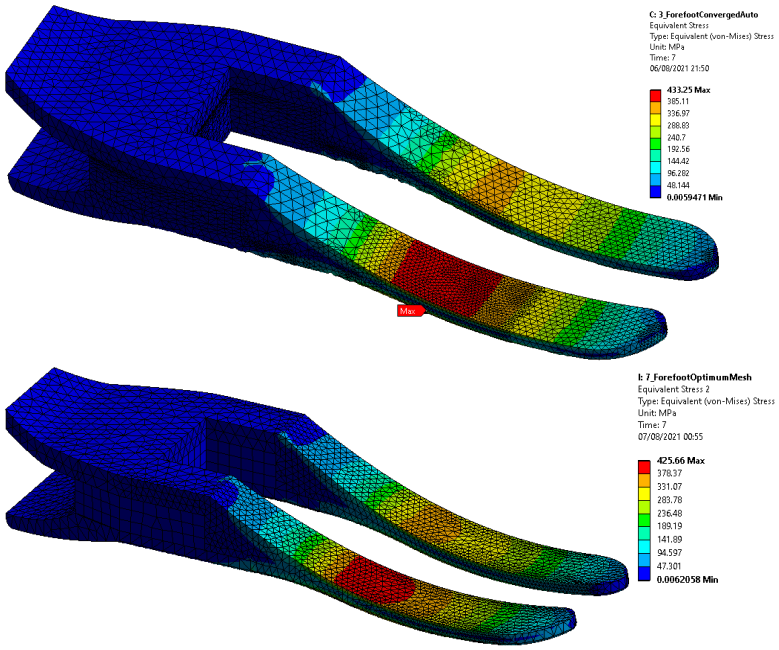


Figure 3.25: Converged solution that had settings left to the solver to determine.

With this success, the next step was to determine an equivalent manual mesh setup to recreate the converged tool solution. A simple decrease to a 3mm element size for the body control on the keel achieved this. However, the solve time for this came to around 8 minutes, a significant increase to the 2m30s solve time for the converged heel solution. The mesh control on body size was replaced with three new control methods. A hexahedron dominant method was applied to the bearing plate, and a tetrahedron method to the heel and keel. To control the keel elements, a face sizing method was applied to the profile and top surfaces of the toe spring portion. This method was set to an element size of 3mm, a growth rate of 1.5, and 3 cells across a gap. With this setup, the stress result produced a converged results within 3 minutes, but with a maximum stress of 425.66MP. Although this is different to the convergence tool solution, the drop is only 2%, which is an acceptable deviation given the approximate nature of FEA models.

3.3.7 Final mesh & contact settings

Through the mesh and contact studies, settings were discovered for the static models that would produce reliable results. For the cyclic models, these boundary conditions are combined as the key components act separately from each other, removing issues of compatibility. The global mesh setting was left unchanged, with no adaptive sizing, and an element size of 5mm. The tetrahedron and hexahedron mesh method controls from the forefoot study were carried over to the heel

Table 3.14: Final mesh settings applied to the foot assembly, used for converged solutions in static and cyclic tests of 22675.

Global Mesh			
Element Order	*Element Size*	*Growth Rate*	*Max Size*
Quadratic	5mm	1.85	20mm
Local Size Control			
Geometry	*Size*	*Curvature*	*Proximity*
Heel Body	3mm	—	3 Cells
Keel Faces	3mm	—	3 Cells
Local Method Controls			
Heel & Keel		10-Node Tetrahedron	
Bearing Plate		20-Node Hexahedron	
Statistics			
Setup	*Elements*	*Nodes*	*Mesh Quality*
Forefoot	56830	94318	0.823
Heel	58612	98477	0.843
Cyclic	76528	127437	0.836

setup with no change in results. These two methods produce the 10-node element SOLID187 seen on the left of Figure 3.26, and the 20-node element SOLID186 on the right. Both are quadratic elements, suitable to recreate the geometry of the prosthetic foot, and handle the large strain deflections.

The summary of all mesh controls and statistics can be found in Table 3.14. Importantly, the mesh quality maintains a respectable value of around 0.83. This statistic is a combined measure of other metrics that quantify the shape characteristics of the elements. Mathematically, it is the ratio of the volume to the sum of the square of the edge lengths. On a scale between 0 and 1, a value closer to 1 is indicative of a perfect geometric shape. Such a shape is ideal for proper discretisation of the model and improved capability to produce a reliable and accurate solution. Beyond the quality, the total element and node count increase is not significant enough to pose concern for excessive solve times; a particular concern with high volume of models ran for a design study.

Table 3.15: Key settings used for the frictionless contacts between prosthetic and force plate. Penetration and stiffness values are for the threshold factor.

Setting	Heel	Keel
Formulation	Augmented Lagrange	
Detection Method	Gauss Point	Projected Contact
Penetration Tolerance	0.1	
Normal Stiffness	1	
Stiffness Update	Aggressive	Normal

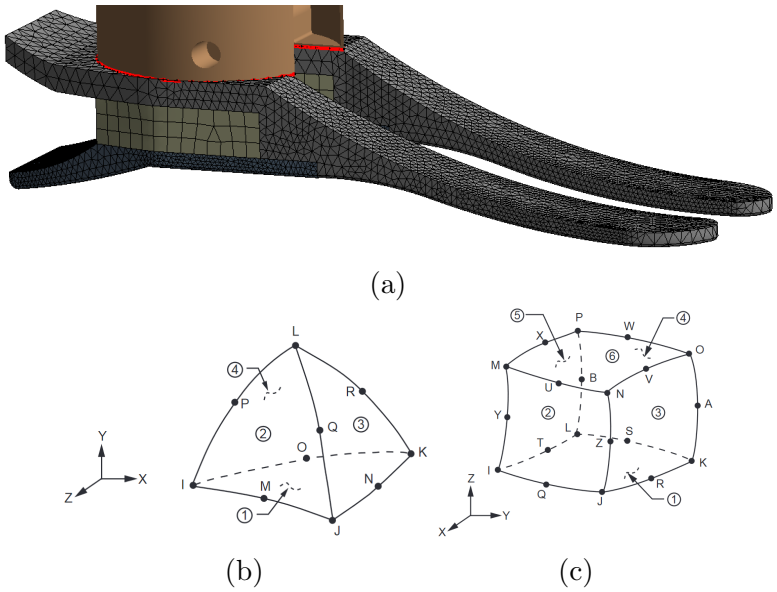


Figure 3.26: Above: The final mesh used for the cyclic studies. Below: The two key elements used in discretising the prosthetic components. On the left is 10-node SOLID187 tetrahedron, and on the right the 20-node SOLID186 hexahedron.

The mesh generated for the cyclic model can be seen in Figure 3.26, alongside schematics for the two main element types that discretise the geometry. Both of these elements are quadratic with mid-side nodes which assist in providing more accurate results. They both also have three translational degrees of freedom within a standard cartesian system.

From the contact studies, it was determined that giving control to the solver to select the optimum values worked the best. However, for purpose of creating consistent results, it was decided that some of these values should be manually defined. This simply involved reading the APDL output script of the simulations to discover what values the solver used. When left to the solver, the penetration and stiffness factor values always defaulted to 0.1 and 1 respectively. Other key settings have been summarised in Table 3.15.

3.3.8 APDL Script: Roll-over Shape

A final addition to the Cyclic model, is a custom APDL script written to extract the rollover shape. The mathematical procedure to generate these shapes is well documented, but to the author's knowledge there is yet to be a FEA model in the literature which directly produces the data points. Traditionally, these shapes are computed from kinetic and kinematic lab data. The centre of pressure data is then transformed into a local coordinate system to produce the rollover shape. However, the setup of the FEA model presented here produces a dataset which is neither one nor the other. Instead, the CoP data is presented along the x-axis, whilst the joint centres remain vertically aligned, and displaces as the foot deforms on the force plate. This data can be seen in the top-left plot of Figure 3.27. In this same figure, the top-right plot is the FEA data transformed into the conventional kinematic progression of the lower leg.

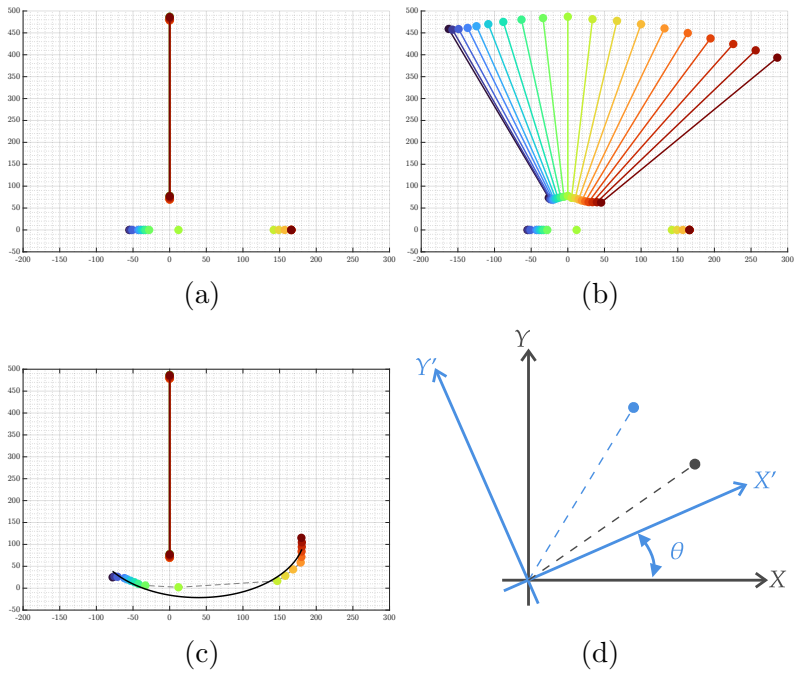


Figure 3.27: Kinematic data transforms. Top-left: joint centre & CoP data from Ansys. Top-right: Ansys data transformed into conventional lab data. Bottom-right: Ansys data transformed into Rollover shape data points (coloured circles). The rollover shape curve is calculated within MATLAB. Bottom-right: the transform of co-ordinates using the series of calculations from 3.8.

The transform matrix used to convert the FEA data into a roll-over shape is the same as used in previous literature [249]. Where COP_x is the x-position of the centre of pressure, and AJC_y is the y-position of the theoretical ankle joint

centre, this equation is given as:

$$\begin{bmatrix} x_{ROS} \\ y_{ROS} \end{bmatrix} = \begin{bmatrix} \cos(\theta_{Plate}) & \sin(\theta_{Plate}) \\ \cos(\theta_{Plate}) & -\sin(\theta_{Plate}) \end{bmatrix} \times \begin{bmatrix} COP_x & -AJC_y \\ -AJC_y & COP_x \end{bmatrix} \tag{3.8}$$

On paper, this is a relatively simple calculation with easily derived variables. However, to achieve the desired autonomy within Ansys, a script was written in the APDL language to scrape the required information from the raw data files. This script can be found in section D.3 of the Appendices.

This code can successfully extract the rollover shape data points, and also includes a modified version of the stiffness script from the static studies, to produce a stiffness curve as a function of the foot length. However, there are limits to the calculations within the APDL script. It is common to fit a circular arc to these points, which provides a smoother approximation of the shape for use in kinematic models. In the literature, the equation for the lower half of a circle is used [250]:

$$y_{circ} = y_o - \sqrt{R_{circ}^2 - (x_{circ} - x_o)^2} \tag{3.9}$$

Where the values x_o and y_o are the centre co-ordinates for the curve, and R_{circ} is the radius of the arc. Following the same methodology as the literature, first approximations of these parameters are found using the least-squares solution of the 2nd order Taylor series expansion of equation 3.9, which is expanded about the mean value of COP_x. These are then fed back into the original shape function which approaches a solution using a non-linear curve fitting algorithm. With the functional limitations of APDL, these final calculations were completed within MATLAB. The fitted curve can be seen in subfigure (c) of Figure 3.27. This has potential to be a useful tool in the design optimisation of prosthetic feet, see Figure 3.28. A parameterised foot created in Solidworks will have the parameters passed into the Ansys model, which through the custom APDL script, controls all operations including the passing of data to Matlab and import of the Matlab fitted curve back into the Ansys parameter set. Ansys can then use the rollover shape in a design optimisation study, however this is just one example, and it is feasible for any prosthetic KPI could be generated in the custom code.

In the following chapter, the prosthetic tool design methodology will be documented. However, as the rollover shape was inconsequential to the goals of that tool, this rollover shape extraction script was not used in the analysis. Despite this, it has been successfully employed in a parallel body of work, which sought to optimise the rollover shape of a printed prosthetic foot [55].

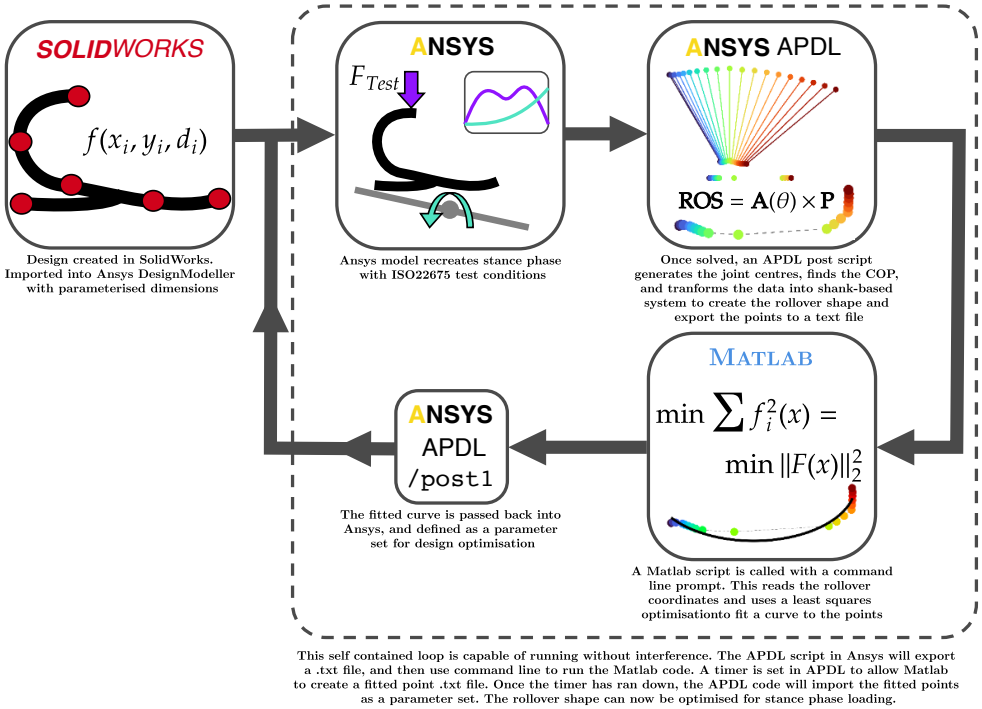


Figure 3.28: A flowchart diagram of the rollover shape optimisation loop.

3.4 Concept ISO 22675 Results

The final section of this chapter will evaluate the simulation results of the Concept design under the newly developed model, based on the test standards of ISO 22675. Firstly, the static test cases, which omitted the mechanical components, and set the housing as a rigid body due to concerns of structural strength. All three levels of loading were attempted for both heel and forefoot setups.

Despite the successful convergence of the heel study, some concerns still remained on whether the peak stress values were indicative of real values, or an FEA artefact due to the stiff geometry. As such, a probe tool was used to discover the stress value on the topside, with the reason being that this is where the stress would accumulate naturally; see Figure 3.29. In this figure, the heel has experience the P3 level of loading, and produced a peak stress of 260.4MPa in the corner. The probe on the upper surface has found the max value to be 130.85MPa. Based on gradation of colour representing the stress, this probe value also appears to occur close to the peak site. Consequently, the St Venant's Principle could be applied here and the stress peak on the first contact point may still not be realistic. The probe result, and its relative closeness in vicinity to the peak value, presents itself as the more reasonable estimate.

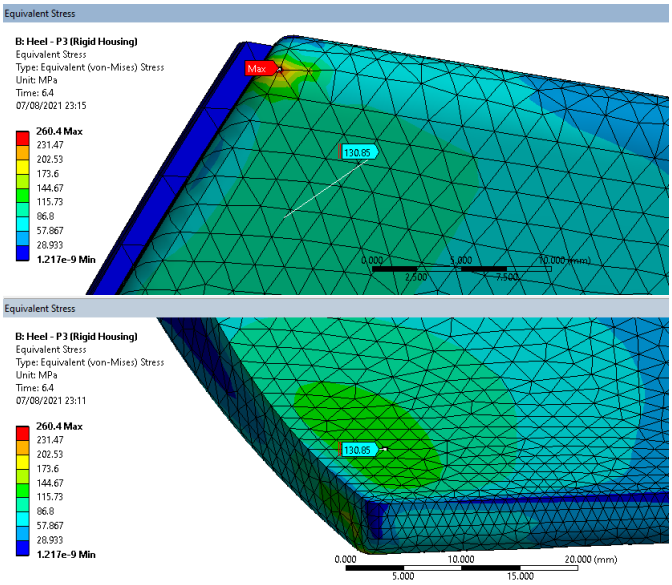


Figure 3.29: Simulation results from the P3 proof load on the heel test condition. Note the concentration of stress and the comparative probe result in the bottom image.

For the sake of comparison, both the heel max and probe have been included in the stress result summary of Figure 3.30. The von-Mises stress is reported as its energy-based approximation is more useful in design analysis than the individual principal stresses. As expected, the increased forces of the sequential loading P-levels causes a linear increase in the peak stress for all reported values. The keel experiences a larger peak stress, which is due to the greater deflection (strain)

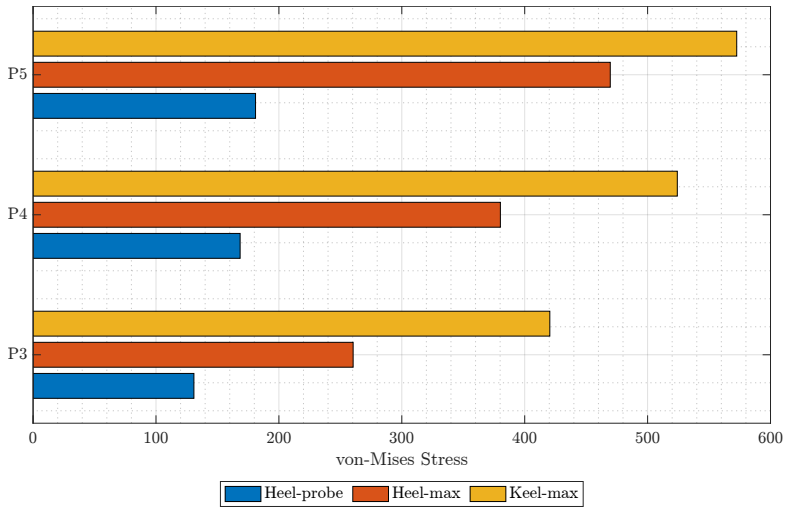


Figure 3.30: Bar chart of von-Mises stress for all three P-levels of the Proof Test. The orange and yellow bars are max values for the heel & keel respectively. A probe was also added to the upper surface of the heel as a comparison value with the concentrated max value; see Figure 3.29.

exhibited by the less stiff geometry. From P3 to P5, the heel experienced maximum deflections of 0.49, 0.58, and 0.63mm. Whereas the keel underwent deflections of 12.95, 16.15, and 17.62mm; an increase of around 2500%. Based on just these proof test results; the heel is clearly an inadequate design to sufficiently dampen the initial contact at heel-strike.

For theses initial studies, the housing was left rigid. To verify the hypothesised structural weakness, the housing structure was made rigid, and the models ran again. The same carbon fibre material properties were applied, with the assumption of quasi-isotropic layup. Under the heel loading condition, the housing structure withstood all levels of loading without experiencing failure. In all levels, the peak of stress occurred on the same corner near the neck of the connection to the pylon, see Figure 3.31.

However, under the forefoot loading condition, the geometry fared much worse and failed at the first level (P3) of loading. The peak stress still occurred at the neck of the pylon connection, but at the front this time. In addition to this, a

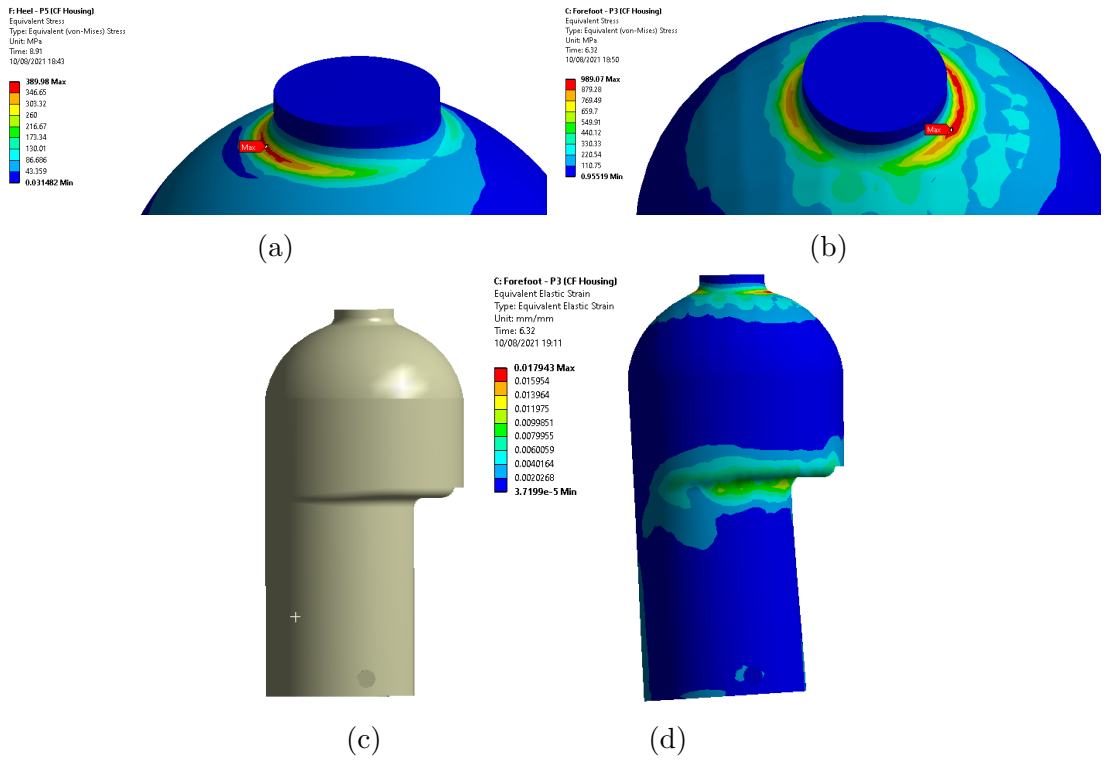


Figure 3.31: A selection of results from studies where the housing component was made flexible. Top: Heel condition P5 loading, with a peak stress on the rear of the neck. Middle: Forefoot condition P3 loading, with the failed peak stress at the front of the neck. Bottom: Comparison of the unloaded geometry on the left, and the buckling strains caused under forefoot P3 loading on the right.

second peak of stress occurred at the front of the housing where the geometry narrows down in diameter and opens up at the front to provide space for the energy limb to deflect. The corresponding strain was large enough to cause significant buckling of the geometry in this area, see Figure 3.31. As a result of this, the Ultimate loading level simulations were disregarded as they would offer no additional information on the design performance. It is evident that the housing component is too thin and lacks the required supporting structure to withstand the magnitude and vector direction, which acts down into the weakest area of the geometry.

3.5 Summary

The work presented in this chapter has led to the establishment of an FEA model that faithfully recreates the boundary conditions for not just static tests, but also the cyclic test, see Figure 3.32. Whereas similar studies have created a transient study from other prosthetic standards [251]. To the authors knowledge, this would be the first model to faithfully represent the full stance cycle from ISO 22675 and extract additional parameters such as the rollover shape. Furthermore, the capacity to replace the ISO force and angle data with personalised experimental data has been demonstrated as a prospective direction to take in future design optimisation work.

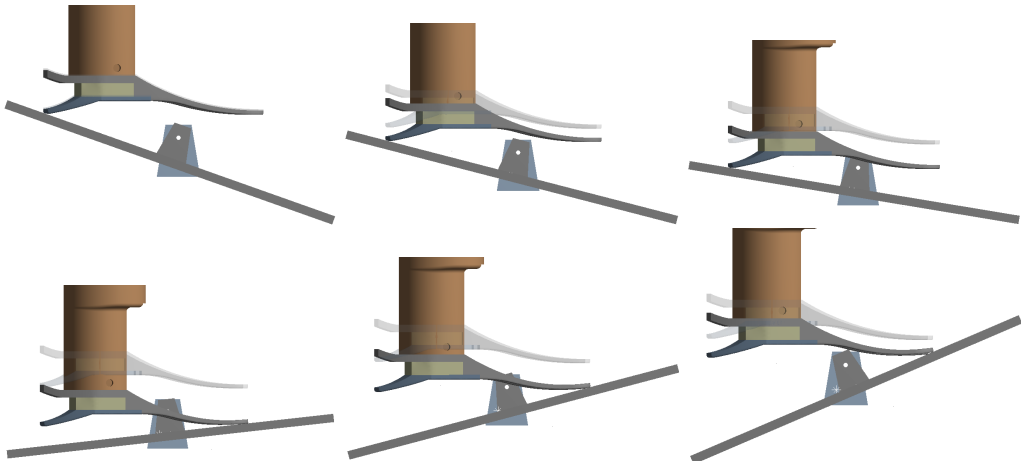


Figure 3.32: A progression of stills taken from the P3 cyclic study. Taken at 30ms, 150ms, 200ms, 350ms, 400ms, and 480ms.

Chapter 4

Prosthetic Design Tool

With the conclusion of the last chapter, a robust FEA model has been created using ISO defined boundary conditions. This model was then used to perform an initial appraisal of the concept design. As the result of those simulations, it was realised that the concept had some significant structural deficiencies and would need to be refined. The work presented in this chapter follows the refinement of the design, utilising various design of experiment tools. A set of design criteria are defined, and each component is reviewed with targets set to achieve these requirements.

4.1 Concept Reflection

The housing and bearing plate are required to hold the spring mechanism components and the shafts they sit on, with the housing also providing vital structural support. The heel spring should provide sufficient shock absorption at heel-strike, whilst the keel spring provides the traditional role of energy storage. Deflection of the keel spring should also be balanced to further facilitate the deflection of the lever, without sacrificing its support function. With the lever sitting in the middle of the keel spring, it creates a split-toe design which assists in the medio-lateral actions of foot inversion and eversion. A selection of key design specs have been defined with quantifiable criteria, see Table 4.1. These are general enough to define the conceptual mechanism, see Figure 4.1b, but also have suitable target values that are used in optimisation studies of specific components.

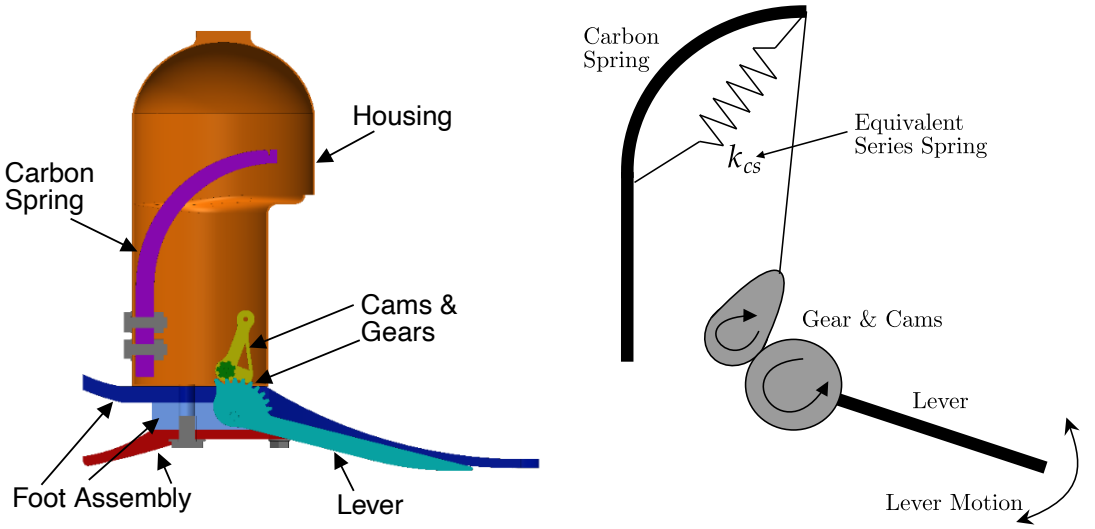
The mass criteria aims to keep the design lightweight to avoid amputees feeling uncomfortable or changing their biomechanics. In the same sense, the foot height and length, and spring diameter criteria have been setup to keep the design compact. Other criteria are all related to the desire performance, with spring energy

Table 4.1: Design specification points for the prosthetic concept revision

ID	Requirement	Acceptance Criteria
PROS-1	Maximum Mass	<1.5kg + 0.5kg
PROS-2	Total Height	<200mm
PROS-3	Total Length	200mm ≤x≤ 300mm
PROS-4	Spring Energy	9J ±3J
PROS-5	Spring Diameter	<60mm
PROS-6	Gear Ratio	>4
PROS-7	Foot Strength	ISO-22675 (P4): FoS>1.5
PROS-8	Toe Deflection	10-15mm
PROS-9	Lever Rotation Angle	$10^\circ \pm 3$

based on papers that have quantified energy patterns of other feet [194]. The gear ratio, toe deflection and lever rotation angle are defined to allow freedom to achieve the spring energy storage, through controlling the amount of spring deflection. Finally, the ISO-22675 Factor of Safety (FoS) requirement at a P4-80kg level, is needed to assure the safety in using this foot on amputees in clinical studies.

From the simulations completed, it can be said that the housing and heel spring have determinedly failed in their respective roles of support and shock absorption. Based on the cross-section view in Figure 4.1, the design is also not compact as there is a significant amount of unused space within the housing. Furthermore,



(a) (b)

Figure 4.1: Section view of CAD model, and schematic of mechanism principle. The carbon spring acts as an effective series spring, which is compressed when the wire connected to the cam is pulled down. This action is generated when the lever is compressed during midstance, causing the gears and attached cam to rotate.

the open front of the housing poses a risk to the mechanical components seizing up due to debris ingress. Thus, a design revision was worked on in order to maintain the desired performance characteristics, whilst solving the issues with the housing.

4.1.1 First Design Revision

Work on the first design revision revolved rearranging the pre-existing components with some modifications to solve the issues identified in the previous subsection. The heel and keel springs were kept separate, a feature that would allow for their individual optimisation to suit the distinct tasks that is required of them. Where the bearing plate was previously used to hold the shafts of the mechanism, in this revision it was removed, and the housing took on that role entirely. Regarding the housing itself, it encloses the mechanism to a higher degree, and is no longer bearing the full weight of the amputee; the keel wraps around and over the top.

Some of the mechanism components were also adapted. The manufacture of the previous lever with an integrated gear would be difficult and expensive, especially as the original plan had proposed a composite material. Considering this, the main gear was separated from the lever and duplicated either side on the same shaft. An additional benefit of this is that the load and shaft torques that pass through the system are now split, reducing the strength requirements of the gear. With this change, the two cams are now reduced to just one, but should still theoretically be capable of fulling the role of pulling back on the composite spring.

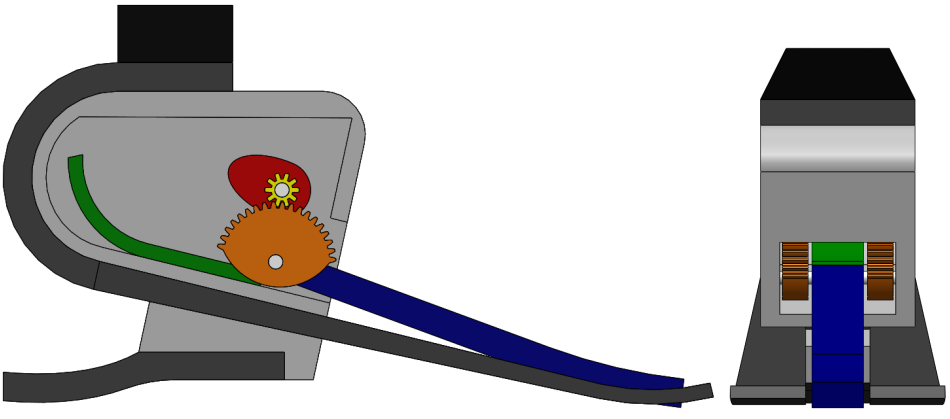


Figure 4.2: Section profile and front view of the first design revision, with the components remaining the same, but the arrangement changing. The keel spring is extended over the housing unit to avoid the structural failure, and there is less of an opening where the lever protrudes.

4.2 Rethinking the Design

Following the first design revision, the decision was made to evaluate the entire design with more constructive scrutiny. With the composite spring being an important component in delivering the stiffness assessment, it made sense to begin the redesign with the key energy storing component.

In the literature, the ankle joint will perform negative work during early stance when it stores energy, which is then released as positive work at push-off. The ankle joint contributes around 60% or 30J of the total mechanical work performed by the lower limb joints [21]. It would be unreasonable to expect the composite spring or a passive mechanism in general to reach the natural energy metrics.

A study on energy properties of passive feet in 1993 found the range of ankle joint energy stored between 8.68-15.22J, whilst the energy released was between 1.81-9.52J [186]. Directly comparing a SACH foot to an ESAR foot revealed the latter produced 9.46J of ankle work compared to the SACH foot's 4.3J [194]. These values of energy return appear to be consistent in the literature. When testing the prototype CESR foot, the researchers compared the novel design against the subject's prescribed foot, and a conventional ESAR prosthetic as a control against user familiarity. The control foot produced 8.9J of push-off work, whilst the prescribed foot and novel prototype fared better with 12.1 and 21.8J of push-off work [43]. This increase in positive work with the prototype foot was beneficial in improving the power and work metrics of the subject's gait.

Before work on the mechanical spring was initiated, the composite spring was analysed with simulations verified with theoretical estimations. The purpose of this brief study was to compare the theoretical energy storage of the composite spring to the literature values and determine a suitable target for the mechanical spring. An explanation of the simulation setup and derivation of the analytical equations can be found in the Appendix Section E.1. Results of these can be found here in Table 4.2.

These results indicate the clearly insufficient design of the composite spring when compared to the values seen in the literature. The simulation results were

Table 4.2: Deflection and strain energy results of the composite spring study

	Deflection (mm)	Strain Energy (mJ)
Simulation	3.32	824
Analytical	2.93	732
% Difference	11.08	11.17

found to be invariant to the mesh element sizing, which suggests the differences are likely due to the simplified calculations used in for the analytical results. With this cursory study completed, attention shifted towards the design of the mechanical spring.

4.2.1 Energy Storage: Spring

Designing a helical compression spring from scratch can be approached from various starting points. In many cases, the spring designer will know the operating loads and will parameterise the spring material properties and dimensions to accommodate these working loads. For this particular use case, a targeted range amount of strain energy stores was the objective. However, this is not a component that can be easily optimised with algorithmic methods, due to the the number of input parameters. The time taken to code such a method would quickly hit a diminishing return, and so it was decided to create a design spreadsheet to organise the calculations and assess the variable design options.

To assist with this process, a selection of mechanical design books were referenced for the calculations and guidance [252, 253, 254]. One of the first key decisions was on the choice of material. In the literature the options are mostly a variation of spring steel or steel alloy, with recommendations pointing to a particular grade known in the industry as Music Wire. The properties of this material were taken from the book from which most of the calculations were based [254]; these can be seen in Table 4.3.

The other key decision to be made was end type of the spring which would define the formation of the coils at the spring ends. Closed and ground were chosen as this creates a better transfer of load due to the zero-degree helix and flat faces of the last coils.

With the operating loads unknown, it was decided that the design of the spring would be primarily based on the geometry. This setup would thus require the following input parameters:

Table 4.3: Material properties used for the Music Wire, which is classified as ASTM A228. This material cannot be easily sources in the UK and so the eventual supplier used EN 10270-1 Hard Drawn Steel with equivalent properties.

Wire Diameter d (mm)	Material Constant B (MPa.mm)	Exponent q	Young's E (GPa)	Shear G (MPa)	Density kg/mm^3
0.1 - 6.5	2211	0.145	203.4	82700	7.75E-06

- Hole Diameter, D_{Hole}: defines the cross sectional area in which the spring is enclosed
- Allowance, a: a buffer dimension between the outer spring diameter and D_{Hole}
- Wire Diameter, d: size of the spring wire
- Free length, L_0: Length of the spring when uncompressed
- Active Coils, N_a: Number of active coils when the spring is in use

From these inputs, the mean spring diameter D_{sp}, solid length L_s, Pitch p_{sp}, total coils N_t, and the spring index $C_{sp} = d/D_{sp}$ can all be calculated. This spring index value is used in calculating a correction factor for the shear stress under load. If a section cut is made through the spring when under load, the cut portion of the wire would contain a direct shear force and a torsion, which when super-positioned can define the max shear stress as:

$$\tau_{max} = \frac{Tr_w}{J} + \frac{F_{sh}}{A_w} \tag{4.1}$$

Subbing in values of $T = F_{sh}D_{sp}/2$, $r_w = d/2$, $J = \pi d^4/32$, $A_w = \pi d^2/4$, and the spring index C_{sp} allows for Equation 4.1 to be rearranged to:

$$\tau = K\frac{8F_{sh}D_{sp}}{\pi d^3} \tag{4.2}$$

Where K is the curvature correction factor. In the current form, equation 4.2 is based on the wire remaining straight at the cross section cut. But the curvature of the wire means the stress is slightly larger on the inside and to account for the variation, the correction must be applied. The literature provides a small selection of different correction factors. In these calculations, the Bergstrasser factor is used:

$$K = K_B = \frac{4C_{sp} + 2}{4C_{sp} - 3} \tag{4.3}$$

Before moving onto check the stress and energy characteristics, a few geometry checks are made. The first is to check that the expansion of the compressed spring does not impact on the sides of the enclosing chamber:

$$D_{exp} = \sqrt{D_{sp}^2 + \frac{p_{sp}^2 - d^2}{\pi^2}} + d \tag{4.4}$$

The other check gives the spring the same consideration of a column under

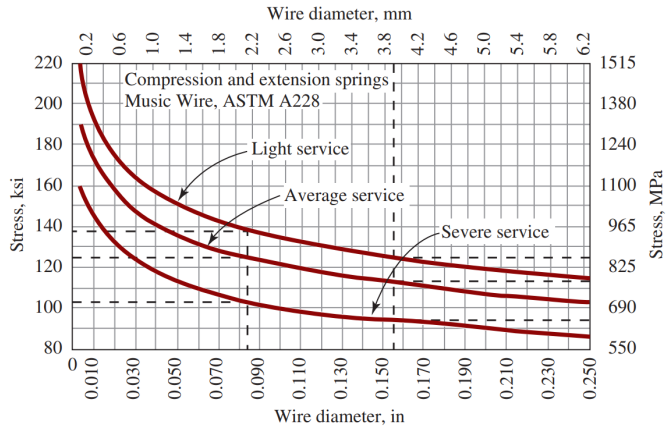


Figure 4.3: Figure taken from a reference book, plotting the wire diameter against tensile strength on a logarithmic scale [253].

vertical load, and determines the critical length to ensure stability and avoidance of buckling:

$$L_0 < \frac{\pi D_{sp}}{S_{ec}} \times \sqrt{\frac{2(E-G)}{2G+E}} \tag{4.5}$$

The ultimate tensile strength of springs can vary to a large degree and can only be defined once the wire diameter has been decided. If the wire size and tensile strength are plotted on a logarithmic scale, the relationship is almost completely linear, see Figure 4.3. This relationship can be defined by the following equation which uses quantities from Table 4.3:

$$S_{ut} = \frac{A_w}{d^q} \tag{4.6}$$

Various research and experimental data analysis has shown how post-processing and effects like spring set can affect the values for maximum shear stress in the wire. It was decided to take the most conservative calculation to ensure the operation of the spring would remain safely with the material capabilities. This led to the maximum allowable shear stress being given as $\tau_{max} = 0.45 S_{ut}$.

Castigliano's theorem can be used to define the total strain energy held in the spring, as well as the deflection and thus the spring rate. Beginning with the total strain energy, which is composed of a torsional and shear component, given as:

$$SE = \frac{T^2 l}{2GJ} + \frac{F_{sh}^2 l}{2A_w G} \tag{4.7}$$

The same substitutions are made here as when defining the shear stress equa-

tion 4.2, but with the addition of $l = \pi D_{sp} N_a$. This gives the following definition:

$$SE = \frac{4F_{sh}^2 D_{sp}^3 N_a}{d^4 G} + \frac{2F_{sh}^2 D_{sp} N_a}{d^2 G} \tag{4.8}$$

The total deflection can then be derived from the basic principle of Castigliano's theorem, taking the partial derivative of strain energy SE with respect to force F_{sh}:

$$y_{sp} = \frac{\partial SE}{\partial F_{sh}} = \frac{8F_{sh} D_{sp}^3 N_a}{d^4 G} + \frac{4F_{sh} D_{sp} N_a}{d^2 G} \tag{4.9}$$

However, the term on the right is negligible in comparison to the left and can be removed. This allows for a simple rearrangement to find the force required for a given deflection as:

$$F_{sh} \doteq \frac{y_{sp} G d^4}{8 N_a D^3} \tag{4.10}$$

Equations 4.2, 4.3, 4.8, and 4.10 can be used to calculate the shear stress, energy, and force created when a spring is deflected. The input parameters are the spring dimensions and material properties. It was decided to base the maximum of these calculated values on a safe proportion of the spring solid condition.

The spring solid condition is when the spring is compressed fully so that all coils are touching. This is a highly unfavourable condition to operate the spring to, but is useful in determining the maximum characteristic values which can then be adjusted based on a clash allowance, which is the operating maximum defined as a proportion of the spring solid condition. Literature recommends this clash allowance should be a minimum of 10% of the solid length for increased operating lifetime. It was therefore decided to set this allowance to 20% for additional assurance.

All input parameters, calculations and outputs were implemented into an Excel spreadsheet to check the calculations. It was stated before that optimisation of these parameters using a response model would be time consuming to setup with limits and then verify. There are three outputs or objective functions: maximising the strain energy, minimising the force, and minimising the shear stress. To explore the sensitivity of these outputs with regards to dimensions, the spring was modelled in MATLAB Simulink®.

The inputs were four geometry parameters. Their upper and lower bounds were selected with the intention of exploring the full design space including any extremes, but the values should still be manufacturable. Spring mean diameter was given bounds first. It was decided to go 10mm above the criteria in Table 4.1 so that the extremes would be captured in the parameter set. Other parameters had

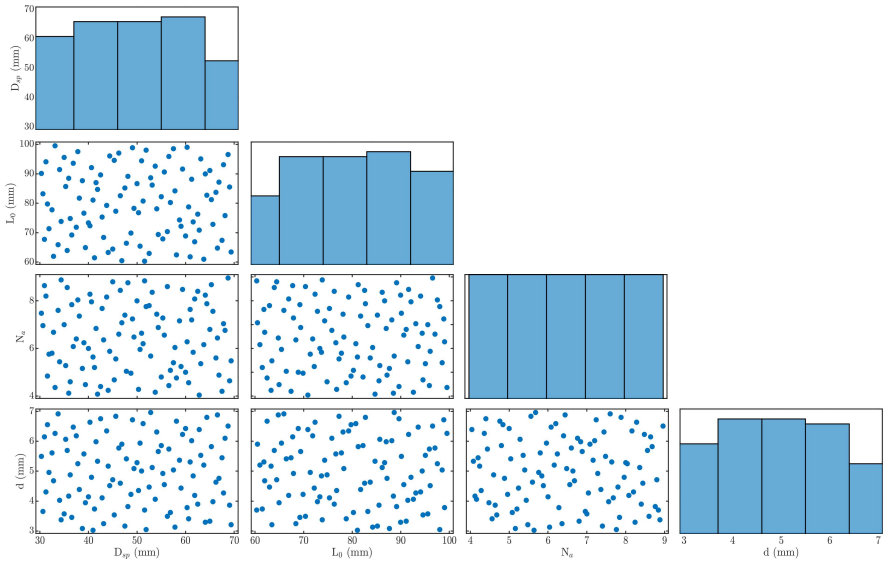


Figure 4.4: Scatter and Histogram plots of the Simulink spring parameter set.

their limits selected based on sensible ranges with respect to the spring diameter. See the following list of parameters and bounds:

- Spring mean diameter, D_{sp}: 30 - 70mm
- Spring wire diameter, d: 3 - 7mm
- Number of active coils, N_a: 4 - 9
- Spring free length, L_0: 60 - 100mm

These parameters were given a uniform distribution as the bounds are both fixed points and the so range is known. A uniform distribution is also desired for highly systematic space-filling when the parameter set is generated. Simulink offers several sampling methods to populate the parameter set, each of which generates random samples of parameter values. By default, the method is set to simple random sampling, but this was changed to a Halton quasi-random sequence with scrambling turned on. With this method, the quasi-random sequence is more efficient at generating a uniform space-filling design space. A parameter set of 100 points was created with the above settings, see Figure 4.4 for a visual representation of the parameter distributions.

This parameter set was then computed within the Simulink model and the resulting design space can be seen in the collection of plots in Figure 4.5. Of the three outputs, the shear stress has been explored the most by the parameter sets. There appears to be some similarity between the applied force and strain energy, possibly due to the representation of material properties in their respective equations.

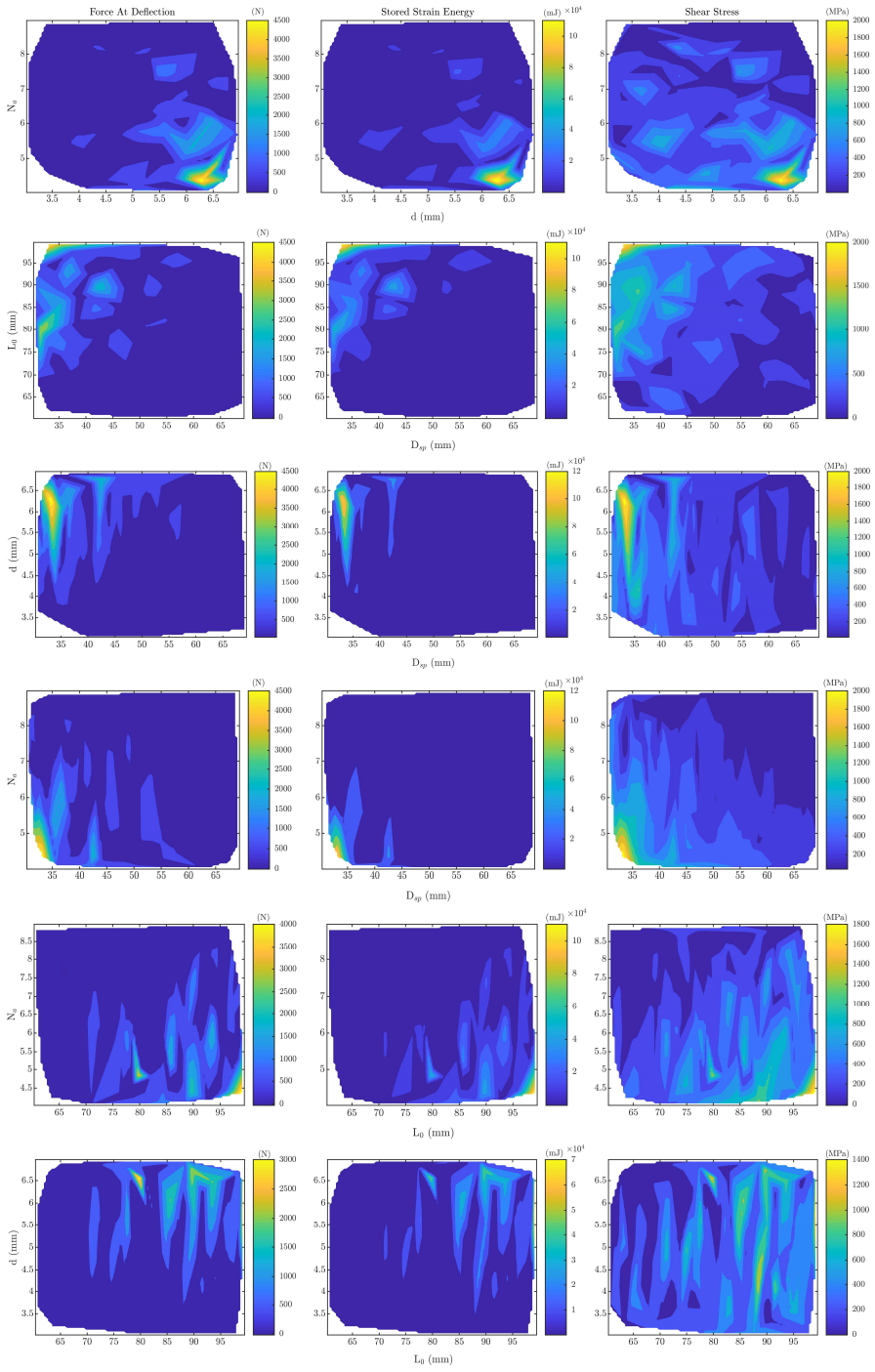


Figure 4.5: Contour plots of the Simulink parameter design space. Each row is a different pair of parameters, and each column is an output from the model.

To assess the parameter sensitivity, a correlation analysis was performed. Due to the uniform parameter distribution, non-linear trends in the results data and presence of outliers, a Spearman rank correlation type was used. As there can be an issue with standard correlation mixing effects of different parameters, a partial correlation method was also employed to remove the effects of other parameters; see Figure 4.6 for a tornado plot of these correlation statistics.

The mean diameter of the spring has the strongest effect with a negative correlation of all three outputs as it increases in size. This makes sense as it is frequently in the numerator of the equations and raised to a power. Its effect is to reduce the amount of deflection for any unit length of a spring, and in doing so will lower the strain energy and shear stress. Despite not directly featuring in the output calculations, the free length L_0 has a comparatively strong positive correlation with the outputs. It is likely this is because a longer spring can accommodate more deflection, which would increase the strain energy stored and also the force and associated shear stress.

The number of coils also has a negative strong correlation with all three outputs, as increasing the coils creates less space for them deflect before touching. Interestingly, the wire diameter has a negative correlation with the shear stress, but positive with the other two outputs. A thicker wire will dissipate a portion of the stress but will also require more force to deflect and store more strain energy. The correlations for strain energy and shear stress are weaker when compared to the stronger parameters, despite the parameter being raised to a power of at least 2 in all output equations. It is clear that this parameter therefore has more room for adjustment, with other parameters being able to moderate its effect.

With the knowledge from this study, the design spreadsheet was revisited to adjust the parameters and seek a satisfactory performance. Based on the literature which revealed most ESAR feet store around 8-9J, it was decided that a spring

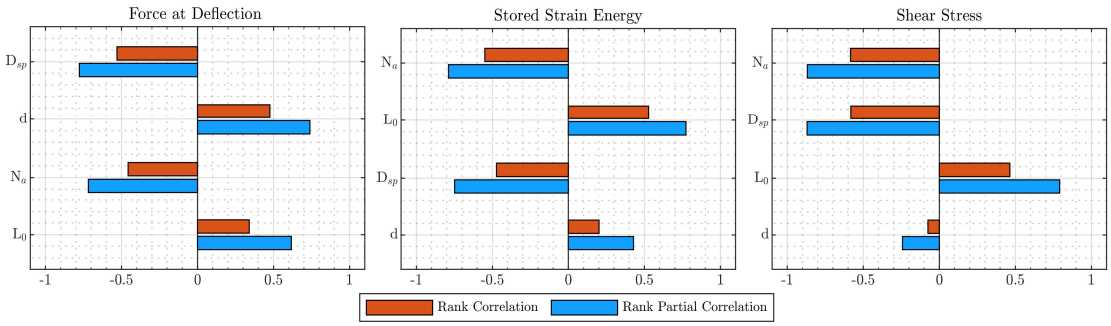


Figure 4.6: Results of the Spearman Ranking correlation, generated from the Simulink parameter study.

Table 4.4: Table of final dimension parameters used to shape the spring, and the characteristics at spring solid condition as the worst operating level and the values at safe operating limit of 20% clash allowance.

Dimensions		
Hole diameter, D_{hole} (mm)		60
Allowance, a (mm)		5
Wire diameter, d (mm)		5
Mean spring diameter, D_{sp} (mm)		50
Active coils, N_a		6
Free length, L_0 (mm)		80
Spring rate, k (N/mm)		8.615
Characteristics		
Metric	Spring Solid Condition	Clash Allowance, 20%
Deflection (mm)	40	33.33
Force (N)	344.58	287.15
Energy stored (mJ)	6926.13	4809.81
Shear stress (MPa)	398.42	332.02
Factor of safety	1.98	2.37

that could deliver an additional 50% of this range would satisfy the initial design requirements. The final design parameters and associated characteristics can be seen in Table 4.2. Under the operating condition with factored clash allowance of 20% the spring can store just short of 5J in strain energy within a safe operating range posing a factor of 2.37.

The last remaining performance metric to account for is the expected life of the spring. It is difficult to calculate this without sufficient experimental data; a resource that suppliers and manufacturers have in abundance. Several national companies were contacted with the specifications detailed in Table 4.4. One of these companies provided a Goodman diagram for the specified design, which predicted a fatigue life of 10^7 cycles, see Figure 4.7.

A different supplier was eventually chosen due to the affordable cost. The design remained unchanged, except for a post-processing option of shot-peened and oiling, which improves the endurance of the spring.

4.2.2 Reconsidering the Cam

The initial concept design was to include a cam that would pull down on the wire connected to the composite spring, using a specifically customised profile to ensure a smooth return of energy. However, the shape of this cam was determined through

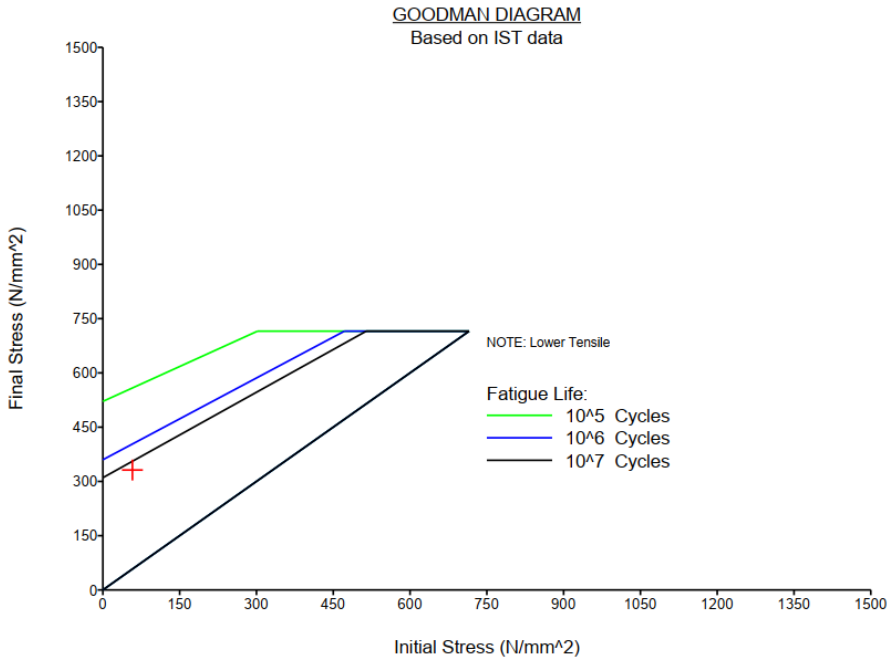


Figure 4.7: A goodman indicating the fatigue life of the spring for three different life cycle levels. The red cross is the operating position of the designed spring, which falls within the fatigue life of 10^7 or 10,000,000 life cycles.

maximising the translation of the wire through the eccentricity from axle centre to cam tip. To aid the redesign two handbooks were referred to: Cam Design Handbook by H.A. Rothbart [255], and Cam Design & Manufacturing Handbook by R.L. Norton [256].

As the composite spring has been replaced with a helical compression spring, the actuation required became a simple cam, translational follower system. Usually, defining the speed and time characteristic requirements is the first step in designing a cam. This is so that the cam dynamics can be synced with other components in the system. However, a preliminary investigation can be made by establishing the motion constraint and evaluating the metrics. In many design cases the cam is created for a full 360° profile, but in the initial concept the cam was to be limited to a reversible 60° rotation, making the cam a simple rise-dwell type. The 60° value was selected under the assumption that the lever would rotate around 15°, which would be increased by the gear ratio of 4.

The shape of a cam is created by wrapping the displacement around a base cylinder as a function of the cam rotation, see Figure 4.8. From this the velocity, acceleration, and jerk characteristics of the cam are derived. A fundamental law of cam design is often employed to ensure smooth operation; the cam-follower function must be continuous through the first and second derivatives of displacement

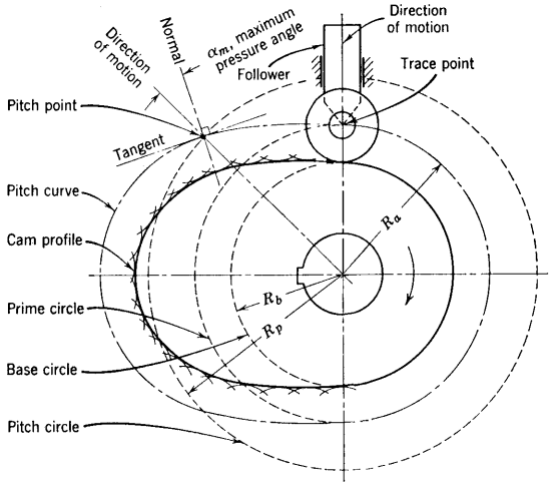


Figure 4.8: Cam design nomenclature. The base circle forms the foundation of the design, from which the displacement profile is wound around.

across the entire interval. The acceleration curve is directly proportional to the stress and inertia forces, in addition to the sharpness of the cam surface, making it an important characteristic to consider. As jerk is the derivative of the acceleration, any discontinuities in this function will cause infinite spikes. However, the operation speed of the proposed cam is significantly slower than those to which the rule applies, and as such, allowances can be made.

To build the displacement plot, a series of piecewise function are employed to describe motion over rotational periodic segments. As it was previously mentioned, continuity over the second derivative can be important, so the ideal functions to use are either polynomials or trigonometric. A selection of seven formulae were used to derive the characteristic curves: Simple Harmonic, Cycloidal, Double Harmonic, Modified Trapezoidal, Modified Sinusoidal, and 3-4-5 & 4-5-6-7 polynomials. Equations 4.11 through to 4.14 are the motion equations for displacement, velocity, acceleration, and jerk of the simple harmonic form.

$$y = \frac{h_r}{2}\left(1 - \cos\frac{\pi\theta_c}{\beta_c}\right) \tag{4.11}$$

$$y' = \frac{h_r\pi}{2\beta_c}\sin\frac{\pi\theta_c}{\beta_c} \tag{4.12}$$

$$y'' = \frac{h_r\pi^2}{2\beta_c^2}\cos\frac{\pi\theta_c}{\beta_c} \tag{4.13}$$

$$y''' = \frac{h_r\pi^3}{2\beta_c^3}\sin\frac{\pi\theta_c}{\beta_c} \tag{4.14}$$

All forms of the equations use the same parameters, where h_r is the total rise,

β_c is the cam angle at total rise, and θ_c is cam angle of rotation; both angles use radians. Each form of the motion equation set was defined in a MATLAB script and the motion plots generated using $h_r = 33mm$ for the spring deflection, and a corresponding angle $\beta_c = 1.05rads$. These plots can be seen in Figure 4.9.

The two harmonic series had unfavourable accelerations resulting in high stresses at either the start or end of the profile. The most favourable plots were that of the modified trapezoidal and sinusoidal, it was decided to evaluate the latter as the initial choice. The profile was created as a cad model to assess whether it would fit within the compact redesign. A recommended piece of software was CamTrax64 (Camnetics Inc.), a standalone program in which the characteristic curves are created and then exported to Solidworks as a full model.

This CAD model was then imported into an assembly with an early revision of the new spring housing. Unfortunately, it was immediately apparent that the required cam displacement profile would be too large to fit within the new design scope. The overall dimensions were around 60mm in width and height, with a diagonal of 67.6mm, see Figure 4.10.

It was evident that the low rotational angle, combined with the relatively

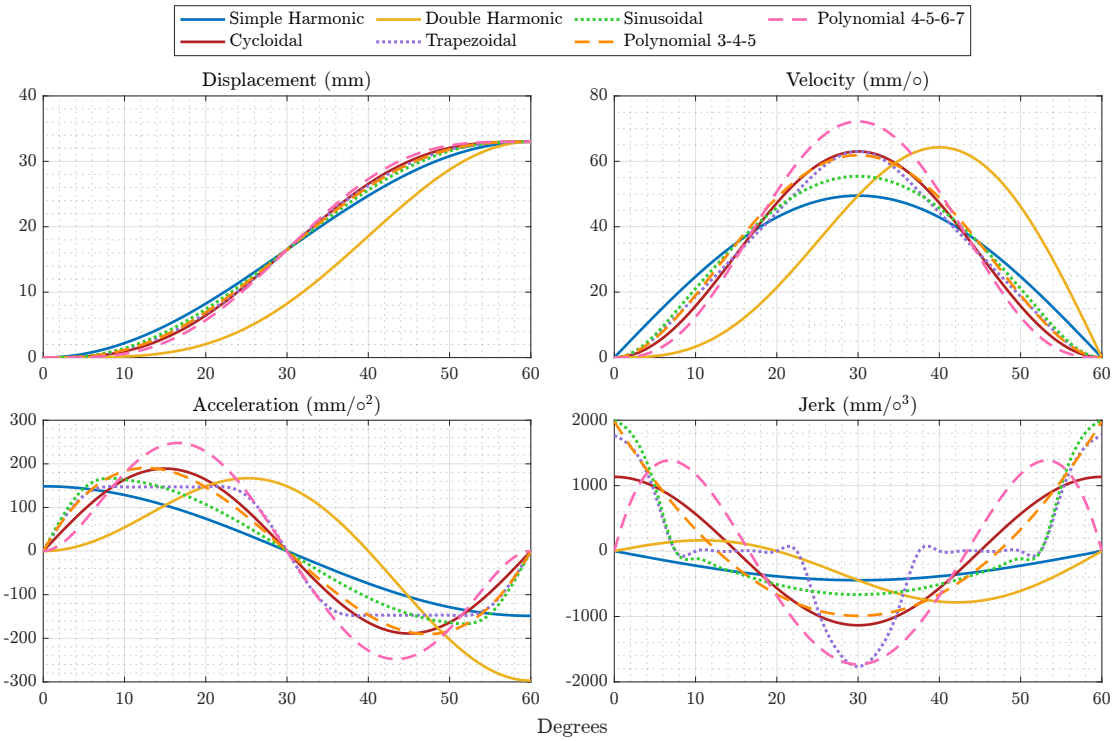


Figure 4.9: Plots of various cam characteristics, generated using equations from [255]. These plots provide preliminary information on cam performance metrics before going into the design stage.

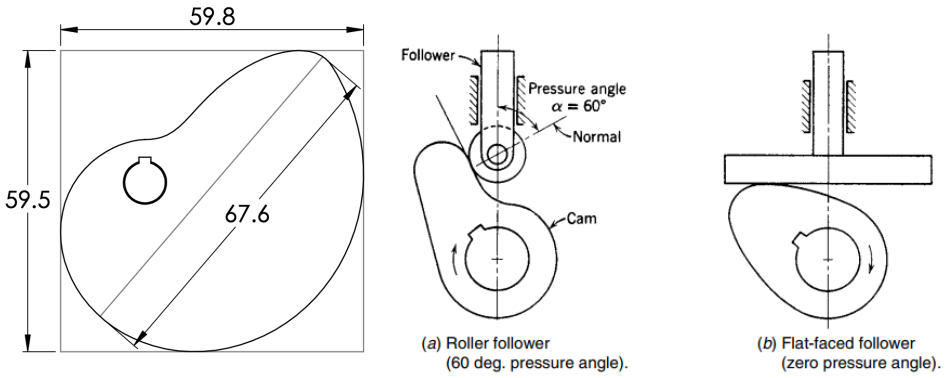


Figure 4.10: Generated cam profile using the sinusoidal equations within the CamTrax64 software built by Camnetics Inc.

large displacement required too sharp a curve. This resulted in an elongated cam shape, which did not have the required space to achieve its displacement. Furthermore, such a steep rise with a cam can create a pressure angle higher than design recommendations. The outcome of this is an increased probability of the follower becoming stuck, although this may not be an issue if a flat-faced follower is used, see Figure 4.10.

Regardless, the cumbersome shape required an alternative approach, which led to considering the basic kinematics of the cam system and attempting to replicate it with a suitable replacement. The main objective of the cam was to convert rotational motion to reciprocating motion to actuate the helical spring; a process found in a wide range of mechanisms such as engines. It was decided that a link pair could accomplish the same objective as the cam, whilst doing so within a confined workspace. The development of this system can be seen in the later Section 4.3.1.

4.2.3 Shaping the Foot with N.U.R.B.S

The simulations in completed in section 3.4 revealed the inadequacies of the concept foot structure. As the mechanism was undergoing a redesign, a new approach was needed to shape the composite foot spring structures. In the concept, these components were roughly shaped to form the general structure of passive feet in the sagittal plane, but with some adaptations to accommodate the components.

A key objective of this new design process would be to parameterise the profile so that the shape can be optimised using design studies. This would allow for enhanced rollover parameterisation using the custom APDL script, whilst ensuring the structure can withstand the ISO strength tests.

A similar design methodology has been detailed in the literature review section 2.2.3, where the MIT research group used Bezier curves to optimise their foot to the LLTE method [3]. The Bezier curve is form of spline, which themselves are parametric curves that are constructed from a series of piecewise polynomials. The shape of the Bezier curve is defined by both a series of control points which create a polygon the curve sits within, and a degree which helps determine the depth of the curve. Generation of the line itself is governed by a recursive algorithm that uses blending functions, which for the sake of brevity will not be detailed here; this is expertly covered in the book "Bezier and B-Spline Techniques" [257].

Bezier curves were only the first stage in the mathematical derivation of spline curves. It can interpolate the end control points, and then approximate a curve to fit between the control polygons. However, a more complex shape can be difficult to define without sacrificing the smoothness of the curve between the polynomial sections. The smoothness of a spline can be defined by grades of continuity based on the derivatives:

- C^0 - Zeroth: requires only that the segments meet at the nodes
- C^1 - Zeroth & First: the first derivative must be differentiable
- C^n - Zeroth through to $n-$th derivative must be continuous

A Bezier curve can achieve C^1 continuity but lose significant local control at C^2 due to the increased number of control points added. B-splines were mathematically derived to solve this issue, being adept are generating long continuous curves and surfaces due to the improved local controls. The following sections will provide an overview of these B-spline basis functions. Again, for the sake of brevity, a full explanation should be sought within these two references [257, 258].

B-spline Basis Functions

There are a few different methods to define the B-spline functions, here the focus will be on the use of the recursive formula as it is best suited to adaptation into a coded program. Basis splines are constructed with piecewise polynomials, which are divided into sections at points designated as knots, see Figure 4.11.

These knots u_i are defined as a series of non-decreasing real numbers, $u_i \leq u_{i-1}, i = 0, ..., m-1$, within a knot vector $U = \{u_0, u_i, ..., u_{m-1}, u_m\}$ where m is the number of knots. The knot sequence and degree p_d are used to define the domain $0 \leq u \geq 1$ divided into the knot spans.

The zeroth function basis function is a step function which is equal to zero at all points except for the span it is computed on:

$$N_{i,0}(u) = \begin{cases} 1 & \text{if } u_i \leq u < u_{i+1} \\ 0 & \text{otherwise} \end{cases} \tag{4.15}$$

The ith basis function of p-degree (order $p_d + 1$), is given as:

$$N_{i,p_d}(u) = \frac{u - u_i}{u_{i+p_d} - u_i} N_{i,p_d}(u) + \frac{u_{i+p_d+1} - u}{u_{i+p_d+1} - u_{i+1}} N_{i+1,p_d-1}(u) \tag{4.16}$$

Thus, the generation of a set of basis functions needs a knot vector, U which helps shape the curve, and a degree, p_d. When a spline is called uniform, the spacing of the knots is even, and non-uniform specifies uneven spacing. A few properties are worth mentioning here, as they help to construct the code to generate the required spline functions for the given knot span and degree. Firstly, the functions generate a truncated triangular table, as seen in Figure 4.12(a). A local support property exists such that $N_{i,p_d} = 0$ if the knot u exists outside the span $[u_i, u_{i+p_d+1})$, and this can be visualised in Figure 4.12(b) for basis function $N_{1,3}$. Likewise, for any knot span $[u_j, u_{j+1})$, at most p_d+1 of the basis functions are nonzero, which can be seen in Figure 4.12(c) where for the span $[u_3, u_4)$ the function $N_{3,0}$ is the only nonzero zeroth-degree function.

These properties are useful in reducing the number of computations in calculating the basis functions of equations 4.15 and 4.16, and thus been incorporated in the algorithm code.

The equation to generate a B-spline curve is given by:

$$C(u) = \sum_{i=0}^{n} N_{i,p_d}(u) P_i \tag{4.17}$$

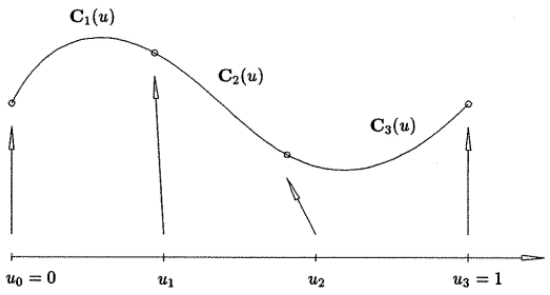


Figure 4.11: A polynomial cubic curve composed of three sections $C_i(u)$, with end points defined by a series of knots u_i [258].

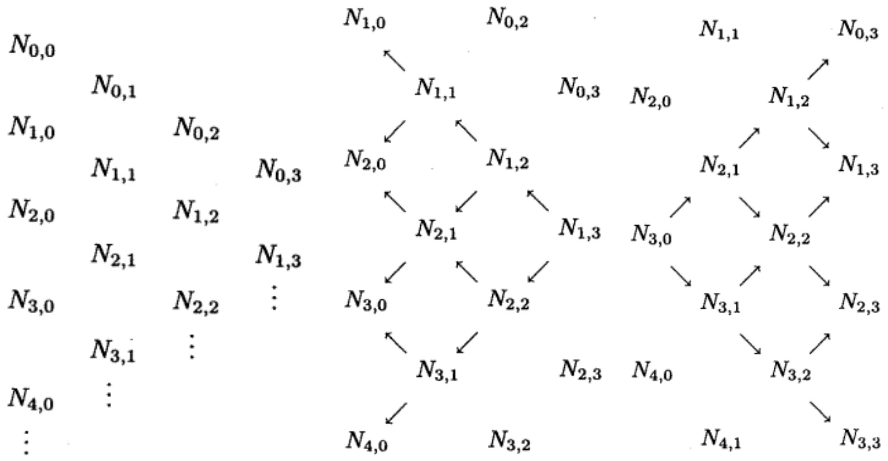


Figure 4.12: Diagrams of the truncated triangular table of basis functions used to explain some important properties in the main text [258].

Where P_i is a control point which is used to control the polygon the B-spline curve is shaped by. This is a property of B-splines and bezier curves, also known as the convex hull property. The function $C(u)$ is the piecewise polynomial curve, where the various parameters are related through the statement, $m = n + p_d + 1$.

Definition of NURBS

The intention in using these curves is to generate a smooth curve which interpolate through a series of defined points. Such a goal requires the use of rational B-splines, specifically NURBS. These are composed in a similar manner to the B-splines, but with the addition of a weight vector, which provides additional control in pushing or pulling the resulting curve to or from the control points. The equation for a NURBS curve is given as:

$$C(u) = \sum_{i=0}^{n} R_{i,p_d}(u) P_i \tag{4.18}$$

Whereas before, the curve is defined with the basis functions $N_{i,p_d}(u)$, these are now replaced with the rational form $R_{i,p_d}(u)$; where the function R_{i,p_d} is:

$$R_{i,p_d}(u) = \frac{N_{i,p_d}(u) w_i}{\sum_{i=0}^{n} N_{i,p_d}(u) w_i} \tag{4.19}$$

The vector $\{w_i\}$ are the weights, which work as scalar values larger than zero. If they are set to 1, then they have no effect. One of the key benefits to the NURBS curves is a property known as local approximation. If a control point is moved or the weight changed, then the effects remain local to that specific area.

Thus, the curve can be finely controlled with these parameter values.

To interpolate the NURBS curve with a series of defined points, a few additional steps are required. If the set of points are defined as $\{Q_k\}, k = 0, ..., n$, which are then each assigned a parameter value $\{u_k\}$, and if a suitable knot vector U is selected, then the following system of equations can be set up as:

$$Q_k = C(\bar{u}_k) = \sum_{i=0}^{n} R_{i,p_d}(\bar{u}_k) P_i \tag{4.20}$$

The control points are the unknowns, which are needed to define the polygon to which the interpolating curve will fit to. A suitable set of parameter values, $\bar{u}_k$ and knot vector, U need to be determined first though. For this, the literature recommends the centripetal method, which begins with defining a parameter, d using the interpolation data points:

$$l_c = \sum_{k=1}^{n} \sqrt{|Q_k - Q_{k-1}|} \tag{4.21}$$

Then specifying the extremes of the parameter vector as $\bar{u}_0 = 0$ and $\bar{u}_k = 1$, the other values in the vector can found as:

$$\bar{u}_k = \bar{u}_{k-1} + \frac{\sqrt{|Q_k - Q_{k-1}|}}{l_c}, \text{ where } k = 1, ..., n-1 \tag{4.22}$$

Finally, an averaging technique is used to determine the knot vector, stating $u_0 = ... = u_{p_d} = 0$, and $u_{m-p_d} = ... = u_m = 1$

$$u_{j+p_d} = \frac{1}{p_d} \sum_{i=j}^{j+p_d-1} \bar{u}_i, \text{ where } j = 1, ..., n - p_d \tag{4.23}$$

MATLAB program method

With the series of equations define across the previous small sections, a series of MATLAB scripts were put together and controlled via a master file, to produce a NURBS curve defined by a series of data points, a degree, and weight vector. The order operation is listed below, and the scripts themselves can be found in Appendix section B.1

1. The **Master** script takes inputs listed below and passes them through the function files to produce and plot the NURBS curve.

    - Data points array, D

- Spline degree, p_d
- Weight vector, w

2. The data points are passed into the **PVector.m** function to generate the parameter vector, using equations 4.21 and 4.22.

3. This parameter vector is then passed into the **KVector.m** function to create the knot vector, using equation 4.23

4. The two vectors are then both passed into a **ControlPoints.m** function which calculates the basis function matrix using the recursive algorithm of equations 4.15 and 4.16. Within the same function file, the system of linear equations 4.20 is rearranged to find the Control points through Gaussian elimination.

5. Finally, the knot vector and control points are passed into the **Nurbs.m** function to generate the curve using equations 4.18 and 4.19.

Generated NURBS curves

An example of simple curve generated with an array of five co-ordinates in the x and y axis can be seen in Figure 4.13. Note how the curve strongly follows the convex hull property, passes through all data points, and retains its smoothness.

The same MATLAB program was then used to define the curves of composite springs used in the second design iteration. There are three of these; a keel spring, a heel spring, and a base spring connecting them both and providing more consistent contact with the ground.

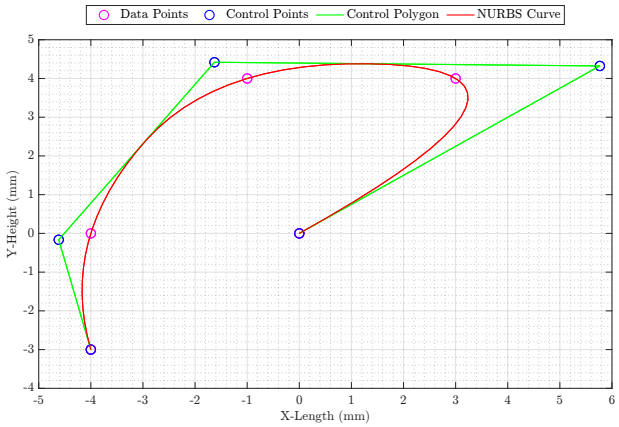
The master script currently prints plots of the generated curves, whilst the control point vectors that are used to parametrise the curve in SolidWorks are simply taken directly from the MATLAB workspace. It is the intention that once the prosthetic optimisation process is fully operational, the control point vector will be extracted as a comma-separated file for easy import into SolidWorks or a controlling Python script.

4.2.4 The Revised Second Design

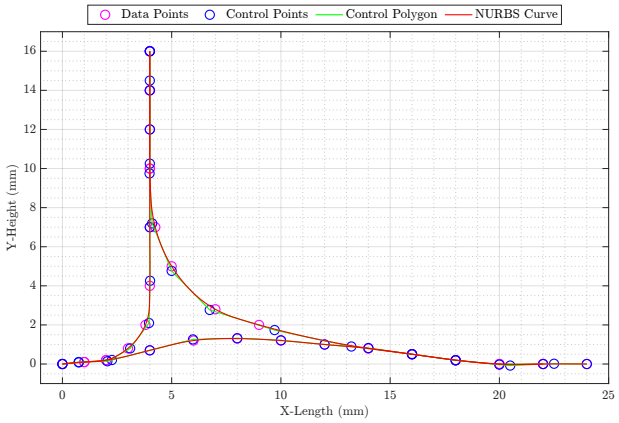
With a new method of generating foot spring shapes, a helical spring replacing the composite spring, and the decision to abandon cams for actuation, it was decided to put together a second design iteration to assess the new direction and determine the next steps in further optimisation, see Figure 4.14.

The shapes generated using the NURBS method in the previous section, seen in Figure 4.13, were used to generate CAD models within SolidWorks. As the spring formed the core of the mechanism; the housing unit core dimensions were set to accommodate the design. A link pair were approximately dimensioned to demonstrate their use in replacing the cam. When the spring is uncompressed, these links will theoretically occupy less space within the housing. Connecting the links to the linear actuation of the spring is a plate that sits within the spring chamber, holding it in place at its preset compression.

The gears were also generally designed to produce a step-up ratio of 4, assuming the lever would be able to rotate somewhere between 10-15°. The smaller gear sits on a shaft that is held within the housing, whereas the position of the larger gear requires the use a structure occupying the space between the composite foot springs. Finally, the lever was shaped to roughly demonstrate how it would sit



(a)



(b)

Figure 4.13: Top: An simple example of a 2nd degree curve generated using the NURBS scripts to pass through an array of five coordinates. Bottom: The same series of scripts then used to generate three profile curves of the composite springs used in the second design iteration.

below the bottom plane of the base spring, allowing for it to initiate compression before the flat foot stage of gait.

4.3 Prototype Optimisation

Whilst the second iteration was helpful in visualising the design changes, it also made apparent several additional design changes that needed solving. The link arms were only roughly dimensioned and would need to be optimised to ensure the reaction forces generated would not be unfavourable to kinetics, and furthermore the space they occupy would need to be minimal so that they can fulfil that advantage they have over the cam.

The gears themselves needed analysing to ensure they were strong enough to transfer the loads between components. In addition to this, their method of retainment within the design should be revisited. The position of the large gear needs to be such that it fulfils the compact design ethos of the system. However, to

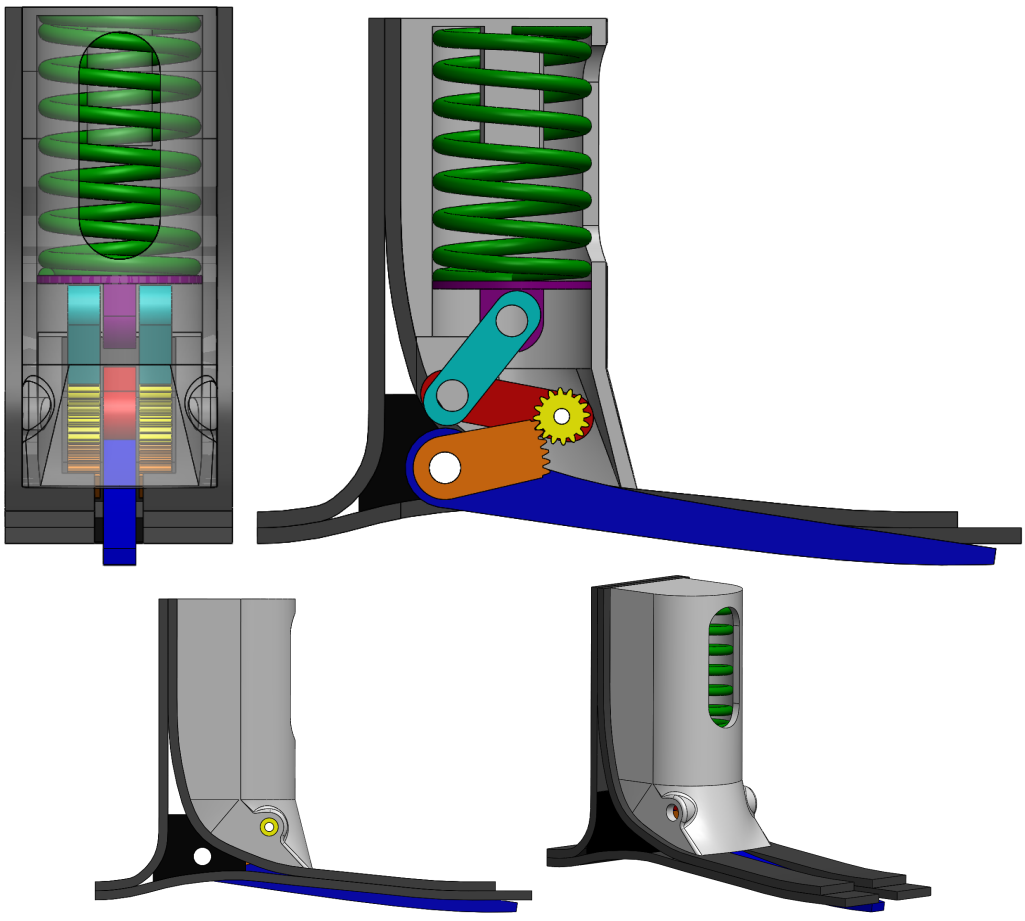


Figure 4.14: The second design iteration featuring the revised mechanism and composite foot springs.

house a plate within the foot springs in this manner would require precise tooling, and a reliable means of securing it within the composite springs.

Whilst the NURBS program was useful in reshaping the composite foot springs, their design still brought concerns on manufacture and performance. The current mechanism impedes on the keel spring, and the heel section would still likely suffer from being too stiff. These components would benefit from being put through a Design of Experiments (DOE) study using the Ansys model.

Other components also needed additional attention, and so the next section of this chapter will cover the final optimisation route towards producing and manufacturing a working prototype.

4.3.1 Revisiting the Links

The first step in refining the design of the link arms was to determine their optimal length to be able to deflect the spring to the operational requirements specified in Table 4.4. A basic model of the links and spring plate were created within Ansys, and three geometry parameters were setup for a response surface study, see Figure 4.15 for the setup.

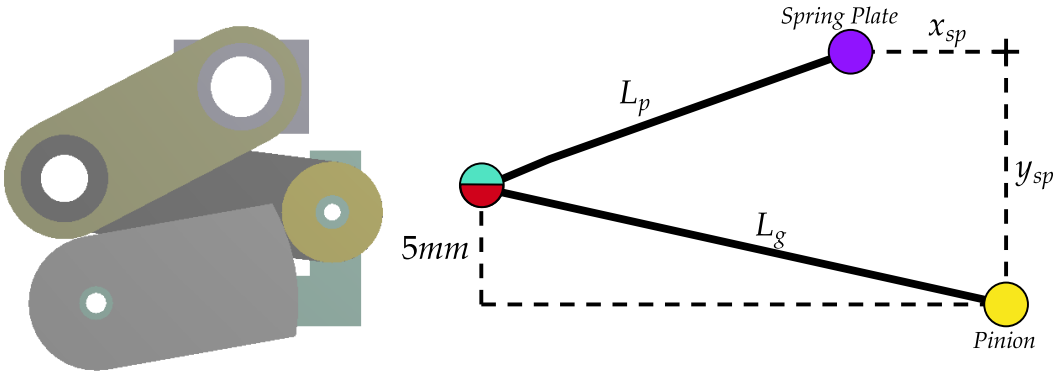


Figure 4.15: Left: Ansys geometry model with roughly dimensioned parts suitable for the design study. Right: A schematic diagram of the parameters. L_g = gear link, L_p = plate link, x_{sp} = horizontal position of plate with respect to pinion, y_{sp} = vertical position of plate with respect to pinion.

A 5mm height was set between the two ends of the gear link as the design needed to be compact when unloaded. Three parameters were selected for study, the gear link length L_g, plate link length L_p, and the horizontal position of the plate x_{sp}, leaving the vertical position y_{sp} as the driven dimension. The different bodies were set as rigid and were linked together with rotational joints. To reduce

the degrees of freedom in the model, the spring plate was restricted to vertical translation. A 40° input rotation was provided to the pinion revolute joint. This value was selected as it was still intended the gears would provide a ratio of 4 in stepping up, thus setting a reasonable target of 10° for the lever rotation specified in the criteria of Table 4.1. The selection of parameter bounds were chosen on the basis of keeping the system compact and able to fit within the mechanism housing unit. With the spring designed to fit a 60mm diameter hole, the maximum value of 40mm was deemed a suitable limit to achieve the desired deflection and still fit within the space constraint. The plate horizontal range was selected such that the spring longitudinal axis would sit closer to the pinion axle, in doing so the reaction forces would pass more vertically through the system when extended.

The parameters bounds of the design experiment were set to the following ranges:

- Gear link length, L_g: 20 - 40 mm
- Plate link length, L_p: 20 - 40 mm
- Plate horizontal, x_{sp}: 10 - 20 mm

A Design of Experiments (DOE) needs outputs to target, and two were set for this model. The first was the maximum vertical displacement of the spring plate from the initial position, the value selected as the maximum clash allowance from Table 4.4. The second output was related to the resultant forces that would be generated during deflection of the spring. Due to the space constraints, a fully extended link system would not be possible without one of the links being too long to fit within a tight housing space. As this means the plate link would be at an angle to the vertical, the corresponding reaction force parallel to the link arm will be larger than the compression force of the spring. So, the second output is the angle the plate link makes with the vertical of the spring plate axis of rotation see the θ angle in Figure 4.17.

Using a central composite design (CCD) algorithm with face centred design type generated 29 design points from the parameter bounds. These parameter sets represent the full design space and are used to generate the response surfaces that can approximate all combinations of parameter values within the bounds. These response surfaces were created using the genetic aggregation algorithm, which for both outputs had an $R^2 > 0.999$ and $RMSE < 1\%$. The plots in Figure 4.16 show a bar chart displaying the parameter rank correlation, and an example of one of the response surfaces. A key detail is the invariance of both

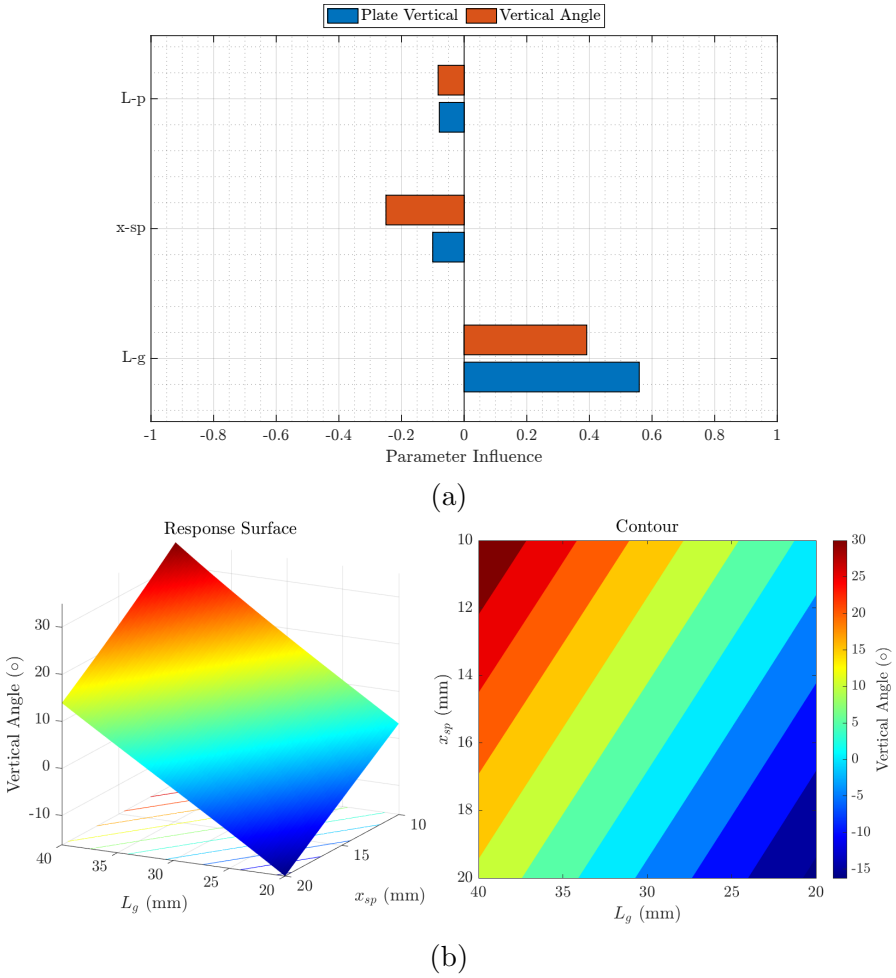


Figure 4.16: Top: A sensitivity plot produced from the response surface algorithm. The outputs are noticeably more sensitive to the gear link length. Bottom: A response surface plot showing the design space of gear link length and plate horizontal with respect to the vertical angle.

outputs with respect to the plate link length, and the high sensitivity of the gear link length. The response surface plot shows how minimising the vertical angle is achievable through increasing the gear link length and horizontal plate position. This response was linear, although the same pair of parameters had a non-linear effect on the vertical displacement. The link parameter pair had the same trend in linear and non-linear effects for the two outputs, and as expected due to their low correlation, the plate link and horizontal distance pair and non-linear surfaces with poor fits.

Following this, an optimisation study was run on the three inputs, targeting an exact vertical spring plate displacement of 33mm, whilst minimising the vertical angle. A multi-objective genetic algorithm was employed, which used all response surface pairs and effects. It was set to produce batches of 100 samples, each

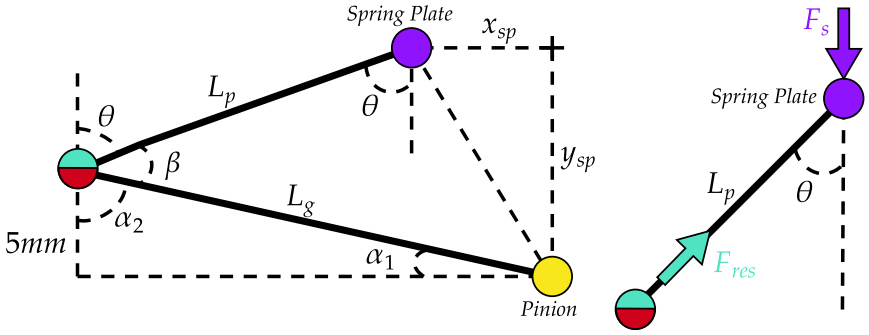


Figure 4.17: A detailed version of the schematic diagram. The additional parameters were derived using Euclidian geometric principles of triangles.

batch would have its mean and standard deviation evaluated against the previous batch. If these metrics are stable within a 2% limit, then the batch is deemed converged and candidate parameter sets are selected; the solution was reached after 777 design points. Using the following values, the optimum set of parameters produced a deflection of 33.5mm with a vertical angle of 17.4°:

- Gear link length, $L_g = 40$mm
- Plate link length, $L_p = 24$mm
- Plate horizontal, $x_{sp} = 20$mm

Link Strength Assessment

The final step in designing the links was to ensure they would withstand the forces in transferring the spring load. To calculate these values, the kinematics of the link system were resolved so that the resultant forces could be calculated. The following system of equations were derived to find the vertical angle, θ, and the resultant force parallel to the link, F_{res}. Figure 4.17 should be used as reference to these equations.

$$\alpha_1 = \arcsin\left(\frac{5}{l_g}\right) \tag{4.24}$$

$$\alpha_2 = 90 - \alpha_1 \tag{4.25}$$

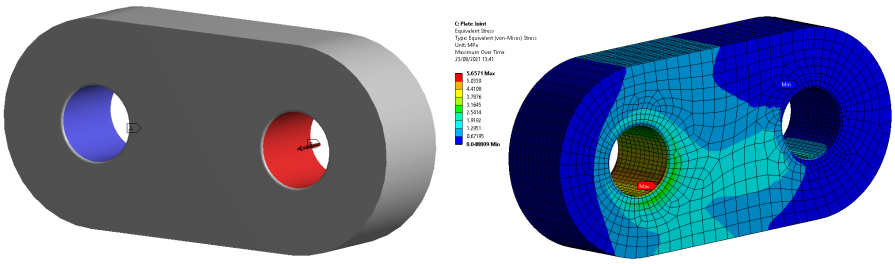
$$\beta = \arccos\left[\frac{l_g^2 + l_p^2 - x_{sp}^2 - y_{sp}^2}{2 l_g l_p}\right] \tag{4.26}$$

$$\theta = 180 - \beta - \alpha_2 \tag{4.27}$$

$$F_{res} = \frac{F_s}{\cos\theta} \tag{4.28}$$

With the θ angle derived, the resultant force applied through the links could be found with equation 4.28. A MATLAB script was put together to analyse the dynamics of the system from uncompressed to compressed length of the spring. Reaction forces on the links were recorded at ten intervals and broken into x and y components. The reaction from the spring was split between the two plate links, whilst the gear link would bear the full force by itself. The links geometries were recreated in Ansys with their width and depth parameterised. For each link, two models were setup to test the pair of reaction force and fixture setups on the link bores, with parameterised outputs of von-Mises stress and deformation.

Each link then went through a design of experiments to generate a result set, which was then used to generate a response surface model and produce an optimal set of dimensions to reduce size and minimise the stress. Two different materials were used in repeating these models, a printable ABS, and Aluminium 6082; properties can be found in the Table of Appendix section D.2. Whilst the Aluminium was strong enough for a considerable size reduction, the ABS was not. The polymer would reach stresses just below yield on the plate links, but the gear link under the full reaction force would fail. Thus, it was decided that the links would be manufactured from Al 6082 plate. Topology optimisation was considered for further weight removal, however the geometries it would produce offer an insignificant reduction at the cost of a more complex shape for manufacture.



(a) (b)

Figure 4.18: FEA setup for the plate link parameter study. Left: The fixture applied to the left bore hole, whilst component forces are applied to the right. The forces were transient, representing the changing vector as the spring is compressed. Right: A von-Mises stress plot, which shows a strong resistance to the loading.

4.3.2 Strengthening the Gears

The gears in the concept were poorly designed. An involute tooth profile was not used, and they did not mesh in a manner that would provide adequate transfer of torque. As the transmission of force between the lever and the helical spring is vital to the operation, the redesign of the gears needed to focus on ensuring these components were completed to a high standard.

The design process of these components involved too many parameters for a design of experiments study to be feasible. Due to the desire to keep the design compact, the first stage was to eliminate possible gear pairs through geometric constraints. In the second design iteration, the axes of the two gears were not vertically aligned due to the gear dimensions and housing size constraints. It was decided to maintain these unaligned gear axes with some additional geometric controls. The horizontal distance between the axes was set to 35mm, leaving the vertical distance to be dictated by the centre distance between the two gears, see the right side of Figure 4.19.

This centre distance needed to be constrained so that the gear axes could both be mounted to the housing unit, where in the second iteration they were on separate parts. A reasonable value to achieve this was limiting this distance to 40mm maximum, as this would limit the vertical to <20mm. To see how much of a limit this would pose on potential gear pairings for a range of ratios, several tables were constructed to calculate the total pitch circle diameter of pairs. Each table calculated the values for a fixed number of pinion teeth against a range of

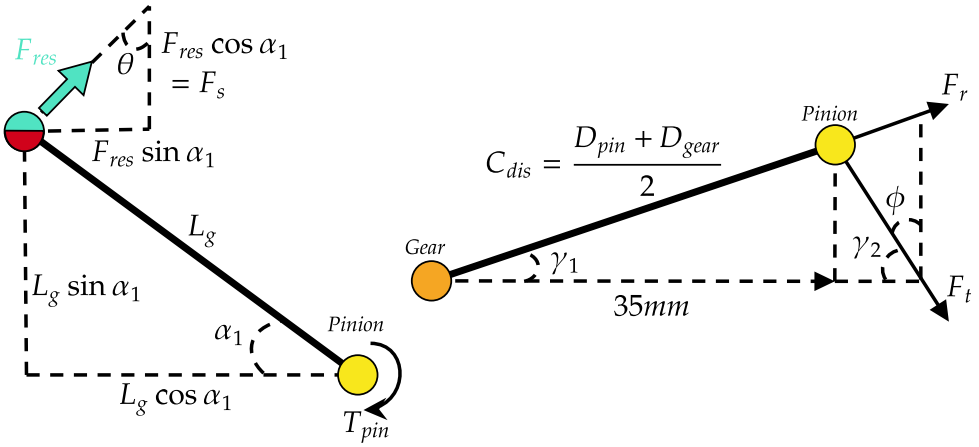


Figure 4.19: Schematic diagrams of pinion torque components, and the geometric relations between the two gears, used in determining dimensional constraints and force components of the gear loads. F_r = gear radial force, F_t = gear tangential force.

gear ratios and teeth module values, an example using 11 pinion teeth can be seen in Figure 4.20. Number of pinion teeth explored included 11, 12, 14, 15, 16, 17, and 18. The gear ratios extended from the minimum value of 4 up to 6 in 0.25 increments. This minimum gear ratio as defined in the criteria of Table 4.1, was chosen to ensure that the angle of rotation of the lever would be stepped up and provide more deflection of the spring. The size of teeth, expressed as the module, was also considered from 1-2 in steps of 0.25.

Some of the fraction gear ratios would also create fractional teeth values which would be problematic for full gears, but not so in this application with limits on the degree of achievable rotation. For the majority of the pinion teeth values, a module > 1 resulted in too large a gear pairing, which significantly reduced the potential pairings. In addition to this, the pinions with 17 and 18 teeth both produced pair dimensions beyond the 80mm limit.

A final check at this stage involved the meshing of the gears, which the concept design had considerable issues with. The meshing of the gears is important in the smooth operation and transfer of torque between the pair. Poor meshing can lead to undercut where tooth profiles can deteriorate from unfavourable contact conditions, leading to a weakening of the tooth. In the literature, an equation is commonly used to define an acceptable minimum number of teeth in a pinion as a function of the gear ratio and pressure angle. Pressure angle is the angle between the tangent of the pitch circle and the line normal to the tooth surface. This angle defines the line of action at teeth contact, through which the tangential force is transferred, see Figure 4.21.

The equation for minimum teeth is taken from Shigley's design book [254], and

Pinion Teeth	11	Pitch circle diameter											
Ratio	Gear Teeth	Module =		1	Module =		1.25	Module =		1.5	Module =		2
		Pinion	Gear	Total	Pinion	Gear	Total	Pinion	Gear	Total	Pinion	Gear	Total
4	44	11	44	55.0	13.8	55.0	68.8	16.5	66.0	82.5	22.0	88.0	110.0
4.25	46.75	11	47	57.8	13.8	58.4	72.2	16.5	70.1	86.6	22.0	93.5	115.5
4.5	49.5	11	50	60.5	13.8	61.9	75.6	16.5	74.3	90.8	22.0	99.0	121.0
4.75	52.25	11	52	63.3	13.8	65.3	79.1	16.5	78.4	94.9	22.0	104.5	126.5
5	55	11	55	66.0	13.8	68.8	82.5	16.5	82.5	99.0	22.0	110.0	132.0
5.25	57.75	11	58	68.8	13.8	72.2	85.9	16.5	86.6	103.1	22.0	115.5	137.5
5.5	60.5	11	61	71.5	13.8	75.6	89.4	16.5	90.8	107.3	22.0	121.0	143.0
5.75	63.25	11	63	74.3	13.8	79.1	92.8	16.5	94.9	111.4	22.0	126.5	148.5
6	66	11	66	77.0	13.8	82.5	96.3	16.5	99.0	115.5	22.0	132.0	154.0

Figure 4.20: A screenshot of one of the Excel tables generated to filter out initial gear pairings based on the dimensional constraints detailed in the text. A conditional formatting was applied for quick visual reference, with total pitch circle diameters of over 80mm being coloured red for disqualification from selection.

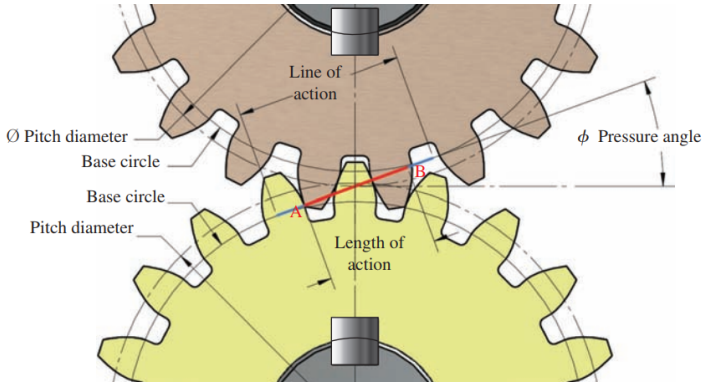


Figure 4.21: Diagram from a textbook, detailing the pressure angle and line of action between the teeth of two mating gears [253].

is given as:

$$N_p = \frac{2}{(1+2r_g)\sin^2\phi}(r_g + \sqrt{r_g^2 + (1+2r_g)\sin^2\phi} \tag{4.29}$$

Where r_g is the gear ratio and ϕ is pressure angle in degrees. For all ratios, this equation demanded a minimum of 16 teeth for $\phi = 20°$, and 11 teeth for $\phi = 25°$. With these dimensional constraints, the selection of possible gear pairs were narrowed down. A summary of this shortlist can be seen in Table 4.5.

The smallest pinion gear presents the best opportunity for a high gear ratio whilst maintaining a compact mechanism. However, it is known that smaller gears can have increased strength and wear issues, particularly the contact between the mating mesh of teeth. The larger pressure angle used on the pinions with less than 16 teeth will help to improve the resistance to the contact stress but a full strength analysis was still warranted. Across most standards, there are two key metrics to assess the strength of gears; the bending stress and contact stress.

Table 4.5: A summary table of possible gear pairs after the initial geometric constraints.

Pinion	11		12		14	15	16
Module	1	1.25	1	1.25	1	1	1
Ratio	*Centre Distances*						
4	27.5	34.4	30	37.5	35	37.5	40
4.5	30.25	37.8	33	—	38.5	—	—
5	33	—	36	—	—	—	—
5.5	35.75	—	39	—	—	—	—
6	38.5	—	—		—	—	—

Bending and Contact Stress Principles

The earliest forms of stress calculations for these metrics were derived using known principles of mechanics at the time. For bending stress, this was the Lewis Equation, which treated the tooth of a loaded gear as a cantilever beam loaded at the tip of the tooth, see Figure 4.22. This was a reasonable approximation due to the less accurate manufacturing methods leading to teeth to take the maximum load at the tip. The equation derived is given as:

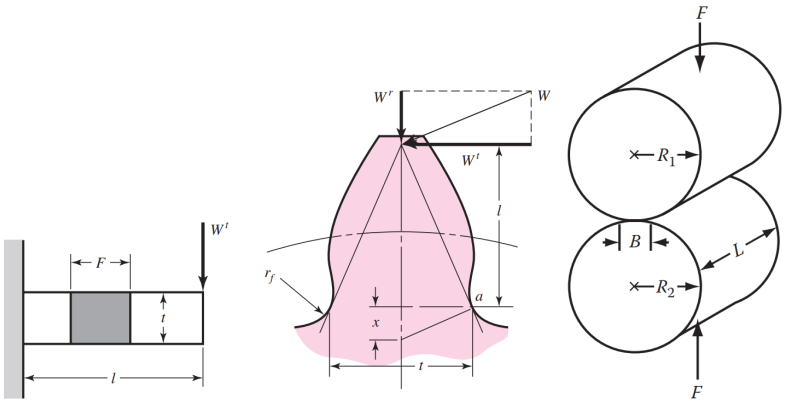
$$\sigma_B = \frac{k_v \ F_t}{b \ m_g \ Y} \tag{4.30}$$

Where F_t is the tangential force, b is the face width, and m_g is the gear module. The other parameters, k_v dynamic factor and Y the Lewis form factor, are characteristic modifications to the basic cantilever beam equation. The dynamic factor adjusts for the effects of high velocity when the gears are meshing, whilst the Lewis factor adjusts to the profile shape of teeth.

Contact stress is derived from the Hertzian contact stress at a small interface between two cylinders compressed together, see Figure 4.22. The common form of the equation is given as:

$$\sigma_C = \sqrt{\frac{F_t}{\pi \ b \ \cos\phi} * \frac{\left(\frac{1}{r_1}\right) + \left(\frac{1}{r_2}\right)}{\left[\frac{1-v_1^2}{E_1}\right] + \left[\frac{1-v_2^2}{E_2}\right]}} \tag{4.31}$$

Where r_1 and r_2 are the radii of the cylinders. If the materials of the two cylinders are the same, then the denominator of the second fraction containing Youngs and poisson's can be reduced. This principle was suitably applied to gear



(a) (b)

Figure 4.22: Diagrams of early derivations for bending stress on the left [254] and contact stress on the right [259].

teeth, as the point where they contact, and force is transferred is on externally curved surfaces.

Both of these equations have the tangential force as the primary load, which is calculated using the torque generated on the shaft the gear is mounted on. In the mechanism, this torque is caused by the reaction force generated on the distal hole of the gear link, see Figure 4.19. Resolving the reaction and link length into components, gives the torque on the pinion shaft as:

$$T_pin = (F_{res} \sin\theta * l_g \cos\alpha_1) + (F_{res} \cos\theta * l_g \sin\alpha_1) \tag{4.32}$$

The tangential is then given as:

$$F_t = \frac{2\ T_pin}{D_t} \tag{4.33}$$

For the Lewis equation, the diameter D_t is taken as the tooth tip diameter, whilst the contact stress can use a range of diameter and radii to calculate the stress at any point of rolling contact. However, there are notable accuracy issues with equations 4.30 and 4.31. They are loose approximations at best, and compared to modern standards, are insufficient in determining accurate stresses. Assumptions made on the loading of teeth were resolved with improved mathematical modelling of gear teeth, once involute profiles were introduced. These curves create teeth profile that ensure at between 1-2 teeth (for spur gears), would be loaded at once when meshed together, the exact value is defined by the contact ratio. A brief explanation of how these involute profile and the gears were generated in a CAD model can be seen in the Appendix section E.3.1. The contact ratio is defined as:

$$m_p = \frac{\sqrt{\frac{d_o}{2}^2 - \frac{d_b}{2}^2} + \sqrt{\frac{D_o}{2}^2 - \frac{D_b}{2}^2} - C_{dis} \sin\phi}{p_b} \tag{4.34}$$

Where the d_b, d_o, D_b, D_o are the base and outside diameters for the pinion and gear, p_b is the base pitch, ϕ the pressure angle, and C_{dis} the centre distance [259]. This was used to check all the gear pairings in Table 4.5, all of which had a contact ratio, $m_p > 1.35$.

ISO 6336 Standards

It was decided that an accurate analysis of the gear strength warranted the use of a set of ISO documents used to assess the strength of spur gears. These documents

fall under the designation BS ISO 6336:2006, of which the following selection were referenced:

- 6336-1: Basic principles, introduction and general influence factors
- 6336-2: Calculation of surface durability (pitting)
- 6336-3: Calculation of tooth bending strength
- 6336-5: Strength and quality of materials
- 6336-6: Calculation of service life under variable load

The second and third documents in this list contain the equations for contact and bending stress, including the associated factors with those stresses. These documents also take the tangential force as occurring at the pitch circle diameter, D_p. Document 6336-1 contains the general influence K-factors, one of which is referenced in the document 6336-6. For brevity, the explanation of these factors and values used have been included in Appendix section E.3.2; they have been summarised here in Table 4.6. Finally, the material properties and material limit values are determined from a series of tables and coefficient values in 6336-5.

The surface durability of gears is assessed by the contact stress experienced during peak loads at the pitch point of tooth contact. Hertzian pressure is the basis for this calculation, but it alone does not fully represent the loading conditions which include the coefficient of friction, sliding mechanics, and surface lubrication. Whilst these cannot be directly resolved into a mathematical representation, the 6336-2 document overcomes this by defining them as a series of modifying factors. The factor of safety for contact stress is define as:

$$S_H = \frac{\sigma_{HG}}{\sigma_H} \tag{4.35}$$

Where σ_{HG} is the pitting stress limit (N/mm^2), and σ_H is the contact stress (N/mm^2). This factor of safety is defined separately for the pinion and gear due to differing factors between them. The pitting stress limit is a function of the material limit σ_{Hlim} and a series of factors that would affect the material properties at any operational instance and over the course the running lifetime. This is defined as:

$$\sigma_{HG} = \sigma_{Hlim} Z_{NT} Z_L Z_v Z_R Z_W Z_X \tag{4.36}$$

The contact stress is a function of the nominal pitting stress and the general influence factors:

$$\sigma_H = \sigma_{H0} Z_{\frac{B}{D}} \sqrt{K_A K_v K_{H\beta} K_{H\alpha}} \tag{4.37}$$

Alongside the general influence factors, there is also a $Z-$factor in this equation which can have two possible subscripts; Z_B is given for the pinion, whilst Z_D is given for the gear. The final step then is deriving the nominal pitting stress σ_{H0}, which is a form of the Hertzian contact stress equation 4.31. In the standard it is defined as:

$$\sigma_{H0} = Z_H Z_E Z_\epsilon Z_\beta \sqrt{\frac{F_t}{D_p\, b} \frac{r_g + 1}{r_g}} \tag{4.38}$$

The factors in this equation serve to modify the terms within the squareroot, so that the nominal stress value accounts for the shape of the tooth, contact, and material properties. In the standard, the tangential force is divided by a reference diameter d, which has been replaced here with the pitch circle diameter D_p.

Bending strength of gear teeth is rated by their ability to withstand a maximum tensile at the tooth root. This focus on the localised stress at the root fillets is due to the high proclivity for crack initiation at these sites. More often these cracks are initiated in the compressive non-working flanks of the tooth, but if the loading is uni-directional then crack propagation to failure is not guaranteed. However, reversal loading of gears can raise this risk due to the cyclic nature and thus a suitable factor must be applied to the limiting stress value. This will be explained in the upcoming discussion.

Much like for the contact stress, the factor of safety for bending is given as:

$$S_F = \frac{\sigma_{FG}}{\sigma_F} \tag{4.39}$$

With σ_{FG} representing the tooth root stress limit (N/mm^2), and σ_F is the tooth root stress (N/mm^2). Again, this is calculated separately for the pinion gear due to differing factor values. The tooth root stress limit is defined as:

$$\sigma_{FG} = \sigma_{Flim} Y_{ST} Y_{NT} Y_{\delta relT} Y_{RrelT} Y_X Y_M \tag{4.40}$$

The nominal bending limit σ_{Flim} is taken from the material property document 6336-5. Factors in this equation are related to the material properties, and stress distribution effects including the surface roughness and tooth size. An additional factor is included here from the standard definition. The mean stress influence factor Y_M which accounts for the reversal loading. Like the contact stress, the tooth root bending is a function of the nominal bending stress and the general influence factors, given as:

$$\sigma_F = \sigma_{F0} K_A K_v K_{F\beta} K_{F\alpha} \tag{4.41}$$

Finally, the definition of the nominal bending stress is:

$$\sigma_{F0} = \frac{F_t}{b\ m_g} Y_F Y_S Y_\beta Y_B Y_{DT} \tag{4.42}$$

The fraction term in this equation is recognisable as the basic Lewis bending stress equation. Where the Lewis equation utilised a dynamic factor and form factor. In the ISO definition, the dynamic factor is captured as K_v in equation 4.41, and the form factor is in equation 4.42 as factor Y_F.

The limiting stress values defined in the 6336-5 document are a function of the surface hardness and constants relating to the material and its quality. There are no specific alloys defined in terms of grades or specification numbers, instead the options are categorised by the general alloy type and hardness condition bases on the post-processing method. For example, the weakest in the selection are grey cast irons, whilst the strongest are nitrided steels. Furthermore, each material category has three levels of strength based on the material and manufacturing quality.

A decision was made to select the induction hardened wrought steel, which provided a high contact strength coupled with an intermediate bending strength. To provide a conservative estimate, the lower range of quality was used in calculating the limiting stress. Using the material constants and hardness value, the contact stress limit, σ_{Hlim} was set to 1057.1MPa, and the bending stress limit

Table 4.6: Summary of the factor symbols, description and value used

Symbol	Description	Value
K_A	Application	1.1
K_v	Internal dynamic	See Appendix
$K_{H\beta}$, $K_{F\beta}$	Face load - Contact, Bending	1.1
$K_{H\alpha}$, $K_{F\alpha}$	Transverse load - Contact, Bending	1.1
Z_{NT}	Contact life	1.3
Z_L, Z_v, Z_R	Lubrication, Velocity, Roughness	1
Z_W, Z_X, Y_X	Work hardening, Size - Contact, Bending	1
Z_B, Z_D	Single tooth contact - Pinion, Gear	1
Z_H	Zone	2.28
Z_E	Elasticity	189.8
Z_ϵ	Contact ratio	0.9
Z_β, Y_β	Helix angle	1
Y_{ST}, Y_S	Stress correction: Reference, Local root	2
Y_{NT}, Y_B, Y_{DT}	Bending life, Rim thickness, Deep tooth	1
$Y_{\delta relT}$, Y_{RrelT}	Relative: notch sensitivity, surface	1
Y_F	Form	See Appendix

σ_{Flim} as 263.6MPA.

The calculations were setup in an excel spreadsheet as this made it simple to check the parameter values and make a quick comparison of resulting safety factors. These values were collated in MATLAB to generate the plots seen in Figure 4.23. Before the calculations were made, it was decided that a minimum factor of safety would be 1.5, which most pairs appear to pass. In terms of the contact stress, all pairs with $N_p = 11$ and $m_g = 1$ fail the minimum requirements, whilst all pairs with $N_p = 12$ and $m_g = 1$ just about pass. The pinion pairs where the module is equal to 1.25 have improved safety factors due to the increased tooth size, so it was decided to eliminate 11 and 12 tooth pairs with $m_g = 1$.

The 16 tooth pair could also be eliminated as the larger gear appeared to offer no strength benefits, likely due to the pressure angle being 20° which changes the tangential force line of action to be more shallow. Whilst the 15-tooth pinion pair also have promising safety factor values, the gear ratio it offers was not better than the remaining pairs, and so it too was eliminated from selection. The most favourable pairs with high safety factors and smaller profiles appeared to be the 11 and 12 tooth pinion pairs, with modules of 1.25. With the marginal increase in the 12 tooth pinion, it was decided to go ahead with this pair.

As a final step in the analysis, it was decided to make a comparison between the analytical bending stress values and FEA values of the selected gear pair. The geometries created as part of the form factor derivation were cut down to a few teeth and imported into Ansys. A fixed boundary condition was applied on the inner bore and cut surface, with the tangential force of 361.4N applied to a thin

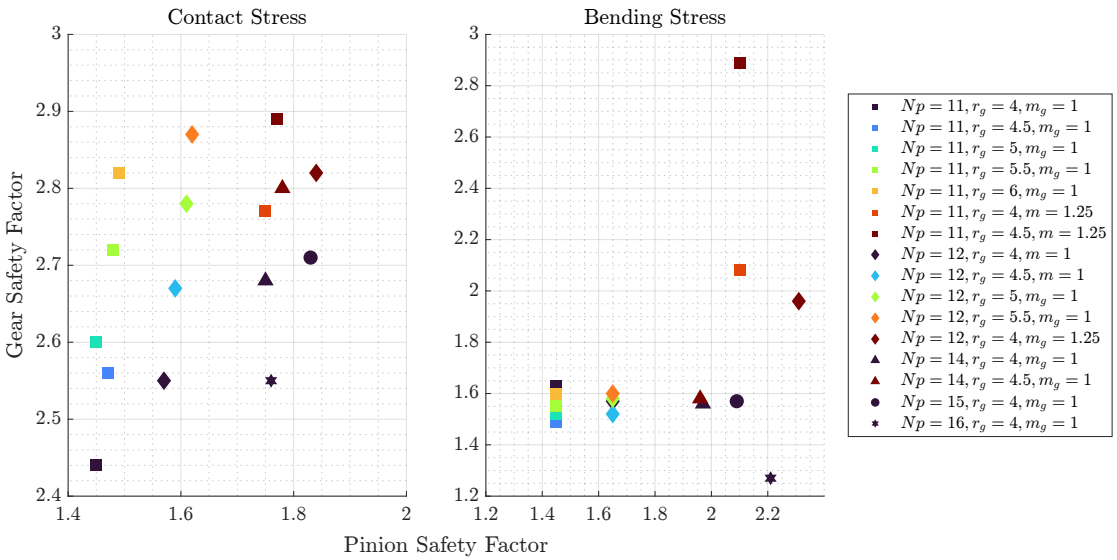


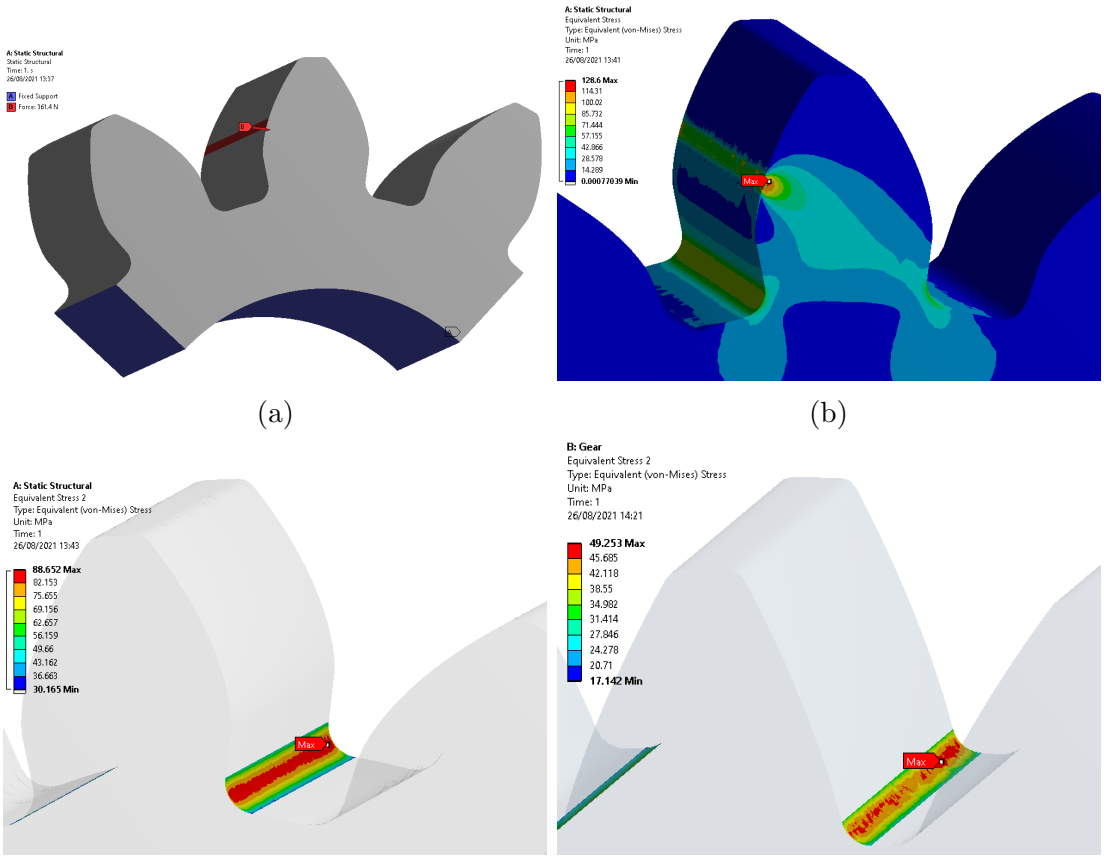
Figure 4.23: Plots of safety factor for contact and bending stress calculations.

Table 4.7: Summary of stress results from ISO analytical calculations, and FEA simulations. All values are in MPa.

	Pinion	**Gear**
Nominal	90.339	62.427
Tooth Root	159.889	188.716
Simulation	88.652	49.253

strip across the face at the pitch diameter, see Figure 4.24(a).

The resulting stress can be seen in the other subfigures of Figure 4.24. All results had a convergence tool applied to ensure mesh independence. The maximum stress would occur on the edge of the tooth profile where the force is applied on the pitch diameter strip. This was ignored as an FEA error, and focused stress plots were made in the root fillets where the maximum values were expected. A summary of these values can be seen with the analytical results in Table 4.7. It is clear that the analytical root stresses capture additional behaviour not seen in the



(a) (b)

(c) (d)

Figure 4.24: Setup and results of the FEA bending stress model for the chosen gear pair.

simulation. The factors applied in equation 4.41 are values which are not easily derived or directly linked to the geometry. A closer comparison can be made between the nominal analytical values and model results, particularly for the pinion. It is unclear why the gear has a larger difference, although this could be due to an overly conservative factor value.

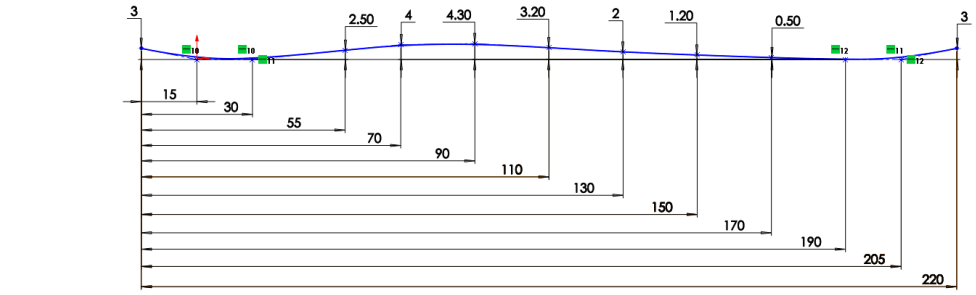
The key takeaway here is that the FEA models are apparently unable to fully capture aspects of the gear operating conditions. Use of just these models to assess the gear strength could lead to under estimations of the strength capability. The analytical results from the ISO equations provide a more conservative value, which when considering the sophisticated nature of calculations provides more confidence in the strength of the gears being suitable to withstand the loads. Furthermore, the safety factors for the chosen gear pair also facilitates the future requirement of testing helical springs with a range of stiffness values.

4.3.3 Foot Structure Parameterisation

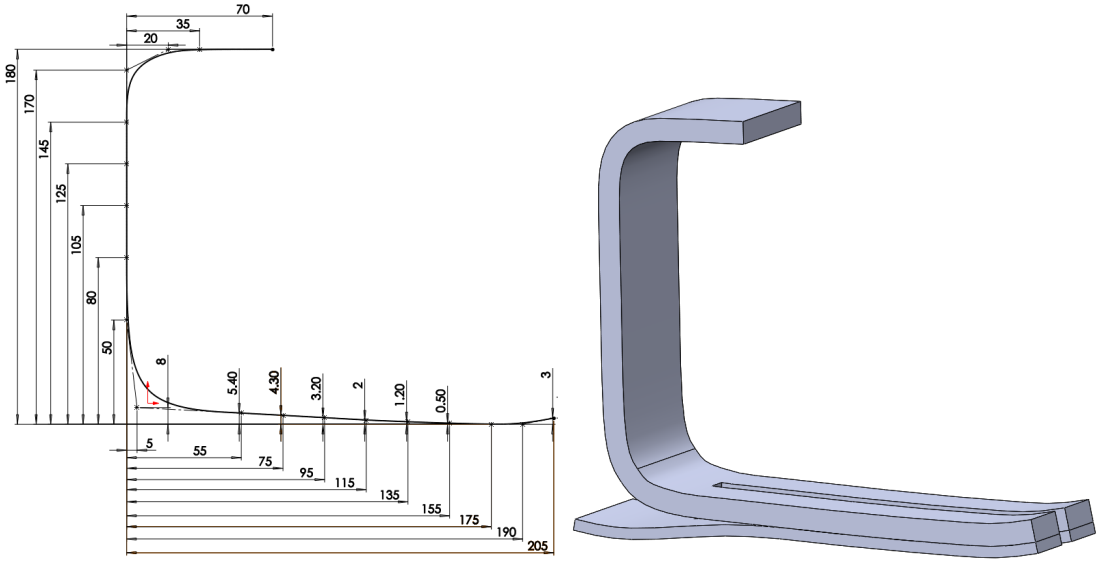
The optimisation of the foot structure formed the final large design analysis stage in this prototype optimisation. It began with re-using the NURBS programme written in MATLAB to generate structure profiles. In the previous iteration, three springs were defined. However, this had a few predictable design issues including over-stiffening the structure, not protecting the top of the housing unit, requiring an additional structure with hold the lever shaft, and posing a potential issue with manufacture and assembly of three springs.

It was decided to reduce the number of spring sections to just two, increase the straight back face of keel spring to accommodate more housing space, curve the keel spring over the top of the housing, and drop the structure closer to the floor for improved contact and spring like behaviour. The resulting splines had their control points transferred to SolidWorks sketches and the springs were extruded to a width of 70mm, see Figure 4.25. Slots were also cut into the two springs for the lever to sit within. The precise control afforded by the generated control points also allowed for a neat connection between the curved surfaces of the springs.

The heel spring would provide the stable base and shock absorption, with improvements to the latter by separating the structures so that the heel could act more independently. As indicated above, the keel now takes on a larger support role so that housing can focus on just containing the mechanism. Whilst the control points could be used in a parameter study to further optimise the shape, the primary purpose of these springs was to facilitate the operation of the mechanism.



(a)



(b) (c)

Figure 4.25: Spline sketches created from points generated in the MATLAB NURBS program; (a)Heel profile and (b)Keel profile. The resulting model can be seen in subfigure (c)

A parameter study involving many variables would be computationally expensive, especially with the modest hardware specifications, see Appendix A.

It was decided to keep the structure profile shape as its low profile would suit the operation of lever by bringing the axis of rotation close to the floor. An optimisation could still be performed by adjusting the thickness of the section along the lengths of the two springs. The entire length of the heel spring was divided into 20mm chord lengths. This same approach would not be useful for the vertical and top section of the keel, within which the housing would sit, and so that section had its thickness parameterised as a whole length. The bottom section of the keel was then parameterised with the same chord lengths as the heel. This resulted in 12 points along the heel, the top section of the keel, and 10 points along the bottom keel section; see Figure 4.26. At each of these points, a

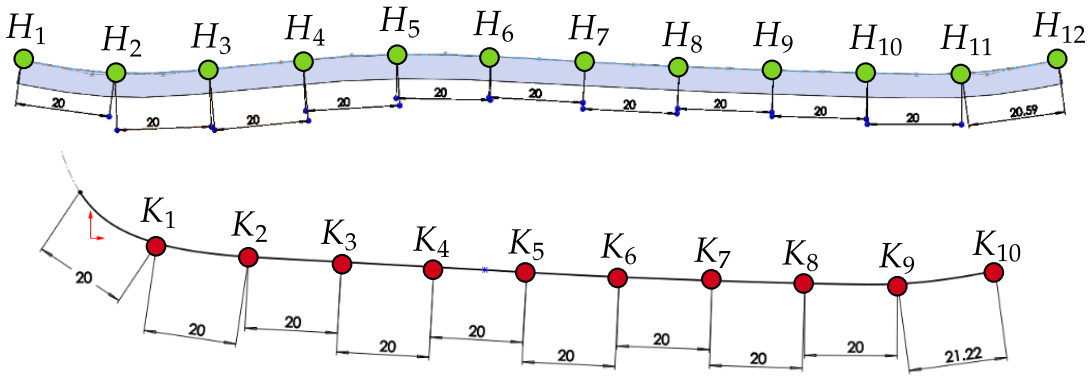


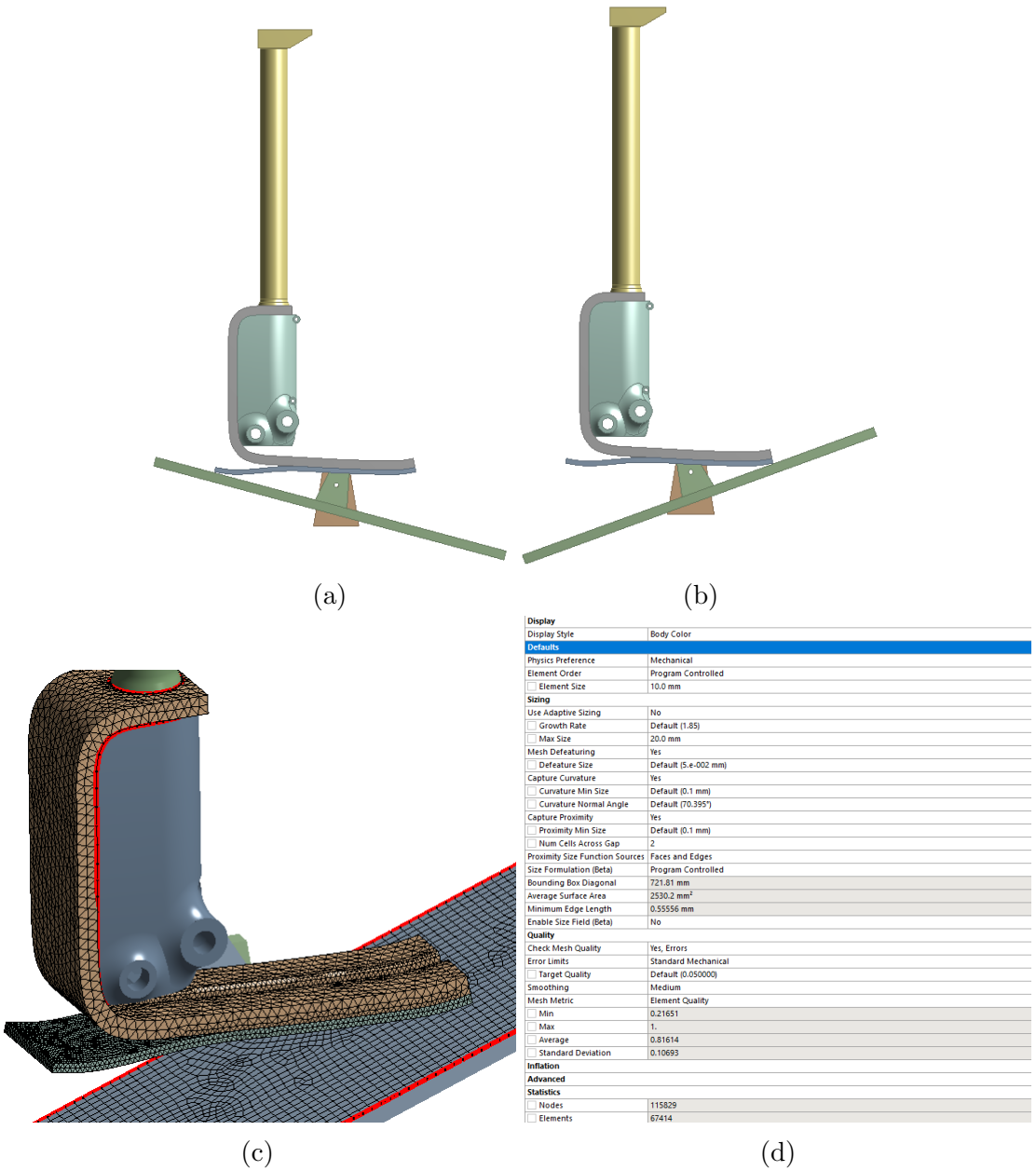
Figure 4.26: The parameter points setup along the profile of the heel (top) and keel (bottom). These were set at distances of 20mm chord lengths.

profile section sketch was created, and the thickness of each sketch was set as a parameter. These sketches were used as the bounds through which the body was extruded.

Model Setup

The force plate and pylon setup detailed in Section 3.3 for the ISO 22675 model were used again, with the pylon length adapted as per the ISO specifications. It was decided to run the optimisation for the static heel and forefoot conditions, but using the peak loads from the cyclic set of forces as these are a more realistic representation of gait loads. From Table 3.10, the P4 level loading was used; a heel setup angle of -15° and force of 1173N, and a forefoot setup of 20° and load of 1158N. The same Isotropic material choice was used again to help expedite the computation time of design points. A composite material model would be completed post-optimisation to verify the design using the Ansys Orthotropic properties detailed in Appendix section D.1 for the ply properties.

The housing had an initial design iteration at this point, and so was included in the model as a rigid body, see Figure 4.27 for views of both static setups. Using the knowledge from the contact studies in section 3.3, the frictionless plate contact and bonded settings were reused. A mesh was setup using the parameters seen in Figure 4.27, and a mesh study completed using the built-in convergence tools. The results converged with a $< 10\%$ change in a single step for each setup. However, this required a fillet of 2mm radius to be added to the edges of the lever cut to avoid a stress singularity. These convergence plots and the max stresses can be seen in the first four images of Figure 4.28. The peaks were localised on the fillet area of the forefoot, and the bonded foot connection boundary on the heel. These



(a) (b)

(c) (d)

Display	
Display Style	Body Color
Defaults	
Physics Preference	Mechanical
Element Order	Program Controlled
Element Size	10.0 mm
Sizing	
Use Adaptive Sizing	No
Growth Rate	Default (1.85)
Max Size	20.0 mm
Mesh Defeaturing	Yes
Defeature Size	Default (5.e-002 mm)
Capture Curvature	Yes
Curvature Min Size	Default (0.1 mm)
Curvature Normal Angle	Default (70.395°)
Capture Proximity	Yes
Proximity Min Size	Default (0.1 mm)
Num Cells Across Gap	2
Proximity Size Function Sources	Faces and Edges
Size Formulation (Beta)	Program Controlled
Bounding Box Diagonal	721.81 mm
Average Surface Area	2530.2 mm²
Minimum Edge Length	0.55556 mm
Enable Size Field (Beta)	No
Quality	
Check Mesh Quality	Yes, Errors
Error Limits	Standard Mechanical
Target Quality	Default (0.050000)
Smoothing	Medium
Mesh Metric	Element Quality
Min	0.21651
Max	1.
Average	0.81614
Standard Deviation	0.10693
Inflation	
Advanced	
Statistics	
Nodes	115829
Elements	67414

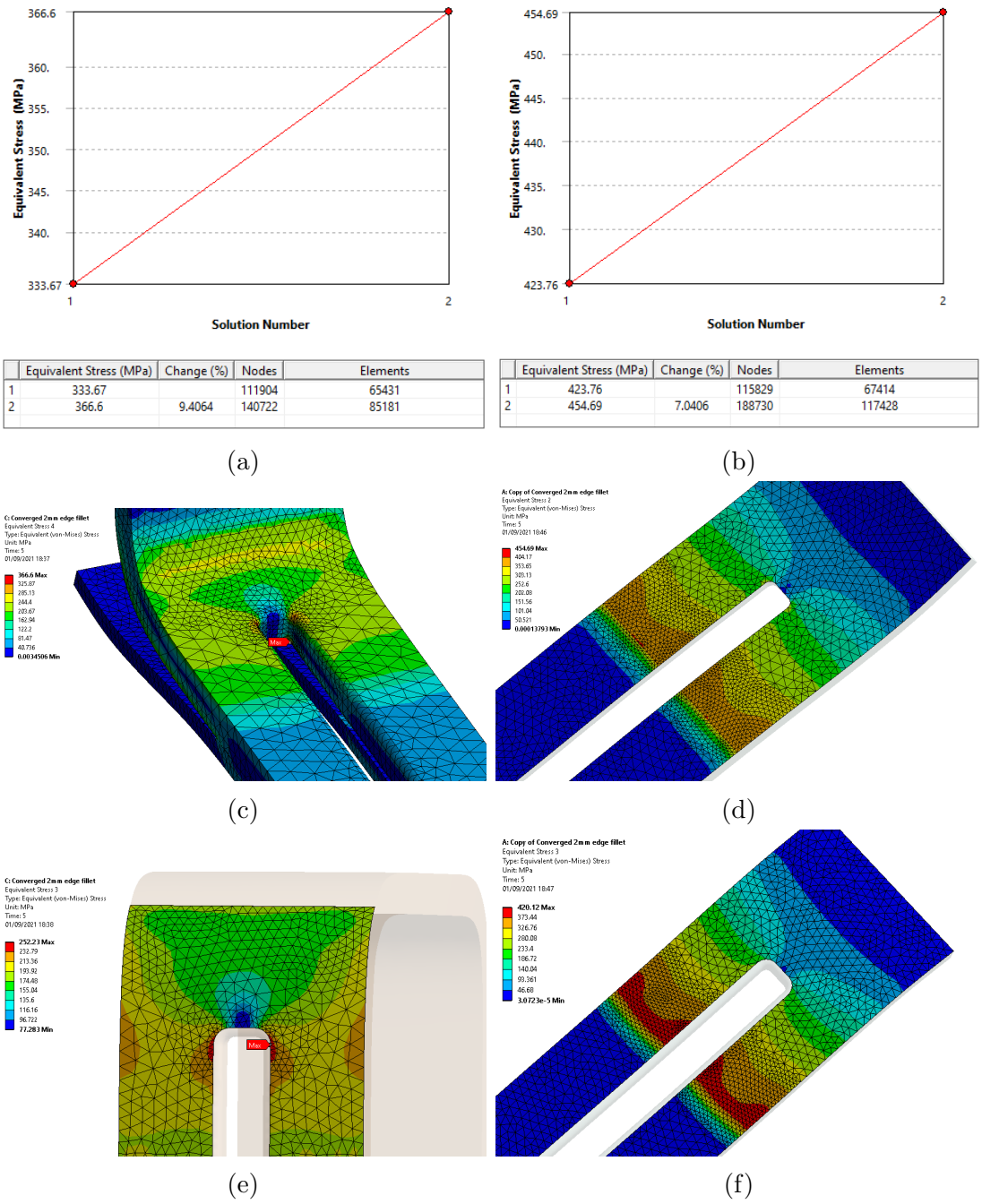
Figure 4.27: Geometry models for the heel (left) and forefoot (right) loading conditions.

were deemed to be less accurate representations and so results were collected on the surfaces, which can be seen on the bottom two images of Figure 4.28.

A final addition to the parameter study models was a new APDL script to close the gap between the force plate and spring structure as the latter changes thickness. This code can be found in the APDL code section D.3 of the appendices.

Parameter Correlation Study and Results

With the profile section points and upper section of the keel, the number of thickness parameters numbered 23. It was unlikely that all of these would have the same



	Equivalent Stress (MPa)	Change (%)	Nodes	Elements
1	333.67		111904	65431
2	366.6	9.4064	140722	85181

(a)

	Equivalent Stress (MPa)	Change (%)	Nodes	Elements
1	423.76		115829	67414
2	454.69	7.0406	188730	117428

(b)

(c)

(d)

(e)

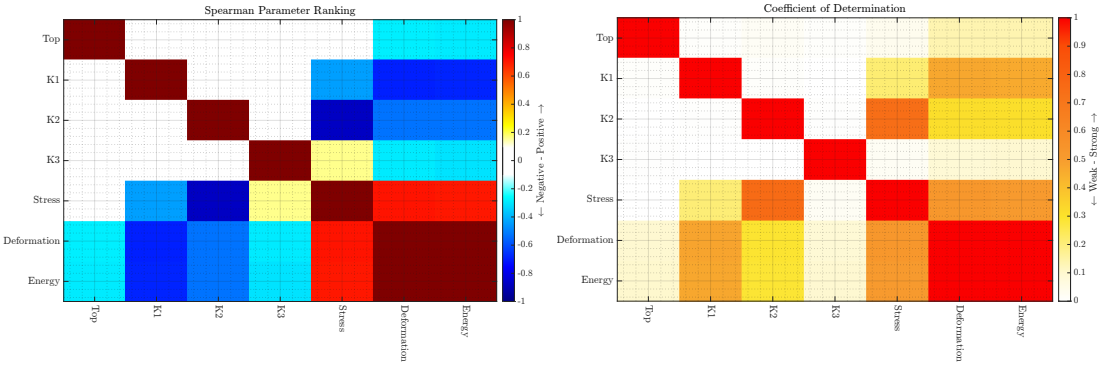
(f)

Figure 4.28: Convergence graphs and stress plots from the mesh studies completed on the forefoot and heel setup. The left column pertains to the forefoot setup, whilst the right is taken from the heel. Middle: stress plots showing focus on the localised stress peaks post convergence. Bottom: stress plots taken on the surfaces, which are a more realistic representation of the results.

effect on the stress and deflection of the structure. Furthermore, a large number of parameters also need a sizeable set of design points to fully cover the design space. As this is not a computationally efficient method, a Spearman Ranking parameter correlation study was ran first. The lower and upper bounds of thickness on the heel sections were set to 3-5mm, whilst the keel was set to 6-11mm including the top section constant thickness.

Using these bounds, a series of 500 design points were generated using a Latin Hypercube sampling method; a brief explanation of sample point generation and correlation method can be found in Appendix section D.5. Not all 500 points are required, and so at every 25th step a convergence check is made against a mean value and standard deviation accuracy. If the last step is within 1% of the cumulative mean and 2% of the standard deviation, then the study is deemed converged having explored enough of the design space.

A correlation and determination matrix were produced for both static conditions. Parameters with a correlation below 0.1 were omitted from the plots produced. The forefoot results can be seen here in the main text of Figure 4.29, whilst the heel results can be found in the appendices Figure D.1. In both sets of results the parameters with the strongest effect on stress and deflection are located in areas where the structure essentially acts as cantilever fixed condition. On the keel this is proximal to the housing, and on the heel it is close to the connection with the heel. These results helped to narrow down the require parameters for a further design optimisation. For the keel, this is the top section, and profiles K1-K3. Whilst the heel focus should be on the profile sections H4-H6.



(a) (b)

Figure 4.29: A parameter correlation and determination matrix for the forefoot parameter study.

Design of Experiments Study and Results

The main concern with the foot structure was to ensure it would not fail under clinical trials and secondary objective of providing some additional deflection that would allow the lever to rotate further. Initial design parameter exploration ran into problems with exploring upper section thickness due to geometry errors, and so it was decided to omit this parameter. Based on the correlation ranking and R^2 values in Figure 4.29, this specific variable would not be missed too much in comparison to the much stronger K1 and K2 profile thicknesses.

Several algorithms exist that generate the design points that represent the full range of possibilities achievable with the selected parameters and their bounds. It was decided to examine some of these to discover which one would produce the most accurate model for optimisation. An explanation of these design algorithms has been provided in the Appendix section D.6. Using the forefoot model and setting K1-K3 bounds as 6-11mm, the following methods were used to generate the design points:

- Box Behnken (BB): 13 points
- Central Composite Design (CCD) - Auto: 15 points
- Optimal Space-Filling (OSF) Design - Max-Min, CCD samples: 15 points
- OSF Design - Max Entropy, CCD samples: 15 points
- OSF Design - Max Entropy, Full Quadratic Model samples: 10 points

With these sample points generated, they could be used to define a response surface model to predict the behaviour and optimise the parameter points. The accuracy of these models will depend on the complexity of the parameter relations, the number of design points generated, and the type of response surface algorithm used. Several of these algorithms are available for selection, including the neural network, or interpolating techniques such as Kriging and Sparse Grid methods. The default method, and the one used for the foot structure is Genetic Aggregation. This method auto-refines the process and selects the response model with the best fit for each output.

All design tables in the list above had response surfaces generated with the genetic aggregation algorithm. The goodness of fit metrics have been correlated together in a single table and placed in Appendix section D.4.2. From this selection, the best and worst overall performing models have had their R^2 and RMSE

Table 4.8: Coefficient of determination R^2, and RMSE values taken from the table in the appendices. BB, the worst performing model. OSF Max Entropy type using full quadratic samples, the best performing model in all outputs except for the Body Stress.

Metric	Body Stress		Deflection		Upper Stress		Lower Stress	
	BB	OSF	BB	OSF	BB	OSF	BB	OSF
R^2	0.749	0.878	0.965	1	0.756	0.999	0.685	1
RMSE	88.912	41.183	0.976	< 0.001	91.644	1.573	89.737	< 0.001

Table 4.9: Results from the response surface optimisation. Values of stress are in MPa, values of deflection in mm. The heel body stress results have been omitted due to it picking up a stress singularity value.

	Body Stress	Deflection	Upper Stress	Lower Stress
Keel	305.03	13.518	257.12	186.58
Heel	-	16.67	86.17	95.823

values extracted and placed in Table 4.8 for discussion here. All models struggled to predict the stress plotted across the entire body due to the peak stresses occurring as FEA singularity artefacts, as indicated in the middle row images of Figure 4.28. The volatility of these localised peaks makes it hard to predict their behaviour to a reasonable level of accuracy. However, the OSF method was able to model the upper and lower surface stresses to a high precision. In comparison, the BB method struggled, likely due to its inability to capture the extremes of parameter variables, as indicated in the discussion of Appendix section D.6.

The disparities between these two methods can be seen in the response surface curves and contour plots in Figure 4.30. In these plots the K1 and K2 parameters are modelling the lower surface stress. The quadratic relationship between the inputs and output is not captured by the Box-Behnken method, as seen by the significantly different shape generated in modelling the lower end of the stress prediction. This coincidently is where the extremes of the parameter variables needed modelling, which only the OSF model was capable of achieving.

This OSF model was used on the heel setup and whilst not quite as effective as the forefoot model, it still provided R^2 values above 0.9, and RMSE of less than 2 for the deflection and surface stresses. Following this, the response surfaces were used to optimise the parameters with the objectives of minimising the stress and targeting between 10-15mm of deflection. The resulting values were used to dimension the keel and heel profile sections.

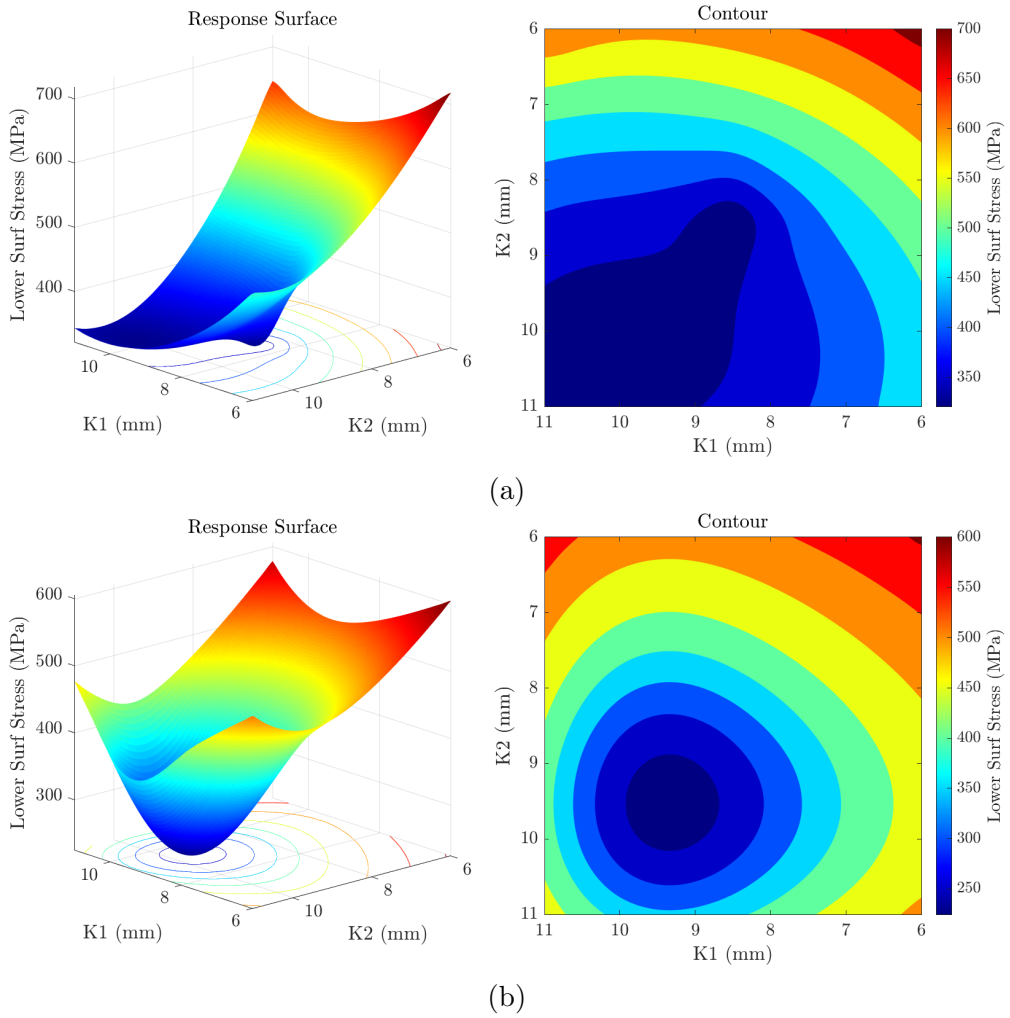


Figure 4.30: Response surface curves modelling the effect of K1 and K2 thicknesses on the lower surface stress. Top: BB. Bottom: OSF

A composite part manufacturer was consulted on the models and possible composite layup structures. It was suggested that the separate springs be constructed from layers of unidirectional ply with surfaces covered in two layers of twill weave. This twill weave would be the XC-130 with the material properties that had been used for the simulations so far. The suppliers of this twill weave prepreg also supplied unidirectional sheets using the same fibre modulus. As mentioned previously, the material study in section 3.3.1 had indicated that the fibre modulus and behaviour of the isotropic XC-130 was similar in behaviour to the Ansys orthotropic materials that are used in composite structure simulations. After consulting the manufacturers, it was decided to run a composite study on the optimised using the suggested twill and unidirectional layup. For brevity, this setup hasn't been detailed here, but has been explained in Appendix section D.7.

The results of this study were different to the optimisation, but this was ex-

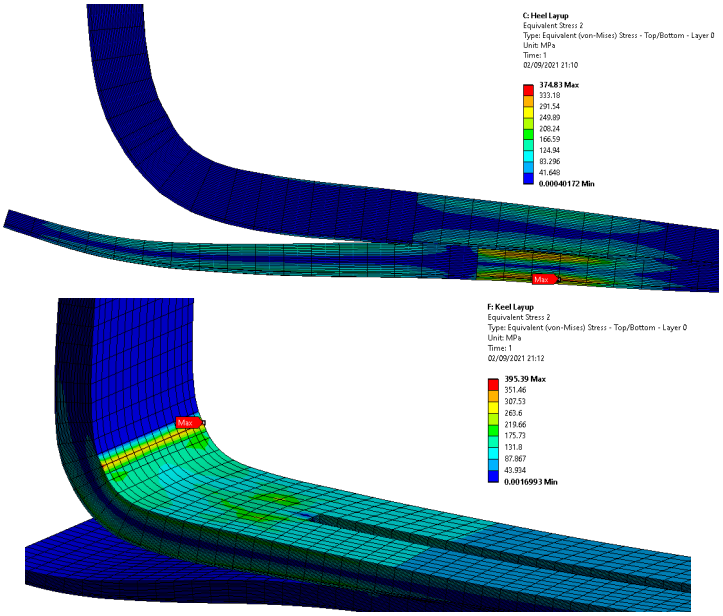


Figure 4.31: Stress results of the full structure, taken from the composite model. Top: Heel loading condition, with a peak stress in between laminates. The ACP module did not indicate that this would lead to failure. Bottom: Keel loading condition. Note the peak stress is occurring on the housing boundary edge and may be deemed as an erroneous FEA artefact.

pected with the switch to a composite material model. Full body stress plots have been included here in Figure 4.31. Peak stress in these were 395.39MPa under forefoot loading, and 374.83MPa for the heel; this amounts to about 20% increase for the forefoot loading. Surface stresses had a larger increase but together with the full body results the peaks have some association with FEA artefacts due to their close proximity to boundary conditions. They can therefore still be judged as relatively safe compared to the yield strength of the material, even if the strength is taken to be the value on the XC-130 data sheet (645MPa) which is less than that of the Ansys database (805MPa). The FoS for the forefoot test is 1.63, and for the heel it is 1.72. Lastly, the deflection results indicated maximum values of 8.43mm and 9.21mm for the heel and keel respectively.

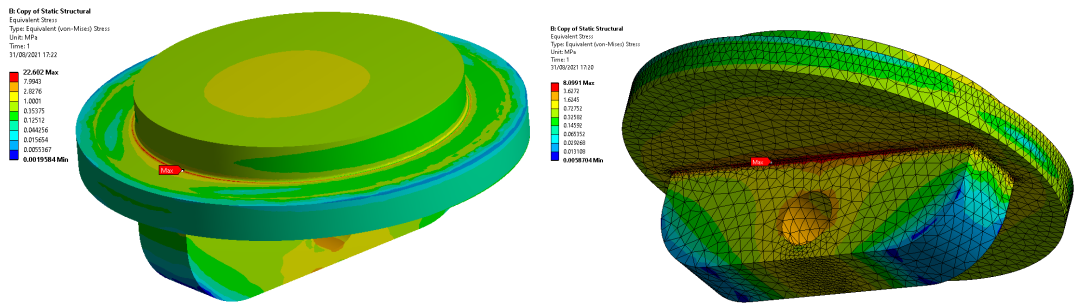
These final simulation results were deemed satisfactory for the performance of the foot structure, locking in the profile shapes and parameter thickness values.

4.3.4 Minor Components

The other minor components were also put through simulations to assess their ability to withstand the loads transferred when compressing the spring. It was decided to start with the spring plate and move down the system, checking each component in turn.

Spring plate & shaft

A basic model of the spring plate was created without the walls to check the compression force on the base and the shaft connection. A fixture was applied to where the spring is in contact with the base and a bearing load representing the maximum reaction applied to the shaft bore. This setup then had the fixture location reversed and the maximum spring load applied to where the fixture was previously. Using the 6082 aluminium plate material, the design withstood the loads on both tests, see Figure 4.32 for stress results. A printable ABS material was also analysed, but this failed the reaction load setup.



(a) (b)

Figure 4.32: FEA results from the spring plate model. Left: Force applied is the bearing reaction load of 302N on the shaft bore. Right: Fixture applied to the bore, and spring load of 287N applied vertically down.

An additional model was created to assess parameters involving the connecting shaft. These were the shaft diameter, shaft length and bushing depth. Using the results, the design was optimised to avoid the primary concern of shaft bending.

Shafts

The shafts all went through strength checks using the reaction forces and torques calculated from the spring deflection. For the pinion and gear shafts, the spacing between components were analysed to avoid stress concentrations in the circlip rings, and performance debilitating deflections. The diameters of all shafts were also examined with the goal of minimising these whilst ensuring a high safety factor. See Figure 4.33 for results of the torque load cases on the pinion and wheel shafts.

The components mounted to the pinion and wheel shaft required strong connections. To speed up this stage of design process, a series of excel calculators based on ISO calculations were purchased from mitcalc.com, which helped select

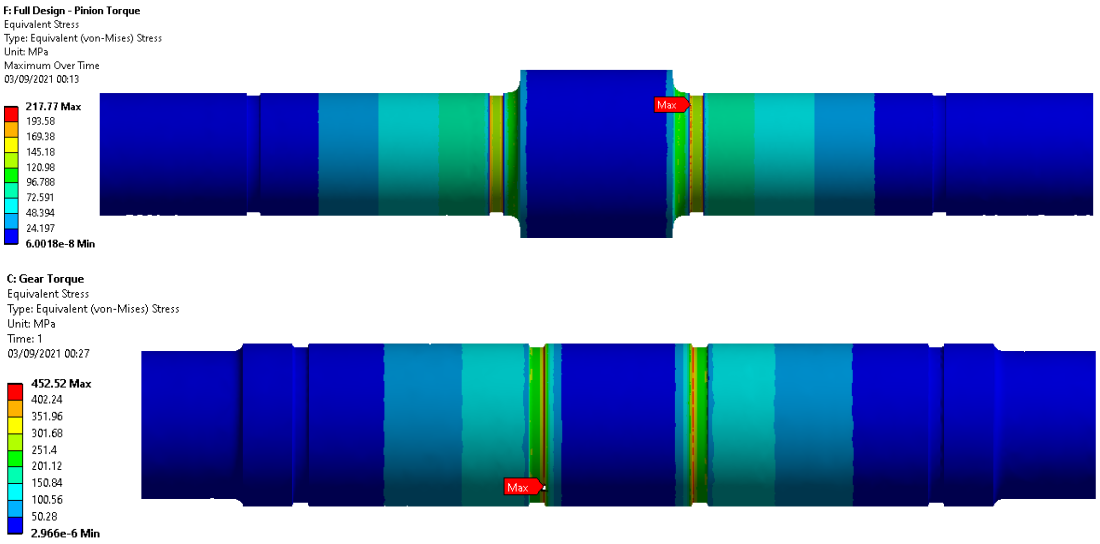


Figure 4.33: FEA stress results for torque load cases on the pinion (top) and wheel (bottom) shafts.

the dimension parameters for spline connections on the wheel shaft for the gear and lever, and link on the pinion shaft, in addition to a key connection for the pinion on its shaft.

4.3.5 Housing

The housing was a component that could have potentially been heavy due to its size. A decision was made to print this body from ABS, which would also allow for an unorthodox shape that would be bespoke to and tightly fit the components it would house. The dimensions were scoped around the spring mechanism, which had its fixture points locked in from the earlier design work. For easy assembly, the design was split in to and given tab features to assist in lining up the two parts. These two pieces would be secured by a series of smaller bolts along the front face, and the bolted connection on the back face to the keel spring; see Figure 4.34.

Bolted Connections

A simulation study was completed to determine the best contact settings for the bolted connections on the front when under a transverse load caused by the spring plate reaction force. A summary of this study has been provided in a table screenshot within Appendices section D.8. From this study, it was determined that the frictional contact resulted in unreliably high stress results, the housing stress was invariant to bolted connection settings. The settings on the bottom two rows of the appendix figure were determined to be the best of the selection, with the bottom

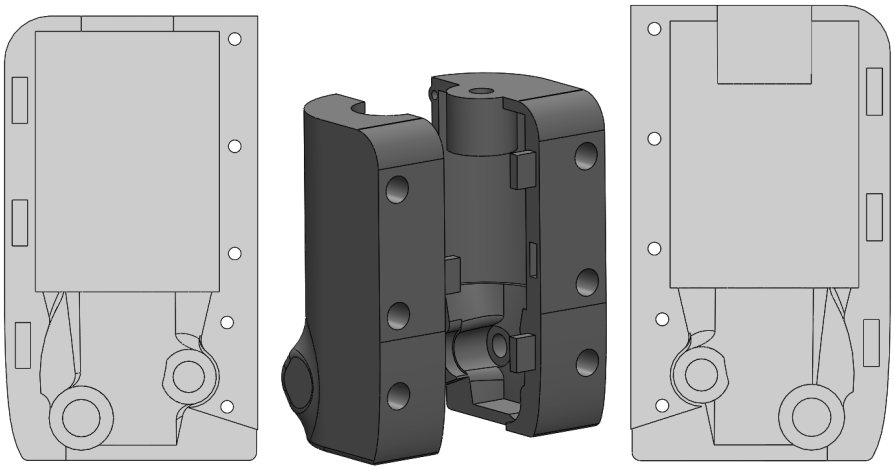


Figure 4.34: Profile views of the housing sections on the left and right. Centre image is an exploded view demonstrating how the parts slot together.

providing a potential worst-case load on the bolt nuts. The connection settings from this study were then used to assess the bolted connections of the housing to the keel, under the full bearing load of all shafts from the spring compression. Variables tested in this study included the type of insert in the housing, diameter & length of the bolt, and number & position of the bolted connections. From the study it was decided to move ahead with helical inserts for six M10x20 bolts. The final stress results on these two simulation studies can be seen in Figure 4.35. The peak stress on the housing is on the rear bolted connection simulation, but this is within the yield of the material; see the properties in table of Appendix section D.2

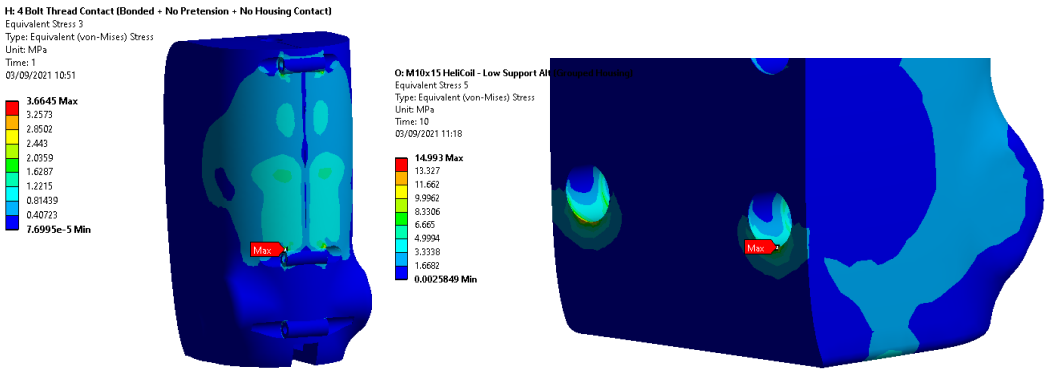


Figure 4.35: Selection of stress results from the housing simulations. Left: front bolted connection housing stress. Right: rear bolted connection showing peak stress on the housing.

4.3.6 Lever Arm

The dimensions of the lever were based upon the requirement of ensuring an angle of rotation of 10°. A table was produced to determine what angles could be produced from combinations of lever length along the hypotenuse and tip deflection, this can be seen in the top image of Figure 4.36. Given the predicted deflection from the keel simulations, a concern was raised on whether this would be enough to guarantee the required rotation should the neutral position of the lever be in line with the foot base. In addition to this, the lever length needed to be long enough so that the mechanism stays active until the push-off event. From the table, a longer lever would produce less rotation for any given tip deflection.

With these considerations, it was decided to set the neutral position of the lever below the base of the foot. The vertical height from centre point of rotation to the foot base was 45mm, and the horizontal length of the lever needed to be 150mm. Based on the table a tip deflection of 20mm would be required to achieve around 7-8° of rotation. It was therefore decided to set the bottom of the lever to be 20mm below the base of the foot, and the rest of the deflection would be accommodated by the deformation of the keel spring.

Angle		Lever length (mm)													
		10	20	30	40	50	60	70	80	100	110	120	130	140	150
Tip Deflection (mm)	2	11.54	5.74	3.82	2.87	2.29	1.91	1.64	1.43	1.15	1.04	0.95	0.88	0.82	0.76
	4	23.58	11.54	7.66	5.74	4.59	3.82	3.28	2.87	2.29	2.08	1.91	1.76	1.64	1.53
	6	36.87	17.46	11.54	8.63	6.89	5.74	4.92	4.30	3.44	3.13	2.87	2.65	2.46	2.29
	8	53.13	23.58	15.47	11.54	9.21	7.66	6.56	5.74	4.59	4.17	3.82	3.53	3.28	3.06
	10	90.00	30.00	19.47	14.48	11.54	9.59	8.21	7.18	5.74	5.22	4.78	4.41	4.10	3.82
	12	#NUM!	36.87	23.58	17.46	13.89	11.54	9.87	8.63	6.89	6.26	5.74	5.30	4.92	4.59
	14	#NUM!	44.43	27.82	20.49	16.26	13.49	11.54	10.08	8.05	7.31	6.70	6.18	5.74	5.36
	16	#NUM!	53.13	32.23	23.58	18.66	15.47	13.21	11.54	9.21	8.36	7.66	7.07	6.56	6.12
	18	#NUM!	64.16	36.87	26.74	21.10	17.46	14.90	13.00	10.37	9.42	8.63	7.96	7.39	6.89
	20	#NUM!	90.00	41.81	30.00	23.58	19.47	16.60	14.48	11.54	10.48	9.59	8.85	8.21	7.66

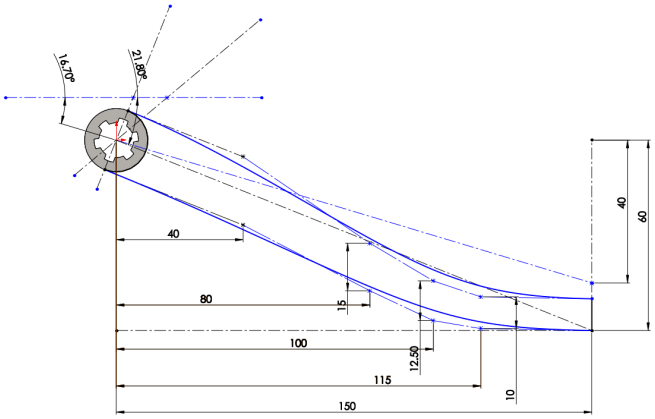


Figure 4.36: Top: Design table generating angles generated for a given lever length and deflection. Bottom: The resulting dimensions used to generate the lever.

4.4 Final Prototype Design

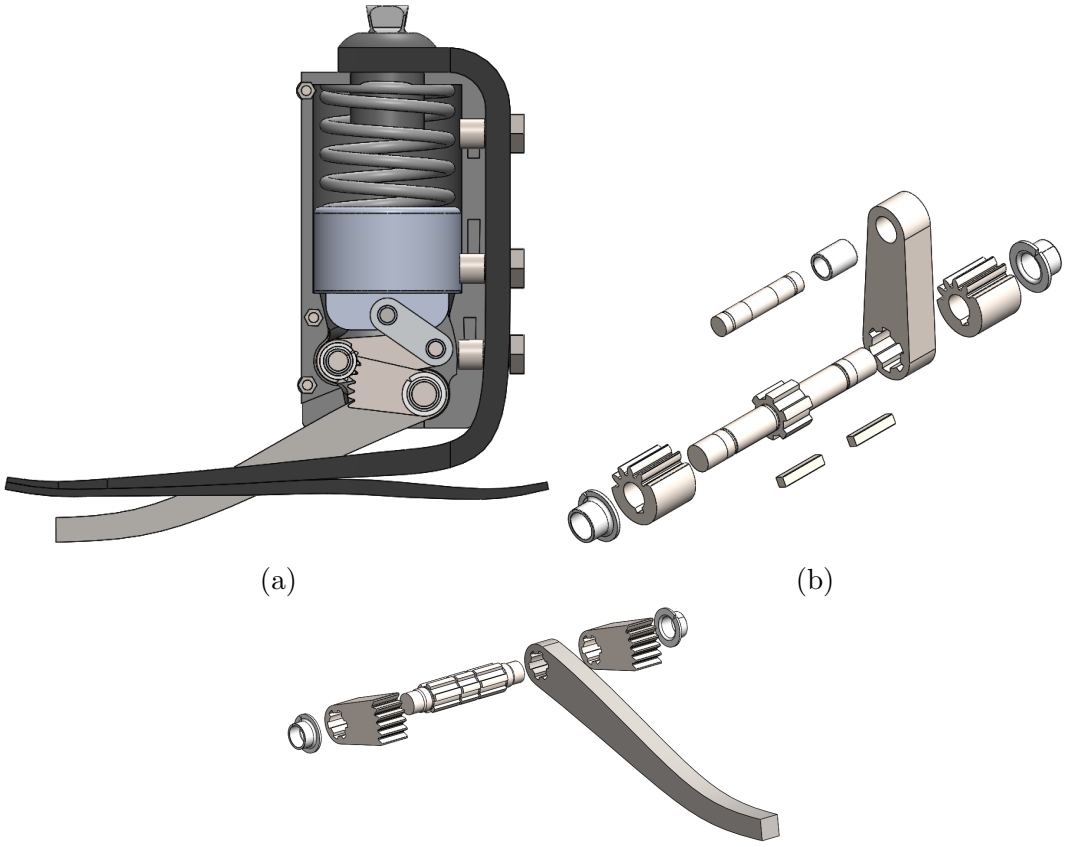


Figure 4.37: Final design CAD renders of the prototype

The final design is presented in this section here, see Figure 4.37. From the material densities applied to the SolidWorks CAD model, the approximate weight of the design is 1.8kg. Whilst this would be too heavy for an everyday prosthetic, it is acceptable for a prototype gait analysis tool used for brief periods under lab conditions. The design is also 220mm long, 185mm high, and 70mm wide, which is more compact than the original concept which was 250x240x80mm.

A hole was bored into the top of the keel and housing unit, the latter of which had a helical insert installed so that a standard pyramid connector was fitted, allowing for a standard connection to prosthetic structures. Teflon coated bushings were inserted into the bore holes of the pinion and lever shaft, providing a reduced friction contact to avoid losses in the mechanism. These bushings were also applied to the link shaft bores. The lever design allowed for the slotted cuts through the keel and heel to be reduced in depth slightly. As mentioned, the housing is secured to the keel with six M10x20 stainless steel bolts, whilst the front of the housing is held together with three M4x20 socket cap screws.

The pinion and wheel gear were cut down such that the only the required number of teeth to achieve full spring deflection are machined. For the pinion, this left enough space on the opposing side to fit the keyway without concerns for



(a) (b)

(c)

Figure 4.38: Section view of the final design showing the mechanism. The other two images are the pinion shaft assembly, and lever shaft assembly.

raising the stress close to the geometry edge. Cutting down the wheel gear was primarily for ensuring the larger geometry would fit within the confined space of the housing, see Figure 4.38.

4.4.1 Manufacture

The manufacture of the prototype was funded through a Global Challenges Research Fund (GCRF) grant. As detailed toward the end of section 4.3.3, a manufacturer for the composite foot structure had already been sourced during the design stage. They produced the tooling mould, and the prepreg XC-130 sheets were shipped to them from the supplier EasyComposites. After manufacture of the proposed design, their engineers proposed a secondary structure be built with the remaining material. This kept the same shape, but the thickness was reduced, see bottom left image of Figure 4.39.

The helical spring had already been shipped from the manufacturer as it was the first component to be designed. A local machinist was used to produce all other



Figure 4.39: Photos of the manufacture prototype. Bottom left is the thinner foot structure built with the remaining prepreg material.

mechanism components, a summary of the materials and finishes can be seen in Table 4.10. They were consulted on the tolerances and fits for the precision parts with technical drawings which can be seen in Appendix section E.4. The precision of the gears, and other mechanism components with tight tolerance fits required them to be machined using Electric Discharge Machining (EDM). The shafts first had their spline connections cut with EDM and were then finished on a lathe. Finally, the housing was printed with ABS on a Stratasys Fortus machine, and the helical inserts installed into the bolt and pyramid connector holes.

Upon assembly of the design, an issue was identified with the housing. When the spring was being compressed, the housing structure was showing signs of opening in the centre. As this was a printed structure, the redesign simply required thickening the front portion such that additional bolts could be used to secure

Table 4.10: Summary of the component materials and finishes used.

Component	Material	Finish
Pinion & wheel shafts	EN40 B	Oil-quenched - Tempered
Pinion & Wheel	EN40 B	Oil-quenched - Tempered
Minor shafts (link and plate)	EN40 B	None
Spring plate	Al 6082	None
Plate links	Al 6082	Anodised
Gear link	EN40 B	Oil-quenched - Tempered

it. This solved the deformation issues under the transverse spring reaction load. These changes to the housing can be seen when comparing the CAD design in Figure 4.37 with the images in Figure 4.39.

4.4.2 Design Specification Appraisal

To conclude the section, the design will be appraised against the design specifications provided in Table 4.1. The estimated mass was found to be 1.8kg, which is above the criteria base, but still within the accepted bounds. It would be expected that this weight could drop in the future. Space constraints were met, with the total height and length, and spring diameter all fell with thin criteria bounds. Height and length were 185mm and 220mm, whilst the spring diameter is 50mm. Energy stored in the spring was lower than desired at between 4.8-6.9J, but this should still have an effect on gait metrics. Lever angle of rotation could only manage 7-8° due to the length. However, this is achieved with 20mm deflection of just the lever. With the estimated toe deflection of 9.21mm, sufficient rotation will be achieved when the gear pair ramp up the angle by a factor of 4. Finally, the foot structure withstood the ISO-22675 strength analysis in the FEA model, estimating FoS of 1.63 for the forefoot test and 1.72 for the heel.

In terms of mechanism effectiveness, the prototype design was put through the full cyclic simulation model, with and without the mechanism. The resulting

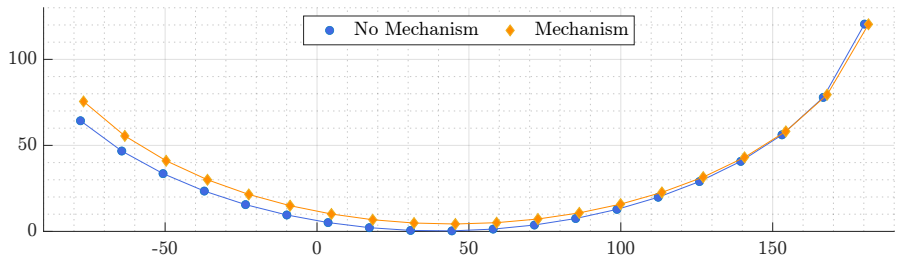


Figure 4.40: Plot displaying rollover shape of prototype, with and without mechanism.

rollover shapes can be seen in Figure 4.40. There is a difference between the data point positions and fitted curve, indicating that there would be a change in the gait metrics once it can be tested in a clinical trial.

4.5 Summary

The design process detailed in this chapter has been thorough. An ISO compliant model developed in Chapter 3 has been used here to optimise a prosthetic foot structure with response surface models. Key components in the mechanism have also gone through extensive parameter analysis and design of experiment refinements to ensure the spring mechanism operates efficiently. The safe design of these components and spring chamber space also provides an opportunity for helical spring to be switched for ones with a varying spring stiffness, which would allow for the exploration of this parameter and its effects on gait metrics.

Chapter 5

Biomechanics Experiments

With a prototype foot designed and ready to test in clinical trials, the final stage in setting up the framework was to develop an experimental method. This chapter begins with an overview of literature explored in Chapter 2, and some insight into experimental methods employed in that published research. A pilot study is presented as the first stage in developing an effective methodology. With the data from this initial experiment, the procedure and setup were refined and a larger sample of subjects were recruited for the main study. Key performance indicators and metrics were derived, and future experimental studies recommended.

5.1 Pilot Study

5.1.1 Justification of the method

With the clear gap in literature on the effects of stiffness on gait initiation (Section 2.3) it would be prudent to explore this direction in clinical trials. With the commentary on issues regarding kinematic analysis, and the effective force plate analysis, it was decided to develop a method that would focus on the latter and build upon the previous knowledge. However, these techniques would be expanded to focus on not just the force generation, but also the impulse and power due to the temporal effects represented in those parameters.

The first stage in developing the experiment was to conduct a pilot study to test the protocol with fewer candidates and develop an analytical method with the data. A rigorous protocol will assist in providing reliable and consistent force measurements.

Within the sports science and rehabilitative physiotherapy industries, consideration has been given to the effect of the subject attention when completing motor

tasks. Providing a dual task to complete alongside the gait initiation helped the reaction time and CoP displacement of elderly subjects with balance control issues [260]. Internal and external focus instructions are another common protocol explored, where internal emphasises the motor task directly, and external on the end goal of a task. The latter has been proven to help stroke patients with their rehabilitative therapy [261]. However, a postural control study found the internal and external commands to be less effective than one that required consistent cognitive attention [262]. Such a result may be linked to the neurological aspect involved during the anticipation of a motor task. When an instruction is clear, a task is completed to a higher standard [263]. This neurological process was seen in other literature when the prosthetic limb was trailing, which required a longer anticipatory period [155].

External focus controls are not always reported as beneficial. In one study it was reported as increasing the variability in gait metrics of elderly subjects [264]. However, the external focus protocol in this study required the subjects to match their gait to a metronome set their regular walking pace.

Arguably this does not fit the definition of an external goal, as the metronome pacing was directly linked to the motor task. A separate study on gait stability also found no benefit to external focus commands, but the researchers identified this could be related to the lack of an external object to act upon [265]. It was decided to define a selection of three protocol instructions to assess in the pilot study: a control, an external focus, and an external focus. These instructions can be found for both initiation and termination setups in Table 5.1

Table 5.1: Instructions for the control, external focus attention (EFA), and internal focus attention (IFA) protocols.

Protocol	Initiation	Termination
Control	Walk off the plate, stop at the end	From the marker, walk onto the plate and stop
External	Walk to the table and place the pen standing upright	
Internal	Pushing off with your trailing foot, walk to the end	Looking forward, walk to the plate making centre clean contact

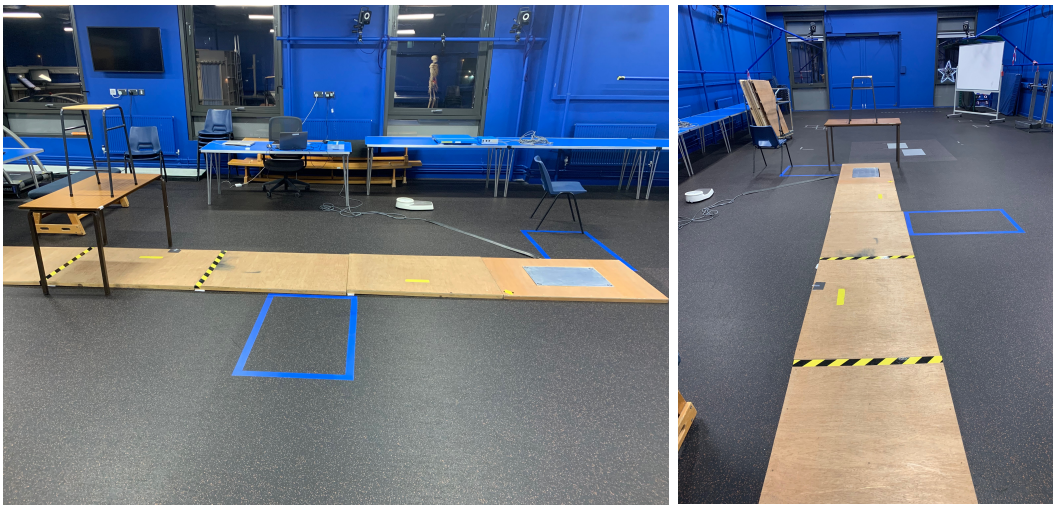
5.1.2 Subjects

All subjects were given an information sheet, and a consent form and health to questionnaire to complete before data collection. These documents can be found in a link provided in Appendix section F.1, together with the ethics application submitted and given approval to run the study. The five subjects were all male, 28yrs $\pm$ 2.3, 1.76m $\pm$ 0.12, and 89.2kg $\pm$ 16.3.

5.1.3 Method

The walkway was setup with four 1m long wooden platforms, one of which had a cut-out for a force platform. This force plate was a Kistler type 9286AA, with the single received by a 16-channel Kistler Data Acquisition (DAQ) system, which itself was plugged into a laptop with the Kistler Bioware recording software. The recording frequency was set to 1000Hz, and the recording length 10 seconds.

Subjects wore their chosen footwear as instructed on the participant information sheet. They were instructed to have a few practice runs to identify an appropriate starting point for the gait termination trials; this was marked with tape on the board. A table and chair were placed at the opposing end from the starting position; for initiation this was at the termination starting marker, and for termination this was at the far edge of the force plate. See Figure 5.1 for photos of initiation and termination activities.



(a) (b)

Figure 5.1: Left: Gait initiation, with subject starting on plate and walking to the table. Right: Gait termination, where subjects starting on the first board seen at the bottom and walk to the table and force plate at the other end.

For both setups, the subjects were instructed to select the one foot they felt most comfortable with leading during the practice runs. This ensured the same foot would produce the push-off for initiation, and starting from the marker, the same foot would hit the plate for at termination. Each setup had the subjects run five successful trials, with the criteria being a clean reaction force generated. The start of each trial was initiated with the relevant command based on the protocol and gait task, see Table 5.1.

5.1.4 Data Analysis

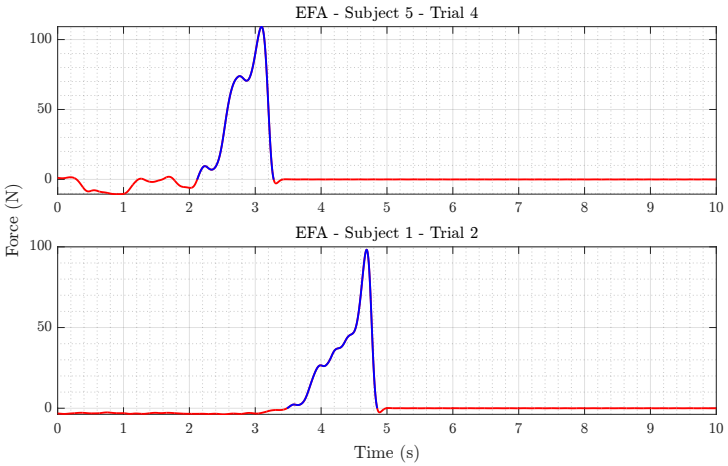
The trial data was exported from the Bioware software into .txt files that were read by a MATLAB script and set up as data matrices. A discrete Fourier transform was applied to the force data to discover a cut-off frequency of 5Hz for a zero-phase, second-order low-pass Butterworth filter, which was applied to all trials and subjects.

Time-slicing the data

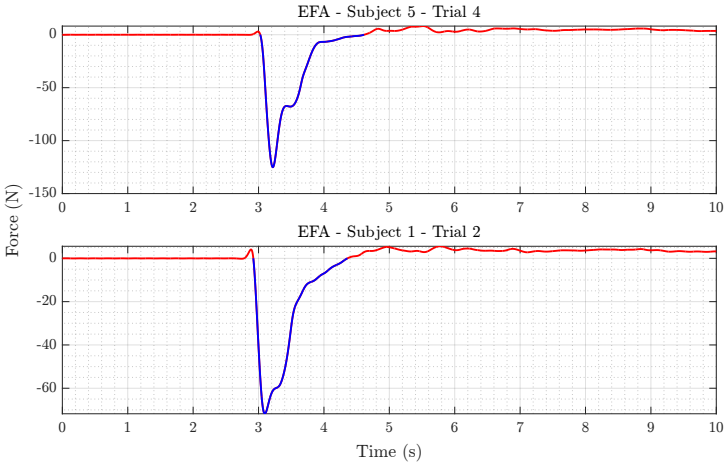
Once the data was filtered, the code could be applied to time-slice the data. The detection of when gait starts is vital in generating realistic and accurate parameters that are derived from integrating the force time domain. An error in detecting the point of this start can result in misreporting metrics such as the power generated. For powered prosthetics, generating the detection signal in timely manner is required for the sophisticated control system to make adjustments for the motor task. Solutions for this have involved the use of kinematic and Electromyography (EMG) sensors detecting inertial movements and muscle activation patterns [266, 267]. However, such methods are unnecessarily complicated for simple force plate analyses. In the previously mentioned gait initiation studies, various methods have been employed:

- Time between onset of increased swing limb vertical forces and termination of stance limb vertical forces [73].
- Once the CoM acceleration passes a certain threshold, the exact value of which is unreported [155].
- Visual identification of leading limb toe-off from video recording, or kinematic markers [70, 224].
- Medial-lateral CoP displacement [268].

It was decided that a slightly different method to the CoM acceleration threshold would be explored in the pilot study. Given that the parameter is simply anterior-posterior force divided by the subject mass, the detection can be made on just the force instead. The average was taken during a stationary period and set as the threshold. Initiation start point was when the force passed above the threshold, and termination when the force passed below the threshold. The end points of these phases were defined in the same manner, see Figure 5.2 for examples of sliced force.



(a) Gait Initiation



(b) Gait Termination

Figure 5.2: Time sliced data of two subjects completing single trials of both setups. Line section coloured blue is the time-sliced portion used in the calculation of gait metrics.

With the force data sliced, the gait metrics could be calculated:

- CoM acceleration:

$$a_{CoM} = \frac{Force_{AP}}{m_{subject}} \tag{5.1}$$

- CoM velocity:

$$V_{CoM} = \int apGRF \; dt \tag{5.2}$$

- CoM power:

$$P_{CoM} = apGRF \cdot V_{CoM} \tag{5.3}$$

- Total CoM work:

$$W_{CoM} = \int P_{CoM} \; dt \tag{5.4}$$

- CoM impulse:

$$I_{CoM} = \int apGRF \; dt \tag{5.5}$$

As this pilot study was concerned with test-retest reliability, the subjects data was statistically analysed. Peak values of force and power were calculated to go alongside the final velocity, impulse and total work calculated in the listed equations 5.2, 5.4, and 5.5. Subjects trials were averaged for each condition. The data was also normalised to subject mass so total result set averages could be compared between protocol instructions.

A two-way ANOVA test was completed on the gait metrics, with the raters set as number of trials. The mean squares for the row and column interaction and the mean square error were then used in the calculation of Intra Class Correlation (ICC) values. These correlation values have different equations forms depending on the experiment setup, and so a guide was consulted to select the most appropriate version [269]. Using this article, a Two-way random effects, for a single rater, where the absolute agreement is important; this is given the convention ICC (2,1) and the equation is:

$$ICC(2,1) = \frac{MS_R - MS_E}{MS_R + (n_k - 1)MS_E + \frac{n_k}{n_s}(MS_C - MS_E)} \tag{5.6}$$

Where MS_R is the mean square for rows, MS_E is the mean square error, MS_C is the mean square for columns, n_k is the number of measurements, and n_s is the number of subjects. This stat was calculated for all peak values of the gait metrics.

5.1.5 Results

The data was run through the automated MATLAB script and processed into metric results to gauge the test-retest reliability of the different instruction protocols. Boxplots were generated for the the peak anterior force, velocity, power, work, impulse, and the duration of the initiation or termination period. Figure 5.3 has the results for the gait initiation trials for all five subjects under the three protocols. Values are not normalised as the comparisons are made within within-subject for each parameter. There does not appear to a consistent pattern in protocol response across-subjects for the peak force, whereas the duration of force application has a larger range. Across the other parameters, subjects have an increased propensity protocol ranges to overlap, whilst also having a smaller range of the dataset. Of all the parameters, impulse generated seems to be highly con-

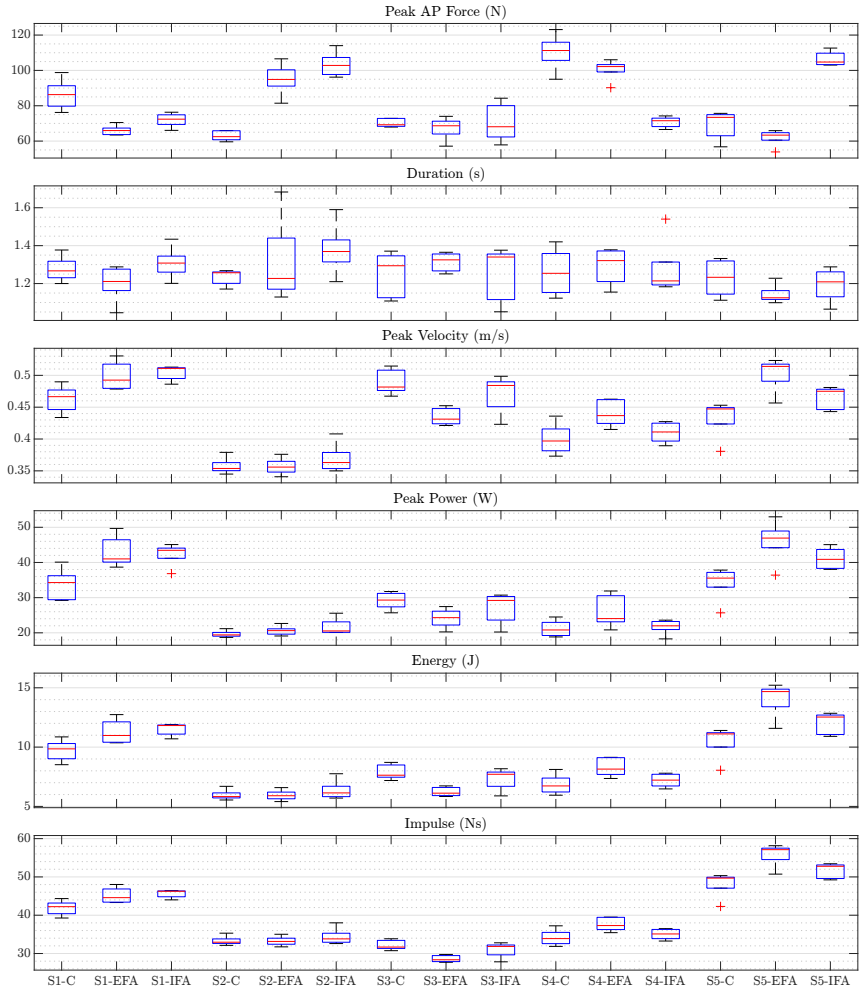


Figure 5.3: Box-plots of the key gait metrics under the initiation task. The subject is presented along the x-axis, where S1-C refers to Subject 1 - Control protocol. EFA is the external focus, and IFA the internal focus.

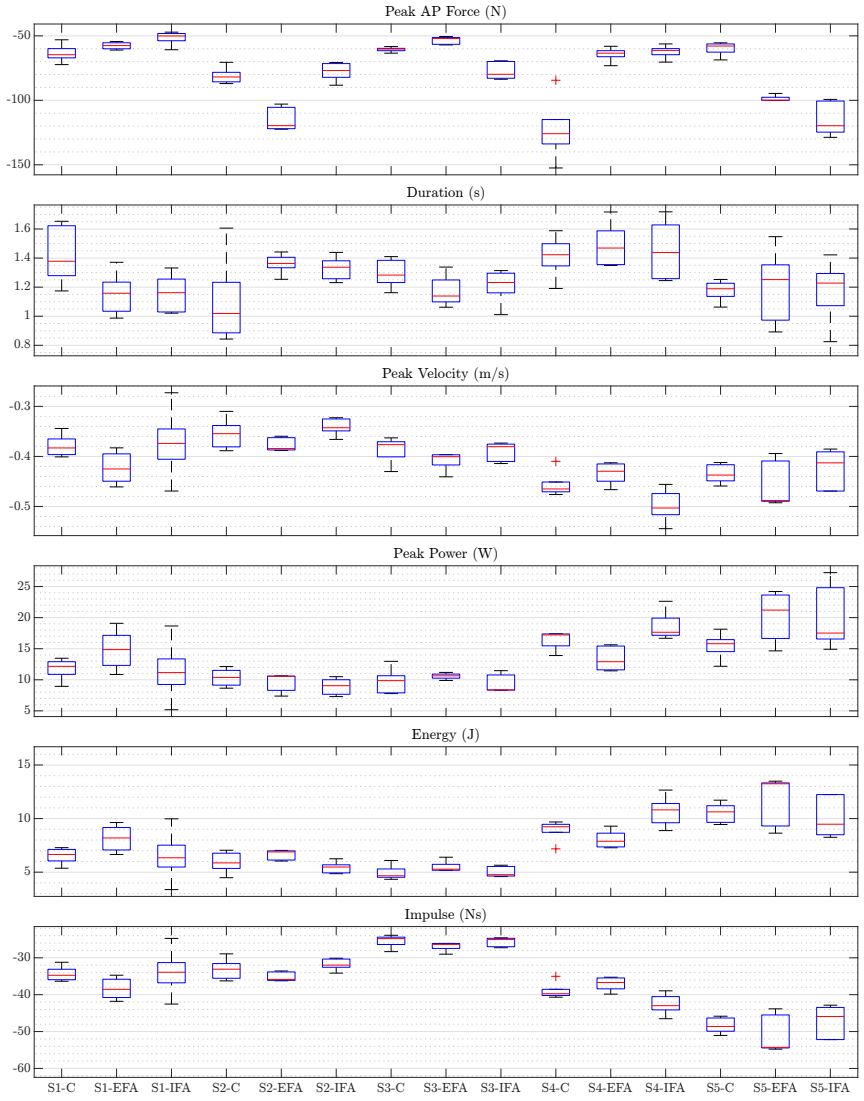


Figure 5.4: Box-plots of the key gait metrics under the termination task. The subject is presented along the x-axis, where S1-C refers to Subject 1 - Control protocol. EFA = external focus. IFA = internal focus.

trolled across all protocols for each subject. Subject 5 appeared to have increased difficulty with consistent gait metrics for the internal and external focus.

The same set of boxplots were generated for the gait termination task and can be seen in Figure 5.4. Similar trends were seen with narrower force ranges and larger variation in duration of gait event. For most subjects, the ranges across the three protocols were closer together than they were for gait initiation. However, subject 5 appeared to again have difficulty with the consistency of derived gait metrics for the internal and external focus.

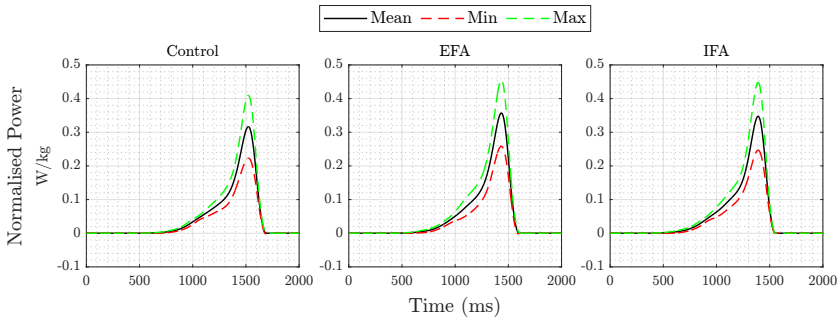
Intraclass correlation statistics were generated for the peak values in the box-plots using Equation 5.6. These values have been presented in Table 5.2 and

Table 5.2: Table of Intraclass correlation ICC(2,1) results for gait metrics in both initiation and termination activities.

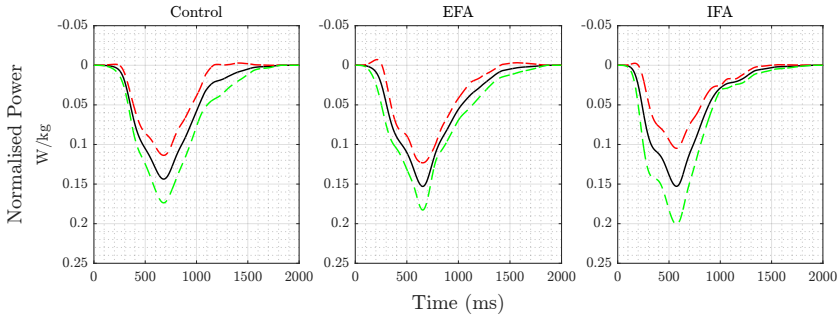
Metric	Gait Initiation			Gait Termination		
	Control	External	Internal	Control	External	Internal
AP peak	0.8296	0.8699	0.9305	0.9377	0.8345	0.9193
Velocity	0.8391	0.8954	0.8662	0.7145	0.4679	0.6684
Impulse	0.9121	0.9686	0.9605	0.9325	0.8929	0.8332
Power	0.7990	0.8858	0.9124	0.7242	0.7184	0.6875
Work	0.8110	0.9353	0.9222	0.8658	0.7569	0.7386

represent the test re-test reliability of the methods to have absolute agreement between trials. Under gait initiation, the force and power were most consistent with the internal focus instruction, whilst external focus produced a tighter spread of values for velocity, impulse, and work. Under gait termination, the external focus had the lowest rating in peak force and velocity. For this gait task, the control protocol produced the most reliable results across all gait metrics.

As a final measure of the protocol differences, the subject power profiles were normalised to mass and then aligned to the peak values. With the curves aligned,



(a) Gait Initiation



(b) Gait Termination

Figure 5.5: Mass normalised power curves for all subjects and trials under each protocol instruction. EFA = external focus of attention. IFA = internal focus of attention.

mean, maximum, and minimum curves were produced for each protocol instruction using all subject data. These curves can be seen in Figure 5.5. The mean curves under the external and internal protocols are higher than the control for both gait tasks. For gait initiation, the external and internal peak means are similar at around 0.35-0.36W/kg, with the min and max peaks also having a similar range between the protocols. The max and min range for all three protocols appears to be similar, at approximately 0.19-0.2W/kg. Gait termination protocols have similar mean peaks at around 0.14-0.15W/kg, but the ranges fluctuate much more between protocol sets. This is noticeable so when comparing the IFA range of 0.1W/kg to the EFA range of 0.05W/kg.

5.1.6 Discussion

The results collected in this pilot study offer plenty of data points to use in assessing the test-retest reliability. Intraclass correlation values are an effective metric to judge this. Literature indicates that smaller samples with less repeats can affect the accuracy of the ICC score. Values below 0.5 are poor, between 0.5 and 0.75 is adequate, between 0.75 and 0.9 is good, and above 0.9 is excellent [269]. Given that this pilot study includes only five subjects, some criticism can be directed to the precision of the values reported here if the distribution of the subjects from the population is narrow. The subjects formed a convex distribution, with the upper and lower bounds of mass represented by two subjects, and the other three placed around the median. This type of distribution has been shown to under-predict the ICC [270]. Other papers have indicated that a smaller sample size can still return precise correlation values with a statistical power >80% by increasing repeat measurements, or by increasing the null and alternative hypothesis estimations. [271].

There are methods to check whether the ICC value is reliable [272]. Under the absolute agreement form of the two-way random effects model, both random and systematic error are considered. If the model considering consistency produce a similar value, then the systematic differences are small. This was tested on the anterior-posterior peak forces under the control condition. The two-way random effects model with consistency (3,1) was used and found $ICC_{Inititation} = 0.8439$ and $ICC_{Termination} = 0.9477$, both marginal increases of the values seen in Table 5.2.

In addition to the above, the effect strength and p-values of the two-way ANOVA models can be checked. These models generate the mean square values used in the ICC calculations. With an $\alpha = 0.05$, almost every data set failed

Table 5.3: Table of Intraclass correlation ICC(2,1) confidence intervals with α=0.05, for gait initiation.

	Control		External		Internal	
Metric	Lower	Upper	Lower	Upper	Lower	Upper
AP peak	0.5484	0.9774	0.6199	0.9834	0.7851	0.9915
Velocity	0.5616	0.9789	0.6894	0.9868	0.6139	0.9829
Impulse	0.7356	0.9891	0.8904	0.9963	0.8709	0.9953
Power	0.4884	0.9727	0.6558	0.9856	0.7359	0.9891
Work	0.5154	0.9745	0.7882	0.9921	0.7632	0.9904

to show a significant effect across trials, and as expected indicated a strong effect across subjects. However, the gait termination under the external focus protocol demonstrated some effect across the trials which places doubt on the precision of the ICC values generated.

Finally, the confidence interval of the ICC values can be calculated [273, 274]. Setting $\alpha = 0.05$, these confidence intervals were calculated for all metrics and have been presented in Tables 5.3 and 5.4. The upper bounds of all metrics across both the studies are high as the estimated values in Table 5.2 are all large in value. It is the lower bounds which show the uncertainty in method reliability. For gait initiation, the lower bounds on the control protocol drop close to 0.5, except for the impulse. The other focus protocols appear to be more closely matched, echoing the same trends in Table 5.2, the internal focus was tighter bounds for the peak force and power. Gait termination intervals in Table 5.4 indicate significant issues with reliable velocity or peak power for all protocols. The control instruction has the narrowest interval bounds.

The results of the ICC tests can be related back to the boxplots of Figures 5.3 and 5.4. Of all the metrics tested across the protocols, the impulse value is

Table 5.4: Table of Intraclass correlation ICC(2,1) confidence intervals with α=0.05, for gait termination.

	Control		External		Internal	
Metric	Lower	Upper	Lower	Upper	Lower	Upper
AP peak	0.7961	0.9924	0.5331	0.9783	0.7524	0.9900
Velocity	0.3456	0.9585	0.1256	0.8955	0.2976	0.9492
Impulse	0.7909	0.9917	0.6509	0.9867	0.5465	0.9780
Power	0.3756	0.9600	0.2829	0.9597	0.3129	0.9530
Work	0.6271	0.9827	0.3928	0.9659	0.3839	0.9625

the most consistent, even for the termination motor task. This parameter can be seen to have significantly smaller subject ranges. Subjects 1 and 5 who show some inconsistency with other metrics, had a relatively tight control over the impulse. With the force and duration of application being the two controlling factors of impulse, the relatively larger range of the duration would indicate that an increased temporal control is applied by the subjects to maintain a consistent impulse; an adaptation amputees have demonstrated in accounting for lost push-off amplitude [70]. A similar trend can be seen in the work and power data, where the ICC estimates and confidence intervals for work are higher and tighter than the power, which can also be seen to fluctuate more across subjects and protocols.

The purpose of this pilot study was to determine the most suitable protocol to produce reliable results. For gait initiation the choice falls between the internal and external focus protocols. Under the external focus, the impulse, velocity, and work show marginal improved reliability, and the internal produces more consistent peak force and power. However, this latter trend could be related to the instruction seen in Table 5.1. Directing the subject to push-off with the trailing foot, has resulted in more consistent peaks. When the power is normalised to subject mass, and full dataset means are taken, the differences between these means and even the min/max curves are small; see Figure 5.5. This indicates an effect caused by subjects themselves. Given the difference between subject variation, it is possible that the consistency of results came down to a subject preference.

A series of Bland-Altman plots were generated using the external and internal focus metrics, see Figure 5.6. These diagrams are used to show the agreement between two different methods by plotting the average of the measures against the difference. The mean and confidence intervals for the difference are also plotted. This mean line indicates the average difference between the two measures, whilst the intervals specify the expected range. Using these lines, the arrangement of data points around them can help to infer the similarity between methods, or where the statistical differences are occurring [275].

In the force, power, work, and to a lesser extent impulse diagrams, the split between the subjects can clearly be identified by the grouping of the scatter points. This doesn't exist in the velocity, and by inference can be attributed to the subject mass. If the force, power, and work data is normalised to subject mass and plotted again in the diagram, the grouping disappears, see Figure 5.7.

The mean difference line being slightly above or close to zero on all metrics is an indication that on average the EFA method will produce marginally higher

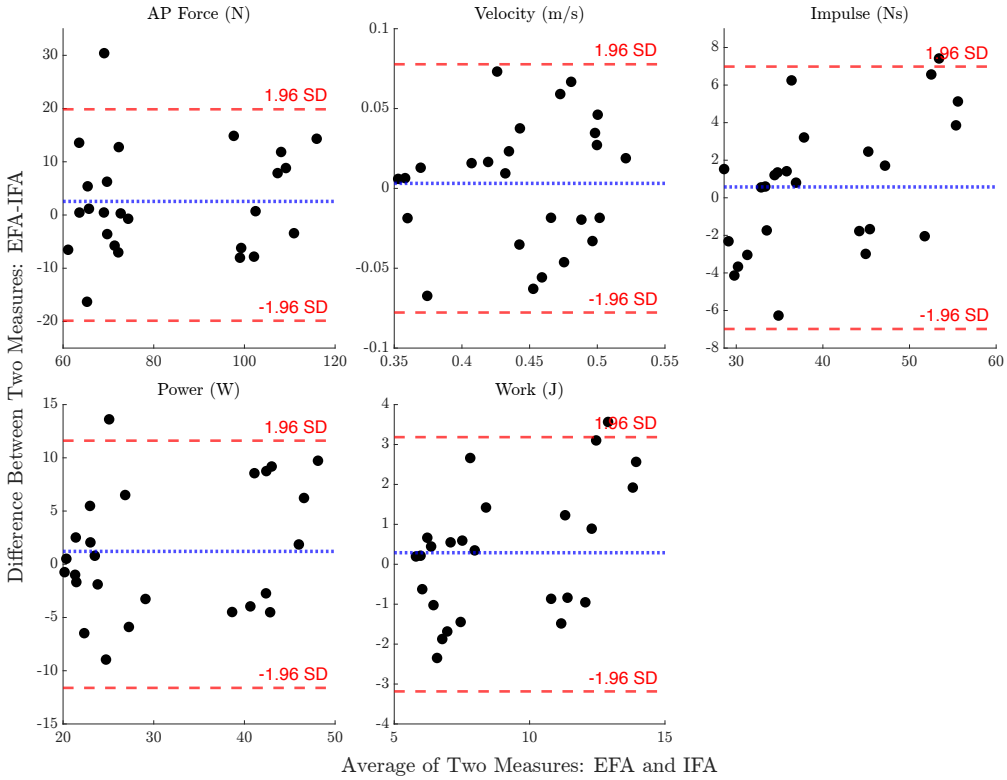


Figure 5.6: Gait metrics plotted in Bland-Altman diagrams. These are useful for determining agreement between two measurement methods.

values, and that there is little systematic error in the values. If scatter points lie close to this mean line, then it can be said that the methods also have good agreement. More points above or below indicate a bias towards a single method. The normalised force indicates good agreement at lower values with the IFA side having scatter points more proximal to the mean line. The difference between measurements increases as the magnitude average increases, and this can also be seen in the normalised power and work diagrams.

This trend and the relatively even distribution of scatter points across the mean suggest that both protocols struggled with consistent results when the magnitude of the metrics was larger; an effect that can be corroborated by the plots in Figure 5.5. Overall, it is difficult to determine which method is more reliable. However, two protocols cannot be used in a larger study, and it was decided that the external focus protocol would be used with some additional tweaks to the methodology.

Under the gait termination motor task, the external and internal focus protocols were far less consistent with results in comparison to the control protocol. It could be argued that these instructions were too distracting for the subjects. Knowing that the plate needed to be hit, the external focus runs may have involved many minor adjustments as the neurological control system is aiming to

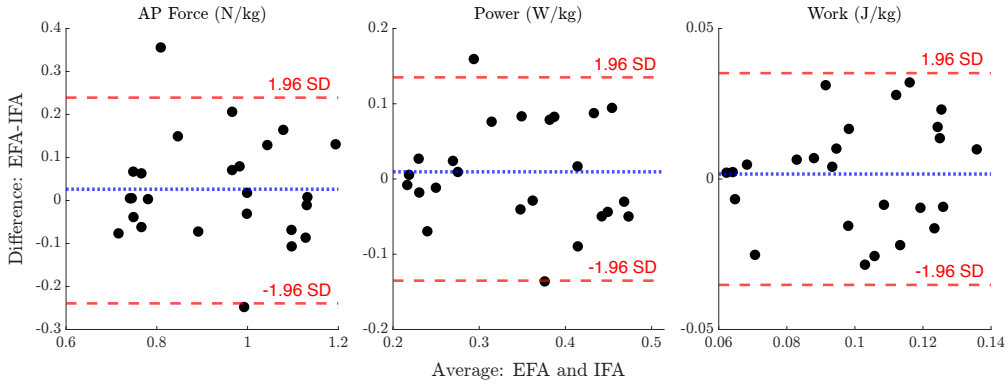


Figure 5.7: Mass normalised peak force, power and work plotted on Bland-Altman diagrams. This removes the grouping of data seen in Figure 5.6.

hit the plate and also balance a pen at eye-line. These tasks could conflict, and the resulting adjustments would be highly variable from trial to trial. With the internal focus directing clean contact be made, this could also cause last minute adjustments to be made. Such effects have been seen in studies that focus on force plate targeting.

Should a subject change their step length in apprehension of hitting the plate, then the magnitudes of vertical and horizontal components can be significantly altered. Although the time duration of the step remains unchanged, and the magnitude differences occur mostly during the initial weight bearing [276]. Other studies have found the anterior-posterior forces to be the most sensitive [277], which is possibly linked to adaptations made in braking and subsequent propulsion. The changes in step length are typically made with the final "target" step, but the effects can be minimised with an effective instructional protocol and averaging the time domain results over from several trials [278]. More detailed studies have shown that the heel to target distance variability decreases on approach to the target plate, but no significant ($p < 0.05$) effects were seen on the gait parameters. As was the case in a previous study [278], adjusting the start position on a subject basis removed all effects on gait measures [279].

These results corroborate some of the issues seen with the gait termination trials. The subject specific starting marker was employed for all protocols, but the simpler instruction from the control instruction helped reduce the neurological uncertainty upon approaching the plate. It would appear that using a subject specific starting marker and less complicated instructions would result in a more reliable set of data.

Limitations and general comments

There are some limitations to the study. Firstly, the low number of subjects used, which could lead to extreme trial values skewing the reliability metrics. As already noted in the discussion, subjects 1 and 5 appear to have a larger range of values in the boxplots, notably so for the gait termination task. However, the other subjects also displayed some variation albeit less frequently occurring.

During the data collection, notes were taken on subject feedback. Most admitted to focusing on the plate during gait termination trials, even under the instruction to look ahead. There was also an issue with the gait initiation trials, with subjects exhibiting considerable rocking motion prior to stepping off the plate. This can be seen in the top example of Figure 5.2 and caused issues with clearly defining the gait initiation point.

Going forward, some adjustments were made to the protocol. With the external focus selected for gait initiation, it was decided to remove the pen balance aspect, and instead simply place a target for the pen to be placed upon. The reason for the change was subjects would take time at the end of the trial trying to balance the pen. As the external focus purpose was to distract the subject from the motor task, a simpler instruction was given. To resolve the balance and rocking issues before initiating gait, subjects should be instructed to remain still for a period of time, and then given the instruction to walk. It would be helpful to test this modified protocol on a larger number of subjects and re-assess the reliability of measurements. Finally, the inclusion of a second force plate would allow for additional metrics to be derived for later use in amputee studies.

5.2 Larger Study

As mentioned in the comments concluding the last section, a larger study would be completed with slightly revised protocol. The main objective would be to re-assess the test-retest reliability and see if the pilot study statistics still hold true. A secondary objective would be to define a set of gait metrics to be used in future amputee studies.

5.2.1 Subjects

The full set of recruited subjects were used in this study. Including the five that were used in the pilot study, the total number for this experiment was 26. As an extension of the pilot study, this larger subject group included 8 female subjects

alongside 18 males; 26yrs $\pm$ 2.1, 1.73m $\pm$ 0.12, and 78.4kg $\pm$ 16.8. All subjects had been given the documents from Appendix section F.1 to read and sign.

5.2.2 Method

The revised method utilised two force plates so that the leading foot force data could be captured. These force plates were originally placed in close proximity to each other and were then moved based on the subject's natural step length to ensure clean contact. Unlike the pilot study, the wooden platform was cut shorter, with a 1m long raised section and 1m ramp. However, the total length from starting position to the table remained the same, see Figure 5.8. Data acquisition rate was kept to 1000Hz for a 10 second period.

Modifications were made to the protocol to fixe several issues from the pilot study:

- Subjects were instructed to stand as still as possible until the instruction to go was given.
- Once the data collection period was started, the instruction to go was not given until after 5 seconds.
- A marker was placed on the table edge closest to the walkway, and subjects were given a small object to hold.
- The new instruction given was: "Walk to the table and place the object on the centre of the marker"



Figure 5.8: Force plate and walkway setup for the larger study.

By instructing subjects to remain still and waiting 5 seconds before moving, the data should be less noisy which will facilitate easier time slicing of data. Each subject would provide ten sets of data, five with the left foot leading and five with the right. Subjects were permitted to practice walking across the plates to ensure good placement for step length, and familiarity of ambulating down the ramp.

5.2.3 Data Analysis

The data was analysed using modified versions of the MATLAB script from the pilot study analysis, with all force data passing through a second-order 5Hz low-pass Butterworth filter. Due to the changes in subject behaviour prior to gait initiation, the method of determining initiation with the average defined time start points too earlier. A built-in MATLAB function, *findchangepts*, was employed which searched for changes in the standard deviation. This was equally as effective, see the example given in Figure 5.9.

With the increased data samples, further comparisons could be analysed. Firstly, the effect of calculating metrics with and without combining the force plate data. As per the literature in Section 2.1.3, mechanical work is more accurately predicted if the feet are analysed separately [89]. That analysis will be extended to explore changes of all gait metrics in the pilot study using ANOVA. The other major objective is to define symmetry metrics that can be used in future studies. Differences between peaks of force, impulse, and power have been

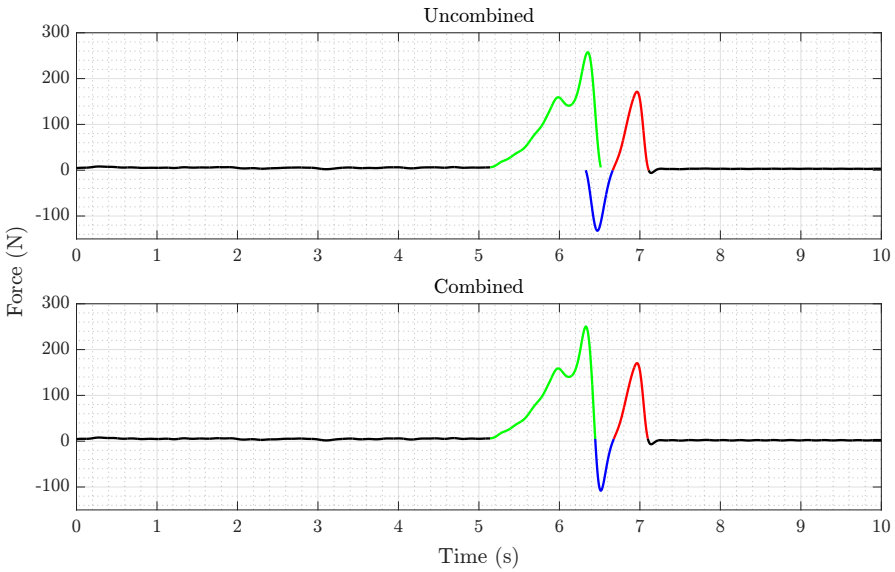


Figure 5.9: Example trials displaying the time sliced data for when the plate forces are un-combined and combined. Green = Trailing foot push-off. Blue = Leading foot braking. Red = Leading foot push-off.

calculated and tested against the mechanical external work.

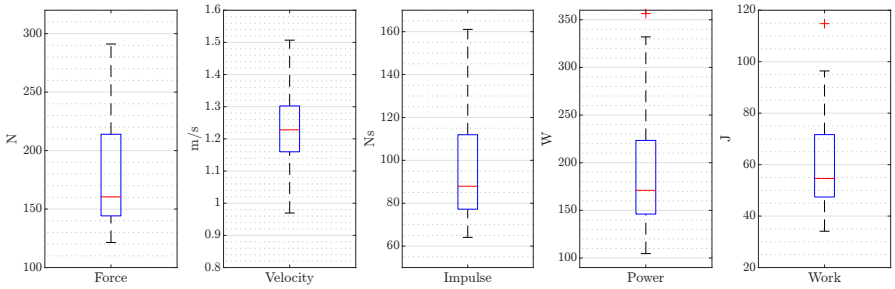
5.2.4 Results & Discussion

Uncombined & Combined Plate Data

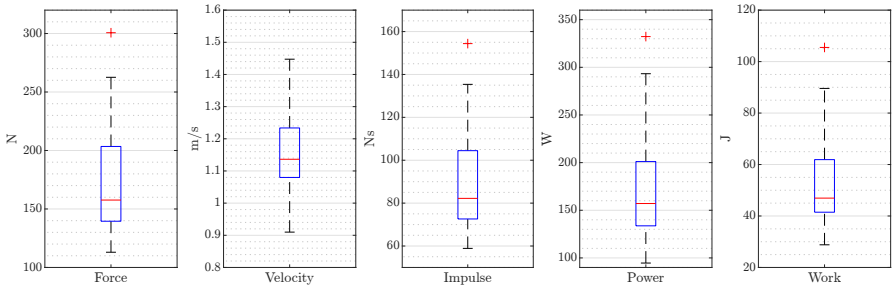
Comparison between the uncombined and combined force data used subjects peaks generated from the means of all trials N_t=10. These were then configured into boxplots of each gait metric which can be seen in Figure 5.10. For all metrics, the combined method is lower in value, with some narrowing of the minimum and maximum. Medians and 75th/25th percentile ranges do not appear to change between the methods.

Other than velocity, the ranges between the 75th percentile and maximum are larger than between the 25th percentile and minimum. The extreme outliers in the data also only occur beyond the maximum, with the combined data method appearing to be more sensitive to their definition. In itself, the velocity appears to be well distributed about the median.

It is likely the extended upper quartile is caused by the heavier portion of the subjects, as the velocity has no mass component in the units. In general, the crossover between the ranges indicates minor differences between the two methods.



(a) Un-combined Data



(b) Combined Data

Figure 5.10: Box plots of key gait metrics. Peaks were defined for all subjects and trials. Data was then averaged across the trials for subjects means. These were then used to generate the box plots.

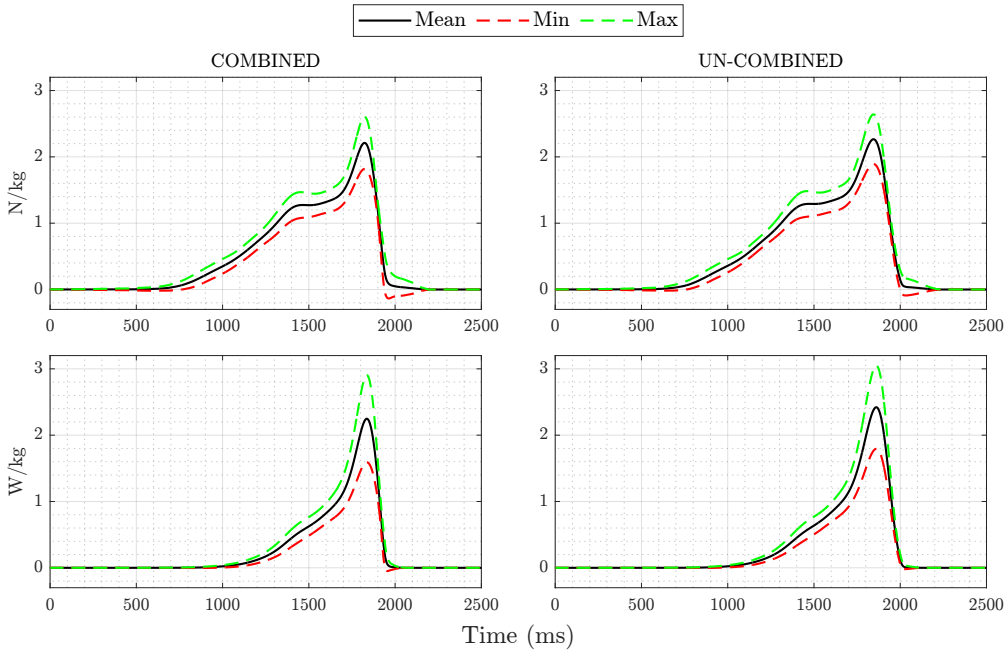


Figure 5.11: Mass normalised force and power curves. Subject data is averaged across trials, and peaks are aligned. Curves of mean, minimum, and maximum data points are then generated and plotted.

The mass normalised plots of force and power have been derived and plotted in Figure 5.11. No noticeable changes can be seen between the force plots of the two methods, with the maximum, minimum and mean peaks falling within 0.1N/kg of each other. Power curves are also similar, but there is a small narrowing of the range for un-combined plates, which can also be seen in the boxplots of Figure 5.10.

These figures so far have only provided a visual comparison. More robust statistics were employed to determine a significant difference between the peaks. Bland-Altman diagrams were generated to determine how different the data was, and agreement between the two methods; see Figure 5.12. Across all the metrics, the mean is skewed negatively which indicates the combined method as calculating lower peaks. However, the magnitude of theses biases is small relative to the scale of the average measures. The spread of the scatter points fit mostly within the confidence intervals, but not tight to the mean, which suggests random error remains equal. Two-sample t-tests were completed on the subject trial means for all metrics; the null hypothesis being that the data comes from random samples. With an $\alpha = 0.05$, the test failed to reject the null-hypothesis on almost every metric apart from the velocity which returned $p = 0.026$.

A final set of statistics generated in this comparison are intraclass correlations

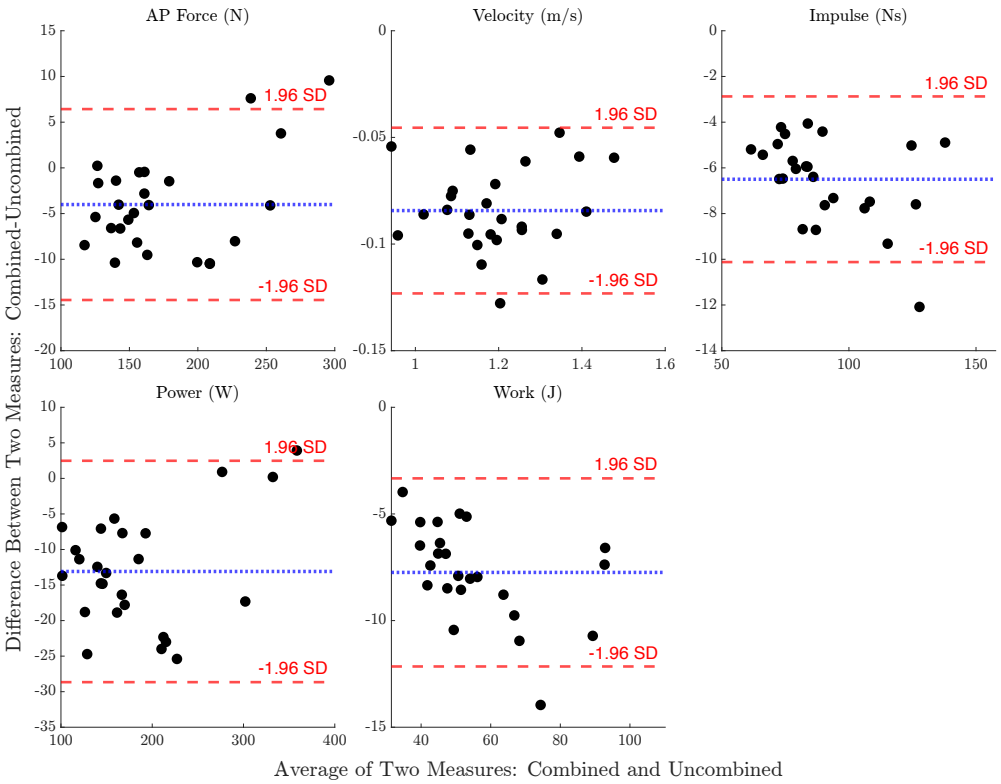


Figure 5.12: Bland-Altman plots of the gait metric peaks, comparing differences between combined and un-combined plate forces.

for each metric. The previous set of figures have helped determine little statistical difference between the two methods. As such these ICC values are not to adding to that conclusion. Instead, they are for comparison to the pilot study values to assess whether the method has remained reliable with an increased number of subjects. The same equation 5.6 was used again, with the error metrics generated with 2-way ANOVA models, the results with confidence intervals can be seen in Table 5.5

Table 5.5: Table of Intraclass correlation ICC(2,1) results for gait metrics from the main study. Both force plates data methods are shown with the 95% confidence intervals.

	Combined			Un-combined		
Metric	Lower	ICC	Upper	Lower	ICC	Upper
AP peak	0.8326	0.8943	0.9431	0.8464	0.9035	0.9482
Velocity	0.7013	0.8013	0.8881	0.7072	0.8056	0.8908
Impulse	0.9254	0.9546	0.9762	0.9339	0.9599	0.9790
Power	0.7941	0.8680	0.9280	0.8031	0.8743	0.9316
Work	0.8448	0.9025	0.9477	0.8541	0.9087	0.9511

The differences of reliability between the two methods are insignificant, as expected from the prior statistics. A key finding here, is that the reliability of the gait metrics has not drastically changed from those seen in the pilot results of Table 5.2. When comparing the confidence intervals, the previous uncertainty due to a lower number of subjects has been diminished. The lower and upper bounds have become significantly tighter in range to the standard ICC value. This confirms that the method and protocol are effective at providing excellent test-retest results.

Symmetry Metrics

The final objective was to explore the metrics and determine which would be most suitable for symmetry analysis. With the un-combined plate method producing higher peak values, and the literature finding this to be a better estimate [89], the symmetry metrics were developed using that method's data.

With the additional force plate capturing data from the leading limb, it was decided to explore the effects of peak metrics of the first plate on the change in peaks. Two proportional ratios were defined by the peak values with respect to the trailing limb peak. Firstly, the ratio between trailing limb push-off and leading limb contact:

$$\text{Braking Ratio}, x_{br}^{n} = \frac{P1^{n} - P2_{br}^{n}}{P1^{n}} \tag{5.7}$$

Then the ratio between the two propulsive peaks:

$$\text{Propulsive Ratio}, x_{po}^{n} = \frac{P1^{n} - P2_{po}^{n}}{P1^{n}} \tag{5.8}$$

These proportional ratios describe the change between their respective peak values. Each metric was calculated using these ratios and then compared against the trailing limb peak values. The metrics are denoted in the ratio nomenclature by the first letter of the metric replacing n; such that the braking impulse ratio is given as x_{br}^{I}. Scatter plots have been generated, see Figure 5.13 for the braking scatter plots, and Figure 5.14 for the propulsive scatter plots.

For the braking ratio, the force and impulse of the braking component are vectors and negative in sign. As such, the ratios for these metrics will always be $x_{br}^{F,I} < 1$, with larger ratios indicating an increase in peak difference. Power and work are given in absolute values, and so $0 > x_{br}^{P,W} > 1$ as the braking values are typically less than the trailing limb propulsive values. Larger gaps between the propulsive and braking power or work values are indicated by $x_{br}^{P,W} \to 1$.

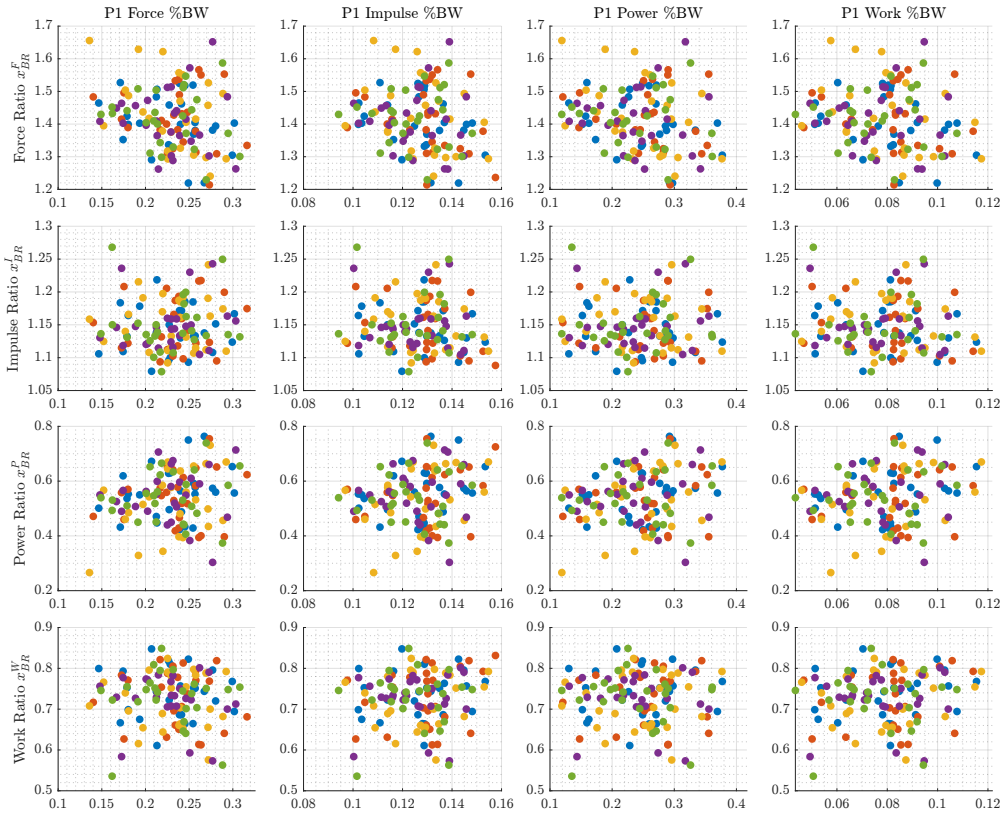


Figure 5.13: Braking ratio scatter plots, generated using left foot trailing data. The x-axis plots the trailing limb peak metrics, across the columns are the Peak force, Impulse, Peak power, and Work. The y-axis then plots the ratios, working down the rows of plots are the Force, Impulse, Power, and Work ratios. Colours denote different trials numbers, and so there should be no distinction between them.

The propulsive ratio is simpler in terms of all values being positive in magnitude. Negative values of this ratio indicate the leading leg propulsive metric is larger than the trailing leg, with $x^n_{po} \to -1$ as $P2^n_{po} \to 2P1^n$; although this is an unlikely occurrence. As with the power and work braking ratios, the decrease from $P1^n$ to $P2^n_{po}$ is denoted by $0 > x^{P,W}_{br} > 1$. Likewise, $x^n_{po} \to 1$ signifies that $P2_{po} \to 0$.

The braking ratio metrics can indicate whether there is some relationship between the trailing leg push-off and leading leg contact kinetics. Based on the scatter plots of Figure 5.13, there are a few weak correlations between trailing limb metrics and braking peak ratios, and so some interpretations can be made. Higher values of the P1 force and impulse appear to coincide with smaller braking forces on the leading foot. As expected, these large forces also coincide with less braking power applied, whilst the braking impulse is small across the full range of P1 forces.

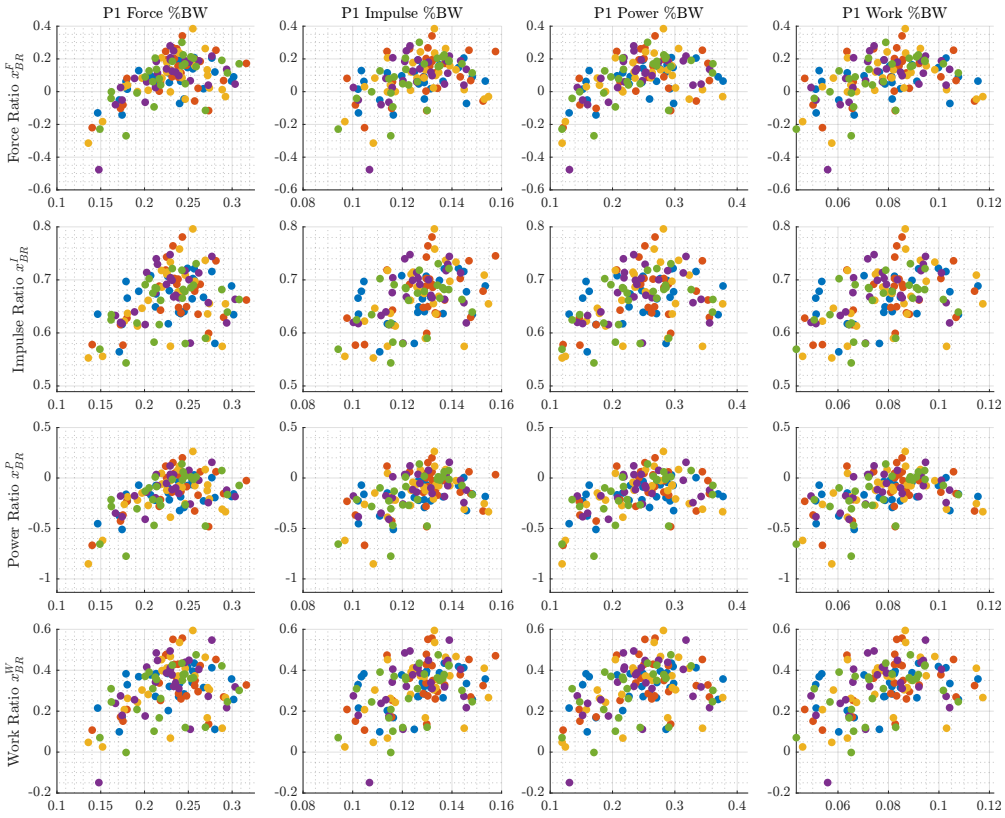


Figure 5.14: Propulsive ratio scatter plots, generated using left foot trailing data. The x-axis plots the trailing limb peak metrics, across the columns are the Peak force, Impulse, Peak power, and Work. The y-axis then plots the ratios, working down the rows of plots are the Force, Impulse, Power, and Work ratios. Colours denote different trials numbers, and so there should be no distinction between them.

The impulse has a similar trend on the power ratio, but with the data points skewed more to the top right corner demonstrating a stronger effect. As the power is derived from the force, the patterns are mirrored for the force and impulse ratios, but with a larger spread and weaker effect. The work data is too evenly distributed to discern a relationship with the ratios.

The propulsive force ratio scatter plots have much clearer trends, although again some of these are repeated across the related metrics. The force ration has a strong trend across all metrics, where a few anomalous results see a larger leading foot force, but most data is skewed toward a relative 20% drop in peaks. It appears an unusually low push-off power is the most likely factor, whereas the spread of the trailing foot positive work suggests an invariance to the force.

Impulse ratio data follows the force data, but with more dispersion of the data. Apart from a few anomalous results, there seems to be a preference to

minimising the difference in peaks, which would be preferable to maintain the forward momentum generated in the initiating step.

Whilst the power ratio follows a similar pattern and distribution to the force ratio, the trend is indicating an increase in the leading foot propulsive power. As this difference is largest when the push-off power is low, it likely that this trend is from ramping up energy delivery to account for the shorter duration of push-off on the leading limb.

Data for the work ratio is more distributed, with a consistent drop from the work required to initiate gait. With this spread, it can be said that the amount of work is largely invariant to the other metrics, and instead the rate of force and energy delivery is more influential.

These non-dimensional ratios could be used as metrics to judge symmetry, alongside peaks which are traditionally used in the literature [140]. Subject trial means were generated for both the left and right sets of data and have been plotted on a selection of x^n_{po} plots for comparison; see Figure 5.15. The trends in these plots match with their counterparts in Figure 5.14. However, the distribution suggests symmetry is not achieved for all subjects.

These bodyweight normalised subject trial means were then averaged between themselves, split between two comparison pairs; left & right, and male & female. The values have been copied into Table 5.6. With the data averaged together, the left and right pairing have differences in the magnitude of $\frac{1}{1000}\%BW$. More differ-

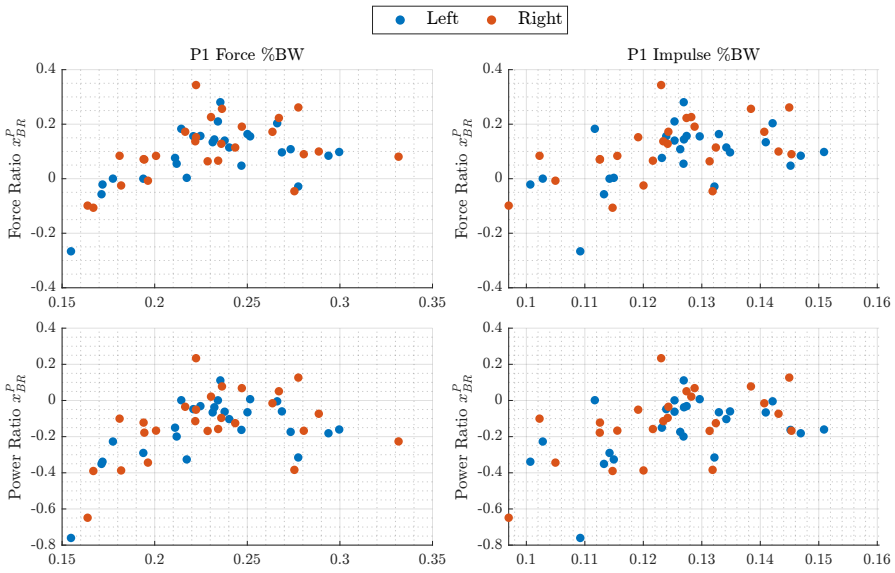


Figure 5.15: Comparison of the peak ratio scatter plots between left and right foot leading data sets. Note the similarity in trends and distribution, with similar anomalous results.

Table 5.6: Full cohort means of peak metrics in terms of bodyweight. Comparisons are made between left and right, and the sex of subjects.

Metric	Left	Right	Male	Female
AP1 Force	0.2311	0.2309	0.2308	0.2312
AP1 Impulse	0.1265	0.1257	0.1271	0.1246
AP1 Power	0.2475	0.2461	0.2491	0.2431
AP1 Work	0.0794	0.0786	0.0769	0.0804
AP2br Force	0.0004	0.0004	0.0004	0.0005
AP2br Impulse	0.0186	0.0192	0.0189	0.0189
AP2br Power	0.1111	0.1129	0.1070	0.1199
AP2br Work	0.0215	0.0220	0.0218	0.0215
AP2po Force	0.2083	0.2037	0.2065	0.2053
AP2po Impulse	0.0420	0.0416	0.0418	0.0418
AP2po Power	0.2792	0.2717	0.2794	0.2691
AP2po Work	0.0534	0.0526	0.0536	0.0520

ences occur between female and male averages, but these are still on a small scale of $\%BW$. Previous research has found peaks ineffective at determining significant differences between sexes, instead suggesting waveforms are compared with statistical parametric mapping [280].

Other papers have explored the use of symmetry metrics, such as the Symmetry in External Work method, which provides a simple percentage difference between the two sides [281]. Comparisons have been made between these symmetry calculation methods, finding a percentage difference index to be the most reliable [282]. When this experimental method is extended to amputee subjects, these symmetry methods could be used on the peak values in conjunction with the trailing-leading limb ratios defined above.

5.3 Future experimental work

With the successful development of the gait initiation protocol, and demonstration of useful force plate metrics, this experiment can be used in larger clinical studies and be expanded to provide more complete sets of data of transitionary gait tasks. The digital acquisition box used in these studies was only two-channel. However, a newer model exists with 8-channels, increasing the number of force plates and successive steps that can have force data collected.

The core ethos of the experiments would still be shorter transitionary gait tasks, moving from room to room, or moving between floors. However, the in-

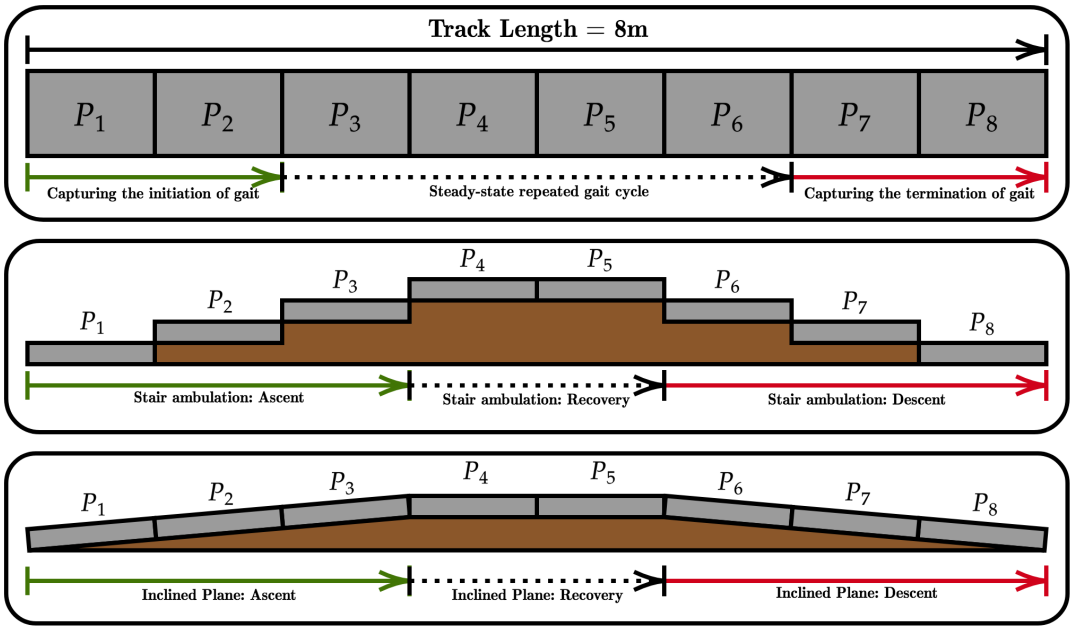


Figure 5.16: Potential force plates setups for future studies with amputees. These would allow for force plate data to be captured under gait initiation through steady-state walking and ending with gait termination. Stair and ramp ambulation could also be captured with a suitable platform to embed the plates in.

creased number of force plates would capture the initiation, steady-state walking, and gait termination. As the gait initiation protocol developed here has shown strong reliability it could be used to initiate the motor tasks. The pilot study gait termination results and literature indicate that this particular motor task is given no instruction other than to stop on the plate. It would be better for subjects to repeat the trial should there be an issue with force recording.

A series of potential setups have been drawn up in diagrams of Figure 5.16. With eight force plates, the minimum walkway length with the plates in close proximity would be about 8m. The initiation and termination motor tasks would be captured by the first and last two plates, allowing the four middle plates to capture steady-walking forces. The setup would not be limited to level walking, a stepped or ramped platform could be constructed so that these common gait tasks can also be captured.

Sample Size

When designing experimental studies, researchers can calculate a sample size number that enables effects to be determined with statistical confidence that they represent the true population.

Such a calculation is particularly important in medical studies to avoid Type I and Type II errors which can lead to missed effects or false conclusions [283]. However, in the fields of prosthetics and biomechanics, a sample size power calculation is rarely given. Some studies will recruit as few as 8 subjects [169], whilst others may reach as many as 20 [164]. Not all researchers will acknowledge sample size calculations or limitations of small samples, but these omissions have been recognised early on in the field [284]. A recent biomechanics study on running suggests varying sample size and number of steps both effect the statistics, and that a minimum of 25 subjects and 25 steps be used for suitable statistics [285].

For the initial pilot study, a sample size calculation was not needed as the purpose of the study was to test some protocols and equipment setup for the larger main study. No calculation was made for the larger study either. The main purpose of the larger study was to confirm the test re-test reliability, and concerns about effects were minor. A paper on sample size requirements for ICC statistics indicates that suitable numbers of subjects are in line with the work in this chapter, especially when repeated observations per subject increase [271].

Translating healthy subject conclusions to amputee population

A possible limitation of the work completed in this chapter is how to translate the conclusions from healthy subjects to an elderly amputee population. Recruiting a sufficient number of amputees for a study can be problematic, as discussed in Section 5.1.1 of this chapter. It was decided that prioritising recruitment for a larger number of healthy subjects would be preferable to recruiting a limited number of amputees. This facilitated an easier recruitment process as subjects were sought from within the large student body population. As a secondary benefit, any unexpected absences were better suited for substitution.

Furthermore, as this study was concerned with defining a simple protocol and equipment setup, the data collected did not need to be from an amputee sample population. None of the metrics collected were focused on amputee specific effects, and these KPI definitions will be easily transferred to an amputee population. In the future experimental work explained above, adequate adjustments can be made to the setup to account for the amputee subjects. For example, a supporting handrail on the sides of the platform can be provided as a safety precaution. Additional time can also be provided for an amputee subject to become familiar with walking along the platform.

5.4 Summary

The work presented in this chapter began with a pilot study that uncovered effects of different instruction protocols on force kinetics during initiation and termination. Through statistical ANOVA analyses, these protocols were assessed for test-retest reliability. Modifications were made and the number of subjects was increased for a larger experiment on the gait initiation motor task. Results confirmed strong reliability in repeating results. Proportional ratios were defined as potential metrics to be used in symmetry analysis alongside the traditional method of using peak values. Future developments have been discussed, and the framework developed shows promise for clinical trials using amputees.

Chapter 6

Conclusion

6.1 Main Contributions

As identified in the introduction to this thesis, the direction of prosthetic feet research has been driven towards powered ankles matching joint powers, or passive feet recreating kinematic profiles. This focus has been to provide natural gait for a more active amputee. However, in achieving these goals, the less active and elderly amputee has been somewhat neglected.

In Chapter 2, the literature review explored the biomechanics research from the functionality of the musculoskeletal system to the design of feet themselves. The objective was to uncover the key functionality provided by the ankle-foot complex and methods of control through the neuromuscular system. Whilst an amputee suffers from the loss of the catapult like action of the tendons, and precise control with the muscles, the motor redundancy of the entire system offers multiple control schemes to work around these losses. It is possible that optimisation for a less active amputee will result in passive feet different to what has been developed in research and what is available in healthcare systems.

At the end of the literature review of Chapter 2, the research question was revised to:

> "Can a disability focused approach, targeting personal stiffness optimisation in a passive foot design, improve the gait of less active amputees?"

Whilst this question has not been directly answered, the scope and novelty of the idea required significant work to setup the tools needed to seek a solution to the question. The work presented in this thesis has created the necessary framework

for a new prosthetic optimisation pathway, that targets less active amputees and the gait motor tasks that are more common for them.

Contribution 1: Development of a computational model for prosthetic foot optimisation

An advanced FEA model has been developed in Ansys using boundary conditions defined with ISO 22675 and verified with a contact experiment. Extensive modelling with contact conditions and mesh convergence studies have helped to refine the model to a high quality with consistent results. The cyclic test replicates the stance phase of gait, and it was demonstrated how the forces and angles could be replaced with experimental force plate and marker data. A novel addition is the generation of the rollover shape within the software through a custom APDL code. This rollover shape can be parameterised to workspace for use in parametric design optimisation. Whilst the model used steady-gait ground reaction forces and leg angles, these can easily be replaced with initiation or termination data.

Contribution 2: Prosthetic experimentation tool to test effect of small stiffness changes during gait initiation and termination

A prosthetic experimental tool has been redesigned from a proof-of-concept design to a working prototype ready for use in clinical trials. The spring mechanism was optimised using ISO standard strength analyses, and parametric design studies with genetic algorithms generating the response surfaces. A program was written in MATLAB to generate control points of a NURBS curve, interpolated through a series of defined points. This type of curve has more control over the shape than Bezier curves used in similar research but retains the use as parametric points in future designs of printed feet. The prototype foot structure was optimised using the FEA model under static cases and with Isotropic materials. The models were then replicated with the Ansys composite modelling module and results compared. All the components were manufactured and assembled, ready for use in clinical trials.

Contribution 3: Development of a reliable experimental protocol for gait initiation and termination tasks

With the prosthetic tool ready, the experimental protocol to test it under has been developed. A pilot study helped to identify potential issues with different protocol instructions, and refinements were made. The final larger study with 26 subjects performing the gait initiation task provided reliable results with high

intraclass correlation values. Proportional ratios were defined which quantified the relationship between trailing limb and leading limb force metrics as a proportion of the trailing push-off limb. Together with the peaks, these can provide a complementary set of statistics to analyse an amputee's performance.

6.2 Limitations

The design of a prosthetic device can be a laborious effort involving the coordination of multiple disciplines. At MIT, the development of the now industry-famous BiOM powered prosthetic ankle-foot system was in development under a team of researchers for the best part of a decade [197, 2]. The work presented here sets the foundation to begin a new research effort, attempting to change the method of thought used to design passive prosthetic feet. What began with a concept has evolved into a prototype ready for testing in a lab with the novel experimental method. From a theoretical point of view, the prototype design should enact a change in gait behaviour, see the change in rollover shapes of Figure 4.40. However, due to the nature of gait analysis and implementation of concept prosthetic designs, until experiments are carried out the true success cannot be gauged.

It could be argued that a physical test should be conducted to verify the theoretical performance. However, it was not deemed necessary to conclude the work in this thesis. A very robust design methodology was employed in refining the prosthetic, using high quality FEA models and experimentation to verify contact conditions. The results of these models have provided results that give enough confidence that the prototype is safe and ready to be used in a study. Whilst a physical test may verify the simulations, at this stage of prototype development, the primary need is to conduct a clinical study and gain feedback from amputees. This direct assessment would provide more value than what an experiment under perfect test conditions could provide; a "real world" application can assist in ensuring the prosthetic will deliver the desired metrics.

The appraisal of the design itself has been presented in sub-section 4.4.2. Not all of the design criteria were met, but adjustments were made elsewhere to ensure the overall performance would still be as intended. At the end of Chapter 5, two limitations of the experimental study have been addressed. Sample size calculations were not used, but this is not an abnormality in the field given the difficulties with recruiting sufficient numbers of subjects. Whilst the experimental method can easily be adjusted for an amputee sample population.

6.3 Future Directions

The work presented here will be linked in future work with a bipedal spring-loaded passive walker developed in a previous doctoral thesis [27]. Using these tools, a series of work packages were conceptualised to help guide the future research.

Work Package 1: Prosthetic Tool Clinical Trial

The prosthetic foot tool has been designed with a robust optimisation methodology. However, it needs to undergo clinical trial testing to assess its effectiveness under amputee loading. With this the design can be assessed and any required adjustments made. This process has been demonstrated in Figure 6.1.

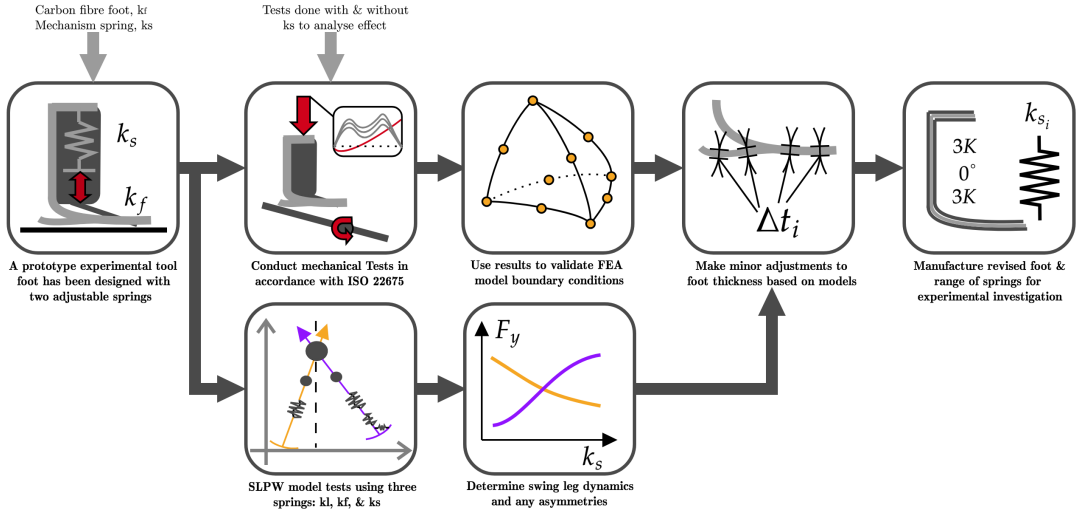


Figure 6.1: Possible steps that may be taken to refine the prototype tool in preparation for the stiffness exploration studies of the second work package.

Work Package 2: Stiffness Exploration

Once the prosthetic tool has been assessed with small clinical trial, a larger study can be completed in confidence. A series of springs will be manufactured with small delta changes to the stiffness. Using the developed experimental protocol, amputees will perform trials with the proposed setups in Section 5.3 to assess the effects of stiffness changes for the gait initiation and termination tasks. See Figure 6.2 for a visual demonstration of this process.

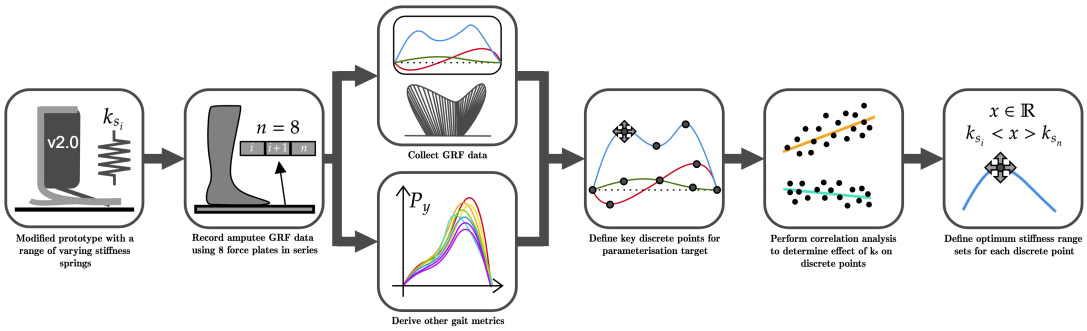


Figure 6.2: Flow diagram representing the process to be taken in defining effects of spring stiffness on amputee gait force metrics.

Work Package 3: Prosthetic Optimisation

In the final work package, the full complement of tools will be employed; the NURBS program to generate the shape, the Ansys model to assess stance phase loading, and the bipedal model to evaluate the swing leg dynamics. This process has been detailed in Figure 6.3, where the example presents an optimisation of matching ground reaction forces to avoid unhealthy loading. This method has been successfully demonstrated in a parallel thesis [55], using the FEA model from Chapter 3.

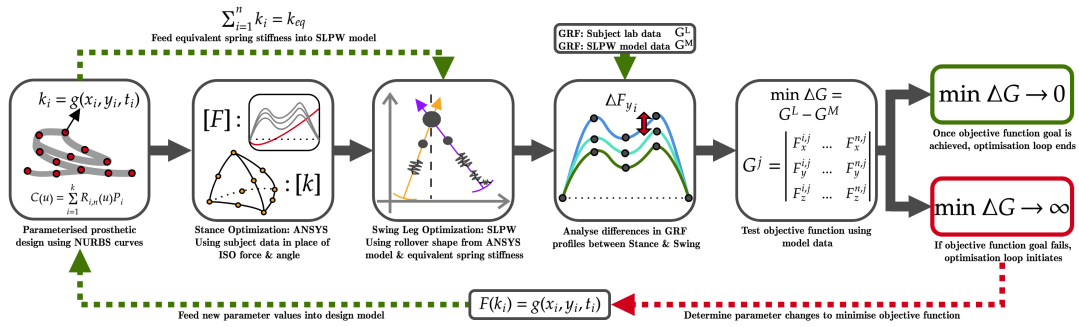


Figure 6.3: Flow diagram representing the framework to be used in future prosthetic optimisation as a result of the contributions presented in this thesis, and the research they can be used for.

References

[1] Cherelle, P et al. "Advances in Propulsive Bionic Feet and Their Actuation Principles". *Advances in Mechanical Engineering* 2014 (2014), pp. 1–21. DOI: 10.1155/2014/984046.

[2] Rouse, EJ et al. "Design and Testing of a Bionic Dancing Prosthesis". *PLoS ONE* 10.8 (2015). DOI: 10.1371/journal.pone.0135148.

[3] Olesnavage, KM and Winter, AG. "Lower Leg Trajectory Error: A novel optimization parameter for designing passive prosthetic feet". *2015 IEEE International Conference on Rehabilitation Robotics (ICORR)*. IEEE, 2015, pp. 271–276. DOI: 10.1109/ICORR.2015.7281211.

[4] Winter, DA et al. "Adaptability of Motor Patterns in Pathological Gait". *Multiple Muscle Systems*. 1990, pp. 680–693. DOI: 10.1007/978-1-4613-9030-5_44.

[5] Selles, RW et al. "Adaptations to mass perturbations in transtibial amputees: Kinetic or kinematic invariance?" *Archives of Physical Medicine and Rehabilitation* 85.12 (2004), pp. 2046–2052. DOI: 10.1016/j.apmr.2003.10.013.

[6] Prinsen, EC, Nederhand, MJ, and Rietman, JS. "Adaptation Strategies of the Lower Extremities of Patients With a Transtibial or Transfemoral Amputation During Level Walking: A Systematic Review". *Archives of Physical Medicine and Rehabilitation* 92.8 (2011), pp. 1311–1325. DOI: 10.1016/j.apmr.2011.01.017.

[7] Takahashi, KZ, Horne, JR, and Stanhope, SJ. "Comparison of mechanical energy profiles of passive and active below-knee prostheses: A case study". *Prosthetics and Orthotics International* 39.2 (2015), pp. 150–156. DOI: 10.1177/0309364613513298.

[8] Manring, MM et al. "Treatment of war wounds: A historical review". *Clinical Orthopaedics and Related Research* 467.8 (2009), pp. 2168–2191. DOI: 10.1007/s11999-009-0738-5.

[9] Noe, A. "Extremity Injury in War: A Brief History". *The Journal of the American Academy of Orthopaedic Surgeons* 14.10 (2006), S1–6.

[10] Stansbury, LG, Branstetter, JG, and Lalliss, SJ. "Amputation in Military Trauma Surgery". *The Journal of Trauma Injury Infection and Critical Care* 63 (2007), pp. 940–944. DOI: 10.1097/TA.0b013e31814934d8.

[11] Demet, K et al. "Health related quality of life and related factors in 539 persons with amputation of upper and lower limb". *Disability and Rehabilitation* 25.9 (2003), pp. 480–486. DOI: 10.1080/0963828031000090434.

[12] Ebrahimzadeh, MH et al. "Long-term clinical outcomes of war-related bilateral lower extremities amputations". *Injury* 46.2 (2015), pp. 275–281. DOI: 10.1016/j.injury.2014.10.043.

[13] Ziegler-Graham, K et al. "Estimating the Prevalence of Limb Loss in the United States: 2005 to 2050". *Archives of Physical Medicine and Rehabilitation* 89.3 (2008), pp. 422–429. DOI: 10.1016/j.apmr.2007.11.005.

[14] Deans, Sa, McFadyen, AK, and Rowe, PJ. "Physical activity and quality of life: A study of a lower-limb amputee population". *Prosthetics and Orthotics International* 32.2 (2008), pp. 186–200. DOI: 10.1080/03093640802016514.

[15] Ahmad, N et al. "Lower limb amputation in England: prevalence, regional variation and relationship with revascularisation, deprivation and risk factors. A retrospective review of hospital data". *Journal of the Royal Society of Medicine* 107.12 (2014), pp. 483–489. DOI: 10.1177/0141076814557301.

[16] Ahmad, N et al. "The prevalence of major lower limb amputation in the diabetic and non-diabetic population of England 2003–2013". *Diabetes and Vascular Disease Research* 13.5 (2016), pp. 348–353. DOI: 10.1177/1479164116651390.

[17] Eide, AH and Oderud, T. "Assistive Technology in Low-Income Countries". *Disability & International Development: Towards Inclusive Global Health*. Ed. by M MacLachlan and L Swartz. New York, NY: Springer US, 2009, pp. 149–160.

[18] Neptune, R, Zajac, F, and Kautz, S. "Muscle force redistributes segmental power for body progression during walking". *Gait and Posture* 19.2 (2004), pp. 194–205. DOI: 10.1016/S0966-6362(03)00062-6.

[19] Bogey, R, Gitter, A, and Barnes, L. "Determination of ankle muscle power in normal gait using an EMG-to-force processing approach". *Journal of Electromyography and Kinesiology* 20.1 (2010), pp. 46–54. DOI: 10.1016/j.jelekin.2008.09.013.

[20] Zelik, KE and Adamczyk, PG. "A unified perspective on ankle push-off in human walking". *Journal of Experimental Biology* 219.23 (2016), pp. 3676–3683. DOI: 10.1242/jeb.140376.

[21] Sawicki, GS, Lewis, CL, and Ferris, DP. "It Pays to Have a Spring in Your Step". *Exercise and Sport Sciences Reviews* 37.3 (2009), pp. 130–138. DOI: 10.1097/JES.0b013e31819c2df6.

[22] Lipfert, SW et al. "Impulsive ankle push-off powers leg swing in human walking". *Journal of Experimental Biology* 217.8 (2014), pp. 1218–1228. DOI: 10.1242/jeb.097345.

[23] Lewis, CL and Ferris, DP. "Walking with increased ankle pushoff decreases hip muscle moments". *Journal of Biomechanics* 41.10 (2008), pp. 2082–2089. DOI: 10.1016/j.jbiomech.2008.05.013.

[24] Lloyd, CH et al. "Strength asymmetry and osteoarthritis risk factors in unilateral trans-tibial, amputee gait". *Gait and Posture* 32.3 (2010), pp. 296–300. DOI: 10.1016/j.gaitpost.2010.05.003.

[25] Selles, RW et al. "The effect of prosthetic mass properties on the gait of transtibial amputees - a mathematical model". *Disability and Rehabilitation* 26.12 (2004), pp. 694–704. DOI: 10.1080/09638280410001704296.

[26] Smith, JD and Martin, PE. "Effects of Prosthetic Mass Distribution on Metabolic Costs and Walking Symmetry". *Journal of Applied Biomechanics* 29.3 (2013), pp. 317–328. DOI: 10.1123/jab.29.3.317.

[27] Charles, WG. "Dynamic Walking Models to Understand Asymmetric Gait Characteristics". PhD thesis. Swansea: Swansea University, 2018. DOI: 10.23889/Suthesis.48133.

[28] Au, SK, Weber, J, and Herr, H. "Biomechanical Design of a Powered Ankle-Foot Prosthesis". *2007 IEEE 10th International Conference on Rehabilitation Robotics*. 2007, pp. 298–303. DOI: 10.1109/ICORR.2007.4428441.

[29] Au, S and Herr, H. "Powered ankle-foot prosthesis". *IEEE Robotics and Automation Magazine* 15.3 (2008), pp. 52–59. DOI: 10.1109/MRA.2008.927697.

[30] Zhu, J, Wang, Q, and Wang, L. "On the Design of a Powered Transtibial Prosthesis With Stiffness Adaptable Ankle and Toe Joints". *IEEE Transactions on Industrial Electronics* 61.9 (2014), pp. 4797–4807. DOI: 10.1109/TIE.2013.2293691.

[31] Olesnavage, KM et al. "Passive Prosthetic Foot Shape and Size Optimization Using Lower Leg Trajectory Error". *Journal of Mechanical Design* 140.10 (2018). DOI: 10.1115/1.4040779.

[32] Deans, S et al. "Motivations and barriers to prosthesis users participation in physical activity, exercise and sport: A review of the literature". *Prosthetics and Orthotics International* 36.3 (2012), pp. 260–269. DOI: 10.1177/0309364612437905.

[33] Bohannon, RW. "Number of Pedometer-Assessed Steps Taken Per Day by Adults: A Descriptive Meta-Analysis". *Physical Therapy* 87.12 (2007), pp. 1642–1650. DOI: 10.2522/ptj.20060037.

[34] Miller, R and Brown, W. "Steps and sitting in a working population". *International Journal of Behavioral Medicine* 11.4 (2004), pp. 219–224. DOI: 10.1207/s15327558ijbm1104_5.

[35] Pernot, HF et al. "Daily functioning of the lower extremity amputee: An overview of the literature". *Clinical Rehabilitation* 11.2 (1997), pp. 93–106. DOI: 10.1177/026921559701100202.

[36] Bilodeau, S, Hébert, R, and Desrosiers, J. "Lower limb prosthesis utilisation by elderly amputees". *Prosthetics and Orthotics International* 24.2 (2000), pp. 126–132. DOI: 10.1080/03093640008726535.

[37] Condie, E, Scott, H, and Treweek, S. "Lower Limb Prosthetic Outcome Measures: A Review of the Literature 1995 to 2005". *JPO Journal of Prosthetics and Orthotics* 18.6 (2006), pp. 13–45.

[38] Fortington, LV et al. "Mobility in Elderly People With a Lower Limb Amputation: A Systematic Review". *Journal of the American Medical Directors Association* 13.4 (2012), pp. 319–325. DOI: 10.1016/j.jamda.2010.12.097.

[39] Winter, DA. *Biomechanics and Motor Control of Human Movement*. Waterloo, Ontario: John Wiley and Sons, 2009.

[40] Riemer, R, Hsiao-Wecksler, ET, and Zhang, X. "Uncertainties in inverse dynamics solutions: A comprehensive analysis and an application to gait". *Gait and Posture* 27.4 (2008), pp. 578–588. DOI: 10.1016/j.gaitpost.2007.07.012.

[41] Sawers, AB and Hahn, ME. "The Potential for Error With Use of Inverse Dynamic Calculations in Gait Analysis of Individuals With Lower Limb Loss: A Review of Model Selection and Assumptions". *JPO Journal of Prosthetics and Orthotics* 22.1 (2010), pp. 56–61. DOI: 10.1097/JPO.0b013e3181cba08b.

[42] Collins, SH and Kuo, AD. "Recycling Energy to Restore Impaired Ankle Function during Human Walking". *PLoS ONE* 5.2 (2010), e9307. DOI: 10.1371/journal.pone.0009307.

[43] Segal, AD et al. "The effects of a controlled energy storage and return prototype prosthetic foot on transtibial amputee ambulation". *Human Movement Science* 31.4 (2012), pp. 918–931. DOI: 10.1016/j.humov.2011.08.005.

[44] Rouse, EJ et al. "The Difference Between Stiffness and Quasi-Stiffness in the Context of Biomechanical Modeling". *IEEE Transactions on Biomedical Engineering* 60.2 (2013), pp. 562–568. DOI: 10.1109/TBME.2012.2230261.

[45] Rouse, EJ et al. "Estimation of Human Ankle Impedance During the Stance Phase of Walking". *IEEE Transactions on Neural Systems and Rehabilitation Engineering* 22.4 (2014), pp. 870–878. DOI: 10.1109/TNSRE.2014.2307256.

[46] Shepherd, MK and Rouse, EJ. "The VSPA Foot: A Quasi-Passive Ankle-Foot Prosthesis With Continuously Variable Stiffness". *IEEE Transactions on Neural Systems and Rehabilitation Engineering* 25.12 (2017), pp. 2375–2386. DOI: 10.1109/TNSRE.2017.2750113.

[47] Shepherd, MK et al. "Amputee perception of prosthetic ankle stiffness during locomotion". *Journal of NeuroEngineering and Rehabilitation* 15.1 (2018), p. 99. DOI: 10.1186/s12984-018-0432-5.

[48] Hansen, AH and Childress, DS. "Investigations of roll-over shape: Implications for design, alignment, and evaluation of ankle-foot prostheses and orthoses". *Disability and Rehabilitation* 32.26 (2010), pp. 2201–2209. DOI: 10.3109/09638288.2010.502586.

[49] Fey, NP, Klute, GK, and Neptune, RR. "The influence of energy storage and return foot stiffness on walking mechanics and muscle activity in below-knee amputees". *Clinical Biomechanics* 26.10 (2011), pp. 1025–1032. DOI: 10.1016/j.clinbiomech.2011.06.007.

[50] Shell, CE et al. "The effects of prosthetic foot stiffness on transtibial amputee walking mechanics and balance control during turning". *Clinical Biomechanics* 49 (2017), pp. 56–63. DOI: 10.1016/j.clinbiomech.2017.08.003.

[51] Hansen, A et al. "Effects of flat prosthetic foot rocker section on balance and mobility". *Journal of Rehabilitation Research and Development* 51.1 (2014), pp. 137–148. DOI: 10.1682/JRRD.2012.12.0229.

[52] Olesnavage, KM and Winter, AG. "Design and qualitative testing of a prosthetic foot with rotational ankle and metatarsal joints to mimic physiological roll-over shape". *Proceedings of the ASME Design Engineering Technical Conference*. Vol. 5A-2015. 2015, pp. 1–9. DOI: 10.1115/DETC2015-46518.

[53] Prost, V, Olesnavage, KM, and Winter, AG. "Design and testing of a prosthetic foot prototype with interchangeable custom rotational springs to adjust ankle stiffness for evaluating lower leg trajectory error, an optimization metric for prosthetic feet". *Proceedings of the ASME Design Engineering Technical Conference*. Vol. 5B-2017. American Society of Mechanical Engineers, 2017, pp. 1–7. DOI: 10.1115/DETC2017-67820.

[54] Olesnavage, KM and Winter, AG. "Passive Prosthetic Foot Shape and Size Optimization Using Lower Leg Trajectory Error". *International Design Engineering Technical Conferences and Computers and Information in Engineering Conference* (2017), pp. 1–10.

[55] AlQemlas, TK. "A Loosely-Coupled Passive Dynamics and Finite Element based Model for Minimising Biomechanically Driven Unhealthy Joint Loads during Walking in Transtibial Amputees". PhD thesis. Swansea University, 2020.

[56] Yang, L et al. "Continuous graded Gyroid cellular structures fabricated by selective laser melting: Design, manufacturing and mechanical properties". *Materials and Design* 162 (2019), pp. 394–404. DOI: 10.1016/j.matdes.2018.12.007.

[57] Shi, X et al. "Comparison of Compression Performance and Energy Absorption of Lattice Structures Fabricated by Selective Laser Melting". *Advanced Engineering Materials* 22.11 (2020), pp. 1–9. DOI: 10.1002/adem.202000453.

[58] Ma, S et al. "Mechanical behaviours and mass transport properties of bone-mimicking scaffolds consisted of gyroid structures manufactured using selective laser melting". *Journal of the Mechanical Behavior of Biomedical Materials* 93 (January 2019), pp. 158–169. DOI: 10.1016/j.jmbbm.2019.01.023.

[59] Maconachie, T et al. "The compressive behaviour of ABS gyroid lattice structures manufactured by fused deposition modelling". *International Journal of Advanced Manufacturing Technology* 107.11 (2020), pp. 4449–4467. DOI: 10.1007/s00170-020-05239-4.

[60] Sathishkumar, N et al. "Mechanical Properties of Triply Periodic Minimal Surface based lattices made by Polyjet Printing". *Materials Today: Proceedings* 22 (2019), pp. 2934–2940. DOI: 10.1016/j.matpr.2020.03.427.

[61] Whittle, MW. *Gait Analysis An Introduction*. 4th Edition. Publication Title: Butterworth-Heinemann. Butterworth Heineman, 2007.

[62] Perry, J. *Gait Analysis: Normal and Pathological Function*. SLACK Incorporated, 1992.

[63] Winter, DA. "Kinematic and kinetic patterns in human gait: Variability and compensating effects". *Human Movement Science* 3.1 (1984), pp. 51–76. DOI: 10.1016/0167-9457(84)90005-8.

[64] Jordan, K, Challis, JH, and Newell, KM. "Walking speed influences on gait cycle variability". *Gait and Posture* 26.1 (2007), pp. 128–134. DOI: 10.1016/j.gaitpost.2006.08.010.

[65] Plotnik, M et al. "Effects of walking speed on asymmetry and bilateral coordination of gait". *Gait and Posture* 38.4 (2013), pp. 864–869. DOI: 10.1016/j.gaitpost.2013.04.011.

[66] Forner-Cordero, A, Koopman, H, and Helm, F van der. "Describing gait as a sequence of states". *Journal of Biomechanics* 39.5 (2006), pp. 948–957. DOI: 10.1016/j.jbiomech.2005.01.019.

[67] Esquenazi, A. "Gait Analysis in Lower-Limb Amputation and Prosthetic Rehabilitation". *Physical Medicine and Rehabilitation Clinics of North America* 25.1 (2014), pp. 153–167. DOI: 10.1016/j.pmr.2013.09.006.

[68] Ren, L, Jones, RK, and Howard, D. "Predictive modelling of human walking over a complete gait cycle". *Journal of Biomechanics* 40.7 (2007), pp. 1567–1574. DOI: 10.1016/j.jbiomech.2006.07.017.

[69] Michael, JM et al. "Biomechanics of the ankle joint and clinical outcomes of total ankle replacement". *Journal of the Mechanical Behavior of Biomedical Materials* 1.4 (2008), pp. 276–294. DOI: 10.1016/j.jmbbm.2008.01.005.

[70] Vrieling, A et al. "Gait initiation in lower limb amputees". *Gait and Posture* 27.3 (2008), pp. 423–430. DOI: 10.1016/j.gaitpost.2007.05.013.

[71] Sadeghi, H et al. "Symmetry and limb dominance in able-bodied gait: a review". *Gait and Posture* 12.1 (2000), pp. 34–45. DOI: 10.1016/S0966-6362(00)00070-9.

[72] Schaarschmidt, M et al. "Functional gait asymmetry of unilateral transfemoral amputees". *Human Movement Science* 31.4 (2012), pp. 907–917. DOI: 10.1016/j.humov.2011.09.004.

[73] Rossi, SA, Doyle, W, and Skinner, HB. "Gait initiation of persons with below-knee amputation: The characterization and comparison of force profiles". *Journal of Rehabilitation Research and Development* 32.2 (1995), pp. 120–127.

[74] Silverman, AK et al. "Compensatory mechanisms in below-knee amputee gait in response to increasing steady-state walking speeds". *Gait and Posture* 28.4 (2008), pp. 602–609. DOI: 10.1016/j.gaitpost.2008.04.005.

[75] Nolan, L et al. "Adjustments in gait symmetry with walking speed in transfemoral and trans-tibial amputees". *Gait and Posture* 17.2 (2003), pp. 142–151. DOI: 10.1016/S0966-6362(02)00066-8.

[76] Winter, DA and Sienko, SE. "Biomechanics of below-knee amputee gait". *Journal of Biomechanics* 21.5 (1988), pp. 361–367. DOI: 10.1016/0021-9290(88)90142-X.

[77] Boonstra, AM et al. "The Gait of Unilateral Transfemoral Amputees". *Scandinavian Journal of Rehabilitation Medicine* 26 (1994), pp. 217–223.

[78] Hurley, GR et al. "The role of the contralateral limb in below-knee amputee gait". *Prosthetics and Orthotics International* 14.1 (1990), pp. 33–42. DOI: 10.3109/03093649009080314.

[79] Lemaire, ED and Fisher, F. "Osteoarthritis and Elderly Amputee Gait". *Archives of Physical Medicine and Rehabilitation* 75.10 (1994), pp. 1094–1099. DOI: 10.1016/0003-9993(94)90084-1.

[80] Morgenroth, DC et al. "The effect of prosthetic foot push-off on mechanical loading associated with knee osteoarthritis in lower extremity amputees". *Gait and Posture* 34.4 (2011), pp. 502–507. DOI: 10.1016/j.gaitpost.2011.07.001.

[81] Esposito, ER and Wilken, JM. "Biomechanical risk factors for knee osteoarthritis when using passive and powered ankle-foot prostheses". *Clinical Biomechanics* 29.10 (2014), pp. 1186–1192. DOI: 10.1016/j.clinbiomech.2014.09.005.

[82] Viteckova, S et al. "Gait symmetry measures: A review of current and prospective methods". *Biomedical Signal Processing and Control* 42 (2018), pp. 89–100. DOI: 10.1016/j.bspc.2018.01.013.

[83] Adamczyk, PG and Kuo, AD. "Mechanisms of Gait Asymmetry Due to Push-Off Deficiency in Unilateral Amputees". *IEEE Transactions on Neural Systems and Rehabilitation Engineering* 23.5 (2015), pp. 776–785. DOI: 10.1109/TNSRE.2014.2356722.

[84] Cavagna, GA and Margaria, R. "Mechanics of walking." *Journal of Applied Physiology* 21.1 (1966), pp. 271–278. DOI: 10.1152/jappl.1966.21.1.271.

[85] Winter, DA. "A new definition of mechanical work done in human movement". *Journal of Applied Physiology Respiratory Environmental and Exercise Physiology* 46.1 (1979), pp. 79–83. DOI: 10.1152/jappl.1979.46.1.79.

[86] Willems, PA, Cavagna, GA, and Heglund, NC. "External, internal and total work in human locomotion." *The Journal of Experimental Biology* 198 (1995), pp. 379–393.

[87] Kuo, AD, Donelan, JM, and Ruina, A. "Energetic Consequences of Walking Like an Inverted Pendulum: Step-to-Step Transitions". *Exercise and Sport Sciences Reviews* 33.2 (2005), pp. 88–97. DOI: 10.1097/00003677-200504000-00006.

[88] Garcia, M et al. "The Simplest Walking Model: Stability, Complexity, and Scaling". *Journal of Biomechanical Engineering* 120.2 (1998), pp. 281–288. DOI: 10.1115/1.2798313.

[89] Donelan, JM, Kram, R, and Kuo, AD. "Simultaneous positive and negative external mechanical work in human walking". *Journal of Biomechanics* 35.1 (2002), pp. 117–124. DOI: 10.1016/S0021-9290(01)00169-5.

[90] Donelan, JM, Kram, R, and Kuo, AD. "Mechanical work for step-to-step transitions is a major determinant of the metabolic cost of human walking." *The Journal of Experimental Biology* 205 (2002). ISBN: 0022-0949, pp. 3717–3727.

[91] Kuo, AD and Donelan, JM. "Dynamic Principles of Gait and Their Clinical Implications". *Physical Therapy* 90.2 (2010), pp. 157–174. DOI: 10.2522/ptj.20090125.

[92] Kuo, AD. "Energetics of Actively Powered Locomotion Using the Simplest Walking Model". *Journal of Biomechanical Engineering* 124.1 (2002), pp. 113–120. DOI: 10.1115/1.1427703.

[93] Soo, CH and Donelan, JM. "Mechanics and energetics of step-to-step transitions isolated from human walking". *Journal of Experimental Biology* 213.24 (2010), pp. 4265–4271. DOI: 10.1242/jeb.044214.

[94] Ruina, A, Bertram, JE, and Srinivasan, M. "A collisional model of the energetic cost of support work qualitatively explains leg sequencing in walking and galloping, pseudo-elastic leg behavior in running and the walk-to-run transition". *Journal of Theoretical Biology* 237.2 (2005), pp. 170–192. DOI: 10.1016/j.jtbi.2005.04.004.

[95] Adamczyk, PG, Collins, SH, and Kuo, AD. "The advantages of a rolling foot in human walking". *Journal of Experimental Biology* 209.20 (2006), pp. 3953–3963. DOI: 10.1242/jeb.02455.

[96] Vanderpool, MT, Collins, SH, and Kuo, AD. "Ankle fixation need not increase the energetic cost of human walking". *Gait and Posture* 28.3 (2008), pp. 427–433. DOI: 10.1016/j.gaitpost.2008.01.016.

[97] Adamczyk, PG and Kuo, AD. "Mechanical and energetic consequences of rolling foot shape in human walking". *Journal of Experimental Biology* 216.14 (2013), pp. 2722–2731. DOI: 10.1242/jeb.082347.

[98] Houdijk, H et al. "The energy cost for the step-to-step transition in amputee walking". *Gait and Posture* 30.1 (2009), pp. 35–40. DOI: 10.1016/j.gaitpost.2009.02.009.

[99] Geyer, H, Seyfarth, A, and Blickhan, R. "Compliant leg behaviour explains basic dynamics of walking and running". *Proceedings of the Royal Society B: Biological Sciences* 273.1603 (2006), pp. 2861–2867. DOI: 10.1098/rspb.2006.3637.

[100] Gordon, KE, Ferris, DP, and Kuo, AD. "Metabolic and Mechanical Energy Costs of Reducing Vertical Center of Mass Movement During Gait". *Archives of Physical Medicine and Rehabilitation* 90.1 (2009), pp. 136–144. DOI: 10.1016/j.apmr.2008.07.014.

[101] Kuo, AD. "The six determinants of gait and the inverted pendulum analogy: A dynamic walking perspective". *Human Movement Science* 26.4 (2007), pp. 617–656. DOI: 10.1016/j.humov.2007.04.003.

[102] Ijmker, T et al. "Energy cost of balance control during walking decreases with external stabilizer stiffness independent of walking speed". *Journal of Biomechanics* 46.13 (2013), pp. 2109–2114. DOI: 10.1016/j.jbiomech.2013.07.005.

[103] Selinger, JC et al. "Humans Can Continuously Optimize Energetic Cost during Walking". *Current Biology* 25.18 (2015), pp. 2452–2456. DOI: 10.1016/j.cub.2015.08.016.

[104] Sasaki, K, Neptune, RR, and Kautz, SA. "The relationships between muscle, external, internal and joint mechanical work during normal walking". *Journal of Experimental Biology* 212.5 (2009), pp. 738–744. DOI: 10.1242/jeb.023267.

[105] McNeill Alexander, R. "Tendon elasticity and muscle function". *Comparative Biochemistry and Physiology Part A: Molecular and Integrative Physiology* 133.4 (2002), pp. 1001–1011. DOI: 10.1016/S1095-6433(02)00143-5.

[106] Alexander, RM. "Energy-saving mechanisms in walking and running." *The Journal of Experimental Biology* 160 (1991), pp. 55–69.

[107] Biewener, AA and Roberts, TJ. "Muscle and Tendon Contributions to Force, Work, and Elastic Energy Savings: A Comparative Perspective". *Exercise and Sport Sciences Reviews* 28.3 (2000), pp. 99–107. DOI: 10916700.

[108] Fukunaga, T et al. "Muscle and Tendon Interaction During Human Movements". *Exercise and Sport Sciences Reviews* 30.3 (2002), pp. 106–110. DOI: 10.1097/00003677-200207000-00003.

[109] Roberts, TJ. "The integrated function of muscles and tendons during locomotion". *Comparative Biochemistry and Physiology Part A: Molecular and Integrative Physiology* 133.4 (2002), pp. 1087–1099. DOI: 10.1016/S1095-6433(02)00244-1.

[110] Ishikawa, M et al. "Muscle-tendon interaction and elastic energy usage in human walking". *Journal of Applied Physiology* 99.2 (2005), pp. 603–608. DOI: 10.1152/japplphysiol.00189.2005.

[111] Lichtwark, G and Wilson, A. "Is Achilles tendon compliance optimised for maximum muscle efficiency during locomotion?" *Journal of Biomechanics* 40.8 (2007), pp. 1768–1775. DOI: 10.1016/j.jbiomech.2006.07.025.

[112] Neptune, R, Kautz, S, and Zajac, F. "Contributions of the individual ankle plantar flexors to support, forward progression and swing initiation during walking". *Journal of Biomechanics* 34.11 (2001), pp. 1387–1398. DOI: 10.1016/S0021-9290(01)00105-1.

[113] Zajac, FE. "Understanding muscle coordination of the human leg with dynamical simulations". *Journal of Biomechanics* 35.8 (2002), pp. 1011–1018. DOI: 10.1016/S0021-9290(02)00046-5.

[114] Anderson, FC and Pandy, MG. "Individual muscle contributions to support in normal walking". *Gait and Posture* 17.2 (2003), pp. 159–169. DOI: 10.1016/S0966-6362(02)00073-5.

[115] Liu, MQ et al. "Muscles that support the body also modulate forward progression during walking". *Journal of Biomechanics* 39.14 (2006), pp. 2623–2630. DOI: 10.1016/j.jbiomech.2005.08.017.

[116] Liu, MQ et al. "Muscle contributions to support and progression over a range of walking speeds". *Journal of Biomechanics* 41.15 (2008), pp. 3243–3252. DOI: 10.1016/j.jbiomech.2008.07.031.

[117] Neptune, RR, Clark, DJ, and Kautz, SA. "Modular control of human walking: A simulation study". *Journal of Biomechanics* 42.9 (2009), pp. 1282–1287. DOI: 10.1016/j.jbiomech.2009.03.009.

[118] Farris, DJ and Sawicki, GS. "The mechanics and energetics of human walking and running: a joint level perspective". *Journal of The Royal Society Interface* 9.66 (2012), pp. 110–118. DOI: 10.1098/rsif.2011.0182.

[119] Allen, JL and Neptune, RR. "Three-dimensional modular control of human walking". *Journal of Biomechanics* 45.12 (2012), pp. 2157–2163. DOI: 10.1016/j.jbiomech.2012.05.037.

[120] Pandy, MG, Lin, YC, and Kim, HJ. "Muscle coordination of mediolateral balance in normal walking". *Journal of Biomechanics* 43.11 (2010). Publisher: Elsevier, pp. 2055–2064. DOI: 10.1016/j.jbiomech.2010.04.010.

[121] Zajac, FE, Neptune, RR, and Kautz, SA. "Biomechanics and muscle coordination of human walking. Part I: Introduction to concepts, power transfer, dynamics and simulations". *Gait and Posture* 16.3 (2002), pp. 215–32. DOI: 10.1016/S0966-6362(02)00068-1.

[122] Zajac, FE, Neptune, RR, and Kautz, SA. "Biomechanics and muscle coordination of human walking Part II: Lessons from dynamical simulations and clinical implications". *Gait and Posture* 17.2 (2003), pp. 1–17. DOI: 10.1016/S0966-6362(03)00035-3.

[123] Lloyd, DG and Besier, TF. "An EMG-driven musculoskeletal model to estimate muscle forces and knee joint moments in vivo". *Journal of Biomechanics* 36.6 (2003), pp. 765–776. DOI: 10.1016/S0021-9290(03)00010-1.

[124] Kimmel, SA and Schwartz, MH. "A baseline of dynamic muscle function during gait". *Gait and Posture* 23.2 (2006), pp. 211–221. DOI: 10.1016/j.gaitpost.2005.02.004.

[125] Erdemir, A et al. "Model-based estimation of muscle forces exerted during movements". *Clinical Biomechanics* 22.2 (2007), pp. 131–154. DOI: 10.1016/j.clinbiomech.2006.09.005.

[126] Miller, RH. "A comparison of muscle energy models for simulating human walking in three dimensions". *Journal of Biomechanics* 47.6 (2014), pp. 1373–1381. DOI: 10.1016/j.jbiomech.2014.01.049.

[127] Kent, J and Franklyn-Miller, A. "Biomechanical models in the study of lower limb amputee kinematics: a review". *Prosthetics and Orthotics International* 35.2 (2011), pp. 124–139. DOI: 10.1177/0309364611407677.

[128] Czerniecki, JM and Morgenroth, DC. "Metabolic energy expenditure of ambulation in lower extremity amputees: what have we learned and what are the next steps?" *Disability and Rehabilitation* 39.2 (2017), pp. 143–151. DOI: 10.3109/09638288.2015.1095948.

[129] John, CT et al. "Contributions of muscles to mediolateral ground reaction force over a range of walking speeds". *Journal of Biomechanics* 45.14 (2012), pp. 2438–2443. DOI: 10.1016/j.jbiomech.2012.06.037.

[130] Lin, SJ et al. "Physical activity, functional capacity, and step variability during walking in people with lower-limb amputation". *Gait and Posture* 40.1 (2014), pp. 140–144. DOI: 10.1016/j.gaitpost.2014.03.012.

[131] Turns, LJ, Neptune, RR, and Kautz, SA. "Relationships Between Muscle Activity and Anteroposterior Ground Reaction Forces in Hemiparetic Walking". *Archives of Physical Medicine and Rehabilitation* 88.9 (2007), pp. 1127–1135. DOI: 10.1016/j.apmr.2007.05.027.

[132] Francis, CA et al. "The modulation of forward propulsion, vertical support, and center of pressure by the plantarflexors during human walking". *Gait and Posture* 38.4 (2013), pp. 993–997. DOI: 10.1016/j.gaitpost.2013.05.009.

[133] Seliktar, R and Mizrahi, J. "Some gait characteristics of below-knee amputees and their reflection on the ground reaction forces". *Engineering in Medicine* 15.1 (1986), pp. 27–34. DOI: 10.1243/EMED_JOUR_1986_015_009_02.

[134] Peterson, CL, Kautz, SA, and Neptune, RR. "Braking and propulsive impulses increase with speed during accelerated and decelerated walking". *Gait and Posture* 33.4 (2011), pp. 562–567. DOI: 10.1016/j.gaitpost.2011.01.010.

[135] Hamill, J, Bates, BT, and Knutzen, KM. "Ground Reaction Force Symmetry During Walking and Running". *Research Quarterly for Exercise and Sport* 55.3 (1984), pp. 289–293. DOI: 10.1080/02701367.1984.10609367.

[136] Muniz, AM and Nadal, J. "Application of principal component analysis in vertical ground reaction force to discriminate normal and abnormal gait". *Gait and Posture* 29.1 (2009), pp. 31–35. DOI: 10.1016/j.gaitpost.2008.05.015.

[137] Giakas, G and Baltzopoulos, V. "Time and frequency domain analysis of ground reaction forces during walking: An investigation of variability and symmetry". *Gait and Posture* 5.3 (1997), pp. 189–197. DOI: 10.1016/S0966-6362(96)01083-1.

[138] Crenshaw, SJ and Richards, JG. "A method for analyzing joint symmetry and normalcy, with an application to analyzing gait". *Gait and Posture* 24.4 (2006), pp. 515–521. DOI: 10.1016/j.gaitpost.2005.12.002.

[139] Nüesch, C et al. "Gait patterns of asymmetric ankle osteoarthritis patients". *Clinical Biomechanics* 27.6 (2012), pp. 613–618. DOI: 10.1016/j.clinbiomech.2011.12.016.

[140] Vaverka, F et al. "System of gait analysis based on ground reaction force assessment". *Acta Gymnica* 45.4 (2015), pp. 187–193. DOI: 10.5507/ag.2015.022.

[141] Soares, DP et al. "Principal component analysis in ground reaction forces and center of pressure gait waveforms of people with transfemoral amputation". *Prosthetics and Orthotics International* 40.6 (2016), pp. 729–738. DOI: 10.1177/0309364615612634.

[142] Latash, ML and Anson, JG. "What are "normal movements" in atypical populations?" *Behavioral and Brain Sciences* 19.1 (1996), pp. 55–106. DOI: 10.1017/S0140525X00041637.

[143] Winter, DA and Eng, P. "Kinetics: our window into the goals and strategies of the central nervous system". *Behavioural Brain Research* 67.2 (1995), pp. 111–120. DOI: 10.1016/0166-4328(94)00154-8.

[144] Darter, BJ et al. "Locomotor adaptability in persons with unilateral transtibial amputation". *PLoS ONE* 12.7 (2017), pp. 1–18. DOI: 10.1371/journal.pone.0181120.

[145] Sandra Oliveira de Cerqueira Soares, A et al. "Biomechanical parameters of gait among transtibial amputees: a review". *Sao Paulo Med J* 127.5 (2009), pp. 302–311.

[146] Silverman, AK and Neptune, RR. "Muscle and prosthesis contributions to amputee walking mechanics: A modeling study". *Journal of Biomechanics* 45.13 (2012), pp. 2271–2278. DOI: 10.1016/j.jbiomech.2012.06.008.

[147] Sanderson, DJ and Martin, PE. "Lower extremity kinematic and kinetic adaptations in unilateral below-knee amputees during walking". *Gait and Posture* 6.2 (1997). ISBN: 0966-6362, pp. 126–136. DOI: 10.1016/S0966-6362(97)01112-0.

[148] Schmitz, A et al. "Differences in lower-extremity muscular activation during walking between healthy older and young adults". *Journal of Electromyography and Kinesiology* 19.6 (2009), pp. 1085–1091. DOI: 10.1016/j.jelekin.2008.10.008.

[149] Zmitrewicz, RJ, Neptune, RR, and Sasaki, K. "Mechanical energetic contributions from individual muscles and elastic prosthetic feet during symmetric unilateral transtibial amputee walking: A theoretical study". *Journal of Biomechanics* 40.8 (2007), pp. 1824–1831. DOI: 10.1016/j.jbiomech.2006.07.009.

[150] Koelewijn, AD and Bogert, AJ van den. "Joint contact forces can be reduced by improving joint moment symmetry in below-knee amputee gait simulations". *Gait and Posture* 49 (2016), pp. 219–225. DOI: 10.1016/j.gaitpost.2016.07.007.

[151] Childers, WL and Kogler, GF. "Symmetrical kinematics does not imply symmetrical kinetics in people with transtibial amputation using cycling model". *Journal of Rehabilitation Research and Development* 51.8 (2014), pp. 1243–1254. DOI: 10.1682/JRRD.2013.11.0241.

[152] Bateni, H and Olney, SJ. "Kinematic and kinetic variations of below-knee amputee gait". *Journal of Prosthetics and Orthotics* 14.1 (2002), pp. 2–10. DOI: 10.1097/00008526-200203000-00003.

[153] Smith, JD and Martin, PE. "Short and longer term changes in amputee walking patterns due to increased prosthesis inertia". *Journal of Prosthetics and Orthotics* 23.3 (2011), pp. 114–123. DOI: 10.1097/JPO.0b013e3182248d90.

[154] McGowan, C, Kram, R, and Neptune, R. "Modulation of leg muscle function in response to altered demand for body support and forward propulsion during walking". *Journal of Biomechanics* 42.7 (2009), pp. 850–856. DOI: 10.1016/j.jbiomech.2009.01.025.

[155] Michel, V and Chong, RK. "The strategies to regulate and to modulate the propulsive forces during gait initiation in lower limb amputees". *Experimental Brain Research* 158.3 (2004), pp. 356–365. DOI: 10.1007/s00221-004-1908-z.

[156] Prilutsky, BI and Zatsiorsky, VM. "Optimization-based models of muscle coordination". *Exercise and Sport Sciences Reviews* 30.1 (2002), pp. 32–38. DOI: 10.1097/00003677-200201000-00007.

[157] Glazier, PS and Davids, K. "The problem of measurement indeterminacy in complex neurobiological movement systems". *Journal of Biomechanics* 42.16 (2009). Publisher: Elsevier, pp. 2694–2696. DOI: 10.1016/j.jbiomech.2009.08.001.

[158] McGowan, CP et al. "Modular control of human walking: Adaptations to altered mechanical demands". *Journal of Biomechanics* 43.3 (2010), pp. 412–419. DOI: 10.1016/j.jbiomech.2009.10.009.

[159] Ranganathan, R et al. "Learning new gait patterns: Exploratory muscle activity during motor learning is not predicted by motor modules". *Journal of Biomechanics* 49.5 (2016), pp. 718–725. DOI: 10.1016/j.jbiomech.2016.02.006.

[160] Latash, M. "There is no motor redundancy in human movements. There is motor abundance." *Motor Control* 4.3 (2000), pp. 259–260. DOI: 10.1123/mcj.4.3.259.

[161] Latash, M et al. "Motor control theories and their applications". *Medicina* 46.6 (2010), p. 382. DOI: 10.3390/medicina46060054.

[162] Wurdeman, SR et al. "Adaptation and prosthesis effects on stride-to-stride fluctuations in amputee gait". *PLoS ONE* 9.6 (2014), pp. 2–8. DOI: 10.1371/journal.pone.0100125.

[163] Boonpratatong, A and Ren, L. "The Human Ankle-Foot Complex as a Multi-Configurable Mechanism during the Stance Phase of Walking". *Journal of Bionic Engineering* 7.3 (2010), pp. 211–218. DOI: 10.1016/S1672-6529(10)60243-0.

[164] Kitaoka, HB et al. "Foot and Ankle Kinematics and Ground Reaction Forces During Ambulation". *Foot and Ankle International* 27.10 (2006), pp. 808–813. DOI: 10.1177/107110070602701010.

[165] Gefen, A. "The in Vivo Elastic Properties of the Plantar Fascia during the Contact Phase of Walking". *Foot and Ankle International* 24.3 (2003), pp. 238–244. DOI: 10.1177/107110070302400307.

[166] Cheung, JTM, Zhang, M, and An, KN. "Effects of plantar fascia stiffness on the biomechanical responses of the ankle–foot complex". *Clinical Biomechanics* 19.8 (2004), pp. 839–846. DOI: 10.1016/j.clinbiomech.2004.06.002.

[167] Dawe, EJC and Davis, J. "Anatomy and biomechanics of the foot and ankle". *Orthopaedics and Trauma* 25.4 (2011), pp. 279–286. DOI: 10.1016/j.mporth.2011.02.004.

[168] Sawicki, GS and Ferris, DP. "Mechanics and energetics of level walking with powered ankle exoskeletons". *Journal of Experimental Biology* 211.9 (2008), pp. 1402–1413. DOI: 10.1242/jeb.009241.

[169] Huang, TwP et al. "Mechanical and energetic consequences of reduced ankle plantar-flexion in human walking". *Journal of Experimental Biology* 218.22 (2015), pp. 3541–3550. DOI: 10.1242/jeb.113910.

[170] Malcolm, P et al. "The influence of push-off timing in a robotic ankle-foot prosthesis on the energetics and mechanics of walking". *Journal of NeuroEngineering and Rehabilitation* 12.1 (2015), p. 21. DOI: 10.1186/s12984-015-0014-8.

[171] Qian, Z, Ren, L, and Ren, L. "A Coupling Analysis of the Biomechanical Functions of Human Foot Complex during Locomotion". *Journal of Bionic Engineering* 7 (S4 2010), S150–S157. DOI: 10.1016/S1672-6529(09)60229-8.

[172] Takahashi, KZ and Stanhope, SJ. "Mechanical energy profiles of the combined ankle–foot system in normal gait: Insights for prosthetic designs". *Gait and Posture* 38.4 (2013), pp. 818–823. DOI: 10.1016/j.gaitpost.2013.04.002.

[173] Bruening, DA, Cooney, KM, and Buczek, FL. "Analysis of a kinetic multi-segment foot model part II: Kinetics and clinical implications". *Gait and Posture* 35.4 (2012), pp. 535–540. DOI: 10.1016/j.gaitpost.2011.11.012.

[174] Rusaw, D and Ramstrand, N. "Sagittal plane position of the functional joint centre of prosthetic foot/ankle mechanisms". *Clinical Biomechanics* 25.7 (2010), pp. 713–720. DOI: 10.1016/j.clinbiomech.2010.04.005.

[175] Takahashi, KZ, Kepple, TM, and Stanhope, SJ. "A unified deformable (UD) segment model for quantifying total power of anatomical and prosthetic below-knee structures during stance in gait". *Journal of Biomechanics* 45.15 (2012), pp. 2662–2667. DOI: 10.1016/j.jbiomech.2012.08.017.

[176] Hansen, AH et al. "The human ankle during walking: implications for design of biomimetic ankle prostheses". *Journal of Biomechanics* 37.10 (2004), pp. 1467–1474. DOI: 10.1016/j.jbiomech.2004.01.017.

[177] Zelik, KE et al. "The role of series ankle elasticity in bipedal walking". *Journal of Theoretical Biology* 346 (2014), pp. 75–85. DOI: 10.1016/j.jtbi.2013.12.014.

[178] Shamaei, K, Sawicki, GS, and Dollar, AM. "Estimation of Quasi-Stiffness and Propulsive Work of the Human Ankle in the Stance Phase of Walking". *PLoS ONE* 8.3 (2013). Ed. by HA Awad. DOI: 10.1371/journal.pone.0059935.

[179] Safaeepour, Z et al. "Quantitative analysis of human ankle characteristics at different gait phases and speeds for utilizing in ankle-foot prosthetic design". *BioMedical Engineering OnLine* 13.1 (2014), pp. 1–8. DOI: 10.1186/1475-925X-13-19.

[180] Pailler, D et al. "Évolution des prothèses des sprinters amputés de membre inférieur". *Annales de Réadaptation et de Médecine Physique* 47.6 (2004), pp. 374–381. DOI: 10.1016/j.annrmp.2004.05.007.

[181] Hafner, BJ et al. "Transtibial energy-storage-and-return prosthetic devices: a review of energy concepts and a proposed nomenclature." *Journal of Rehabilitation Research and Development* 39.1 (2002), pp. 1–11.

[182] Sam, M, Hansen, AH, and Childress, D. "Characterisation of prosthetic feet used in low-income countries". *Prosthetics and Orthotics International* 28.2 (2004), pp. 132–140. DOI: 10.1080/03093640408726698.

[183] Gitter, A, Czerniecki, JM, and DeGroot, DM. "Biomechanical Analysis of the Influence of Prosthetic Feet on Below-Knee Amputee Walking". *American Journal of Physical Medicine and Rehabilitation* 70.3 (1991), pp. 142–148. DOI: 10.1097/00002060-199106000-00006.

[184] Colborne, GR et al. "Analysis of Mechanical and Metabolic Factors in the Gait of Congenital Below Knee Amputees. A comparison of the SACH and Seattle feet." *American Journal of Physical Medicine and Rehabilitation* 71 (1992), pp. 272–278. DOI: 10.1097/00002060-199210000-00004.

[185] Powers, C et al. "Influence of Prosthetic Foot Design on Sound Limb Loading in Adults with u Unilateral Below-Knee Amputations". *Archives of Physical Medicine and Rehabilitation* 75.7 (1994), pp. 825–829. DOI: 10.5555/uri:pii:0003999394901465.

[186] Ehara, Y et al. "Energy Storing Property of So-Called Energy-Storing Prosthetic Feet". *Archives of Physical Medicine and Rehabilitation* 74.1 (1993), pp. 68–72.

[187] Prince, F et al. "A New Technique for the Calculation of the Energy Stored, Dissipated, and Recovered in Different Ankle-Foot Prostheses". *IEEE Transactions on Rehabilitation Engineering* 2.4 (1994), pp. 247–255. DOI: 10.1109/86.340873.

[188] Hafner, BJ et al. "Energy storage and return prostheses: does patient perception correlate with biomechanical analysis?" *Clinical Biomechanics* 17.5 (2002), pp. 325–344. DOI: 10.1016/S0268-0033(02)00020-7.

[189] Hsu, MJ et al. "The Effects of Prosthetic Foot Design on Physiologic Measurements, Self-Selected Walking Velocity, and Physical Activity in People With Transtibial Amputation". *Archives of Physical Medicine and Rehabilitation* 87.1 (2006), pp. 123–129. DOI: 10.1016/j.apmr.2005.07.310.

[190] Klute, GK, Berge, JS, and Segal, AD. "Heel-region properties of prosthetic feet and shoes". *The Journal of Rehabilitation Research and Development* 41.4 (2004), p. 535. DOI: 10.1682/JRRD.2003.02.0025.

[191] Klute, GK and Berge, JS. "Modelling the effect of prosthetic feet and shoes on the heel-ground contact force in amputee gait". *Proceedings of the Institution of Mechanical Engineers, Part H: Journal of Engineering in Medicine* 218.3 (2004), pp. 173–182. DOI: 10.1243/095441104323118897.

[192] Hansen, A, Childress, D, and Knox, E. "Prosthetic foot roll-over shapes with implications for alignment of trans-tibial prostheses". *Prosthetics and Orthotics International* 24.3 (2000), pp. 205–215. DOI: 10.1080/03093640008726549.

[193] Paradisi, F et al. "The Conventional Non-Articulated SACH or a Multiaxial Prosthetic Foot for Hypomobile Transtibial Amputees? A Clinical Comparison on Mobility, Balance, and Quality of Life". *The Scientific World Journal* 2015 (2015), pp. 1–10. DOI: 10.1155/2015/261801.

[194] Wezenberg, D et al. "Differentiation between solid-ankle cushioned heel and energy storage and return prosthetic foot based on step-to-step transition cost". *Journal of Rehabilitation Research and Development* 51.10 (2014), pp. 1579–1590. DOI: 10.1682/JRRD.2014.03.0081.

[195] Arya, A et al. "A biomechanical comparison of the SACH, Seattle and Jaipur feet using ground reaction forces". *Prosthetics and Orthotics International* 19.1 (1995), pp. 37–45. DOI: 10.3109/03093649509078230.

[196] Zmitrewicz, RJ et al. "The Effect of Foot and Ankle Prosthetic Components on Braking and Propulsive Impulses During Transtibial Amputee Gait". *Archives of Physical Medicine and Rehabilitation* 87.10 (2006), pp. 1334–1339. DOI: 10.1016/j.apmr.2006.06.013.

[197] Au, SK, Dilworth, P, and Herr, H. "An Ankle-Foot Emulation System for the Study of Human Walking Biomechanics". *Proceedings - IEEE International Conference on Robotics and Automation*. 2006, pp. 2939–2945. DOI: 10.1109/ROBOT.2006.1642148.

[198] Au, SK et al. "Powered Ankle-Foot Prosthesis for the Improvement of Amputee Ambulation". *2007 29th Annual International Conference of the IEEE Engineering in Medicine and Biology Society*. IEEE, 2007, pp. 3020–3026. DOI: 10.1109/IEMBS.2007.4352965.

[199] Au, S, Berniker, M, and Herr, H. "Powered ankle-foot prosthesis to assist level-ground and stair-descent gaits". *Neural Networks* 21.4 (2008), pp. 654–666. DOI: 10.1016/j.neunet.2008.03.006.

[200] Gates, D et al. "Characterization of Ankle Function during Stair Ambulation". *The 26th Annual International Conference of the IEEE Engineering in Medicine and Biology Society*. Vol. 4. IEEE, 2004, pp. 4248–4251. DOI: 10.1109/IEMBS.2004.1404184.

[201] Versluys, R et al. "From Conventional Prosthetic Feet to Bionic Feet: A Review Study". *2nd IEEE RAS & EMBS International Conference on Biomedical Robotics and Biomechatronics*. IEEE, 2008, pp. 49–54. DOI: 10.1109/BIOROB.2008.4762839.

[202] Versluys, R et al. "Prosthetic feet: State-of-the-art review and the importance of mimicking human ankle–foot biomechanics". *Disability and Rehabilitation: Assistive Technology* 4.2 (2009), pp. 65–75. DOI: 10.1080/17483100802715092.

[203] Grimmer, M et al. "A powered prosthetic ankle joint for walking and running". *BioMedical Engineering Online* 15 (2016). DOI: 10.1186/s12938-016-0286-7.

[204] Hitt, J et al. "Robotic transtibial prosthesis with biomechanical energy regeneration". *Industrial Robot: An International Journal* 36.5 (2009), pp. 441–447. DOI: 10.1108/01439910910980169.

[205] Grabowski, AM and D'Andrea, S. "Effects of a powered ankle-foot prosthesis on kinetic loading of the unaffected leg during level-ground walking". *Journal of NeuroEngineering and Rehabilitation* 10.1 (2013), p. 49. DOI: 10.1186/1743-0003-10-49.

[206] Bellman, RD, Holgate, MA, and Sugar, TG. "SPARKy 3: Design of an active robotic ankle prosthesis with two actuated degrees of freedom using regenerative kinetics". *Proceedings of the 2nd Biennial IEEE/RAS-EMBS International Conference on Biomedical Robotics and Biomechatronics, BioRob 2008* (2008), pp. 511–516. DOI: 10.1109/BIOROB.2008.4762887.

[207] Eilenberg, MF, Geyer, H, and Herr, H. "Control of a Powered Ankle–Foot Prosthesis Based on a Neuromuscular Model". *IEEE Transactions on Neural Systems and Rehabilitation Engineering* 18.2 (2010), pp. 164–173. DOI: 10.1109/TNSRE.2009.2039620.

[208] Jiménez-Fabián, R and Verlinden, O. "Review of control algorithms for robotic ankle systems in lower-limb orthoses, prostheses, and exoskeletons". *Medical Engineering and Physics* 34.4 (2012), pp. 397–408. DOI: 10.1016/j.medengphy.2011.11.018.

[209] Ferris, AE et al. "Evaluation of a Powered Ankle-Foot Prosthetic System During Walking". *Archives of Physical Medicine and Rehabilitation* 93.11 (2012), pp. 1911–1918. DOI: 10.1016/j.apmr.2012.06.009.

[210] Cherelle, P et al. "Design and Validation of the Ankle Mimicking Prosthetic (AMP-) Foot 2.0". *IEEE Transactions on Neural Systems and Rehabilitation Engineering* 22.1 (2014), pp. 138–148. DOI: 10.1109/TNSRE.2013.2282416.

[211] Mancinelli, C et al. "Comparing a Passive-Elastic and a Powered Prosthesis in Transtibial Amputees". *33rd Annual International Conference of the IEEE Engineering in Medicine and Biology Society*. IEEE, 2011, pp. 8255–8258. DOI: 10.1109/IEMBS.2011.6092035.

[212] South, BJ et al. "Manufacture of Energy Storage and Return Prosthetic Feet Using Selective Laser Sintering". *Journal of Biomechanical Engineering* 132.1 (2010), p. 015001. DOI: 10.1115/1.4000166.

[213] Ventura, JD, Klute, GK, and Neptune, RR. "The effects of prosthetic ankle dorsiflexion and energy return on below-knee amputee leg loading". *Clinical Biomechanics* 26.3 (2011), pp. 298–303. DOI: 10.1016/j.clinbiomech.2010.10.003.

[214] Ventura, JD, Klute, GK, and Neptune, RR. "The effect of prosthetic ankle energy storage and return properties on muscle activity in below-knee amputee walking". *Gait and Posture* 33.2 (2011), pp. 220–226. DOI: 10.1016/j.gaitpost.2010.11.009.

[215] Zhu, J, Wang, Q, and Wang, L. "Effects of toe stiffness on ankle kinetics in a robotic transtibial prosthesis during level-ground walking". *Mechatronics* 24.8 (2014), pp. 1254–1261. DOI: 10.1016/j.mechatronics.2014.06.005.

[216] Fey, NP, Klute, GK, and Neptune, RR. "Optimization of Prosthetic Foot Stiffness to Reduce Metabolic Cost and Intact Knee Loading During Below-Knee Amputee Walking: A Theoretical Study". *Journal of Biomechanical Engineering* 134.11 (2012), p. 111005. DOI: 10.1115/1.4007824.

[217] Klodd, E et al. "Effects of prosthetic foot forefoot flexibility on oxygen cost and subjective preference rankings of unilateral transtibial prosthesis users". *The Journal of Rehabilitation Research and Development* 47.6 (2010), p. 543. DOI: 10.1682/JRRD.2010.01.0003.

[218] Adamczyk, PG, Roland, M, and Hahn, ME. "Sensitivity of biomechanical outcomes to independent variations of hindfoot and forefoot stiffness in foot prostheses". *Human Movement Science* 54 (2017), pp. 154–171. DOI: 10.1016/j.humov.2017.04.005.

[219] Quraishi, HA. "A novel design for decoupling the energy storage and return in passive ankle foot prostheses : A redesign of the VSPA foot". Masters. Delft University of Technology, 2017.

[220] Major, MJ et al. "The effects of prosthetic ankle stiffness on ankle and knee kinematics, prosthetic limb loading, and net metabolic cost of transtibial amputee gait". *Clinical Biomechanics* 29.1 (2014), pp. 98–104. DOI: 10.1016/j.clinbiomech.2013.10.012.

[221] Quesada, RE, Caputo, JM, and Collins, SH. "Increasing ankle push-off work with a powered prosthesis does not necessarily reduce metabolic rate for transtibial amputees". *Journal of Biomechanics* 49.14 (2016), pp. 3452–3459. DOI: 10.1016/j.jbiomech.2016.09.015.

[222] Mitchell, M et al. "Design and development of ankle-foot prosthesis with delayed release of plantarflexion". *The Journal of Rehabilitation Research and Development* 50.3 (2013), p. 409. DOI: 10.1682/JRRD.2011.06.0107.

[223] Mickelborough, J et al. "Muscle activity during gait initiation in normal elderly people". *Gait and Posture* 19.1 (2004), pp. 50–57. DOI: 10.1016/S0966-6362(03)00016-X.

[224] Peterson, TJ et al. "The Effect of Prosthetic Foot Component Stiffness on Gait Initiation and Termination of Transtibial Amputees". *ASME 2012 Summer Bioengineering Conference, Parts A and B*. American Society of Mechanical Engineers, 2012, pp. 803–804. DOI: 10.1115/SBC2012-80460.

[225] Reinbolt, J et al. "Are Patient-Specific Joint and Inertial Parameters Necessary for Accurate Inverse Dynamics Analyses of Gait?" *IEEE Transactions on Biomedical Engineering* 54.5 (2007), pp. 782–793. DOI: 10.1109/TBME.2006.889187.

[226] Hatze, H. "The fundamental problem of myoskeletal inverse dynamics and its implications". *Journal of Biomechanics* 35.1 (2002), pp. 109–115. DOI: 10.1016/S0021-9290(01)00158-0.

[227] Hatze, H. "Towards a comprehensive large-scale computer model of the human neuromusculoskeletal system". *Theoretical Issues in Ergonomics Science* 6.3 (2005), pp. 239–250. DOI: 10.1080/14639220412331330346.

[228] Pàmies-vilà, R et al. "Analysis of different uncertainties in the inverse dynamic analysis of human gait". *Mechanism and Machine Theory* 58 (2012), pp. 153–164. DOI: 10.1016/j.mechmachtheory.2012.07.010.

[229] Miller, LA and Childress, DS. "Problems associated with the use of inverse dynamics in prosthetic applications: An example using a polycentric prosthetic knee". *Robotica* 23.3 (2005), pp. 329–335. DOI: 10.1017/S0263574704001353.

[230] Dumas, R, Branemark, R, and Frossard, L. "Gait Analysis of Transfemoral Amputees: Errors in Inverse Dynamics Are Substantial and Depend on Prosthetic Design". *IEEE Transactions on Neural Systems and Rehabilitation Engineering* 25.6 (2017), pp. 679–685. DOI: 10.1109/TNSRE.2016.2601378.

[231] Saunders, MM et al. "Finite Element Analysis as a Tool for Parametric Prosthetic Foot Design and Evaluation. Technique Development in the Solid Ankle Cushioned Heel (SACH) Foot". *Computer Methods in Biomechanics and Biomedical Engineering* 6.1 (2003), pp. 75–87. DOI: 10.1080/1025584021000048974.

[232] Chen, NZ, Lee, WC, and Zhang, M. "A robust design procedure for improvement of quality of lower-limb prosthesis". *Bio-medical Materials and Engineering* 16.5 (2006), pp. 309–318.

[233] Lee, W et al. "Gait Analysis of Low-Cost Flexible-Shank Transtibial Prostheses". *IEEE Transactions on Neural Systems and Rehabilitation Engineering* 14.3 (2006), pp. 370–377. DOI: 10.1109/TNSRE.2006.881540.

[234] Omasta, M et al. "Finite element analysis for the evaluation of the structural behaviour, of a prosthesis for trans-tibial amputees". *Medical Engineering and Physics* 34.1 (2012), pp. 38–45. DOI: 10.1016/j.medengphy.2011.06.014.

[235] Bonnet, X et al. "Finite element modelling of an energy–storing prosthetic foot during the stance phase of transtibial amputee gait". *Proceedings of the Institution of Mechanical Engineers, Part H: Journal of Engineering in Medicine* 226.1 (2012), pp. 70–75. DOI: 10.1177/0954411911429534.

[236] International Organization for Standardization. *Structural testing of lower-limb prostheses: Requirements and test methods*. BS EN ISO 10328:2016. Brussels: BSI, 2016.

[237] Jia, X, Zhang, M, and Lee, WC. "Load transfer mechanics between transtibial prosthetic socket and residual limb - Dynamic effects". *Journal of Biomechanics* 37.9 (2004), pp. 1371–1377. DOI: 10.1016/j.jbiomech.2003.12.024.

[238] Ginestra, PS, Ceretti, E, and Fiorentino, A. "Potential of modeling and simulations of bioengineered devices: Endoprostheses, prostheses and orthoses". *Proceedings of the Institution of Mechanical Engineers, Part H: Journal of Engineering in Medicine* 230.7 (2016), pp. 607–638. DOI: 10.1177/0954411916643343.

[239] International Organization for Standardization. *Prosthetics - Testing of ankle-foot devices and foot units: Requirements and test methods*. BS EN ISO 22675:2016. Brussels: BSI, 2016.

[240] Stratasys Ltd. *PolyJet Materials Data Sheet*. Pages: 3. 2016.

[241] Cantrell, J et al. "Experimental characterization of the mechanical properties of 3D printed ABS and polycarbonate parts". *Conference Proceedings of the Society for Experimental Mechanics Series* 3 (2017), pp. 89–105. DOI: 10.1007/978-3-319-41600-7_11.

[242] Hearn, E. *Mechanics of Materials*. 3rd Edition. Butterworth Heineman, 2000.

[243] Mallick, PK. *Fiber-reinforced composites: Materials, manufacturing, and design, third edition*. 3rd Edition. Taylor and Francis, 2007.

[244] Aalco Metals Ltd. *Aluminium Alloy 6082 - T6/T651 Plate*. Pages: 24-25. 2013.

[245] BSI Standards Publication. *Aluminium and aluminium alloys - Sheet , strip and plate*. BS EN 485-2:2016+A1:2018. Brussels: BSI Standards Publication, 2018.

[246] Granta Design Limited. *CES Edupack software*. Cambridge, UK, 2016.

[247] Easy Composites Ltd. *XC130 Autoclave Cure Component Prepreg System*. 2017.

[248] Toray CA Inc. *T700S Technical Data Sheet*. Pages: 2. 2005.

[249] Mahmoodi, P et al. "Prosthetic foot design optimisation based on roll-over shape and ground reaction force characteristics". *Proceedings of the Institution of Mechanical Engineers, Part C: Journal of Mechanical Engineering Science* 231.17 (2017), pp. 3093–3103. DOI: 10.1177/0954406216643110.

[250] Hansen, AH, Childress, DS, and Knox, EH. "Roll-over shapes of human locomotor systems: effects of walking speed". *Clinical Biomechanics* 19.4 (2004), pp. 407–414. DOI: 10.1016/j.clinbiomech.2003.12.001.

[251] Tryggvason, H et al. "Modeling and simulation in the design process of a prosthetic foot". *58th Conference on Simulation and Modelling*. Issue: 138. 2017, pp. 398–405. DOI: 10.3384/ecp17138398.

[252] Collins, JA, Busby, HR, and Staab, GH. *Mechanical Design of Machine Elements and Machines: A Failure Prevention Perspective*. 2nd Edition. John Wiley and Sons, 2009.

[253] Mott, RL, Vavrek, EM, and Wang, J. *Machine Elements in Mechanical Design*. 6th Edition. Pearson, 2018.

[254] Budynas, RG and Nisbett, JK. *Shigley's Mechanical Engineering Design*. 9th Edition. McGraw-Hill, 2011.

[255] Rothbart, HA. *Cam Design Handbook*. McGraw-Hill, 2004.

[256] Norton, RL. *Cam Design and Manufacturing Handbook*. Industrial Press, 2002.

[257] Prautzsch, H, Boehm, W, and Paluszny, M. *Bezier and B-Spline Techniques*. Springer, 2002.

[258] Piegl, L and Tiller, W. *The NURBS Book*. Springer, 1997.

[259] Radzevich, SP. *Dudley's Handbook of Practical Gear Design and Manufacture*. 2nd Edition. Taylor and Francis, 2012.

[260] Uemura, K et al. "Effects of dual-task switch exercise on gait and gait initiation performance in older adults: Preliminary results of a randomized controlled trial". *Archives of Gerontology and Geriatrics* 54.2 (2012). DOI: 10.1016/j.archger.2012.01.002.

[261] Johnson, L, Burridge, JH, and Demain, SH. "Internal and External Focus of Attention During Gait Re-Education: An Observational Study of Physical Therapist Practice in Stroke Rehabilitation". *Physical Therapy* 93.7 (2013), pp. 957–966. DOI: 10.2522/ptj.20120300.

[262] Polskaia, N et al. "Continuous cognitive task promotes greater postural stability than an internal or external focus of attention". *Gait and Posture* 41.2 (2015), pp. 454–458. DOI: 10.1016/j.gaitpost.2014.11.009.

[263] Tard, C et al. "How does visuospatial attention modulate motor preparation during gait initiation?" *Experimental Brain Research* 234.1 (2016). Publisher: Springer Verlag, pp. 39–50. DOI: 10.1007/s00221-015-4436-0.

[264] Yogev-Seligmann, G, Sprecher, E, and Kodesh, E. "The Effect of External and Internal Focus of Attention on Gait Variability in Older Adults". *Journal of Motor Behavior* 49.2 (2017), pp. 179–184. DOI: 10.1080/00222895.2016.1169983.

[265] Melker Worms, JL de et al. "Effects of attentional focus on walking stability in elderly". *Gait and Posture* 55 (2017), pp. 94–99. DOI: 10.1016/j.gaitpost.2017.03.031.

[266] Novak, D et al. "Automated detection of gait initiation and termination using wearable sensors". *Medical Engineering and Physics* 35.12 (2013), pp. 1713–1720. DOI: 10.1016/j.medengphy.2013.07.003.

[267] Wentink, E et al. "Detection of the onset of gait initiation using kinematic sensors and EMG in transfemoral amputees". *Gait and Posture* 39.1 (2014), pp. 391–396. DOI: 10.1016/j.gaitpost.2013.08.008.

[268] Moineau, B et al. "A new method to assess temporal features of gait initiation with a single force plate". *Gait and Posture* 39.1 (2014), pp. 631–633. DOI: 10.1016/j.gaitpost.2013.07.007.

[269] Koo, TK and Li, MY. "A Guideline of Selecting and Reporting Intraclass Correlation Coefficients for Reliability Research". *Journal of Chiropractic Medicine* 15.2 (2016), pp. 155–163. DOI: 10.1016/j.jcm.2016.02.012.

[270] Mehta, S et al. "Performance of intraclass correlation coefficient (ICC) as a reliability index under various distributions in scale reliability studies". *Statistics in Medicine* 37.18 (2018), pp. 2734–2752. DOI: 10.1002/sim.7679.

[271] Bujang, MA and Baharum, N. "A simplified guide to determination of sample size requirements for estimating the value of intraclass correlation coefficient: a review". *The Journal of the School of Dental Sciences* 12.1 (2017), pp. 1–11.

[272] Weir, JP. "Quantifying Test-Retest Reliability Using The Intraclass Correlation Coefficient And The SEM". *Journal of Strength and Conditioning Research* 19.1 (2005), pp. 231–240.

[273] Shrout, PE and Fleiss, JL. "Intraclass Correlations: Uses in Assessing Rater Reliability". *Psychological Bulletin* 86.2 (1979), pp. 420–428.

[274] Mcgraw, KO and Wong, SP. "Forming Inferences About Some Intraclass Correlation Coefficients". *Psychological Methods* l.1 (1996), pp. 30–46.

[275] Giavarina, D. "Understanding Bland Altman analysis". *Biochemia Medica* 25.2 (2015). Publisher: Biochemia Medica, Editorial Office, pp. 141–151. DOI: 10.11613/BM.2015.015.

[276] Sanderson, DJ, Franks, IM, and Elliott, D. "The effects of targeting on the ground reaction forces during level walking". *Human Movement Science* 12 (1993).

[277] Grabiner, MD et al. "Visual guidance to force plates does not influence ground reaction force variability". *Journal of Biomechanics* 28.9 (1995), pp. 1115–1117.

[278] Wearing, SC, Urry, SR, and Smeathers, JE. "The effect of visual targeting on ground reaction force and temporospatial parameters of gait". *Clinical Biomechanics* 15 (2000).

[279] Verniba, D, Vergara, ME, and Gage, WH. "Force plate targeting has no effect on spatiotemporal gait measures and their variability in young and healthy population". *Gait and Posture* 41.2 (2015), pp. 551–556. DOI: 10.1016/j.gaitpost.2014.12.015.

[280] Castro, MP et al. "Pooling sexes when assessing ground reaction forces during walking: Statistical Parametric Mapping versus traditional approach". *Journal of Biomechanics* 48.10 (2015), pp. 2162–2165. DOI: 10.1016/j.jbiomech.2015.05.027.

[281] Agrawal, V et al. "Symmetry in External Work (SEW): A Novel Method of Quantifying Gait Differences Between Prosthetic Feet". *Prosthetics and Orthotics International* 33.2 (2009), pp. 148–156. DOI: 10.1080/03093640902777254.

[282] Błazkiewicz, M, Wiszomirska, I, and Wit, A. "Comparison of four methods of calculating the symmetry of spatial-temporal parameters of gait". *Acta of Bioengineering and Biomechanics* 16.1 (2014), pp. 29–35. DOI: 10.5277/abb140104.

[283] Pourhoseingholi, MA, Vahedi, M, and Rahimzadeh, M. "Sample size calculation in medical studies". *Gastroenterology and Hepatology* 6 (2013).

[284] Mullineaux, DR, Bartlett, RM, and Bennett, S. "Research design and statistics in biomechanics and motor control". *Journal of Sports Sciences* 19.10 (2001), pp. 739–760. DOI: 10.1080/026404101317015410.

[285] Oliveira, AS and Pirscoveanu, CI. "Implications of sample size and acquired number of steps to investigate running biomechanics". *Sci Rep* 11.1 (2021), p. 3083. DOI: 10.1038/s41598-021-82876-z.

[286] Bovi, G et al. "A multiple-task gait analysis approach: Kinematic, kinetic and EMG reference data for healthy young and adult subjects". *Gait and Posture* 33.1 (2011), pp. 6–13. DOI: 10.1016/j.gaitpost.2010.08.009.

Appendix A

PC Specifications

- Intel i7-6700 CPU 4 Cores @ 3.40GHz
- Ram 16GB - 32GB
- NVIDIA GeForce GTX 745 - 4GB VRAM

Appendix B

MATLAB Code

B.1 NURBS Interpolation Code

B.1.1 Master Control File

```
clear
clc
%% INPUTS:

% Indepenent variables
%   Define data point array - D
D = [0 3 -1 -4 -4; 0 4 4 0 -3];
%   Spline degree - p
p = 2;
% Weight Vector
w = ones(1,length(D));

% Dependent variables
%   Number of data or control points
n = size(D,2);
%   Number of knots
m = n + p + 1;
%   Coordinate dimension - CoDim
CoDim = size(D,1);
%   Number coordinates points - nCoordP
nCP = CoDim*n;

%% FUNCTION CALLUPS

%   Parameter Vector
t = PVector(n, nCP, D);
```

```
%   Knot Vector
U = KVector (m, p, t);
%   Control Points
P = ControlPoints(n, m, U, t, p, CoDim, D);
%   Call Nurbs function
C = Nurbs(U, P, n, m, p, w);

%% PLOT NURBS CURVE
lw = 1.2;
mk = 10;

%   Generate Plot
% figure('Name','NURBS')
F1 = figure(1);
F1.Position = [1,1,800,500];F1.PaperType = 'a4';
set(F1,'DefaultTextInterpreter','latex','defaultAxesTickLabelInterpreter'...
    ,'latex','defaultLegendInterpreter','latex')
%   Data
p1 = plot(D(1, :), D(2, :), 'mo','MarkerSize',mk,'LineWidth',lw);hold on
%   Control Points
p2 = plot(P(1, :), P(2, :), 'bo','MarkerSize',mk,'LineWidth',lw);hold on
%   Control Polygon
p3 = plot(P(1, :), P(2, :), 'g','LineWidth',lw);hold on
%   NURBs Curve
p4 = plot(C(1, :), C(2, :), 'r','LineWidth',lw);hold on
axF1 = findobj(gcf,'type','axes');
axF1.XLim = [-5 6];axF1.YLim = [-4 5];
axF1.ClippingStyle = 'rectangle';
axF1.XGrid = 'on';axF1.XMinorGrid = 'on';
axF1.YGrid = 'on';axF1.YMinorGrid = 'on';
axF1.FontSize = 14;axF1.XLabel.String = 'X-Length (mm)';
axF1.YLabel.String = 'Y-Height (mm)';
axF1.XLabel.FontSize = 14; axF1.YLabel.FontSize = 14;
legd5 = legend({'Data Points','Control Points','Control Polygon',...
    'NURBS Curve'});
set(legd5,'FontSize',14,'Location','northoutside','Orientation',...
    'horizontal')
exportgraphics(F1,'BasicNURB.pdf','ContentType','Vector',...
    'BackgroundColor','w')
exportgraphics(F1,'BasicNURB.png','ContentType','Image','Resolution',...
    150,'BackgroundColor','w')
```

B.1.2 Parameter Function

```
function [t] = PVector (n, nCP, D)
%% CALCULATE PARAMETER VECTOR

%% INPUTS:

%   Number of Data/Control points - n
%   Number of coordinate points - nCP
%   Data point matrix - D

%% OUTPUT: PARAMETER KNOT USING CENTRIPETAL METHOD

%   Chord length, cl
cl = zeros(1, n);
for i = 1:2:(nCP-3)

    cl(uint8(i/2+.5)) = sqrt(sum((abs(D((i+2):(i+3))-D((i):(i+1)))).^2));
end

%   Find 'total length' d by summing all chord lengths
d = sum(cl);

%   Find parameter values t(i)
%   Initialise vector of zeros with length equal to number of data points
t = zeros(1, n);

%   Set final knot in vector equal to 1
t(n) = 1;

%   Calculate interior parameter knots
for i = 2:(n-1)

    t(i) = t(i-1)+cl(i-1)/d;
end
end
```

B.1.3 Knot Function

```
function [U] = KVector (m, p, t)
%% CALCULATE KNOT VECTOR

%% INPUTS:
```

```
%   Total number of knots - m
%   Spline degree - p
%   Parameter vector - t

%% OUTPUT: KNOT VECTOR

%   Generate knot vector of zeros with length m
U = zeros(1, m);

%   Set clamped ends (p+1) knots
U((m-p):m) = 1;

%   Calculate internal knots
for i = (1+(p+1)):(m-(p+1))

    k = (i-p):(i-1);

    U(i) = (1/p).*sum(t(k));
end
end
```

B.1.4 Control Point Function

```
function [P] = ControlPoints(n, m, U, t, p, CoDim, D)
%% CALCULATE CONTROL POINTS

%% INPUTS:

%   Number of Data/Control points - n
%   Total number of knots - m
%   Knot vector - U
%   Parameter vector - t
%   Spline degree - p
%   Coordinate dimension - CoDim
%   Data points vector - D

%% OUTPUT: CALCULATION OF BASIS FUNCTIONS
%   Modified from BasisFunctions.m file to create n x n matrix

%   Setup array for population
N = zeros(n);

%   Calculate 0th degree functions
```

```
for j = 1 : n
    for i = 1 : m - 1
        if U(i) == U(i+1)
            N(j,i) = 0;
        elseif t(j) >= U(i) && t(j) <= U(i+1)
            N(j,i) = 1;
        else
            N(j,i) = 0;
        end
    end

%   Calculate higher degree basis functions up to degree p
    for k = 2 : p + 1
        for i = 1 : n
            if N(j,i) ~= 0
                d = ((t(j) - U(i)) * N(j,i)) / (U(i + k - 1) - U(i));
            else
                d = 0;
            end
            if N(j,i+1) ~= 0
                e = ((U(i + k) - t(j)) * N(j,i+1)) / (U(i + k) - U(i + 1));
            else
                e = 0;
            end
            N(j,i) = d + e;
        end
    end
end

N(:,all(N==0))=[];
N(abs(N)<1e-4)=0;


%% OUTPUT: SOLVING MATRICES FOR CONTROL POINTS

%   Set array for control points
P = zeros(CoDim, n);
%   Transpose data point matrix
D = D';
%   Solve for P using backslash operator, Gaussian Elimination algorithm
P = N\D;
%   Transpose control point matrix
P = P';

end
```

B.1.5 NURBS Function

```
function [C, N, R, S, U] = Nurbs (U, P, n, m, p, w)
%% CALCULATE NURBS FUNCTION ALONG DOMAIN VECTOR X

%% INPUTS:

%   Setup domain vector
X = linspace(U(1), U(end), 10*size(P,2));

%   Total elements to evaluate
totalX = numel(X);
N = zeros(totalX, n);

%% OUTPUT: NURBS CURVE POINTS

%   Calculate basis function
for i = 1 : totalX
    u = X(i);
    N(i, :) = BasisFunctions(n, m, u, U, p);
end

%   Calculate denominator of rational basis functions
S = zeros(totalX, 1);
for i = 1 : totalX
    tmp = N(i, :);
    for j = 1 : size(tmp, 2)
        S(i) = S(i) + (tmp(j) * w(j));
    end
end

%   Calculate rational basis functions
R = zeros(totalX, n);
for i = 1 : totalX
    tmp = N(i, :);
    for j = 1 : size(tmp, 2)
        if(S(i) ~= 0)
            R(i, j) = (tmp(j) * w(j)) / S(i);
        else
            R(i, j) = 0;
        end
    end
end
```

```
%   Calculate curve points
C = zeros(2, totalX);
for i = 1 : totalX
    tmp = R(i, :);
    sum = [0; 0];
    for j = 1 : size(tmp, 2)
        sum = sum + (P(:, j) * tmp(j));
    end
    C(:, i) = sum;
end
end
```

Appendix C

ISO Standards

C.1 Prosthetics

C.1.1 ISO 22675:2016

Prosthetics - Testing of ankle-foot devices and foot units - Requirements and test methods [239]. Used in this thesis to form the boundary conditions for the Ansys FEA simulations.

Table 6 — Total length of test samples and segmental lengths of end attachments

Dimensions in millimetres

u-level	Typical combinations of segmental lengths of end attachments [a]		
	A	B	C
uT, L [b]	—	—	—
u_K	$u_{T,26} - u_K = 78$ $(u_{T,L} - u_K$ = Total length − 500)	$u_{T,26} - u_C = 328$ $(u_{T,L} - u_C$ = Total length − 250)	— $u_{T,26} - u_A = 498$ $[u_{T,L} - u_A = 578 \cdot (L/26) - 80]$
$u_C = 250$ [c]	$(u_K - u_A)_{\text{Any foot length}} = 420$	—	—
u_A	—	—	—
zero	$u_{A,\text{Any foot length}} = 80$	uA, Any foot length = 80	uA, Any foot length = 80
Total length [a] $u_{T,L}$ [b]	$u_{T,26} = 578$	$u_{T,26} = 578$ $u_{T,L} = 578 \cdot (L/26)$; ($L$ in cm)	$u_{T,26} = 578$

The total length and the segmental lengths also apply to the additional test loading levels P6, P7, and P8 as specified in Annex C [see C.3 a)].

[a] The total length of test samples can be achieved by different combinations of segmental lengths of end attachments. Examples of combinations of segment lengths, typical of the different types of end attachments, are listed in columns A, B and C, where

– column A specifies the segmental lengths of a test sample set-up using end attachments extending from the knee level to the top load application level.

– column B specifies the segmental lengths of a test sample set-up using end attachments extending from a connecting level at $u_C = 250$ mm [see c)] to the top load application level, and

– column C specifies the segmental lengths of a test sample set-up using end attachments extending from the ankle level to the top load application level. This specific set-up is illustrated in Figure 4.

[b] The value of $u_{T,L}$ is dependent on the foot length L, as indicated. The foot length L is shown in Figures 2 and 4 and specified in Table 7. The dimension $u_{T,L}$ is shown in Figures 4 and 5 and specified in Table 7.

[c] The value of u_C specifies any connecting level between the knee and ankle level, to be determined in consideration of the individual design of ankle-foot device or foot unit under test. For the example used in this table, u_C has been given the value of 250 mm.

Figure C.1: The first of two tables used to define the major dimensions of the test setup. Table 6 includes equations to calculate dimensions along the vertical u axis.

Table 7 — Coordinates of top load application point P_T and tilting axis TA of foot platform based on given values of foot length L, for all test loading levels

Subject	Test procedure		Foot length L [a, b] cm												
			20	21	22	23	24	25	26	27	28	29	30	31	32
			Related values of f- and u-offsets of P_T [c] and TA [d]												
		Direction and location	Numerical value mm												
Position of top load application point, P_T [c]	All tests	$f_{T,L}$	$f_{T,L} = f_{T,26} \cdot (L/26)$												
			17	18	19	19	20	21	**22**	23	24	25	25	26	27
		$u_{T,L}$	$u_{T,L} = u_{T,26} \cdot (L/26)$												
			445	467	489	511	534	556	**578**	600	622	645	667	689	711
Position of tilting axis TA of foot platform [d]	All tests	$f_{TA,L}$	$f_{TA,L} = 0{,}365 \cdot L$												
			73	77	80	84	88	91	**95**	99	102	106	110	113	117
		$u_{TA,L}$	$u_{TA,L} = 0{,}1 \cdot L$												
			20	21	22	23	24	25	**26**	27	28	29	30	31	32

The specified dimensions also apply to the additional test loading levels P6, P7, and P8 as specified in Annex C [see C.3 a)].

[a] The foot length L is specified in cm, taking into account that in many countries the foot size determining the foot length is measured in cm.

[b] The selection of appropriate sizes of ankle-foot devices and foot units for test purposes is not limited by the range given in this table. The formulae allow the calculation of f- and u-offsets of P_T and TA relating to any foot length L.

[c] See 6.3 and Figures 1, 4 and 5. (For further information see 16.1.1 and A.2.2.3.)

[d] See 13.4.2.3 and Figure 5. (For further information see 16.1.1, E.3.2 and E.3.3.)

Figure C.2: The second of two tables used for dimensions the test setup. Table 7 includes co-ordinates for the load point and tilting axis.

Appendix D

ANSYS

D.1 Intermediate Material Study

This section contains the composite's names, mechanical properties, and simulation results for reference in the intermediate material study of Chapter 3.

D.1.1 Materials & Mechanical Properties

A selection of five different carbon fibre prepreg materials from three different sources were used in this study. The first three are quasi-isotropic or biaxial, sourced from a supplier's data sheet [247] and the EduPack materials database [246]. These three also have information on the composition of the composite,

Table D.1: General material information and mechanical properties for the isotropic woven prepregs. CF = Carbon Fibre.

General Information			
Name	XC130 210g	Biaxial Prepreg	Quasi-isotropic Prepreg
Source	EasyComposites	CES Edupack	CES Edupack
Matrix	Epoxy	Epoxy	Epoxy
Fabric	CF 3K Twill	CF Weave	CF Weave
Layup	-	[0/90]	[0/90,+45/-45]s
V_f **Fraction**	-	0.65	0.65
Behaviour	Quasi-isotropic	Biaxial	Quasi-isotropic
Mechanical Properties			
Young's modulus	55.2GPa	68.7GPa	48.2GPa
Poisson's ratio	0.399	0.058	0.399
Tensile Strength	645MPa	910MPa	649MPa

Table D.2: Mechanical properties for the orthotropic woven prepregs found in the Ansys materials library. Both Young's modulus and Tensile limit are given in units of MPa.

Prepreg Designation	**Young's Modulus**			**Poisson's Ratio**			**Tensile Limit**		
	x	y	z	xy	yz	xz	x	y	z
230GPa	61340	61340	6900	0.04	0.3	0.3	805	805	50
395GPa	91820	91820	9000	0.05	0.3	0.3	829	829	50

helpful in providing a relative context for comparisons. The final two materials are orthotropic carbon fibre prepregs found in the Ansys material database and have only mechanical properties. Relevant information on these materials is presented in the reference Tables D.1 and D.2 of this section, for use in the main chapter.

The XC130 composite data sheet had no poisson's ratio value. However, as it was similar to the Quasi-isotropic prepreg from the EduPack database, the same poisson ratio value was assigned.

Due to the orthotropic properties of the Ansys materials, it was important to have the model orientated to the correct axes. For these studies, this required the y-axis to be vertical, and the x-axis aligned along the longitudinal axis of the foot, pointing forward. Even with the orthotropic properties, this is still only an approximation. These two database materials are intended to be used in the Ansys ACP module, where they are applied to elements capable of modelling the composite laminate behaviour.

The results of these studies can be found in Table D.3, and are discussed in the material study section 3.3.1

Table D.3: Results of the material study involving data from the materials in the other tables of this section.

Source	**Name**	**Stress** MPa	**Deformation** mm	**Stiffness** N/mm
Easy Composites	XC130 210g	440.54	13.247	119.27
CES Edupack	Biaxial	434.87	10.644	148.44
	Quasi-isotropic	432.99	14.927	105.85
Ansys	230GPa	431	13.512	116.93
	395GPa	460.96	10.442	151.31

Table D.4: Material properties used in the link parametric study

Material	Young's (GPa)	Poisson's	Yield (MPa)	Ultimate (MPa)
Al 6082	70	0.34	255	300
ABS	1.6	0.35	22	-

D.2 Link FEA Data

D.3 APDL Code

D.3.1 Maximum Static Stiffness

The code used here calculates the stiffness from a static loading position by finding the maximum deflection and force in the nodes of the mesh.

```
!----------------Deflection Extraction
   --------------------------------

SET,LAST,LAST,,,,,,
!set dataset to be read

ALLSEL
CMSEL,S,SPRING_BODY,NODE
!selects nodes of spring body

*GET,NC,NODE,0,COUNT,
!stores number of selected nodes as NC

*DIM,NL,ARRAY,NC,2
*DIM,NN,ARRAY,NC,

*VGET,NN,NODE,ALL,NLIST
!stores list of nodes in array

UY_MAX = 0
!creates initial value for conditional statement

*DO,i,1,NC,1
!loop cycling through nodes on pylon face
    ALLSEL
    *GET,U_Y,NODE,NN(i),U,Y,
    !finds the y-deflection of node
    NL(i,1) = NN(i)
```

```
    NL(i,2) = U_Y
    !stores node number and deflection
    *IF,UY_MAX,GT,U_Y,THEN
        UY_MAX = U_Y
        !heel spring conditional
    !*IF,UY_MAX,LT,U_Y,THEN
    !   UY_MAX = U_Y
        !forefoot spring conditional
    *ENDIF
    !conditional statement to determine maximum deflection, factoring
        in change of sign
*ENDDO

my_DEF_YMAX = UY_MAX
!stores the maximum deflection of entire model

!-----------------------Load & Stiffness Extraction
   ---------------------------------
ALLSEL
*GET,MXNODE,NODE,0,NUM,MAXD
MXNODE2 = MXNODE - 50
!select all nodes in system and stores full count as parameter value

!SET,LAST,LAST,,,,,,
!sets data to be read at last substep of loadstep
FY_MAX = 1

*DO,i,MXNODE2,MXNODE,1
!loops through all nodes in system
    *GET,TEMP_L,NODE,i,F,FY
    *IF,FY_MAX,GT,TEMP_L,THEN
        FY_MAX = TEMP_L
    *ENDIF
    !conditional statement to find the full load applied at each
       loadstep and store in temp value
*ENDDO

my_LOAD = FY_MAX
!store final value from node loop in load array

*DIM,STIFF_K,ARRAY,LSNUM,1
!creates stiffness array and plot table

my_STIFF_K = my_LOAD/my_DEF_YMAX
```

```
!calculates stiffness from applied loads and relative spring
   deflection
```

D.3.2 Rollover Shape Extraction

The code here calculates the rollover shape using the raw data in the solution folder.

```
ALLSEL

/POST1
!enter post processing command module
!------------------Initial Script Stuff-------------------
SET,LAST,
!reads last data step
*GET,LSNUM,ACTIVE,0,SOLU,NCMLS
!finds the number of loadsteps and stores as var LSNUM
LSNUM = LSNUM - 1
!initial zero loadstep is alreadyt cut off, this removes the last
   zero loadstep
r = LSNUM
!set array row parameter = LSNUM
SET,FIRST,,,,,,,
!read the first data set
CSLIST
!lists coordinate system
*AFUN,DEG
!sets angular calcs to degrees
!-------------------------------------------------------
!replace this block with loadstep block to collect all data
!LSNUM swapped for DSNUM
!SET,t,LAST,,,,,, must be replaced with SET,,,,,,,t,
!*GET,DSNUM,ACTIVE,0,SET,NSET
!finds the number of data sets and stores as var DSNUM
!r = DSNUM
!set array row parameter = DSNUM
!-------------------------------------------------------
!-----------------CoP Extraction-----------------------
*DIM,COP_X,ARRAY,r,4
!creates an array called COP_X of row=r and col=1

*DO,t,1,LSNUM,1
!initiates a loop counting from 1 to DSNUM in steps of 1
    SET,t,LAST,,,,,,
```

```
!sets dataset number t to be read
ALLSEL
CMSEL,S,FOOT_SURF,NODE
!selects all nodes on heel surf
ESLN
!selects elements associated with nodes
ESEL,U,ENAME,,187
!unselects all solid187 elements to leave only contact elements
NSLE
!selects nodes of elements
*GET,NODE_COUNT,NODE,0,COUNT,
!stores number of nodes as NODE_COUNT
*DIM,NODE_LIST,ARRAY,NODE_COUNT,4
!creates array
*DIM,NODE_NUM,ARRAY,NODE_COUNT,
!creates array
*VGET,NODE_NUM,NODE,ALL,NLIST
!stores list of nodes in array
RY_MAX = 0
RY_MAX_X = 0
SUM = 0
WT_SUM = 0
!creates initial values for loop

*DO,i,1,NODE_COUNT,1
!initiates loop through list of nodes
    ALLSEL
    *GET, X_i, NODE, NODE_NUM(i), LOC, X,
    *GET,X_f, NODE, NODE_NUM(i), U, X,
    NODE_X = X_i + X_f
    !find and store the sum of x-location and displacement for
       nodes
    *GET,Y_i,NODE,NODE_NUM(i),LOC,Y,
    *GET,Y_f,NODE,NODE_NUM(i),U,Y,
    NODE_Y = Y_i - Y_f
    !find and store the sum of y-location and displacement for
       nodes
    NSEL,S,NODE, , NODE_NUM(i)
    ESLN
    FSUM,
    *GET, TEMP_LOAD, FSUM, 0, ITEM, FY,
    !finds and temporarliy stores y-load at node
    NODE_LOAD = TEMP_LOAD
    !assigns temp loads to uncoupled parameter
    NODE_LIST(i,1) = NODE_NUM(i)
    NODE_LIST(i,2) = NODE_X
```

```
        NODE_LIST(i,3) = NODE_LOAD
        NODE_LIST(i,4) = NODE_Y
        !stores found values in array
        SUM = SUM + NODE_LOAD
        WT_SUM = WT_SUM + NODE_LOAD*NODE_X
        !sums of node loads and moments
        !*IF,RY_MAX,LT,NODE_LOAD,THEN
        !   RY_MAX = NODE_LOAD
        !   RY_MAX_X = NODE_X
        !   RY_MAX_Y = NODE_Y
        !*ENDIF
        !alternate method of simply taking highest load value, not as
            accurate
    *ENDDO

    COP_X(t,1) = WT_SUM/SUM
    !finds the x-location of COP by dividing the moment by force
*ENDDO

!*MWRITE,COP_X,C:\Users\Ben\Documents\Ansys\Concept\ISO_22675\CoP_X,
   txt
!%7.2F

!----------------Plate Angle Extraction
   ---------------------------------
CSYS,21
!selects coordinate system centered on point of rotation

*DIM,PLATE_ANG,ARRAY,r,5
!creates plate angle array

*DO,t,1,LSNUM,1
!initiates loop through timesteps
    SET,t,LAST,,,,,
    !set dataset to be read
    ALLSEL
    CMSEL,S,PLATE_BACK,NODE
    *GET,PNNUM1,NODE,,NUM,MAX
    *GET,XB,NODE,PNNUM1,LOC,X
    *GET,YB,NODE,PNNUM1,LOC,Y
    *GET,X1,NODE,PNNUM1,U,X
    *GET,Y1,NODE,PNNUM1,U,Y
    !finds x,y location and deformation of plate back edge
    ALLSEL
    CMSEL,S,PLATE_FRONT,NODE
    *GET,PNNUM2,NODE,,NUM,MAX
```

```
    *GET,XF,NODE,PNNUM2,LOC,X
    *GET,YF,NODE,PNNUM2,LOC,Y
    *GET,X2,NODE,PNNUM2,U,X
    *GET,Y2,NODE,PNNUM2,U,Y
    !finds x,y location and deformation of plate front edge
    PLATE_ANG(t,1) = XB+X1
    PLATE_ANG(t,2) = YB+Y1
    PLATE_ANG(t,3) = XF+X2
    PLATE_ANG(t,4) = YF+Y2
    !stores the actual coordinate location of the front & back edge
       at the timestep
    X_ABS = (XF+X2)-(XB+X1)
    Y_ABS = (YB+Y1)-(YF+Y2)
    !creates absolute values of the coordinates to find angles
    PI = ACOS(-1)
    PLATE_ANG(t,5) = ATAN(Y_ABS/X_ABS)
    !finds the angle of the plate, this is the equivalent to the
       boundary condition
*ENDDO

!*MWRITE,PLATE_ANG,C:\Users\Ben\Documents\Ansys\Concept\ISO_22675\
   PANG,txt
!%10.4F %10.4F %10.4F %10.4F %10.4F

!----------------Deflection Extraction
   ---------------------------------
CSYS,20
!selects coordinate system centered at rear of plate
*DIM,DEF_YMAX,ARRAY,r,5
KJH = 489
!IMPORTANT: sets parameter value for knee joint height, check
   ISO22675 table values

*DO,t,1,LSNUM,1
!initiates loop through timesteps
    SET,t,LAST,,,,,
    !set dataset to be read
    ALLSEL
    CMSEL,S,END_CON,NODE
    !selects nodes on bottom face of pylon
    *GET,NC_END_CON,NODE,0,COUNT,
    !stores number of selected nodes as NC_END_CON
    *DIM,NL_END_CON,ARRAY,NC_END_CON,2
    *DIM,NN_END_CON,ARRAY,NC_END_CON,
    *VGET,NN_END_CON,NODE,ALL,NLIST
    !stores list of nodes in array
```

```
UY_MAX = 0
!creates initial value for conditional statement

*DO,i,1,NC_END_CON,1
!loop cycling through nodes on pylon face
    ALLSEL
    *GET,U_Y,NODE,NN_END_CON(i),U,Y,
    !finds the y-deflection of node
    NL_END_CON(i,1) = NN_END_CON(i)
    NL_END_CON(i,2) = U_Y
    !stores node number and deflection
    *IF,UY_MAX,LT,U_Y,THEN
        UY_MAX = U_Y
    *ELSEIF,UY_MAX,GT,U_Y,THEN
        UY_MAX = U_Y
    *ENDIF
    !conditional statement to determine maximum deflection,
       factoring in change of sign
*ENDDO
DEF_YMAX(t,1) = UY_MAX
!stores the maximum deflection of entire model

ALLSEL
CMSEL,S,CF_SPRING,NODE
!selects profile nodes of prosthetic
*GET,NC_CF_SPRING,NODE,0,COUNT,
*DIM,NL_CF_SPRING,ARRAY,NC_CF_SPRING,2
*DIM,NN_CF_SPRING,ARRAY,NC_CF_SPRING,
*VGET,NN_CF_SPRING,NODE,ALL,NLIST
!creates arrays to store nodes and deflection values
UY_MAX1 = -100
!creates offset value for conditional statement

*DO,i,1,NC_CF_SPRING,1
!loop cycling through nodes on profile
    ALLSEL
    *GET,U_Y1,NODE,NN_CF_SPRING(i),U,Y,
    !find the y-deflection of node
    NL_CF_SPRING(i,1) = NN_CF_SPRING(i)
    NL_CF_SPRING(i,2) = U_Y1
    !store the node number and y-deflection
    *IF,UY_MAX1,LT,U_Y1,THEN
        UY_MAX1 = U_Y1
    !*ELSE,UY_MAX1,GT,U_Y1,THEN
        !UY_MAX1 = U_Y1
    *ENDIF
```

```
    *ENDDO
    DEF_YMAX(t,2) = UY_MAX1
    !stores maximum deflection of prosthetic shape
    DEF_YMAX(t,3) = UY_MAX1-UY_MAX
    !actual deflection of prosthetic spring
    DEF_YMAX(t,4) = 80-(UY_MAX1-UY_MAX)
    !translation of ankle joint centre
    DEF_YMAX(t,5) = KJH-(UY_MAX1-UY_MAX)
    !translation of knee joint centre
*ENDDO

!*MWRITE,DEF_YMAX,C:\Users\Ben\Documents\Ansys\Concept\ISO_22675\DEF,
   txt
!%10.4F %10.4F %10.4F %10.4F %10.4F

!-----------------Joint Cenre Extraction
   ---------------------------------
JC_X = 0
!set joint centre x-position
*DIM,AJC,ARRAY,r,2
*DIM,KJC,ARRAY,r,2
!create arrays for ankle and knee joint centre

*DO,t,1,LSNUM,1
!loop through every timestep, transforming joint centres into pseudo-
   kinematic-gait form
    AJC(t,1) = (JC_X*COS(PLATE_ANG(t,5))) - (DEF_YMAX(t,4)*SIN(
       PLATE_ANG(t,5)))
    AJC(t,2) = (DEF_YMAX(t,4)*COS(PLATE_ANG(t,5))) + (JC_X*SIN(
       PLATE_ANG(t,5)))
    KJC(t,1) = (JC_X*COS(PLATE_ANG(t,5))) - (DEF_YMAX(t,5)*SIN(
       PLATE_ANG(t,5)))
    KJC(t,2) = (DEF_YMAX(t,5)*COS(PLATE_ANG(t,5))) + (JC_X*SIN(
       PLATE_ANG(t,5)))
*ENDDO

!*MWRITE,AJC,C:\Users\Ben\Documents\Ansys\Concept\ISO_22675\AJC,txt
!%10.4F %10.4F
!*MWRITE,KJC,C:\Users\Ben\Documents\Ansys\Concept\ISO_22675\KJC,txt
!%10.4F %10.4F

*DIM,AJC_T,TABLE,r,2
*DIM,KJC_T,TABLE,r,2
!creates table for line plotting
*DO,t,1,LSNUM,1
    AJC_T(t,1) = AJC(t,1)
```

```
    AJC_T(t,2) = AJC(t,2)
    KJC_T(t,1) = KJC(t,1)
    KJC_T(t,2) = KJC(t,2)
*ENDDO
!stores array values in table
/show,png
*VPLOT,AJC_T(1,1),AJC_T(1,2)
*VPLOT,KJC_T(1,1),KJC_T(1,2)
!line plot of joint centres

!------------------Rollover Shape Extraction
   ---------------------------------
*DIM,ROS,ARRAY,r,2
!create array for cop transform into rollover shape

*DO,t,1,LSNUM,1
!loop through every timestep, transforming original ansys data into
   rollover shape
    ROS(t,1) = (COP_X(t,1)*COS(PLATE_ANG(t,5))) + ((-DEF_YMAX(t,4))*
       SIN(PLATE_ANG(t,5)))
    ROS(t,2) = ((-DEF_YMAX(t,4))*COS(PLATE_ANG(t,5))) - (COP_X(t,1)*
       SIN(PLATE_ANG(t,5))) + 80
*ENDDO

!*MWRITE,ROS,C:\Users\Ben\Documents\Ansys\Concept\ISO_22675\ROS,txt
!%10.4F %10.4F

*DIM,ROS2,TABLE,11,2
!creates table for line plotting ROS values, as array will plot bar
   graph
*SET,ANG,15,13,10.5,7.5,4,0,-4,-8,-12,-16,-20
!creates array of loadstep angles from peak to peak

*DO,i,1,11,1
    *DO,j,1,LSNUM,1
        *IF,PLATE_ANG(j,5),EQ,ANG(i),THEN
            ROS2(i,1) = ROS(j,1)
            ROS2(i,2) = ROS(j,2)
        *ENDIF
    *ENDDO
*ENDDO
!indexes through plate angle to match loadsteps and ROS values from
   array, storing in table

!*MWRITE,ROS2,C:\Users\Ben\Documents\Ansys\Concept\ISO_22675\ROS2,txt
!%10.4F %10.4F
```

```
/show,png
*VPLOT,ROS2(1,1),ROS2(1,2)

!-----------------------Load & Stiffness Extraction
   ---------------------------------
ALLSEL
*GET,MXNODE,NODE,0,NUM,MAXD
MXNODE2 = MXNODE - 50
!select all nodes in system and stores full count as parameter value
*DIM,LOAD,ARRAY,LSNUM,1
!creates array to store loads

*DO,t,1,LSNUM,1
!initiates loop through loadstep numbers
    SET,t,LAST,,,,,,
    !sets data to be read at last substep of loadstep
    FY_MAX = 1
    *DO,i,MXNODE2,MXNODE,1
    !loops through all nodes in system
        *GET,TEMP_L,NODE,i,F,FY
        *IF,FY_MAX,GT,TEMP_L,THEN
            FY_MAX = TEMP_L
        *ENDIF
        !conditional statement to find the full load applied at each
           loadstep and store in temp value
    *ENDDO
    LOAD(t,1) = FY_MAX
    !store final value from node loop in load array
*ENDDO

!*MWRITE,LOAD,C:\Users\Ben\Documents\Ansys\Concept\ISO_22675\LOAD,txt
!%10.4F

*DIM,STIFF_K,ARRAY,LSNUM,1
*DIM,COP_STIFF,TABLE,LSNUM,2
!creates stiffness array and plot table
*DO,t,1,LSNUM,1
    STIFF_K(t,1) = -LOAD(t,1)/DEF_YMAX(t,3)
    COP_STIFF(t,1) = COP_X(t,1)
    COP_STIFF(t,2) = STIFF_K(t,1)
*ENDDO
!calculates stiffness from applied loads and relative spring
   deflection

/show,png
```

```
*VPLOT,COP_STIFF(1,1),COP_STIFF(1,2)

!----------------------Matlab File Export
   ----------------------------------

*DIM,CYCLIC_IMPORT,ARRAY,LSNUM,11

*DO,t,1,LSNUM,1
    CYCLIC_IMPORT(t,1) = PLATE_ANG(t,5)
    CYCLIC_IMPORT(t,2) = LOAD(t,1)
    CYCLIC_IMPORT(t,3) = DEF_YMAX(t,3)
    CYCLIC_IMPORT(t,4) = STIFF_K(t,1)
    CYCLIC_IMPORT(t,5) = DEF_YMAX(t,4)
    CYCLIC_IMPORT(t,6) = DEF_YMAX(t,5)
    CYCLIC_IMPORT(t,7) = AJC(t,1)
    CYCLIC_IMPORT(t,8) = KJC(t,1)
    CYCLIC_IMPORT(t,9) = COP_X(t,1)
    CYCLIC_IMPORT(t,10) = ROS(t,1)
    CYCLIC_IMPORT(t,11) = ROS(t,2)
*ENDDO

*MWRITE,CYCLIC_IMPORT,C:\Users\Ben\Documents\Ansys\Concept\ISO_22675\
   CYCLIC_IMPORT_PX,txt
%5.1F %7.1F %7.3F %10.2F %5.2F %6.2F %6.2F %7.2F %7.2F %7.2F %7.2F

!----------------------Parameterise Outputs
   --------------------------------

my_STIFF_K_H = STIFF_K(5,1)
my_SIIFF_K_F = STIFF_K(15,1)
```

D.3.3 Plate Spring Gap Close

This code closes the mesh gap between the force plate and foot structure.

```
/prep7

CMSEL,S,HEEL_SURF,NODE
*GET,HS_YMIN,NODE,,MNLOC,Y

CMSEL,S,PLATE_SURF,NODE
*GET,Y_SURF,NODE,,MXLOC,Y

OFFSET = Y_SURF - HS_YMIN
```

```
ABS_OFFSET = ABS(OFFSET)
TOLERANCE = 1E-6

*IF,ABS_OFFSET,GT,TOLERANCE,THEN
CMSEL,S,FOOT_NODES,NODE
ESLN
NSLE
NGEN,2,0,ALL,,,0,ABS_OFFSET,0
*ENDIF

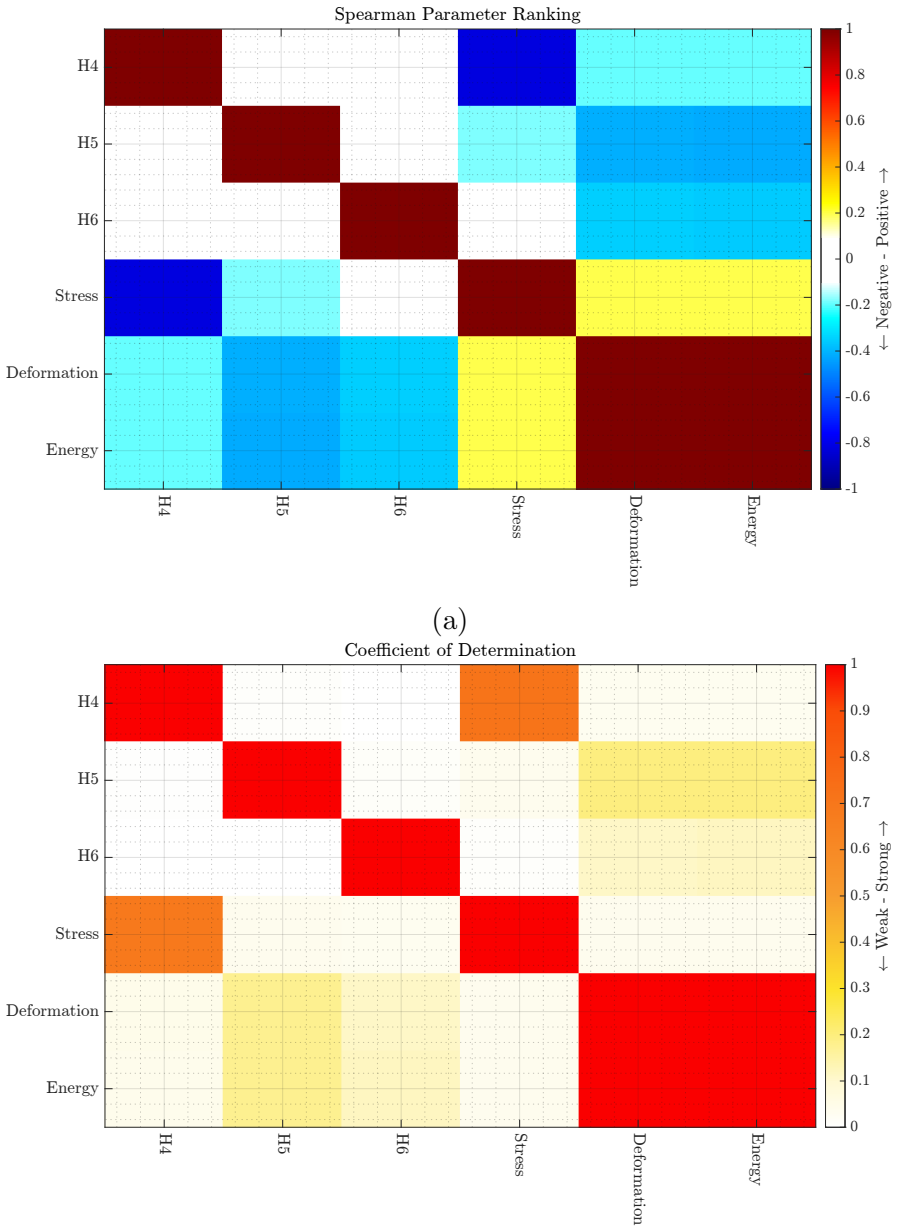
ALLSEL

/SOLU
```

D.4 Foot Structure DOE

D.4.1 Heel Parameter Study

The keel parameter study plots are found in the main text. In Figure D.1, the heel results are presented. These will be discussed in the main text Sub-section 4.3.3.



(a)

(b)

Figure D.1: Heel parameter correlation study. Top: Spearman ranking correlation matrix. Bottom: Determination matrix assessing the strength of relation.

D.4.2 Response Surface - Goodness of Fit Metrics

A table collecting all goodness of fit metrics from the response surfaces generated with the genetic aggregation algorithm, using the data produced in various studies detailed in section 4.3.3 of the main text.

	Body Stress Maximum					Deflection					Upper Surface Stress					Lower Surface Stress				
	BB	CCD	OSF-MnMx	OSF-MxEnt-CCD	OSF-MxEnt-FQM	BB	CCD	OSF-MnMx	OSF-MxEnt-CCD	OSF-MxEnt-FQM	BB	CCD	OSF-MnMx	OSF-MxEnt-CCD	OSF-MxEnt-FQM	BB	CCD	OSF-MnMx	OSF-MxEnt-CCD	OSF-MxEnt-FQM
# Coefficient of Determination (Best Value = 1)																				
Learning Points	1	0.9974	0.9947	0.9983	0.9957	0.9943	1.0000	0.9997	0.9999	1	1	0.9996	0.9736	0.9972	1	1	0.9999	0.9858	0.9984	1
Cross-Validation on Learning Points	0.7488	0.8976	0.8142	0.9535	0.8779	0.9647	0.9883	0.9973	0.9997	1	0.7561	0.9454	0.8272	0.9313	0.9998	0.6848	0.9365	0.8400	0.9426	1
# Maximum Relative Residual (Best Value = 0%)																				
Learning Points	0	2.8796	5.1595	2.8046	4.1634	7.0889	0	0.5945	0.3161	0	0	1.8949	13.7966	3.6476	0.2845	0	0.5719	7.4428	3.7338	0
Cross-Validation on Learning Points	38.5829	20.1615	20.6982	11.8158	19.0064	9.7287	5.7178	1.5235	0.5961	<0.0001	49.2543	16.3891	27.4032	17.7912	1.3592	59.1775	12.0303	28.5055	21.4158	<0.0001
# Root Mean Square Error (Best Value = 0)																				
Learning Points	0	7.5624	8.6223	5.0532	7.7594	0.3903	0	0.0545	0.0246	0	0	3.2565	19.9432	6.4486	0.4609	0	1.4523	12.9303	4.0272	0
Cross-Validation on Learning Points	88.9115	47.3543	51.2006	26.4466	41.1828	0.9759	0.4755	0.1695	0.0513	<0.0001	91.6441	37.0787	50.9716	31.9082	1.5734	89.7366	32.9937	43.4461	24.4184	<0.0001
# Relative Root Mean Square Error (Best Value = 0%)																				
Learning Points	0	1.4145	1.9463	1.1500	1.6718	2.3143	0	0.3010	0.1480	0	0	0.7508	5.5807	1.5110	0.1187	0	0.3176	3.4755	1.2804	0
Cross-Validation on Learning Points	17.9880	8.4720	10.1051	4.8211	9.2195	5.1370	2.1021	0.9691	0.3105	<0.0001	19.9296	6.8899	11.4576	6.8528	0.4569	22.3536	6.0772	11.8139	7.0972	<0.0001
# Relative Maximum Absolute Error (Best Value = 0%)																				
Learning Points	0	11.4655	12.8373	10.0109	14.6023	22.0805	0	3.7607	1.4758	0	0.0000	4.1830	35.5228	8.2679	0.7284	0	2.3037	19.5450	10.1413	0
Cross-Validation on Learning Points	94.3565	75.8031	91.9357	55.3460	64.6501	34.9312	33.4367	8.0667	2.6711	<0.0001	96.7504	57.4440	86.8665	68.2161	3.4801	115.7154	61.9563	68.0465	58.1675	0.0001
# Relative Average Absolute Error (Best Value = 0%)																				
Learning Points	0	3.9334	5.8039	2.8041	4.6704	4.4701	0	1.2340	0.6122	0	0	1.6467	11.2503	4.3559	0.3114	0	0.8550	9.8861	2.8549	0
Cross-Validation on Learning Points	40.6693	21.9249	31.6775	16.3715	27.7821	14.5981	6.9985	4.3112	1.3045	<0.0001	38.4748	16.0521	31.8650	18.7620	0.9173	42.0272	18.1001	30.7104	17.1982	<0.0001

Figure D.2: Response surface goodness of fit metrics from the forefoot DOE studies. Green column: best model, Yellow column: 2nd best model, Red column: Worst model

D.5 Parameter Correlation

This section will briefly explain how Ansys analyses the input parameters to find correlation between inputs and outputs. There are two methods to choose from, each calculates a correlation coefficient that is used to characterise the strength and direction of a relation between and input and output. This value is bounded between -1 and $+1$, where the sign is indicative of the direction of the relationship.

D.5.1 Sample Generation

The design space is explored though a set of samples generated using the Latin Hypercube sampling method. It aims to create a near-random set of samples from the input parameters by randomly generating them in a square grid across the design space. As a modification of the Monte Carlo method, it also attempts to avoid clustering of multiple points in an area.

D.5.2 Correlation Coefficient methods

The two methods available for selection are Pearson and Spearman. The Pearson method uses actual data to calculate the correlation coefficient. Only the linear relationship is analysed, assessing the proportional change between the two parameters. On the other hand, Spearman focuses on the monotonic relation between variables, measuring the non-parametric rank correlation.

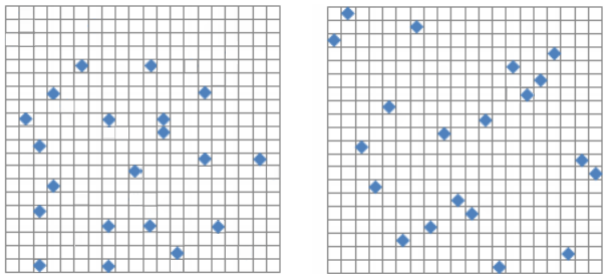


Figure D.3: Monte Carlo sampling method on the left, with the modified Latin Hypercube method on the right.

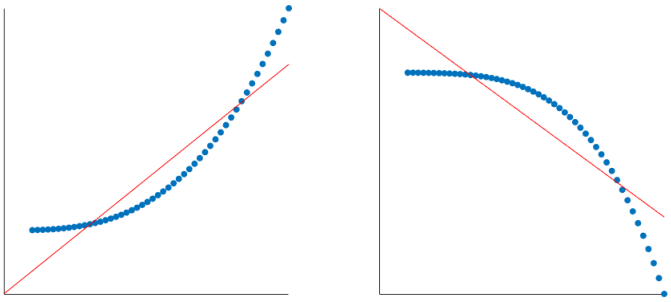
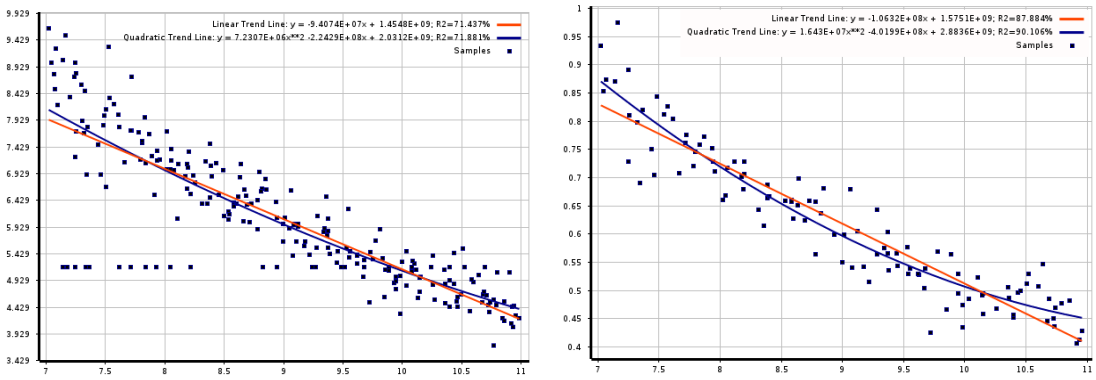


Figure D.4: Correlation Example Plots. Left: Pearson = 0.9342, Spearman = 1 Right: Pearson = -0.8882, Spearman = -1

A quick example can be seen in D.4. Two quadratic plots have been created, each with a linear line of best fit. The correlation measures in both plots recognise the direction of relation in the data. However, as Pearson only focuses on the linear relation, it estimates the strength of the correlation to be less than one, whereas Spearman acknowledges the quadratic relation and adjusts the coefficient accordingly.

This effect can be seen in more detail when comparing results from two parameter studies completed in Ansys. The input and output parameters were kept the same in both, the only difference is method used. Both plots are the correlation of a dimension along the x-axis, to the principal strength along the y-axis. Figure D.5a uses Pearson to calculate the coefficient, whilst figure D.5b uses Spearman. Linear and quadratic trendlines have also been added to both plots.

On immediate inspection, it can be seen that the data in both follow a similar pattern, with Pearson having more outliers. However, the trendlines reveal that the Spearman data is a much stronger predictor of correlation. The linear and quadratic trendlines in the Pearson plot have R^2 values of 71.473% and 71.881% respectively, whereas in the Spearman plot, these two values are 87.884% and 90.106%. This strengthens the argument that, in this case, the linearity assumption of the Pearson method results in a less accurate correlation, and therefore the



(a) Pearson Scatter (b) Spearman Scatter

Figure D.5: Comparison scatter plots with regression lines.

use of the Spearman method is preferential.

D.6 Design of Experiments

Design of experiments (DOE) is an umbrella term given to a selection of methods which use an algorithm to generate sampling points that are representative of a design space. Each technique has its own unique characteristics, but the common goal of all is to place random points such that the entire space is explored, or to collect an accurate depiction with minimal points.

D.6.1 Terminology

The DOE types can be differentiated through two descriptive terms. The rotatability of a method is the extent to which the design point matrix is biased in any direction. If the matrix can be rotated about its centre without change to the prediction variance, then it is said to be rotatable.

The other term is orthogonality, a measure of estimating the effect of any one parameter independently from others in the study. Take the simplified examples in Table D.5. For both experimental pairs, the levels are -1 and 1, with four runs computed. In the first pair of factors, the design has set the same level for both factors in every run. This prevents the observer from being able to calculate the independent effect of each factor on the output variable, thus the design is non-orthogonal. The second pair of factors has been appropriately arranged, so that the upper and lower levels of factor A_2 can be compared with those in factor B_2. This allows for the main effects of each factor to be estimated independently of each other, known as an orthogonal design.

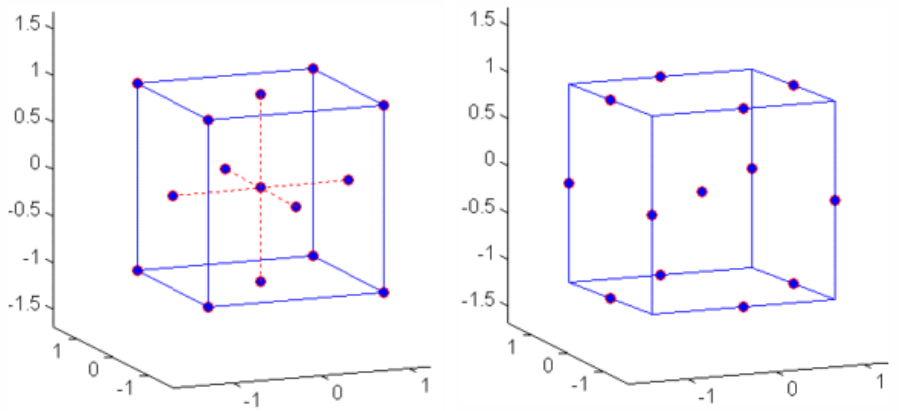
	A_1	B_1	A_2	B_2
Run 1	1	1	1	1
Run 2	1	1	1	-1
Run 3	-1	-1	-1	1
Run 4	-1	-1	-1	-1

Table D.5: Example table of two-factor experiments with the same levels, used to explain orthogonality of DOE types. Subscripts denote experiment factor pairs, A_1 & B_1 separate from A_2 & B_2

D.6.2 Central Composite Design (CCD)

The central composite design is the default selection in the Ansys interface. It is a five-level fractional factorial design that found its popularity in physical experimentation design, being able to generate a quadratic response model. A key benefit of this type is its versatility in selection different types which can help prioritise rotate-ability, orthogonality, or a combination of the two. The template can also be expanded to produce additional design points. However, for a relatively simple experiment, it is recommended to leave the template as normal and allow the solver to automatically detect the best type to populate the design space.

It covers parameter values reasonably well, as can be seen in Figure D.6, where the corners and mid-point face values are generated from the central point. It does, however, require additional design points to achieve this. Furthermore, an accurate response surface is not guaranteed as the sample points can be less effective combinations.



(a) CCD - Face Centered (b) Box-Behnken

Figure D.6: Diagrams representing the variation from a central parameter value by the CCD and Box-Behnken methods.

D.6.3 Box-Behnken

This method was also primarily developed for physical experimentations. It is a three-level quadratic design, which generates samples through midpoint edges of factors. As the oldest type of design space algorithm, its usage primarily passed over in favour of others such as the CCD method, which better represents the extremes of the design space. See Figure D.6, where this method cannot occupy the corners of the parameter factors.

D.6.4 Optimal Space Filling Design (OSF)

This method is based on the Latin Hypercube sampling (LHS), forming the basis of the algorithm which is then optimised. The end result has the same characteristics of a LHS method where points do not share a row or column, but with the additional caveat of a more uniform distribution of points within the design space, see Figure D.7 where clumping of points seen in the LHS method is avoided in OSF.

An OSF method has advantages over the CCD and BB methods which focus on the settings near the perimeter of the design region. Such a limitation was necessary when these were derived without the use of computers. This method is able to distribute the points evenly to accurately model the entire space with minimal design points.

Like the CCD method, there are some additional controls that can be applied. The basic design type aims to maximise the minimum distance between points, whilst the more complicated maximum entropy type aims to minimise uncertainty in unobserved locations. Sampling methods can also be defined, sticking with the basic CCD method, or selecting some variation of quadratic generation.

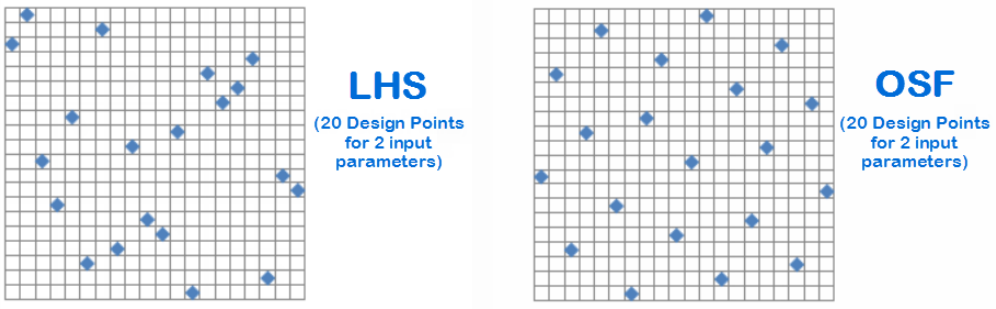


Figure D.7: Comparison of design space distribution between the Latin Hypercube and Optimal Space-Filling methods.

D.7 Foot Structure Composite Model

The setup shown in Figure D.8 was used for the composite simulations. Material properties for the woven and unidirectional ply existed within the software database. In a composite study, two geometry modules are required: the standard full body model and a shell of the inner and outer surfaces. This secondary shell geometry is used to define the bounds within which the ply layers are generated. The standard full body geometry is where the plate and foot are positioned for the static cases, and a mesh generated.

In the ACP (Pre) modules, the fabrics are defined with the imported database material properties and a value of sheet thickness, which was taken from the suppliers website. These fabrics are then used to define sub-laminates which are used for the layup modelling. The surface bodies are also defined in this module as the upper and lower bounds of ply generation . See Figure D.9 for images of the layup generated.

These layups are then imported into a static structural module, within which the boundary conditions are applied. The previously separate heel and keel setups are merged into these static models for a complete representation of the foot laminate structure. Other than this, the module behaves as it would normally and

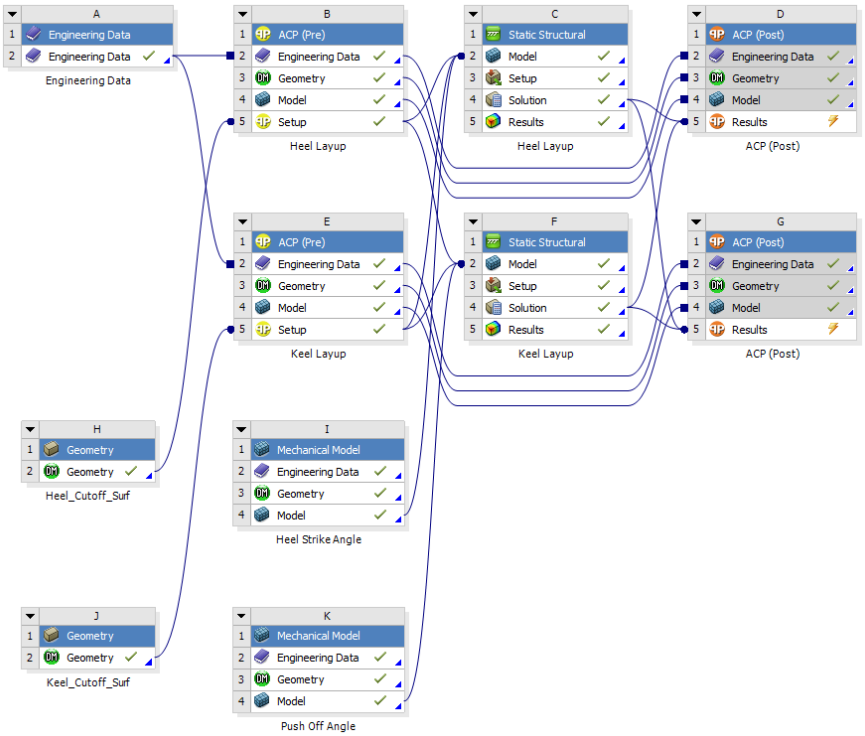


Figure D.8: Screenshot of Ansys workbench project used for the composite model

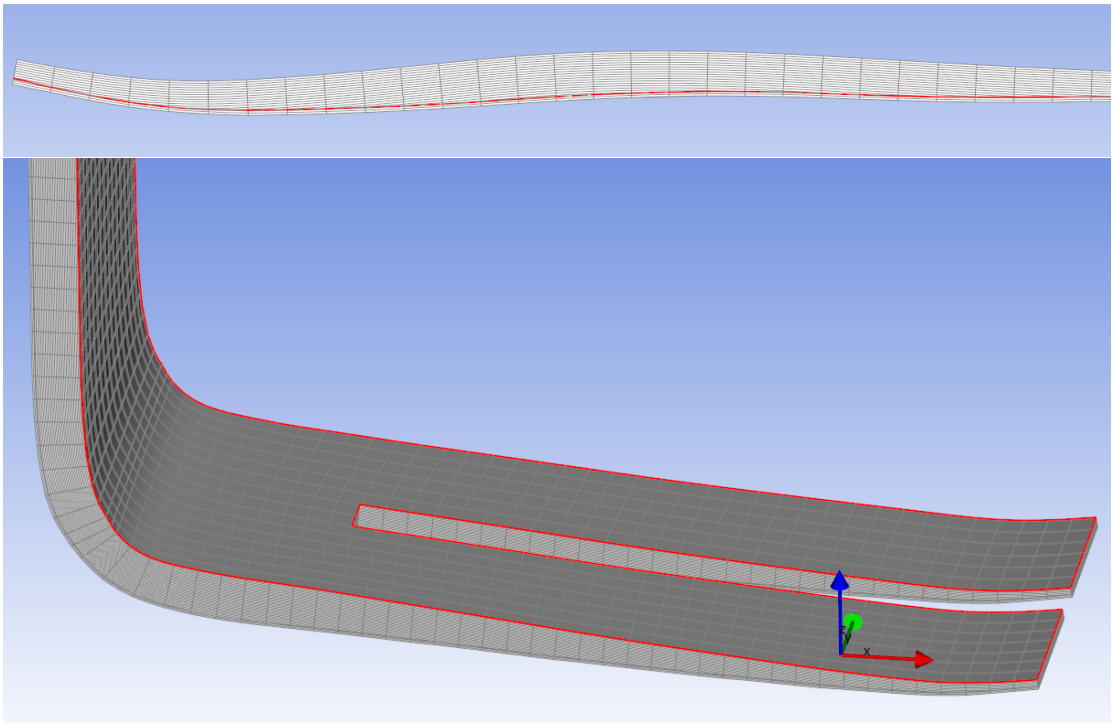


Figure D.9: Screenshots of the layups generated in the ACP (Pre) modules, for Heel (top) and Keel (bottom).

results can of stress and deflection can be collected. What can't be determined in this module are potential failures specific to the laminate structure, such as de-lamination or fibre/matrix fracture; see the example result in Figure D.10

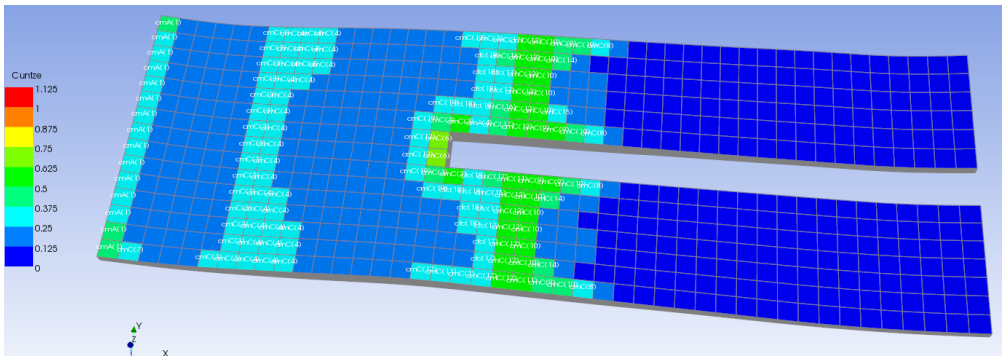


Figure D.10: Laminate failure mode results on the heel

D.8 Housing Supplementary Data & Results

This section contains a table summary of explored parameters, see Figure D.11

Bolt - Nut	Nut - Housing	Bolt head - Housing	Bolt Shank - Housing	Housing	Pretension	Bolt Fillet	Nut Fillet	Mesh Resolution	Solve time	Deformation	Housing	Bolt	Nut
Asymmetric Bond	Asymmetric friction 0.2	Asymmetric friction 0.2	None	None	No	No	No	7	4m4s	0.16976	2.5916	11.887	413.96
Asymmetric Bond	Asymmetric friction 0.2	Asymmetric friction 0.2	None	None	Yes	No	No	7	3m26s	0.14515	2.6523	12.079	413.53
Asymmetric Bond	Asymmetric Bond	Asymmetric Bond	None	Frictionless	Yes	No	No	7	5m24s	0.17788	2.7923	14.029	413.52
Asymmetric Bond	Asymmetric Bond	Asymmetric Bond	None	Frictionless	No	No	No	7	3m43s	0.15655	2.6359	12.439	412.07
Asymmetric Bond	Asymmetric friction 0.2	Asymmetric friction 0.2	None	Frictional 0.3	No	No	No	7	12m8s	0.15758	3.6059	43.561	1749.8
Asymmetric Bond	Asymmetric friction 0.2	Asymmetric friction 0.2	None	Frictional 0.3	Yes	No	No	7	9m21	0.18504	3.6931	43.325	1752.5
Asymmetric Bond	Asymmetric Bond	Asymmetric Bond	Frictionless	None	No	No	Yes	7	2m35s	0.038497	2.3386	12.032	254.84
Asymmetric Bond	Asymmetric Bond	Asymmetric Bond	None	Frictionless	No	Yes	Yes	7	7m41s	0.15796	2.6742	21.094	208.13
Asymmetric Bond	Asymmetric Bond	Asymmetric Bond	None	Bonded	No	No	No	7	37s	0.03855	1.0092	7.4595	2.6327
Asymmetric Bond	Asymmetric Bond	Asymmetric Bond	None	None	No	No	No	7	36s	0.16021	3.6645	57.014	16.864
Asymmetric Bond	Asymmetric Bond	Asymmetric Bond	None	None	Yes	No	No	7	56s	0.14073	3.7182	54.12	26.922
Asymmetric Bond	Asymmetric friction 0.2	Asymmetric friction 0.2	None	Frictional 0.3	No	Yes	Yes	7	49m44s	0.15868	2.6962	90.028	2355
Asymmetric Bond	Asymmetric Bond	Asymmetric Bond	None	Frictionless	No	No	No	7	3m43s	0.15655	2.6359	12.439	412.07
Asymmetric Bond	Asymmetric Bond	Asymmetric Bond	None	Frictionless	No	Yes	Yes	7	7m41s	0.15796	2.6742	21.094	208.13
Asymmetric Bond	Asymmetric friction 0.2	Asymmetric friction 0.2	None	None	No	No	No	7	4m4s	0.16976	2.5916	11.887	413.96
Asymmetric Bond	Asymmetric friction 0.2	Asymmetric friction 0.2	None	Frictional 0.3	No	No	No	7	12m8s	0.15758	3.6059	43.561	1749.8
Asymmetric Bond	Asymmetric friction 0.2	Asymmetric friction 0.2	None	Frictionless	No	No	No	7	7m26s	0.15753	2.6373	12.385	414.52
Asymmetric Bond	Asymmetric Bond	Asymmetric Bond		None	No	No	No	7	36s	0.16021	3.6645	57.014	16.864
Asymmetric Bond	Asymmetric Bond	Asymmetric Bond		Frictionless	No	No	No	7	3m43s	0.15655	2.6359	12.439	412.07

Figure D.11: Summary of connection parameters explored to determine the most suitable settings for reliable results.

Appendix E

Supplementary Design Data

E.1 Composite Spring Study Setup

This study was completed to estimate the strain energy storage capability of the composite spring. To simplify the calculation and simulation, some assumptions were made:

- Deflection only occurs in the curved section of the spring due to the straight vertical face being attached to the housing interior.
- Material is the same as used in the toe and keel springs, which is assumed to behave linear elastically
- Material is therefore also homogenous and isotropic

The composite spring geometry was also simplified, removing the fillets and connection features that would be used for physical assembly. The dimensions are as follows:

- Profile thickness is 10mm along the length
- Width is 10mm, making the cross section a 10mm square
- Vertical is 50mm in length
- Curved section has an arc of $\pi/2$, with a centre radius of 70mm

The body is meshed with quadratic hexahedron 1mm elements. The back vertical face is fixed as this is where the connection to the housing would be. Whilst an arbitrary force of 500N is applied to the edge of the curved section, see Figure E.1. This force was selected as it represents the upper limit of a force that could be applied to the mechanism based on subject mass of 85kg.

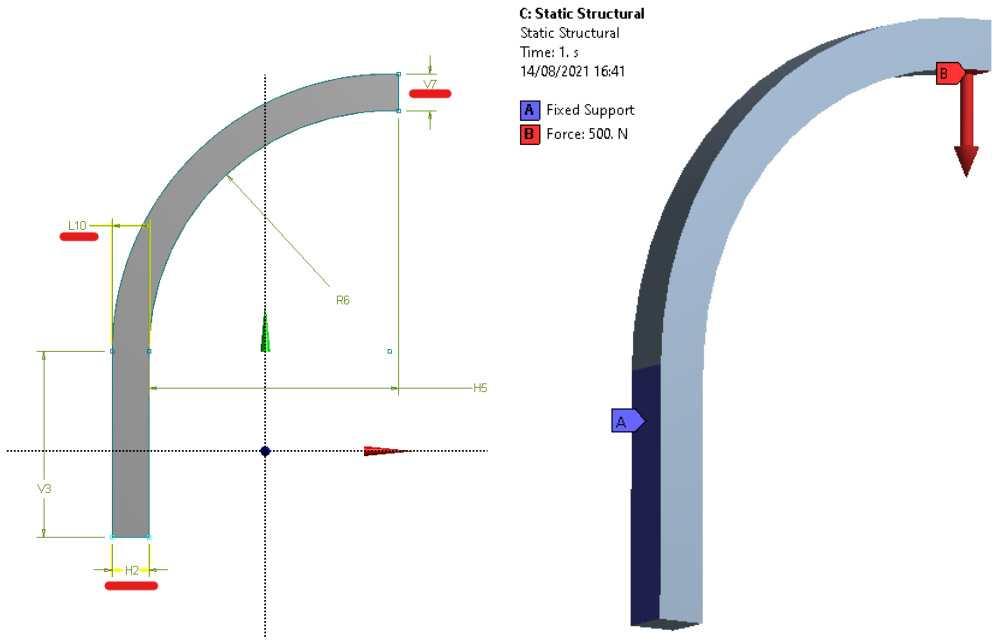


Figure E.1: Screenshots taken from the simulation setup. Left: Geometry of the composite spring. Right: Fixtures on the back face connection to housing, and force applied on edge of curved section.

A comparison was made with an analytical calculation derived from Casigliano's Theorem. The integrals for deflection and strain energy due to bending are given as:

$$\delta = \int_0^s \frac{M}{EI}\frac{dM}{dW}ds \tag{E.1}$$

$$U = \int_0^s \frac{M^2}{2EI}ds \tag{E.2}$$

Where M is the bending moment, E is the elastic modulus, I is the second moment of area, dM/dW is the change in moment with respect to the load, and ds is the finite quantity of the beam.
The moment is expressed as:

$$M = PR\sin\theta \tag{E.3}$$

Where P is the load, R is the radius of curvature, and θ is the angle of curvature.

The integrating factor is given as:

$$ds = Rd\theta \tag{E.4}$$

Whilst the partial derivative of work of deformation with respect to the vertical

component of force is given as:

$$[\frac{dM}{dW}]_v = R\sin\theta \tag{E.5}$$

Subbing these quantities into the integrals and solving for a degree of curvature between 0 and $\frac{\pi}{2}$ gives:

$$\delta = \frac{\pi P R^3}{4EI} \tag{E.6}$$

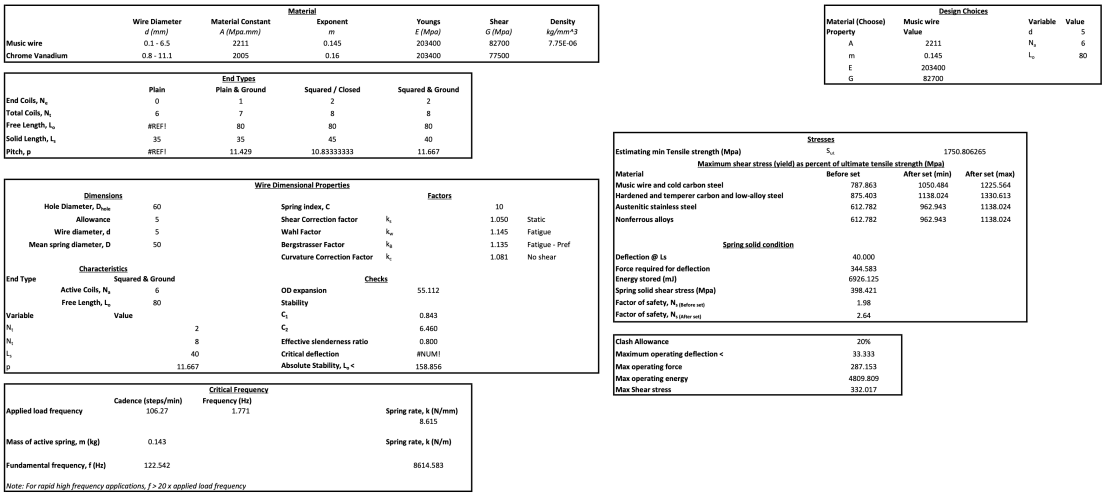
$$U = \frac{\pi P^2 R^3}{8EI} \tag{E.7}$$

The parameter values for these equations were as follows:

- P = 500N
- R = 70mm
- E = 55200MPa
- I = 833.33mm^4

Results of these analytical calculations and simulation have been presented in 4.2

E.2 Helical Compression Spring



Material

	Wire Diameter d (mm)	Material Constant A (Mpa.mm)	Exponent m	Youngs E (Mpa)	Shear G (Mpa)	Density kg/mm^3
Music wire	0.1 - 6.5	2211	0.145	203400	82700	7.75E-06
Chrome Vanadium	0.8 - 11.1	2005	0.16	203400	77500	

Design Choices

Material (Choose)	Music wire	Variable	Value
Property	Value	d	5
A	2211	N_a	6
m	0.145	L_o	80
E	203400		
G	82700		

End Types

	Plain	Plain & Ground	Squared / Closed	Squared & Ground
End Coils, N_e	0	1	2	2
Total Coils, N_t	6	7	8	8
Free Length, L_o	#REF!	80	80	80
Solid Length, L_s	35	35	45	40
Pitch, p	#REF!	11.429	10.8333333	11.667

Stresses

Estimating min Tensile strength (Mpa) S_{ut} 1750.806265

Maximum shear stress (yield) as percent of ultimate tensile strength (Mpa)

Material	Before set	After set (min)	After set (max)
Music wire and cold carbon steel	787.863	1050.484	1225.564
Hardened and temperer carbon and low-alloy steel	875.403	1138.024	1330.613
Austenitic stainless steel	612.782	962.943	1138.024
Nonferrous alloys	612.782	962.943	1138.024

Wire Dimensional Properties

Dimensions

Hole Diameter, D_{hole}	60	
Allowance	5	
Wire diameter, d	5	
Mean spring diameter, D	50	

Factors

Spring index, C		10	
Shear Correction factor	k_s	1.050	Static
Wahl Factor	k_w	1.145	Fatigue
Bergstrasser Factor	k_B	1.135	Fatigue - Pref
Curvature Correction Factor	k_c	1.081	No shear

Characteristics

End Type	Squared & Ground
Active Coils, N_a	6
Free Length, L_o	80

Checks

OD expansion	55.112
Stability	
C_1	0.843
C_2	6.460
Effective slenderness ratio	0.800
Critical deflection	#NUM!
Absolute Stability, $L_o <$	158.856

Variable	Value
N_t	8
L_s	40
p	11.667

Spring solid condition

Deflection @ Ls	40.000
Force required for deflection	344.583
Energy stored (mJ)	6926.125
Spring solid shear stress (Mpa)	398.421
Factor of safety, N_s (Before set)	1.98
Factor of safety, N_s (After set)	2.64

Clash Allowance	20%
Maximum operating deflection <	33.333
Max operating force	287.153
Max operating energy	4809.809
Max Shear stress	332.017

Critical Frequency

	Cadence (steps/min)	Frequency (Hz)	
Applied load frequency	106.27	1.771	Spring rate, k (N/mm) 8.615
Mass of active spring, m (kg)	0.143		Spring rate, k (N/m)
Fundamental frequency, f (Hz)	122.542		8614.583

Note: For rapid high frequency applications, f > 20 x applied load frequency

Figure E.2: Screenshot of the excel design spreadsheet used to check calculations, select parameters, and check critical outputs.

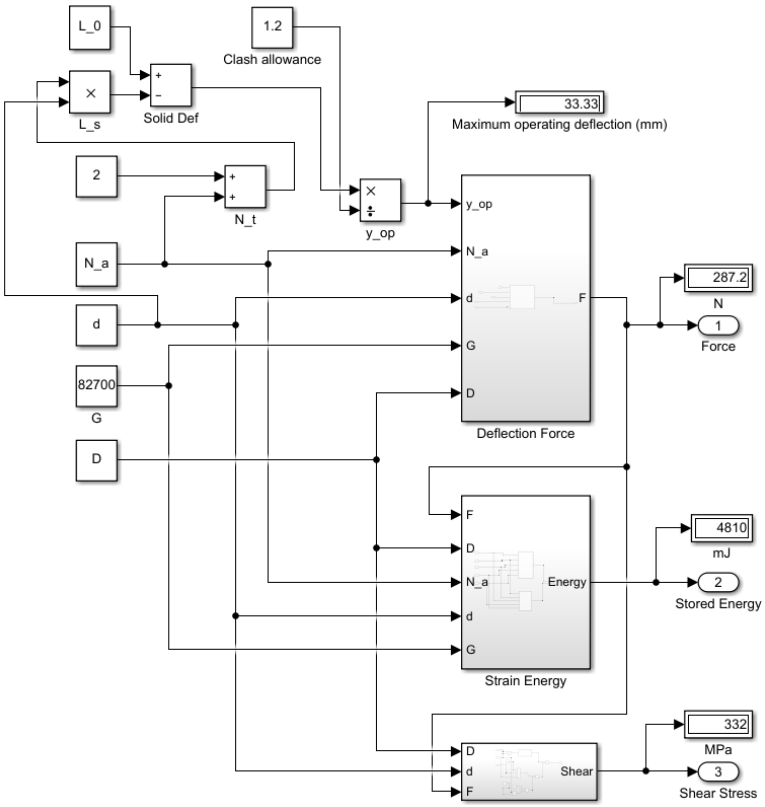


Figure E.3: Top: Simulink model used to perform a sensitivity analysis on the spring geometry parameters.

E.3 Gear Data

E.3.1 Involute Gear Generation in CAD

The following figure shows the equations entered into a gear generating CAD model within SolidWorks. These equations were referenced from the following design books [259, 254].

Name	Value / Equation	Evaluates to	Comments
Global Variables			
"Module"	= 1.25	1.25	Diametral Pitch
"NumTeeth"	= 48	48	Number of Teeth
"PressureAngle"	= 25	25	Pressure Angle
"Addendum"	= 1 * "Module"	1.25	Addendum
"Dedendum"	= 1.25 * "Module"	1.5625	Dedendum
"WorkingDepth"	= 2 * "Module"	2.5	Working Depth - here for REF (Not used in building model)
"WholeDepth"	= 2.25 * "Module"	2.8125	Whole Depth - here for REF (Not used in building model)
"Clearance"	= .19 * "Module"	0.2375	Clearance
"CircularPitch"	= pi * "Module"	3.92699	Circular Pitch - here for REF (Not used in building model)
"PitchCircle"	= "NumTeeth" * "Module"	60mm	Pitch Circle - or - Pitch Diameter
"OutsideDiameter"	= ("NumTeeth" + 2) * "Module"	62.5mm	Outside Diameter
"Fillet"	= "Clearance" * cos ("PressureAngle") * tan ((90 + "PressureAngle") / 2)	0.337872	Fillet
"AddendumCircle"	= "PitchCircle" + (2 * "Addendum")	62.5mm	Addendum Circle - or - Addendum Diameter
"DedendumCircle"	= "PitchCircle" - (2 * "Dedendum")	56.875mm	Dedendum Circle - or - Dedendum Diameter
"BaseCircle"	= "PitchCircle" * cos ("PressureAngle")	54.3785mm	Base Circle - Base Diameter
"PitchAngle"	= 360deg / "NumTeeth"	7.5	Pitch Angle
"Alpha"	= sqr ("PitchCircle" ^ 2 - "BaseCircle" ^ 2) / "BaseCircle" * 180 / PI - "PressureAngle"	1.71746	Alpha - Used for Calculating Beta
"Beta"	= ("PitchAngle" / 4 - ("Alpha" - 90))	90.1575mm	Beta - Used in definition of the parameters for the parametric equation driven curve
"Gamma"	= ("PitchAngle" / 4 - ("Alpha" + 90))	-89.8425mm	Gamma - Used in definition of the parameters for the parametric equation driven curve
"Phi"	= sqr (("AddendumCircle" / 2) ^ 2 - ("BaseCircle" / 2) ^ 2) / ("BaseCircle" / 2)	0.566577	Phi - Used in definition of the parameters for the parametric equation driven curve
Add global variable			
Features			
"DCGTBC"	= iif (("DedendumCircle" + ("Fillet" * 2)) > "BaseCircle" , "unsuppressed" , "suppressed")	"unsuppressed"	if Dedendum Circle +2X Fillet IS GREATER THAN BaseCircle THEN Unsuppress OR Suppress FEATURE
"DCLTBC"	= iif (("DedendumCircle" + ("Fillet" * 2)) > "BaseCircle" , "suppressed" , "unsuppressed")	"suppressed"	if Dedendum Circle +2X Fillet IS GREATER THAN BaseCircle THEN Suppress OR Unsuppress FEATURE
"Cut-Extrude-DCGTBC"	= iif (("DedendumCircle" + ("Fillet" * 2)) > "BaseCircle" , "unsuppressed" , "suppressed")	"unsuppressed"	if Dedendum Circle +2X Fillet IS GREATER THAN BaseCircle THEN UnsuppressORSuppress FEATURE
"Cut-Extrude-DCLTBC"	= iif (("DedendumCircle" + ("Fillet" * 2)) > "BaseCircle" , "suppressed" , "unsuppressed")	"suppressed"	if Dedendum Circle +2X Fillet IS GREATER THAN BaseCircle THEN SuppressORUnsuppress FEATURE
"CirPattern-DCGTBC"	= iif (("DedendumCircle" + ("Fillet" * 2)) > "BaseCircle" , "unsuppressed" , "suppressed")	"unsuppressed"	if Dedendum Circle +2X Fillet IS GREATER THAN "BaseCircle" THEN UnsuppressORSuppress FEATURE
"CirPattern-DCLTBC"	= iif (("DedendumCircle" + ("Fillet" * 2)) > "BaseCircle" , "suppressed" , "unsuppressed")	"suppressed"	if Dedendum Circle +2X Fillet IS GREATER THAN "BaseCircle" THEN SuppressORUnsuppress FEATURE
"Fillet-DCGTBC"	= iif (("DedendumCircle" + ("Fillet" * 2)) > "BaseCircle" , "unsuppressed" , "suppressed")	"unsuppressed"	if Dedendum Circle +2X Fillet IS GREATER THAN "BaseCircle" THEN UnsuppressORSuppress FEATURE
"Fillet-DCLTBC"	= iif (("DedendumCircle" + ("Fillet" * 2)) > "BaseCircle" , "suppressed" , "unsuppressed")	"suppressed"	if Dedendum Circle +2X Fillet IS GREATER THAN "BaseCircle" THEN SuppressORUnsuppress FEATURE
Add feature suppression			
Equations			
"D1@CirPattern-DCGTBC"	= "NumTeeth"	48	
"D1@CirPattern-DCLTBC"	= "NumTeeth"	48	
"D1@DCGTBC"	= "Fillet"	0.3379mm	
"D1@DCLTBC"	= "Fillet"	0.3379mm	
"D1@Fillet-DCLTBC"	= "Fillet" / 2	0.1689mm	
"D1@Fillet-DCGTBC"	= "Fillet" / 2	0.1689mm	

Figure E.4: Screenshot of the equations used to derive the key gear dimensions for generating the various dimeters and parameters used to generate the involute tooth shape.

The involute profile is generated from the base circle of the gear geometry by wrapping or unwrapping a chord length about the cylinder. For a full explanation, the referenced books above should be consulted. The parametric representation of an involute profile is given by the following equations:

$$X(t) = r(\cos t + (t - a)\sin t) \tag{E.8}$$

$$Y(t) = r(\sin t + (t - a)\cos t) \tag{E.9}$$

These variables in these equations were replaced with the relevant parameters from those seen in Figure E.4. An example of one of these curves can be seen in Figure E.5. These curves were then simply repeated in a circular pattern using the number of teeth define in the equation set.

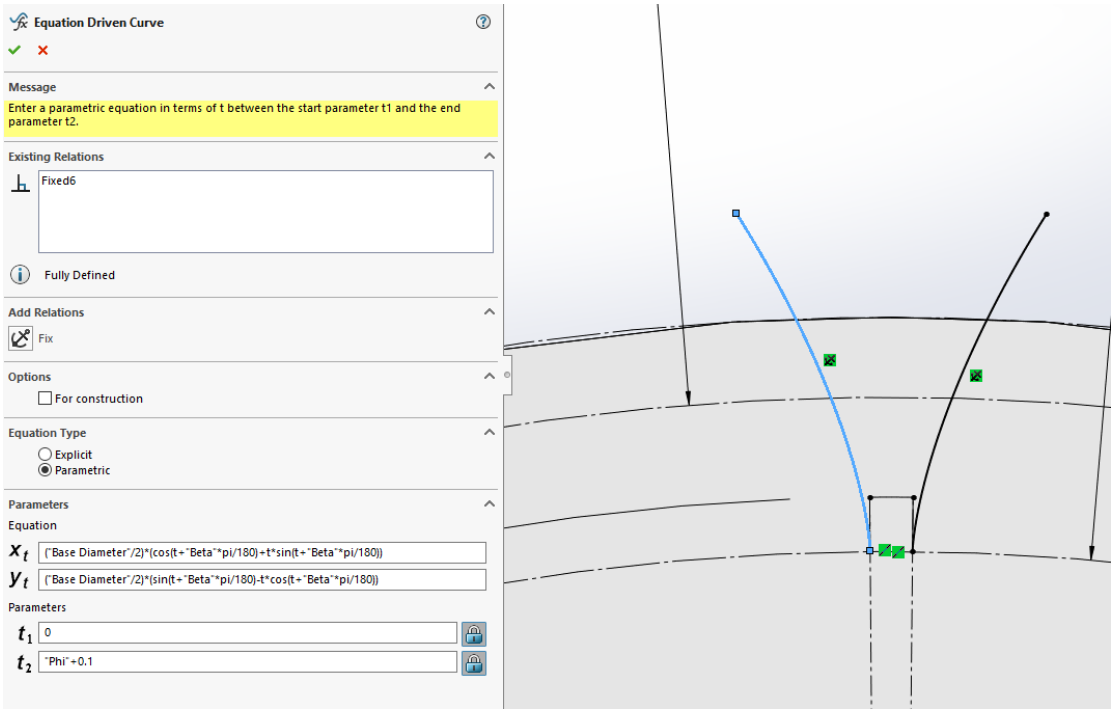


Figure E.5: Involute curve generation using the parametric equations

E.3.2 ISO Strength Calculation Factors

Application factor, K_A

This factor adjusts the tangential load to accommodate for additional loads that may be applied to the system from external sources, such as dynamic rotating masses. When consulting the relevant standard, it is suggested to use an initial value which can then be agreed upon with the manufacturer. A guide table is provided in 6336-6, where the factor is estimated based upon the working characteristic of the driving and driven machine (pinion and gear). Each has four characteristic ratings: uniform, light shocks, moderate shocks, and heavy shocks.

Examples are provided for each type, ranging from continuously running production lines to heavy industrial machinery. The scale of operation within the prosthetic is smaller than examples given but the characteristics are still relevant. It was decided that the light shock characteristic would be applied to both as the uniform condition stipulates that operation is continuous with rare starting torques, whereas the gears in the prosthetic will experience a regular starting torque for each step taken.

Internal dynamic factor, K_v

The dynamic factor considers the effects of tooth accuracy with respect to speed and load. Parameters that affect the factor value are design, manufacturing, transmission perturbations, dynamic response, and resonance. Gears made to a very high accuracy, resulting in the perfect meshing of gears will have a factor approaching 1. The running speed influences the method of calculation:

$$\text{Running speed} = \frac{vz}{100} * \sqrt{\frac{u^2}{1+u^2}} \tag{E.10}$$

Where v is the pitch line velocity (mm/s), z is the number of pinion teeth, and u is the gear ratio. The pitch line velocity was calculated by taking a value of mean step cadence in a study that collected a large database of gait data [286], and then converting that into a frequency and finally the pitch velocity.

For all gears, the running speed was found to be subcritical, and so the dynamic factor was calculated using the following equation:

$$K_v = 1 + \left(\frac{K_1}{K_A \frac{F_t}{b}} + K_2 \right) \frac{vz}{100} K_3 \sqrt{\frac{u^2}{1+u^2}} \tag{E.11}$$

K_1 and K_2 are constants read from a table, given values of 39.1 and 0.019 respectively.

Face load factors, Contact $K_{H\beta}$ and Bending $K_{F\beta}$

These two factors consider the non-uniform distribution of the load over the gear face width and the effects on performance. The scope of both factors include manufacturing accuracy, alignment of axes, deflections of housing/bearings, and shaft loads amongst other causes. Anything that could place the meshing of gear teeth out of alignment is factored in. It was decided to set this to 1.1 for a reasonable estimate .

Transverse load factors, Contact $K_{H\alpha}$ and Bending $K_{F\alpha}$

The factors are applied for surface stress and tooth root stress, accounting for the effect of non-uniform distribution of transverse load between several pairs of contacting teeth. Similar to above they are influenced by deflections under load, tooth profile modifications, manufacturing accuracy and running-in effects. It was decided to set this to 1.1 for a conservative estimate.

Life factor Z_{NT}

Considers higher contact stress, which can be tolerated for a limited number of load cycles. A table is provided in the standard, where the materials from 6336-5 have been grouped together and assigned different levels of load cycle numbers each with a life factor value. A conservative value of 1.3 was applied based upon the expectation that stress cycles will be relatively low for the operating lifetime.

Lubrication Z_L, Velocity Z_v, and Roughness Z_R

These factors are tied together due to the influence they have upon the lubricant film and surface durability. They are presented independently but cannot be realistically separated. The lubricant factor considers the type and viscosity of the liquid, although this only has maximum effect at the long-life stress level. Roughness is determined by the surface finish, where the mean relative peak-to-valley roughness is used to calculate the value or read from a plot of empirical results.

Whereas the other two factors require manufacturer input, the velocity factor could be read off a graph as a function of the pitch line velocity and allowable stress number. Due to the slow velocity and lower allowable stress number, this factor was regularly read off as being 0.95. It was decided to set all as equal to one as it put them in the median to high level range of possible values.

Work hardening factor, Z_W

Considers the effect of work hardening when a pinion and gear have different hardness properties. As the materials for both are the same in this application, the factor was set equal to 1

Size factor, Z_X

Statistical evidence has suggested that stress levels at which fatigue damage is experienced is inversely proportional to the increase of component size. This is believed to be due to the influence of subsurface defects of smaller stress gradients. It seems to be that the derivation of this is not within the scope of the standard and the value is to be taken as one.

Single tooth contact factor, Pinion Z_B and Gear Z_D

Converting the contact stress at the pitch point to contact stress at the inner point of single pair tooth contact. For ratios of greater than 1.5, Z_D is equal to 1. The

formulae for calculating Z_B takes into consideration the gear ratio, teeth number, pressure angle, and contact ratio. For all possible variations it returned a value less than one, in which case the standard declares that the value for ZB be equal to one.

Zone factor, Z_H

Accounts for the influence of Hertzian pressure on the tooth flank curvature at the pitch point and transforms the tangential load at the reference cylinder to normal load at the pitch cylinder. The factor can be derived from the following equation, using the pressure angle:

$$Z_H = \sqrt{\frac{2\cos\phi}{\cos^2\phi\sin\phi}} \tag{E.12}$$

Note, this equation has been reduced from the one in the standard due to a 0 helix angle which set a term $\cos\beta$ equal to 1.

Elasticity factor, Z_E

Considers the influence of elastic material properties, Young's modulus and Poisson's ratio. The material for the pinion and gear are the same, so the equation used can be reduced to the following:

$$Z_E = \sqrt{\frac{E}{2\pi(1-v^2)}} \tag{E.13}$$

Alternatively, the value can be read from an experimental reference table. This was deemed more reliable and so 189.8 was used based on the material category selected from 6336-5.

Contact ration factor, Z_ϵ

The standard provides a graphical reference from which the ratio factor can be selected as a function of the transverse ratio and overlap ratio, which can change the surface load capacity; 0.9 was used.

Helix angle ratio, Z_β

Based upon the helix angle used in helical gears. As spur gears are used in the design, this can be set to one.

Stress correction factor, Y_{ST}

This factor is separate to that which is used to calculate the nominal root stress number. The standard declares it must be equal to 2 to match with the results of tests of standard reference test gears used in 6336-5.

Life factor, Y_{NT}

Accounts for higher tooth root stress which could be endured for a limited number of load cycles. The principal influence come from the material, its heat treatment, and the number of load cycles. It was decided to set this value to 1, which provided a conservative estimate.

Relative notch sensitivity factor, $Y_{\delta relT}$

This indicates the extent to which the tooth root stresses have surpassed the material stress limit, causing fatigue or breakage. The standard included several reference graphs, which indicated a conservative estimate equal to 1 would be suitable.

Surface factor, Y_R

Considers the effect of tooth root stress on the surface condition of the tooth root fillets. The calculation of this is based upon the surface roughness and material. Reference diagrams indicated a value of 1 would be sufficient.

Size factor, Y_X

Considers the effect of size on the distribution of stress concentration points in the geometry. In accordance with strength of materials theory, the stress gradients and weak points will decrease with increasing dimensions. A reference table is provided, where the factor can be read off as a function of the module and material. Due to the module limit for this design, this size factor is equal to 1 for all materials.

Form factor, Y_F

Considers how the tooth shape influences the root stress. Fully numerical derivation of this factor requires extensive experience and expertise. A graphical solution provided a suitable estimation of parameters, see Figure E.6. The gears were modelled, and the values read directly from the geometry for use in the following

equation:

$$Y_F = \frac{\frac{6h_{Fe}}{m}\cos\phi}{\frac{s_{Fn}}{m}^2\cos\phi} \tag{E.14}$$

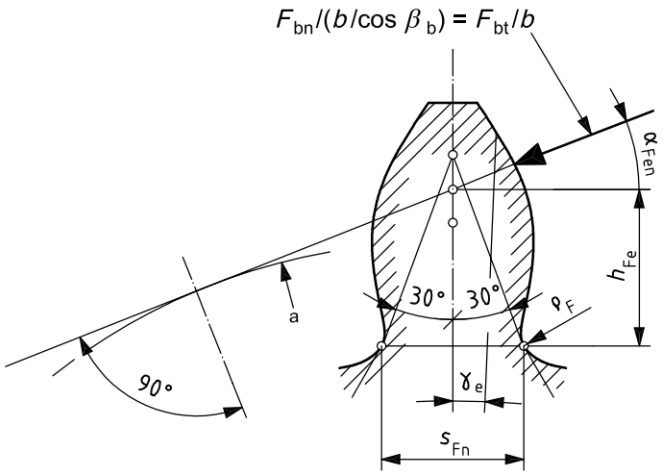


Figure E.6: Reference diagram taken from ISO 6336-3, for selection of dimensional parameters h_{Fe} and S_{Fn}

Stress correction factor, Y_S

Used to convert the nominal tooth root stress to local tooth root stress by considering the stress amplification effect of fillet radius, and the true stress system at the tooth critical section being more complex with local stresses at the tooth root having two components. The calculation of this factor is beyond the scope here. As a measure of safety for the calculations this will be set equal to 2.

Helix angle factor, Y_β

Converts the tooth root stress of a spur gear to that of a corresponding helical gear. Can be ignored and set to one for this design case.

Rim thickness factor, Y_B

If the rim thickness is not able to provide adequate support for the tooth root, the bending fatigue failure may be localised in the gear rim, rather than the fillet. If the ratio of rim thickness to tooth depth is evaluated and above 1.2, then the factor is set equal to one. Else a simple natural logarithm equation is used to calculate the factor value. As the shaft diameter was not decided at this stage, the factor was set to 1 with the intention to revisit later.

Deep tooth factor, Y_{DT}

For high precision gears, with contact ratios between $2 \leq \epsilon \geq 2.5$, the nominal root stress is amended by the deep tooth factor. As gear pair selection has a ration below these bounds, this factor can be set equal to 1.

E.4 Technical Drawings

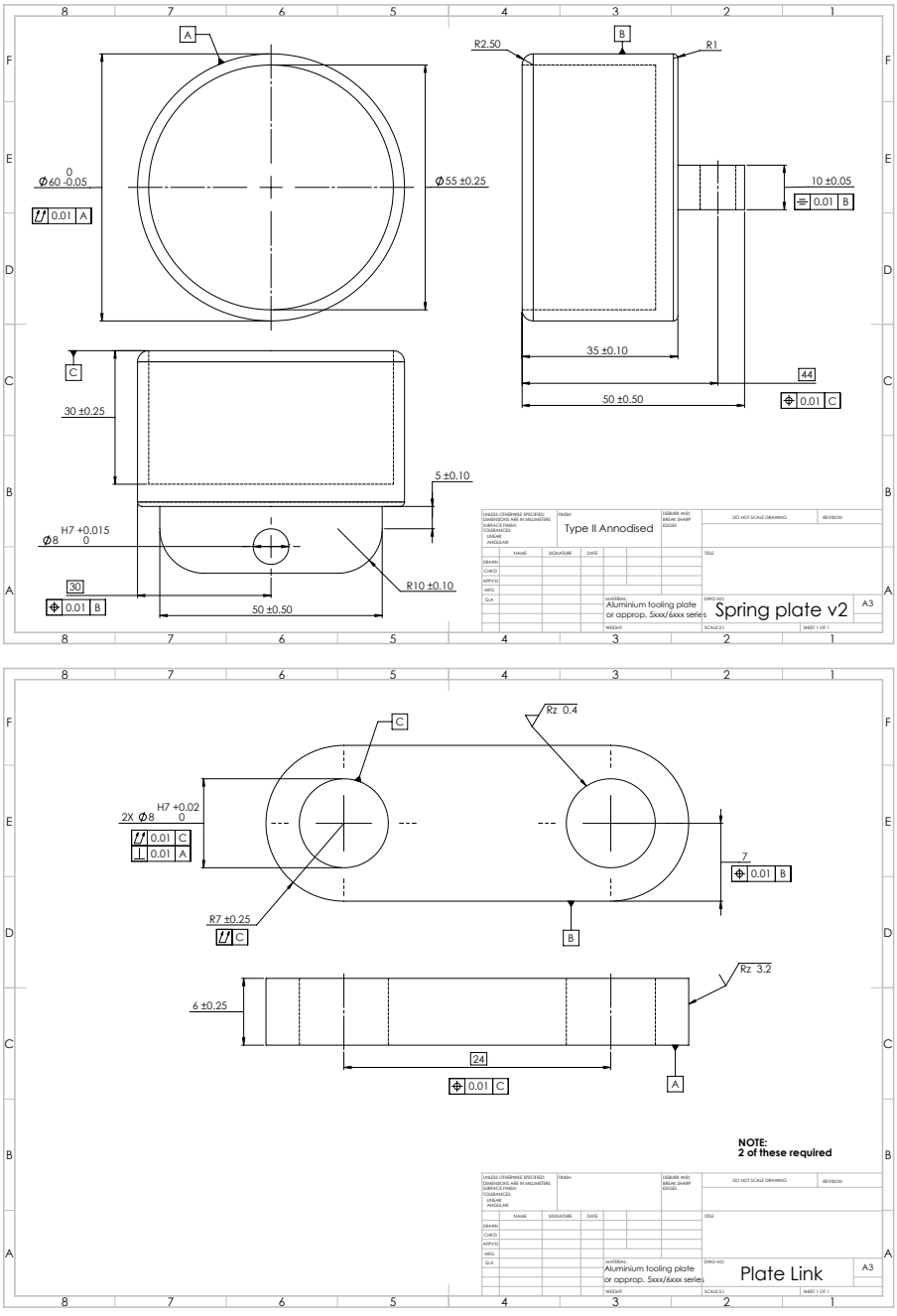


Figure E.7: Spring plate and Plate link

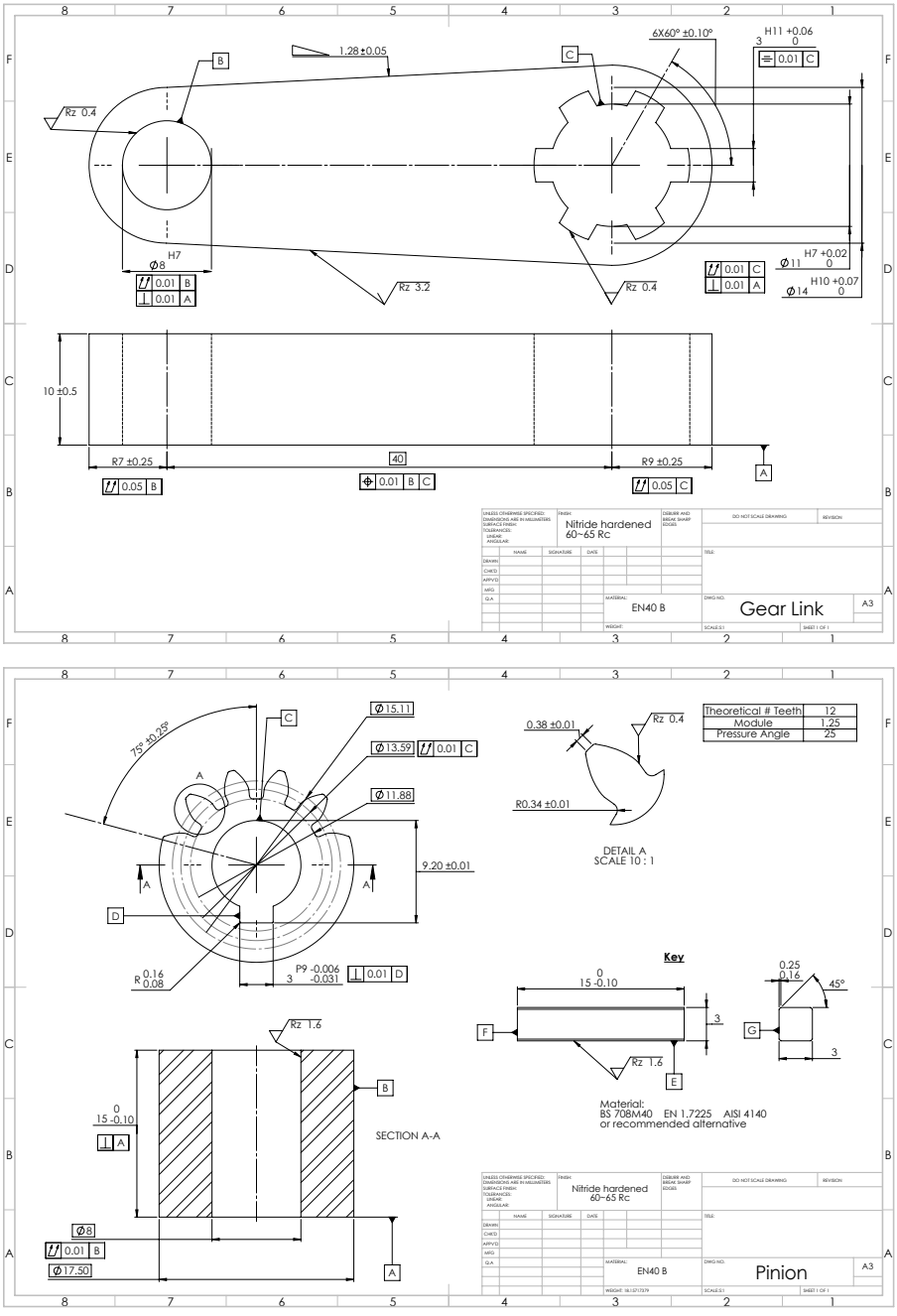


Figure E.8: Gear link and Pinion

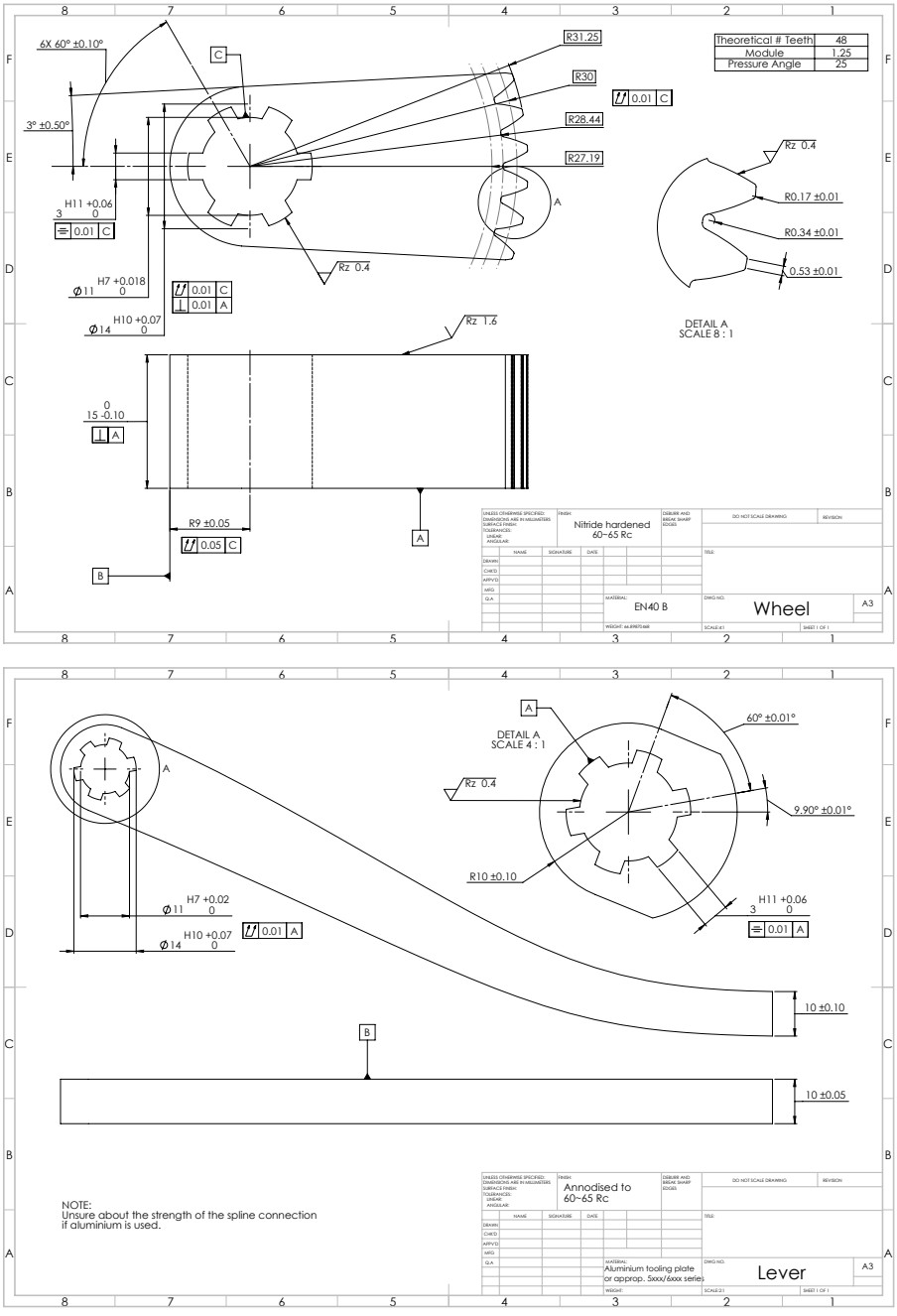


Figure E.9: Wheel and Lever

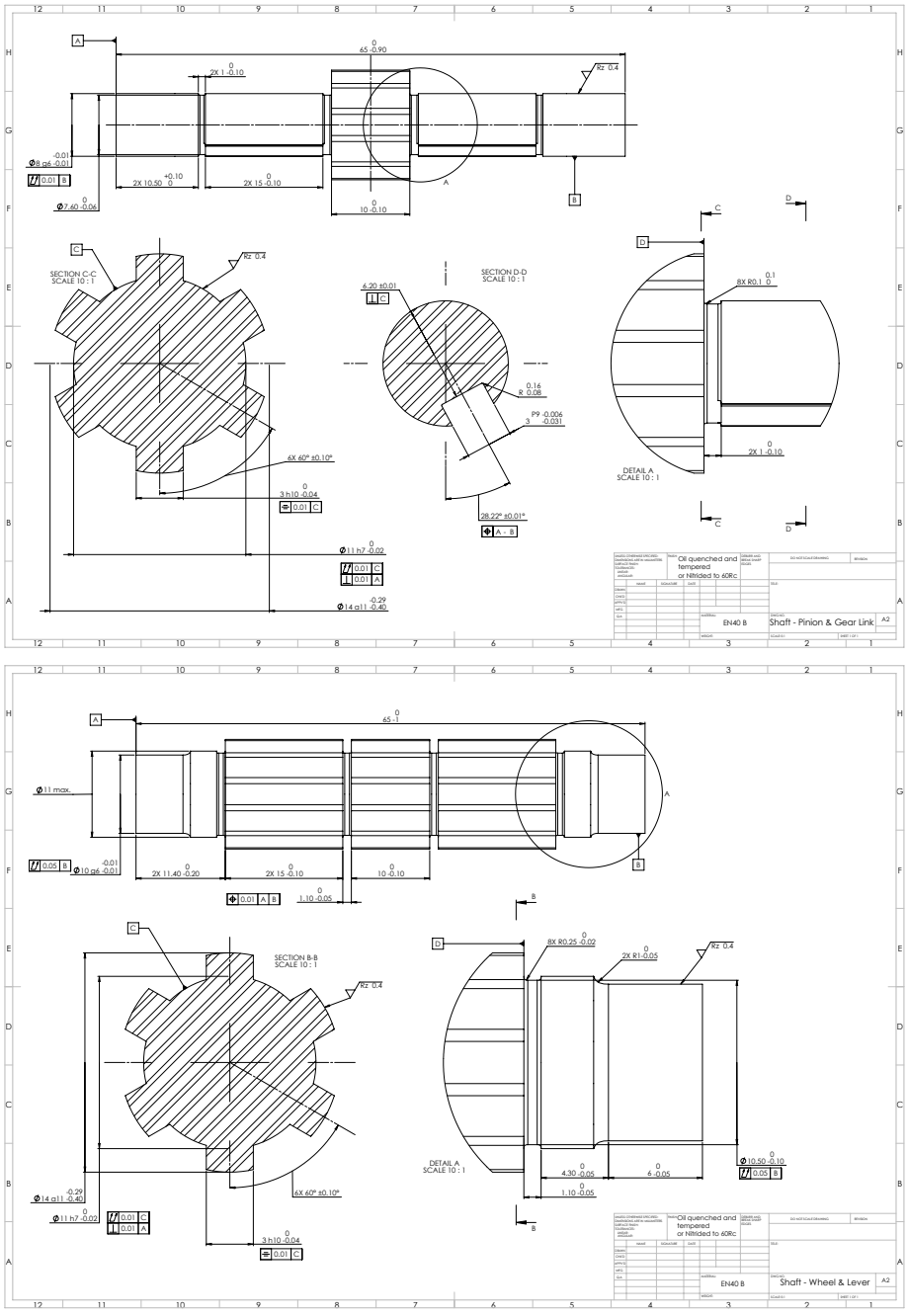


Figure E.10: Pinion shaft and Wheel shaft

Appendix F

Biomechanics study

F.1 Ethics, Consent, and Health questionnaire

To save page space on the final document, the ethics form, consent sheet, and health questionnaire can be requested by emailing the author at:

ben.morgan@swansea.ac.uk